The classified or limited status of this document applies to each page thereof unless otherwise marked. Separate page printouts MUST be marked accordingly.

Experimental Trim Drag Values for Conventional and Supercritical Wings

by

Peter Fredric Jacobs

B.S. May 1974, Iowa State University

A Thesis submitted to

The Faculty

of

The School of Engineering and Applied Science

of the George Washington University in

partial satisfaction of the requirements

for the degree of Master of Science

December 1981

Acknowledgements

The author wishes to thank the National Aeronautics and Space Administration (Langley Research Center) for the opportunity to complete all requirements for this degree. The author also wishes to thank Professor John P. Campbell for his support and advice and Miss Lori Nichols for her efforts in the preparation of this document.

TABLE OF CONTENTS

List of Figures

14. Variation of lift coefficient with angle of attack for supercritical wing configurations ($M_\infty = 0.82$).

a) H_1

b) H_2

c) H_3

d) H_4

e) H_5

15. Variation of drag coefficient with lift coefficient for supercritical wing configurations ($M_\infty = 0.82$).

a) H_1

b) H_2

c) H_3

d) H_4

e) H_5

16. Variation of pitching-moment coefficient with lift coefficient for supercritical wing configurations ($M_\infty = 0.82$, c.g. = 0.33$\bar{c}$).

a) H_1

b) H_2

c) H_3

d) H_4

e) H_5

17. Variation of drag coefficient with c.g. position for wide-body wing configurations ($M_\infty = 0.82$).

a) H_1

b) H_2

c) H_3

d) H_4

e) H_5

18. Variation of drag coefficient with c.g. position for supercritical wing configurations ($M_\infty = 0.82$).

a) H_1

b) H_2

c) H_3

d) H_4

e) H_5

NOMENCLATURE

a	Speed of sound
b	Wing span, for wide-body wing 116.12 cm (45.72 in.), for supercritical wing 134.54 (52.97 in.)
C_D	Drag coefficient, Drag/$q_\infty S$
C_L	Lift coefficient, Lift/$q_\infty S$
C_m	Pitching momemnt cofficient, Pitching moment/$q_\infty S\bar{c}$
C_T	Tail volume coefficient, $l_T S_T / c_W S_W$
c	Local streamwise chord
$\bar{c}$	Mean aerodynamic chord for wide-body wing 18.22 cm (7.175 in.), for supercritical wing 14.58 cm (5.742 in.)
$H_1 \ldots H_5$	Horizontal tails 1 through 5, respectively
$i_{H_1} \cdots i_{H_5}$	Incidence of horizontal tails 1 through 5, respectively, measured from fuselage waterline, positive with tail trailing edge down, degrees
L/D	Lift-to-drag ratio
l_T	Tail arm, distance from c.g. to a.c. of tail
M	Mach number
p	Local static pressure
p_t	Total pressure
p_1, p_2	Total pressure measured at yaw head tubes 1 and 2, respectively
q	Dynamic pressure
R	Universal gas constant
R_n	Reynolds number
R	Resultant velocity vector (see figure 35)
S	Planform area, for wide-body wing 0.193 m^2 (2.075 $ft.^2$), for supercritical wing 0.185 m^2 (1.988 ft^2)
T	Absolute temperature
t	Local maximum wing or tail thickness

U_∞	Free stream velocity in x-direction
u	Velocity perturbation in x-direction
V	Three dimensional velocity vector
V_1, V_2	Vertical tails 1 and 2, respectively
v	Velocity perturbation in y-direction
w	Velocity perturbation in z-direction
x	Streamwise distance
y	Spanwise distance, measured normal to model plane of symmetry
z	Vertical distance, measured normal to x
Γ	Dihedral of wing or tail, degrees
Δ	Incremental value
ΔC_D	Trim drag increment, $C_{D_{(\text{wing-body-vert. and horiz. tail})}} - C_{D_{(\text{wing-body-vert. tail})}}$

Λ Sweep of wing or tail, degrees

α Angle of attack, referred to fuselage waterline, degrees

γ Ratio of specific heat at constant pressure to specific heat at constant volume

ϵ Downwash angle, degrees

ϵ' Local streamwise wing section incidence angle, referred to fuselage waterline, positive for leading edge up, degrees

θ Angle between vectors of flow field (see figure 35)

λ Taper ratio of wing or tail trapezoidal planform

σ Angle between vectors of flow field (see figure 35)

ϕ Angle between vectors of flow field (see figure 35)

Subscripts:

avg Average value

$\bar{c}/4$ quarter chord of MAC

T (Refers to) horizontal or vertical tail

t Total conditions (i.e. conditions that would exist if the gas were brought to rest isentropically)

W (Refers to) the wing

∞ Free stream conditions

Abbreviations:

AR Aspect ratio, b^2/S

a.c. Aerodynamic center

c.g. or (C.G.) Center of gravity

F.S. Fuselage station, inches

MAC Mean aerodynamic chord

SCW Supercritical wing

CHAPTER 1

INTRODUCTION

1.1 General

The advent of fuel shortages and higher fuel prices has had a tremendous impact on the aviation industry. Aircraft designed in the 1950's and 1960's, when fuel was relatively cheap, are no longer profitable when flown at their design speeds. Consequently, airplane and engine manufacturers have been challenged to build more fuel efficient airplanes for today's environment. Within the National Aeronautics and Space Administration's Aircraft Energy Efficiency (ACEE) Program, research is being conducted in the areas of advanced aerodynamics, composite structures, and active control systems. The goal of the ACEE program is to reduce the drag of transport aircraft by 50 percent.

The development of advanced supercritical airfoils by Whitcomb (reference 1) has led to energy efficient transport wings (references 2 and 3) which have higher lift to drag ratios, thicker airfoil sections, less sweep, and higher aspect ratios, and which weigh no more than wings for current wide-body aircraft. Another characteristic of these advanced wings is an increased nose-down pitching moment caused by camber in the aft end of the supercritical airfoil section. The increased pitching-moment is of concern if the drag penalty required to trim it significantly reduces the performance benefits of the advanced wings.

Trim drag penalties are not unique to supercritical wings. Because of inherent static stability requirements, most current transport aircraft tend to have their aerodynamic center (a.c.) behind their center of gravity (c.g.). This arrangement necessitates a down load on the horizontal tail for

trim, which in turn forces the wing to produce more lift. The induced drag of the tail and extra induced drag on the wing constitute a major part of the trim drag, and if the aircraft is flying near its drag-divergence Mach number, the trim drag penalty can be large.

Advances in the area of active control technology may allow the next generation of jet transports to fly with relaxed static stability. It wil then be possible to have a smaller, lighter horizontal tail or a c.g. position further aft. Either o· both would result in smaller trim drag penalties (references 4 and 5). Obviously, much research on all aspects of drag reduction, including synergistic effects, is needed to reduce aircraft drag to an absolute minimum.

1.2 Objectives

The main objective of the present experimental investigation was to assess the trim drag of a high-aspect-ratio supercritical wing configuration relative to the trim drag of a current wide-body technology configuration. In order to have a direct comparison of the two wings, they were both tested on the same fuselage (figure 1). The fuselage closely simulated the fineness ratios of current wide-body aircraft fuselages. Each wing was tested in conjunction with five different horizontal tails, and the trim drag for each configuration was measured at simulated cruise conditions (M_∞ = .82).

One of the factors affecting horizontal tail efficiency is tail location. If the tail is in the wake of the wing (i.e. low tail position) the local dynamic pressure will be less than the free stream value and the tail will be less efficient. Locating the horizontal tail above the wing wake, as in T-tail configurations, insures that the horizontal tail will be

In addition to the force and moment data for these configurations, local flow angles and Mach numbers in the vicinity of the tails were measured with a yaw head rake. The localized flow fields near the tails provide important information on the interaction of the different wings and tails of this investigation.

CHAPTER 2

DESIGN OF TAIL SURFACES

2.1 General

The design of a tail surface is similar to the design of a wing; a compromise must be reached between all the design variables in order to meet the design objectives. In the design of a horizontal tail, for instance, the variables may be geometric (e.g. tail arm, planform area, vertical location, etc.) or aerodynamic (e.g. airfoil section, sweep, aspect ratio, thickness, etc.). The design requirements often drive the variables in opposite directions. The intersection points of these trends define the tail-variable minimums or maximums. The design requirements which tend to define the horizontal tails for current technology aircraft are: (1) sufficient tail download at take off conditions for aircraft rotation, and (2) a positive static stability margin or positive damping of short-period longitudinal oscillations at cruise conditions (references 5 and 6). For future aircraft with active controls and relaxed static stability, the second design requirement above may change to a pitch acceleration for positive control characteristics in the presence of gusts. The satisfaction of these particular design requirements offers the potential of reduced horizontal tail area, weight, and trim drag.

Obviously, optimum tail design is an interactive process for any one configuraton. The tails designed for this investigation were not optimized for either wing, but were representative of current aircraft and allowed comparisons of the trim drag characteristics of the two wings to be made.

2.2 Airfoils

The latest technology, NASA supercritical airfoils (reference 7) were used for all the horizontal and vertical tail surfaces. Supercritical airfoils characteristically have a large leading-edge radius, a relatively flat upper surface, and a reflexed "cusp" region aft on the lower surface. The relatively large leading-edge radius reduces the negative pressure coefficient peak on the upper surface associated with conventional airfoils. This reduced peak lessens the chances of flow separation at subcritical conditions. The flattened upper surface of the airfoils reduces flow velocities ahead of the shock wave and also the vertical extent of the supersonic flow region, thereby reducing the associated shock wave strength. Much of the improvement in the performance of the supercritical airfoils is due to the reduced strength of the shock wave on the upper surface of the airfoil and the elimination of shock-induced boundary-layer separation. It is this boundary-layer separation which causes substantial increases in drag, buffeting, and stability and control problems. Because the larger leading-edge radius and the flattened upper surface reduce the negative pressure coefficients, less lift is produced by the upper surface. To replace this lost lift, the cusp region was added to the lower surface. This region creates significant positive pressures on the lower surface. For this reason, supercritical airfoils are often referred to as "aft-loaded airfoils." It is the highly loaded cusp which produces nose-down pitching moments that are unfavorable from a trim drag point of view.

In a departure from the previously used method of designing airfoils (an iterative experimental procedure), the tail airfoils in this investigation were designed with the two-dimensional airfoil code of reference 8. The airfoils developed with this code follow the three principal guidelines of references 9 and 10. These guidelines produce airfoils with reduced strength shockwaves, little flow separation, and reduced drag.

The airfoils used for the horizontal and vertical tails are shown in figure 2. Relevant tail parameters are presented in table 1. A 10-percent-thick cambered supercritical airfoil was used for the cambered horizontal tails. The cambered tails had inverse camber in anticipation of tail downloads for trim. The cambered airfoil was designed for a lift coefficient of 0.4.

The 10-percent-thick symmetrical airfoil was used for the symmetrical horizontal tails and for the vertical tail of the low tail configuration. The symmetrical airfoil design evolved from the cambered airfoil. First the camber was removed, leaving an airfoil with the same thickness distribution as the cambered airfoil. This intermediate airfoil was unacceptable from a structural standpoint because of its reflexed aft end, which was due to the cove region on the lower surface of the cambered airfoil. The reflexed area did not leave enough thickness for control surface actuators. To alleviate this problem, additional thickness was added by maintaining the same trailing-edge thickness and fairing a straight line between the trailing edge and the coordinates at approximately 0.65 x/c. The new aft end of the airfoil was then blended smoothly into the forward section using the code of reference 8.

The 12-percent-thick symmetrical airfoil was used for the vertical tail of the T-tail configuration. This airfoil was simply a scaled-up version of the 10-percent thick symmetrical airfoil.

2.3 Planform

The planform shapes of the vertical tail and the three horizontal tails for the low tail configuration are shown in figure 3. The two smaller horizontal tails, designated H_1 and H_3, utilize the 10-percent-thick cambered and symmetrical airfoils, respectively. The larger horizontal tail, H_2, also utilizes the cambered airfoil. As previously mentioned, the vertical tail, V_1, has a 10-percent-thick symmetrical airfoil section.

The planform shapes of the vertical tail and two horizontal tails for the T-tail configuration are shown in figure 4. Horizontal tails H_4 and H_5 have cambered and symmetrical 10-percent-thick airfoil sections, respectively. The T-tail vertical tail, V_2, has a 12-percent-thick symmetrical airfoil section.

Planform details for the tails used in this investigation are presented in table 1. The tails were designed to have approximately the same tail volume coefficient as for current technology aircraft. Tail volume coefficient is a measure of the contribution of the tail to the overall stability level of the configuration, and is defined as $C_T = \frac{l_T S_T}{c_W S_W}$

In the design of the tails, the c.g. was set at 0.25 $\bar{c}$. This point occurs at the same fuselage station for both wings. Therefore, the tail arm, l_T, was the same for both wings. In addition, the wing planform area was nearly the same for each wing. The tail volume coefficients for each wing differ because the mean aerodynamic chord, $\bar{c}_W$, for the wide-body configuration is larger than for the supercritical wing configuration.

The tail area listed in table 1 for the horizontal tails is the trapezoidal area extended to the fuselage centerline, but for the vertical tails, the area shown is exposed area. Neglecting tail dihedral, horizontal tails H_1, H_3, H_4 and H_5 have the same geometry and planform. H_2, which is slightly larger than the other horizontal tails, was designed to have the same exposed area and tail volume coefficient as the T-tail horizontal tails H_4 and H_5.

CHAPTER 3

WIND TUNNEL TESTS

3.1 Objectives

Experimental aerodynamic force and moment data were measured at cruise conditions (M_∞ = 0.82, R_n = 5.0 x 10^6/ft.) for combinations of two different wings in conjunction with five separate horizontal tails mounted on a representative wide-body fuselage. Incidence changes of the horizontal tail plane provided sufficient drag coefficient data at trimmed (pitch equilibrium) conditions to compare the trim drag increments for a high aspect-ratio supercritical wing with the increments for a current wide-body-technology wing. The five horizontal tails were chosen to illustrate the effects of tail size, location, and camber on trim drag. In addition, yaw head rake data were taken with the horizontal tail removed, in order to provide local flow angle and Mach number details behind each wing.

3.2 Test Apparatus and Procedures

3.2.1 Test Facility

This investigation was conducted in the Langley 8-Foot transonic pressure tunnel (reference 11). This facility is a continuous-flow single-return rectangular slotted-throat tunnel. Tunnel controls allow independent variation of Mach number, density, stagnation temperature and dewpoint temperature. The test section is approximately 2.2 m (7.1 ft.) square (same cross-sectional area as that of a circle with a 2.4 m (8 ft.) diameter). The upper and lower walls are slotted axially, permitting the

test-section Mach number to be changed continuously throughout the transonic speed range. The slotted top and bottom walls each have an average open ratio of approximately 0.06. The stagnation pressure in the tunnel can be varied from a minimum of 0.25 atmosphere (1 atmosphere = 0.101 MN/m^2) at all Mach numbers to a maximum of approximately 2.00 atmospheres at Mach numbers less than 0.40. At transonic Mach numbers, the maximum stagnation pressure that can be obtained is about 1.5 atmospheres.

3.2.2 Model Description

Drawings of the model are shown in figures 1, 3 and 4. Photographs of the model in the Langley 8-foot transonic pressure tunnel are shown in figures 5 and 6.

The fuselage described in reference 2 was used for this investigation. The fuselage is 125.88 cm (49.56 in.) long and has a maximum diameter of 14.58 cm (5.74 in.). For both wings, the wing lower surface was faired into the fuselage to provide a relatively flat bottom which extended from near the leading edge to approximately 15.24 cm (6.0 in.) aft of the trailing edge.

Planform details for the wide body wing are shown in figure 3. The wing has 35° of sweep at the quarter-chord, 7.5° of dihedral inboard and 5.5° of dihedral outboard, an aspect ratio of 6.99, and a trapezoidal planform area of 0.193 m^2 (2.075 ft^2). Twist and thickness distributions are presented in figures 7 and 8, respectively. This wing was designed for a cruise Mach number of 0.82 and a lift coefficient of 0.45.

Planform details for the supercritical wing are shown in figure 4. The wing has 30° of sweep at the quarter-chord, 5° of dihedral, an aspect ratio of 9.80, and a trapezoidal planform area of 0.185 m^2 (1.988 ft^2). Twist and

thickness distributions are presented in figures 7 and 8, respectively. The airfoil sections used in this wing were designed for a two-dimensional section lift coefficient of 0.7. The three-dimensional effects of sweep, finite span, inboard airfoil modifications (reference 2), and fuselage interference all reduce the lift obtainable for this wing to a design lift coefficient of 0.55 at a cruise Mach number of 0.81.

Both horizontal tail configurations were designed with incidence blocks to allow variation of the tail-plane incidence from -4° to 4° in 0.5° increments. The tails rotated about an axis through the quarter-chord of the mean aerodynamic chord of each tail and perpendicular to the fuselage axis. Filler plugs covered the tail attachments for the tail-off configurations.

3.2.3 Boundary-Layer Transition

The transition location of the boundary layer was fixed for all model components with carborundum grit set in a plastic adhesive. The transition strips were 0.127 cm (0.05 in.) wide and were sized using the techniques of reference 12. Transition strip patterns for the wide-body and supercritical wings are presented in figures 9 and 10, respectively. The aft positions of the grit on the upper surface of the wings was determined from analysis of oil flow photographs (reference 13) of each configuration near its drag-rise Mach number and cruise lift coefficient. The aft grit locations on the wing were used to simulate a higher effective Reynolds number (reference 14). Boundary-layer transition strips of #120 carborundum grit were located 0.3 c back from the leading edges on the upper and lower surfaces of all the horizontal and vertical tails. In addition, a transition strip of #120 carborundum grit was located 2.54 cm (1.00 in.) from the nose of the fuselage.

3.2.4 Measurements

Aerodynamic force and moment data were obtained using a six-component electrical strain-gage balance. The quoted accuracy of the balance is 0.5 percent of the full scale values (normal force 2500 lbs, axial force 200 lbs, pitching moment 3500 in-lbs, rolling moment 2000 in-lbs, yawing moment 2000 in-lb, side-force 500 lbs). The repeatability of the data was generally better than the accuracy, however. Several configurations were repeated at different times during the test and drag coefficient values repeated to within 0.0002. Because of the large number of model configurations, the amount of data required and wind tunnel scheduling problems, this investigation was spread over four separate tunnel entries. An offset in the drag values for the second entry was discovered near the end of the testing. This offset affects only the data for the wide-body wing with horizontal tail H_2. While the absolute values of the drag data are in question, the incremental values due to tail incidence changes are not affected.

An accelerometer attached to the balance block was used to measure angle of attack. Static pressures were measured in the model along the sting cavity by using differential-pressure transducers referenced to tunnel plenum static pressure. Two yaw head rakes were used to measure the crossflow and downwash components of the flow field in the vicinity of the horizontal tails. Details of the rake are presented in the appendix.

The angle of attack of the model was corrected for flow angularity in the tunnel test section. This correction was obtained from upright and inverted tests of the baseline configurations. Drag data presented herein have been adjusted to correspond to the condition of free-stream static pressure acting in the balance chamber and at the base of the fuselage.

No correction to the data have been made to account for wind tunnel wall interference effects. Also, the frontal area of the model was sufficiently small to avoid having to correct Mach number for wind-tunnel blockage effects (reference 15).

CHAPTER 4

RESULTS OF WIND TUNNEL TESTS

The static longitudinal aerodynamic characteristics for the five wide-body configurations are presented in figures 11 - 13 and the data for the five supercritical wing configurations are presented in figures 14 - 16. The longitudinal data were initially reduced to coefficient form using the quarter-chord of the mean aerodynamic chord ($\bar{c}/4$) as the c.g. location. Analysis of the data showed that the longitudinal stability parameter, $\Delta C_m/\Delta C_L$, was too large, resulting in unrealistically stable cruise configurations for both the wide-body and supercritical wings. Due to a longer tail arm, the T-tail configurations were even more stable than the low-tail configurations. Normally, wide-body aircraft at cruise conditions fly with a static margin of approximately 7 - 8 percent. The uncambered low-tail horizontal, H_3, was considered to be closest to the horizontal tails on actual wide-body aircraft, therefore the c.g. position for the wide-body configurations was moved aft to provide a static margin of approximately 7 percent for the H_3 tail at cruise conditions. The c.g. for the supercritical-wing configurations was also moved back to provide a similar static margin for the H_3 tail at cruise conditions. The c.g. position for all the wide-body configurations was fixed at $0.35\bar{c}$ and the position for all supercritical-wing configurations was fixed at $0.33\bar{c}$. All the longitudinal aerodynamic data presented herein have been reduced using these two c.g. positions.

4.1 Force and Moment Data

Several important trends are evident from the aerodynamic force and moment data. From the variation of lift coefficient with angle of attack plots (figures 11 and 14), it can be shown that at low lift coefficients all the horizontal tails are producing downloads for the tail incidences tested. The tail download causes a net loss of lift when compared with the wing-body-vertical tail configurations at the same angle of attack. At some higher angle, however, the wide-body configurations experience more upwash due to angle of attack than downwash due to the wing, resulting in an upload on the tail. Obviously, the point at which the configuration with a horizontal tail produces more total lift than for the wing-body-vertical tail configuration depends on the horizontal tail incidence and airfoil section. Because of its higher design lift coefficient and lift-curve slope, the supercritical wing produces more downwash than the wide-body wing at the same angle of attack. For this reason, the supercritical wing is still producing lift beyond the lift coefficient where the wide-body wing stalls, and in only a few instances at very high lift coefficients do the horizontal tails experience an upload.

The effect of an upload on the tail is apparent from the variation of drag coefficient with lift coefficient (figures 12 and 15). With an upload on the tail, the wing can be at a lower angle of attack to achieve the same total lift. Lowering the angle of attack of the wing reduces the drag for the configuration. The data for the wide-body wing show this tendency for the configurations with tail uploads at higher angles of attack. Due to its higher aspect ratio, the supercritical wing has less induced drag than the wide-body wing and operates at a higher L/D. Even at higher angles of attack, the horizontal tails usually trim with downloads, and although the

drag values for the configurations with horizontal tails approach the values for the wing-body-vertical tail configuration, they do not cross over and become less.

It should be noted that the T-tail vertical tail produces more drag than the low-tail vertical tail (figures 12 a, d, and 15 a, d). The leading- and trailing-edge fairings at the tip of the T-tail vertical were not optimized and some local flow separation may be present. For the purposes of this investigation, the absolute drag level is not as important as the trim drag increments between the different configurations.

The longitudinal stability characteristics of the supercritical and wide-body configurations are shown in figures 13 and 16. The low-tail configurations for both wings are heavily influenced by the downwash and wake of the wings. The three low-tail configurations (figures 13 a, b, c and 16 a, b, c) all tend to pitch up at lift coefficients beyond the cruise lift coefficient, regardless of the wing involved. Notice that the tails are more effective in conjunction with the supercritical wing (i.e. the increment in C_m due to tail incidence changes is greater).

The T-tail configurations (figures 13 d, e and 16 d, e) are more stable than the low-tail configurations because of the longer tail arm. The supercritical wing shows much less tendency to pitch up than the wide-body wing with tails H_4 and H_5; in fact, the supercritical wing configurations pitch down sharply at the higher lift coefficients. It is not known whether these configurations would trim out again at even higher lift coefficients and develop classic "deep stall" problems (references 16 and 17).

From the data presented in figures 11 - 16, it is possible to construct trimmed drag polars for each combination of wing and horizontal tail at a fixed c.g. position (stability level). Another way of presenting the data

is to assume that each configuration can be trimmed at any desired lift coefficient by moving the c.g. position. The resulting plots present the variation of trimmed drag coefficient with c.g. position for a fixed lift coefficient. Because of the interest in relaxed static stability and its effect on trim drag, the latter method was chosen to present the data from this investigation. Data for the wide-body and supercritical wing configurations are presented in figures 17 and 18, respectively. Data for the corresponding wing-body-vertical tail configurations are plotted with centered symbols. The drag increment between each horizontal tail configurations and the corresponding wing-body-vertical tail configuration at the same lift coefficient represents the total drag increment due to the addition of the horizontal tail, including skin friction.

For most lift coefficients, all five tail configurations show reductions in the trim drag as the c.g. is moved aft. The reductions are greater at the higher lift coefficients. At their respective design lift coefficients (0.45 and 0.55), the wide-body configurations trim with tail uploads and the supercritical wing configurations trim with tail downloads for most tail incidence angles tested. The trim drag increments for each wing at its design point are summarized in figures 19 and 20.

Numerous attempts have been made to calculate trim drag increments analytically (references 18 - 27). The various methods used to calculate trim drag tend to produce differing opinions on whether a tail upload or download results in lower trim drag. None of these simplified methods are capable of handling compressibility effects, which may occur at transonic speeds and can be on the order of half of the total trim drag. Accurate predictions of trim drag for specific configurations flying at transonic

speeds await the development of more powerful computers and more accurate methodology. The simplified methods do indicate interesting trends which may be useful as a starting point for tail design, however. In general, most methods agree that rearward movement of the c.g or a longer tail arm result in smaller tail loads and reduced trim drag. Also, the mutual interference between the flow fields of the wing and the tail can be an important factor on trim drag. A wing which has high induced drag benefits from an upload on the tail. As previously mentioned, an upload on the tail unloads the wing and can result in significant trim drag savings. A wing with less induced drag may not require an upload on the tail. In fact, a downloaded tail in the presence of sufficient wing downwash causes the tail lift vector to be rotated in a forward direction, resulting in a "tail thrust" component which reduced trim drag. The data presented in figures 19 and 20 substantiate these trends.

The wide-body wing (figure 19) has more induced drag due to its smaller aspect ratio, and the symmetrical tails H_3 and H_5 show definite trim drag advantages for tail uploads. The cambered tails H_2 and H_4 show an increase in trim drag with tail uploads, probably because the tails were built with the airfoils "upside down" (inverse camber) in anticipation of tail downloads for trim. Obviously, these tails are not efficient at producing uploads and have higher trim drag increments. The behavior of horizontal tail H_1 is dissimilar to the other tails. For some small range of tail incidence, H_1 first experiences reduced trim drag increments due to tail thrust on a downloaded tail. As the tail load becomes more positive, the tail thrust component disappears and the trim drag increases. For further small increases in tail upload, the induced drag of the wide body wing is reduced

until the point at which which the cambered tail becomes inefficient at producing uploads. It is not understood why the larger cambered tail, H_2, does not follow this same trend, however. Nevertheless, after the difference in skin friction is accounted for, the smaller tail H_1 has a trim drag increment 0.0006 less than for the larger tail H_2. Both T-tails, H_4 and H_5 have smaller trim drag increments than any of the low tail configurations. The symmetrical T-tail, H_5, has a trim drag increment which is 0.0003 less than its skin friction increment, which implies that the upload on the tail has significantly reduced the induced drag on the wide-body wing.

With its higher aspect ratio and reduced induced drag, the supercritical wing would be expected to have reduced trim drag increments with a tail download or less of a tail upload than for the wide-body wing. The more negative tail incidence angles required for trim (figure 20), in conjunction with greater downwash substantiates this prediction. As for the low-tail configurations with the wide-body wing, the large cambered tail H_2 has the highest trim drag increments, followed by the smaller cambered tail H_1, and the symmetrical tail H_3. This time, both H_1 and H_2 have peculiar variations of trim drag increment with tail incidence (c.g. position). Again, the cambered tails may experience reduced trim drag due to tail thrust ($i_{H_1} = -2°$, $i_{H_2} = -1.5°$), a loss of tail thrust as the c.g. moves aft and the tail incidence angles become more positive, and then as the c.g. moves further aft, the smaller tail downloads reduce the wing induced drag, lowering the trim drag. The large cambered tail H_2 also has an increase in trim drag at $i_{H_2} = -2°$. This may be due to greater induced drag on the tail itself for this highly downloaded case. To varying extent, all five tails show reduced trim drag increments as the c.g. is moved aft. The T-tails have less trim drag than

the low-tail configurations; and while both H_4 and H_5 have trim drag increments equal to their skin friction values, the symmetrical tail H_6 would appear to have even lower trim drag if the data were extrapolated to a more aft c.g. position.

The most important information to be gained from the increments presented in figures 19 and 20 is that the supercritical wing can be trimmed without a large increase in trim drag compared to the wide-body wing. The maximum increase in trim drag coefficient was $\Delta C_D = 0.0003$, which is less than one percent of the total drag of the supercritical wing at cruise conditions ($M_\infty = 0.82$, $C_L = 0.55$). This means that the performance gains for the supercritical wing are not significantly eroded when a tail is added.

The effect of the tails on the overall performance of each wing is presented in figure 21. The increases in L/D for the supercritical wing over the wide-body wing with just the low-tail vertical and T-tail vertical are 10.9 percent and 11.8 percent, respectively. When the horizontal tails are added, the increases in L/D for the supercritcal wing with the optimum low-tail and T-tail incidences are 11.2 and 11.3, respectively. The L/D's for the best T-tail configurations are lower than those for the best low tail configuration because of the higher drag for the T-tail vertical tail. Hopefully, some of this drag could be reduced with a more optimally shaped fairing at the tip of the T-tail.

4.2 Yaw Head Rake Data

Two yaw head rakes were used to measure the local flow angles and Mach numbers in the vicinity of the horizontal tails. The rakes were attached to the sting aft of the model. Each rake had four five-tube yaw heads like those shown in references 28 and 29, which measure both the downwash and crossflow components of the local flow field.

The principle behind the yaw head rake is illustrated in figure 22. This cut-away view shows three total head tubes with a 90° angle between the faces of the outside tubes. If the local flow angle is inclined at an angle ε to the yaw head axis, then the total pressure measured by tube one (p_1) is greater than the total pressure measured by tube 2 (p_2). The difference in pressure, $p_1 - p_2$, is proportional to the flow angle ε. The rake is calibrated by inclining it at a known angle to the flow and measuring the differences in pressures between the opposite tubes of the yaw head. Then when taking data, the measured pressure difference at the yaw heads can be related back to a flow angle. More details of the design and calibration of the yaw head rakes are presented in the appendix.

A photograph of the yaw head rake used with the low-tail configurations is shown in figure 23 and a drawing of the rake is shown in figure 24. The three static pressure tubes located between the yaw heads are used to calculate local Mach number. Photographs of the rake installations for the low-tail and T-tail configurations are presented in figures 25 and 26, respectively.

The rakes were centered vertically on the horizontal tail reference planes at the root of the horizontal tails for the low-tail and T-tail configurations. Rake data was taken at two spanwise locations for each configuration (figures 27 and 28).

Downwash data for the two wings are presented in figures 29 - 30. In addition to the variation of downwash with angle of attack, the rate of change of downwash with angle of attack is also plotted. It can be shown (reference 30) that the rate of change of downwash with angle of attack, $\Delta\varepsilon/\Delta\alpha$, has an effect on the stability of the configuration. The tail contribution to stability is proportional to $1 - (\Delta\varepsilon/\Delta\alpha)$. A positive increase in $\Delta\varepsilon/\Delta\alpha$ reduces the contribution of the tail to the overall stability level. Usually this happens when the tail is influenced by the wake of the wing.

The rake data show that for the portions of the flow field measured, the T-tail configurations have higher levels of downwash and a fairly linear change in down wash with yaw head position. This effect is described in references 31 and 32, and is caused by the flow field converging toward the wake of the wing. The result is an increase in the downwash above the wake and a decrease in the downwash below the wake. As expected, the supercritical wing has higher levels of downwash for both the low-tail and T-tail configurations due to its higher design lift coefficient and lift curve slope.

From the nonlinearity of the values of $\Delta\varepsilon/\Delta\alpha$, it is obvious that the wing wake influences the low-tail configurations significantly more than the T-tail configurations. The dynamic pressure in the wake of the wing is less than free stream and can adversely affect the performance of the tail, as was shown in the trim drag data previously presented.

From the yaw head rake data, it is possible to compute components of the flow in all three axis directions as well as the local Mach number. The resultant three dimensional flow field velocity vectors have been projected

onto a plane perpendicular to the freestream flow direction in figures 31 - 34 to show the crossflow components of the flow with the corresponding local Mach numbers. The view point is one looking downstream at the left-hand tails. Flow angles for the bottom yaw head of the wide-body low-tail configuration are not presented in figures 29a and 31 due to plugged tubes which gave incorrect pressure measurements. Local Mach numbers are not presented for the top yaw head for the supercritical wing low-tail configuration (figure 33). For this run, the center total head tube was partially plugged, giving small Mach number errors. The flow field velocity vectors shown for this yaw head were computed using the erroneous Mach numbers. However, since the pressure differences at a fixed angle have only a small variation with Mach number in the rake calibration, the error in the computed flow angle is insignificant (see appendix).

The low-tail data (figures 31 and 33) show a definite crossflow toward the body due to the closure angle of the fuselage. The position of the wing wake can be tracked by watching the local Mach numbers decrease as the angle of attack increases. A steady movement of the wake vertically is shown, as well as local flow separation for angles of attack greater than 5°. The influence of the wing wake is more apparent for the supercritical wing due to the thicker airfoils used.

In contrast to the low tail data, the T-tail data (figures 32 and 34) show an outward crossflow component which is due to the flowfield of the T-tail vertical. The local Mach numbers inboard are also higher for the same reason. It should be noted that both T-tail rake positions for the wide-body

wing were further forward than for the supercritical wing (see figure 28), resulting in a greater influence from the flow field of the vertical tail and higher local Mach numbers. Since the horizontal tail is above the wing wake, the local Mach numbers are fairly constant with angle of attack for the T-tail configurations.

CHAPTER 5

SUMMARY AND CONCLUSIONS

5.1 General

The purpose of the present study is to determine if advanced supercritical wings incur higher trim drag values than current wide-body technology wings. In order to measure relative trim drag increments at cruise conditions, an experimental wind tunnel investigation was conducted in the Langley 8-foot transonic pressure tunnel utilizing a high aspect-ratio supercritical wing and a wide-body type wing, in conjunction with five different tail configurations, mounted on a representative wide-body fuselage. Secondary objectives of the investigation included measuring the effects of horizontal tail size, location (height), and camber on the trim drag increments for the two wings.

From the results of this investigation, it is possible to make the following conclusions.

1. The trim drag values for the supercritical wing configurations were not significantly higher than for wide-body configurations. The maximum increase in trim drag coefficient was $\Delta C_D = 0.0003$, which is less than one percent of the total drag of the supercritical wing configurations at cruise conditions. ($M_\infty = 0.82$, $C_L = 0.55$).

2. For the wide-body wing with its higher induced drag, lower trim drag values result with horizontal tail uploads. An upload on the tail reduces the lift the wing must produce, which translates into a lower angle of attack and less overall drag for the configuration. Conversely, the high aspect ratio supercritical wing has less induced drag, and lower trim drag values results with small downloads on the tail. With sufficient downwash, a downloaded tail can produce "tail thrust" which lowers the trim drag.
3. Both wings showed a reduction in trim drag for the smaller cambered low tail H_1 compared with the large cambered tail H_2. In addition, most of the tails showed a reduction in trim drag as the c.g. was moved aft. A configuration with relaxed static stability could take advantage of both a smaller horizontal tail and an aft c.g. position, resulting in significant drag reduction.
4. For the range of tail incidences tested, the cambered tails H_1 and H_4 had higher minimum trim drag increments than the corresponding symmetrical tails H_3 and H_5. Obviously, the inverse camber was inefficient for producing the uploads required to trim the wide-body configurations, and there was probably too much camber to generate the small downloads required to trim the supercritical wing configurations.

5. The T-tail configurations for both wings had lower trim drag increments than the low tail configurations since they were not in the wake of the wing. The dynamic pressures in the wake were less than free stream, reducing the efficiency of the low tail configurations. However, since the T-tail vertical had more drag than the low tail vertical, the overall drag levels for the optimum T-tail configurations were slightly higher than for the optimum low tail configuration.

6. The optimum performance for both wings was achieved with the symmetrical low tail H_3 and the optimum T-tail was the symmetrical tail H_5. The addition of a horizontal tail lowers the maximum L/D for each wing, but the improvement in L/D for the supercritical wing over the wide-body wing remains approximately 11 percent for the optimum low tail and T-tail configurations.

5.2 Suggested Further Research

The results of the present study are very encouraging; however, several areas of interest should be investigated further. First, an attempt should be made to to reduce the drag of the T-tail vertical. If successful, additional trim drag reductions would result. Secondly, horizontal tails with less inverse camber should be tested with the supercritical wing. A tail with only a small amount of camber may produce the downloads required for trim more efficiently than a symmetrical tail. Lastly, the symmetrical tails should be modified to have full span elevators. Both tail uploads and downloads could then be achieved through elevator angle changes instead of tailplane incidence changes.

APPENDIX: YAW HEAD RAKE DESIGN AND CALIBRATION

The resultant velocity vectors plotted in figures 31 - 34 are the projection of the three dimensional flow field velocity vectors at each yaw head projected onto a plane perpendicular to the free stream flow direction. From figure 35, it can be shown that the resultant velocity vector can be calculated if the downwash angle ε, the crossflow angle σ, and the magnitude of the three dimensional flow vector V are known. Assuming this is true, R' and the angle with respect to the y axis ϕ can be calculated as follows.

$$v = \text{TAN}\sigma\ (U_\infty + u) \tag{A.1}$$

$$w = \text{TAN}\varepsilon\ (U_\infty + u) \tag{A.2}$$

$$R' = \sqrt{v^2 + w^2} \tag{A.3}$$

Substituting equations A.1 and A.2 into equation A.3, we have

$$R = (U_\infty + u)\sqrt{\text{TAN}^2\sigma + \text{TAN}^2\varepsilon} \tag{A.4}$$

Also, we can see that

$$\text{TAN}\theta = \frac{R}{U_\infty + u} \tag{A.5}$$

Substituting A.4 into A.5, we have

$$\text{TAN}\theta = \sqrt{\text{TAN}^2 + \text{TAN}^2\varepsilon} \tag{A.6}$$

and $$\theta = \text{TAN}^{-1}\left(\sqrt{\text{TAN}^2\sigma + \text{TAN}^2\varepsilon}\right) \tag{A.7}$$

It can also be shown that

$$R' = V\ \text{SIN}\theta \tag{A.8}$$

Since we know V, σ, and ϵ, we can now compute R'. From figure 37, we see that

$$\text{TAN}\phi = \frac{w}{v} \tag{A.9}$$

Substituting A.1 and A.2 into A.9, we have

$$\text{TAN}\phi = \frac{\text{TAN } \epsilon}{\text{TAN } \sigma} \tag{A.10}$$

and finally

$$\phi = \text{TAN}^{-1} \left(\frac{\text{TAN } \epsilon}{\text{TAN } \sigma} \right) \tag{A.11}$$

As previously mentioned, ϵ and σ can be determined from the pressure differences across the opposite tubes of the yaw head (figure 22). The magnitude of V must be determined from the local static pressure p and the local total pressure pt. If we assume that at the rake, the flow is isentropic (no shock waves), adiabatic (no heat transfer), and that we have a perfect gas, we can use equations 29b, 44, and 46 from reference 33 to calculate V as follows.

$$\frac{p}{p_t} = \left(1 + \frac{\gamma-1}{2} M^2 \right)^{\frac{-\gamma}{\gamma-1}} \qquad \text{(Eqn. 44 Ref. 33)}$$

Solving this equation for the local Mach number M, we have

$$\left(\frac{p}{p_t} \right)^{\frac{-\gamma-1}{\gamma}} = 1 + \frac{\gamma-1}{2} M^2 \tag{A.12}$$

$$\left(\frac{p_t}{p} \right)^{\frac{\gamma-1}{\gamma}} = 1 + \frac{\gamma-1}{2} M^2 \tag{A.13}$$

$$\left(\frac{p_t}{p} \right)^{\frac{\gamma-1}{\gamma}} - 1 = \frac{\gamma-1}{2} M^2 \tag{A.14}$$

$$\frac{2}{\gamma-1}\left(\left(\frac{p_t}{p}\right)^{\frac{\gamma-1}{\gamma}} - 1\right) = M^2 \qquad (A.15)$$

$$M = \sqrt{\frac{2}{\gamma-1}\left(\left(\frac{p_t}{p}\right)^{\frac{\gamma-1}{\gamma}} - 1\right)} \qquad (A.16)$$

Other useful equations are

$$\frac{a}{a_t} = \frac{1}{\sqrt{1 + \frac{\gamma-1}{2} M^2}} \qquad \text{(eqn. 46 ref. 33)}$$

$$a = \sqrt{\gamma RT} \qquad \text{(eqn. 29b ref. 33)}$$

where R in this instance is the gas constant, and Mach number is defined as

$$M = \frac{V}{a} \qquad (A.17)$$

Rewriting eqn. 46, we have

$$a = \frac{a_t}{\sqrt{1 + \frac{\gamma-1}{2} M^2}} \qquad (A.18)$$

Substituting equations 29b and A.17 into equation A.18, we have

$$\frac{V}{M} = \frac{\sqrt{\gamma RT_t}}{\sqrt{1 + \frac{\gamma-1}{2} M^2}} \qquad (A.19)$$

Solving for the magnitude of the local three dimensional flow vector V, we have

$$V = \frac{M\sqrt{\gamma RT_t}}{\sqrt{1 + \frac{\gamma-1}{2} M^2}} \qquad (A.20)$$

The calibration of the yaw head rakes was performed with the tunnel empty. The rakes were attached to the string as far forward as possible to reduce any influence from the front of the string. The calibration consisted of running through an angle of attack sweep at Mach numbers from 0.55 to 0.90. The top and bottom tubes of each yaw head were calibrated with the rake in its normal vertical orientation. To calibrate the left and right tubes of each yaw head, the rake was rotated 90° and a similar angle of attack sweep was taken for each Mach number. The pressure differences for each set of opposing tubes was then nondimensionalized by dividing by the local dynamic pressure at each yaw head. Each yaw head for both rakes then had a three dimensional calibration table of $\frac{\Delta p}{q}$ versus ε or σ for six different free stream Mach numbers. Because the local static and total pressure measurements varied with the angle of attack of the rake, the local Mach numbers measured for each yaw head were less than the free stream values. This effect is described in reference 28. Local Mach number correction tables were set up for each yaw head to eliminate this problem. The tables consisted of an incremental Mach number to be added to each yaw head at each vertical calibration angle. There was a different table for each free stream calibration Mach number. The procedure for correcting local Mach number and flow angle was as follows:

1. Calculate the local downwash angle ε, using the erroneous local Mach number value when interpolating in the calibration tables.

2. Find the local Mach number correction, using the ϵ calculated in step 1 and the free stream Mach number for interpolation in the local Mach number correction table.

3. Add the local Mach number correction found in step 2 to the local Mach number measured in step 1.

4. Recompute the flow angles ϵ and σ using the corrected local Mach number when interpolating in the calibration tables.

As a check, the new procedure was used to compute flow angles and local Mach numbers for the calibration runs. The maximum errors were 0.21 degrees for flow angle and 0.002 for Mach number, indicating that further refinements were unnecessary.

The yaw head rakes had a fairly linear variation of pressure difference $\Delta p/q$ with flow angle. In addition, there was very little change in the calibrations with Mach number (figure 36). Therefore, small errors in the measurement of local Mach number have a negligible effect on flow angle calculations. Minor differences between calibrations of individual yaw heads can be attributed to the accuracy of construction of the rakes. A close up photograph of a typical yaw head is shown in figure 37. Slight imperfections such as this do not significantly affect the data.

REFERENCES

1. Whitcomb, Richard T.: A View of NASA Supercritical Airfoils. Presented at the Ninth Congress of the International Council of the Aeronautical Sciences, Haifa, Israel, August 25-30, 1974.

2. Bartlett, Dennis W.: Wind Tunnel Investigation of Several High Aspect-Ratio Supercritical Wing Configurations on a Wide-Body-Type Fuselage. NASA TM X-71996, July 1977.

3. Bartlett, Dennis W.; and Patterson, James C., Jr.: NASA Supercritical-Wing Technology. NASA TM-78731, July 1978.

4. Pope, G. G.: Prospects for Reducing the Fuel Consumption of Civil Aircraft. Presented at Energy and Aerospace; Proceedings of the Anglo/American Conference, London, England, December 5-7, 1978.

5. Urie, D. M.; and Reaser, J. S.: Aerodynamic Development of a Small Horizontal Tail for an Active Control Relaxed Stability Transport Application. Presented at the Atmospheric Flight Mechanics Conference for Future Space Systems, Boulder, Colorado, August 6-8, 1979.

6. Hofman, L. Gregor; and Clement, Warren F.: Vehicle Design Considerations for Active Control Application to Subsonic Transport Aircraft. NASA CR-2408, August 1974.

7. Bobbitt, Percy J.: Modern Fluid Dynamics of Subsonic and Transonic Flight. Presented at the AIAA "Global Technology 2000", Baltimore, Maryland, May 6-8, 1980.

8. Bauer, F.; Garabedian, P.; Korn, D.; and Jameson, A.: Supercritical Wing Sections II. Lecture Notes in Economics and Mathematical Systems, M. Beckmann and H. P. Lunzi, eds., Springer-Verlag, C. 1975.

9. Harris, Charles D.: Aerodynamic Characteristics of the 10-Percent-Thick NASA Supercritical Airfoil 33 Designed for a Normal-Force Coefficient of 0.7. NASA TM X-72711, July 1975.

10. Harris, Charles D.: Aerodynamic Characteristics of a 14-Percent-Thick NASA Supercritical Airfoil Designed for a Normal-Force Coefficient of 0.7. NASA TM X-72712, July 1975.

11. Schaefer, William T., Jr.: Characteristics of Major Active Wind Tunnels at the Langley Research Center. NASA TM X-1130, 1965.

12. Braslow, Albert L.; and Knox, Eugene C.: Simplified Method for Determination of Critical Height of Distributed Roughness Particles for Boundary-Layer Transition at Mach numbers from 0 to 5. NACA TN 4363, 1958.

13. Loving, Donald L.; and Katzoff, S.: The Fluorescent-Oil Film Method and Other Techniques for Boundary-Layer Flow Visualization. NASA MEMO 3-17-59L, 1959.

14. Blackwell, James A., Jr.: Preliminary Study of Effects of Reynolds Number and Boundary-Layer Transition Location on Shock-Induced Separation. NASA TM D-5003, 1969.

15. Brooks, Joseph D.: Some Anomalies Observed in Wind-Tunnel Tests of a Blunt Body at Transonic and Supersonic Speeds. NASA TN D-8237, 1976.

16. Taylor, Robert T.; and Ray, Edward J.: Deep Stall Aerodynamic Characteristics of T-tail Aircraft. NASA SP-83, pp. 113-121, 1965.

17. Taylor, Robert T.; and Ray, Edward J.: Factors Affecting the Stability of T-Tail Transports. Journal of Aircraft, Vol. 3, July 1966, pp. 359-364.

18. McKinney, Linwood W.; and Dollyhigh, Samuel M.: Some Trim Drag Considerations for Maneuvering Aircraft. Journal of Aircraft, Vol. 8, August 1971, pp. 623-629.

19. Goldstein, S. E.; and Combs, C. P.: Trimmed Drag and Maximum Flight Efficiency of Aft Tail and Canard Configurations. AIAA Paper 74-69, 1974.

20. Lutze, F. H., Jr.: Reduction of Trimmed Drag. NASA CR-145627, pp. 307-318, 1975.

21. Larrabee, E. E.: Trim Drag in the Light of Munk's Stagger Theorem. NASA CR-145627, pp. 319-329, 1975.

22. Lamar, John E.: Minimum Trim Drag Design for Interfering Lifting Surfaces Using Vortex-Lattice Methodology. NASA SP-405, pp. 89-111, 1976.

23. McLaughlin, Milton D.: Calculations, and Comparison with an Ideal Minimum, of Trimmed Drag for Conventional and Canard Configurations Having Various Levels of Stability. NASA TN D-8391, May 1977.

24. Laitone, E. V.: Ideal Tail Load for Minimum Aircraft Drag. Journal of Aircraft, Vol. 15, March 1978, pp. 190-192.

25. Shevell, R. S.: Comment on "Ideal Tail Load for Minimum Aircraft Drag". Journal of Aircraft, Vol. 15, September 1978, page 639.

26. Sachs, G.: Minimum Trimmed Drag and Optimum c.g. Position. Journal of Aircraft, Vol. 15, August 1978, pp. 456-459.

27. Lutze, F. H., Jr.: Trimmed Drag Considerations. Journal of Aircraft, Vol. 14, June 1977, pp. 544-546.

28. Bryer, D. W.; and Pankhurst, R. C.: Pressure-Probe Methods for Determining Wind Speed and Flow Direction, Her Majesty's Stationery Office, 1971.

29. Dudzinski, Thomas J.; and Krause, Lloyd, N.: Flow-Direction Measurement with Fixed-Position Probes. NASA TM X-1904, October 1969.

30. Dommasch, Daniel O.; Sherby, Sydney S.; and Connolly, Thomas F.: Airplane Aerodynamics. Fourth ed. Pitman Publishing Corp. 1967.

31. Silverstein, Abe.; and Katzoff, S.: Experimental Investigation of Wind-Tunnel Interference on the Downwash Behind an Airfoil. NACA Report No. 609, 1937.

32. Silverstein, Abe.; Katzoff, S.; and Bullivant, W. Kenneth: Downwash and Wake Behind Plain and Flapped Airfoils. NACA Report No. 651, 1939.

33. Ames Research Center: Equations, Tables, and Charts for Compressible Flow. NACA Report 1135. U.S. Government Printing Office, 1953.

EXPERIMENTAL TRIM DRAG VALUES FOR CONVENTIONAL AND SUPERCRITICAL WINGS

by

Peter F. Jacobs

(Abstract)

The purpose of the present study was to determine if advanced supercritical wings incur higher trim drag values at cruise conditions than current wide-body technology wings. Significantly higher trim drag would lessen the performance benefits to be gained from the aerodynamically advanced supercritical wings. Relative trim drag increments were measured in an experimental wind tunnel investigation conducted in the Langley 8-foot transonic pressure tunnel. The tests utilized a high aspect-ratio supercritical wing and a current wide-body wing, in conjunction with five different horizontal tail configurations, mounted on a representative wide-body fuselage. The three low-tail configurations and two T-tail configurations were chosen to measure the effects of horizontal tail size, location, and camber on the trim drag increments for the two wings. Longitudinal force and moment data and yaw head rake data were taken at a

Mach number of 0.87 and design cruise lift coefficients for the wide-body and supercritical wings of 0.45 and 0.55, respectively. The data indicate that the supercritical wing does not have significantly higher trim drag than the wide-body wing. The wide-body wing had lowest trim drag increments for tail uploads and the supercritical wing had lowest increments with slight tail downloads. A reduction in tail size, combined with relaxed static stability, produced trim drag reductions for both wings. The cambered tails had higher trim drag increments than the symmetrical tails for both wings, and the T-tail configurations were more efficient than the low-tail configurations. The increase in performance (lift-to-drag ratio) for the supercritical wing over the wide-body wing was 11 percent for both the optimum low-tail and T-tail configurations.

TABLE 1. - TAIL PARAMETERS

	Tail	t/c, Airfoil	S_T $m^2(Ft^2)$	b_T cm(in)	$\Lambda_{c/4}$,deg	λ	AR	Γ,deg	C_T	
									Wide Body	SCW
Low Tail	H_1	.10, cambered	.05 (.55)	6.59 (16.74)	32.5	.35	3.54	10	.69	.90
	H_2	.10, cambered	.07 (.70)	7.72 (19.60)	32.5	.31	3.82	10	.86	1.12
	H_3	.10, symmetrical	.05 (.55)	6.59 (16.74)	32.5	.35	3.54	10	.69	.90
	V_1	.10, symmetrical	.04 (.42)	3.94 (10.0)	35	.35	1.65	--	.51	.67
T-tail	H_4	.10, cambered	.05 (.56)	6.68 (16.98)	32.5	.35	3.59	-3	.84	1.09
	H_5	.10, symmetrical	.05 (.56)	6.68 (16.98)	32.5	.35	3.59	-3	.84	1.09
	V_2	.12, symmetrical	.04 (.47)	2.76 (7.0)	45	.70	.72	--	.52	.68

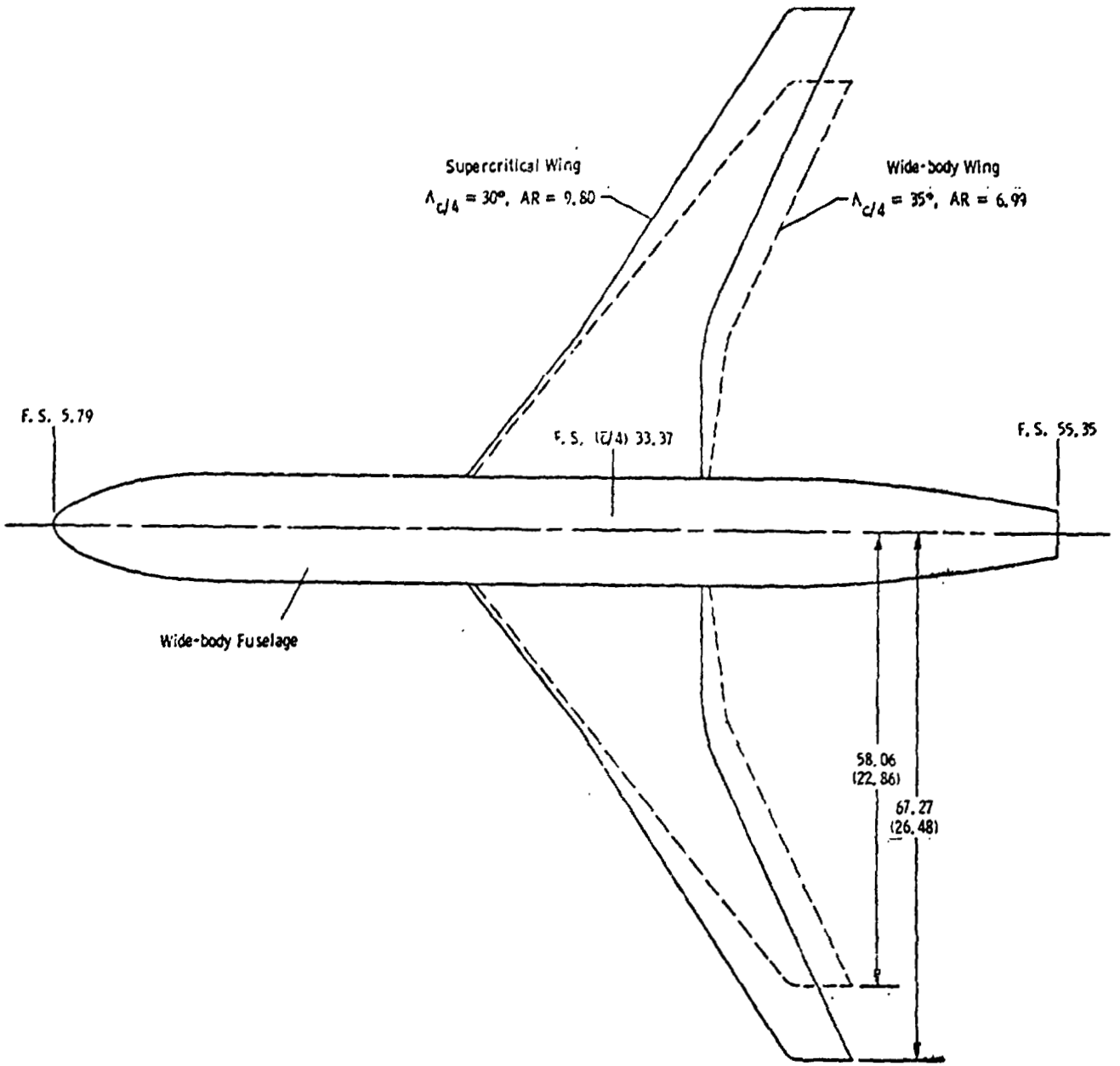

Figure 1. - Drawing of wing planforms on fuselage.

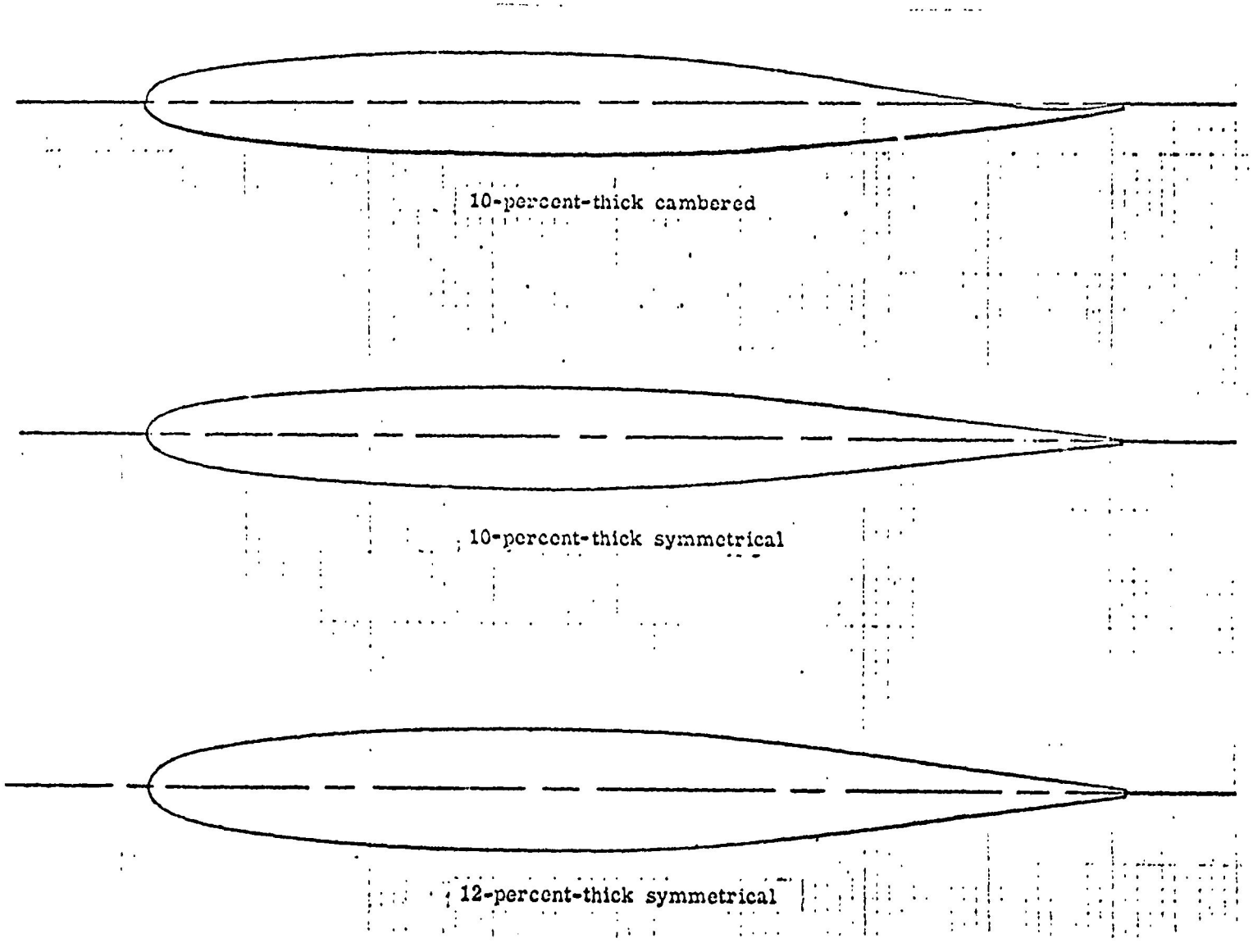

Figure 2. - Horizontal and vertical tail supercritical airfoil sections.

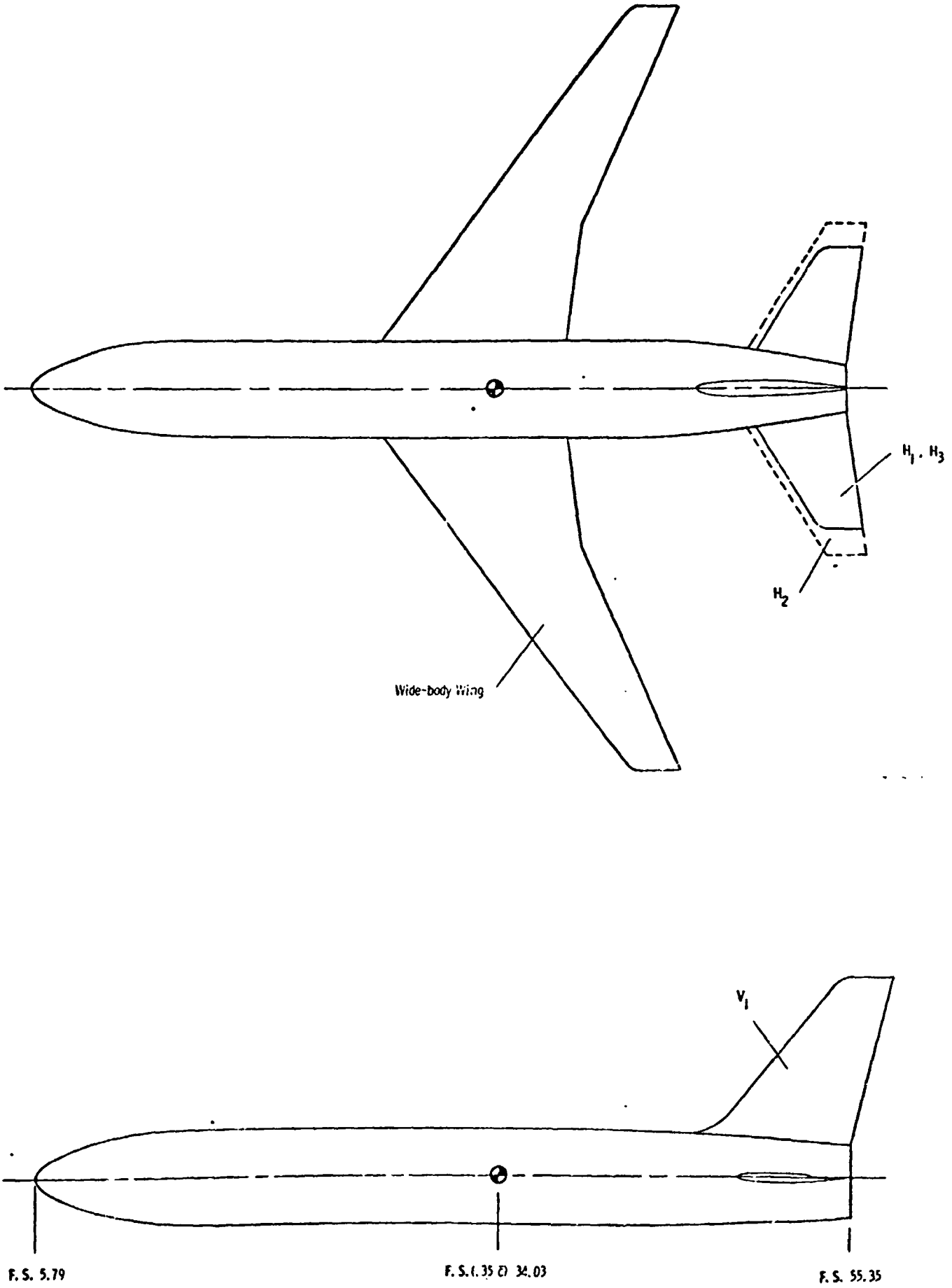

Figure 3.- Drawing of low-tail configurations.

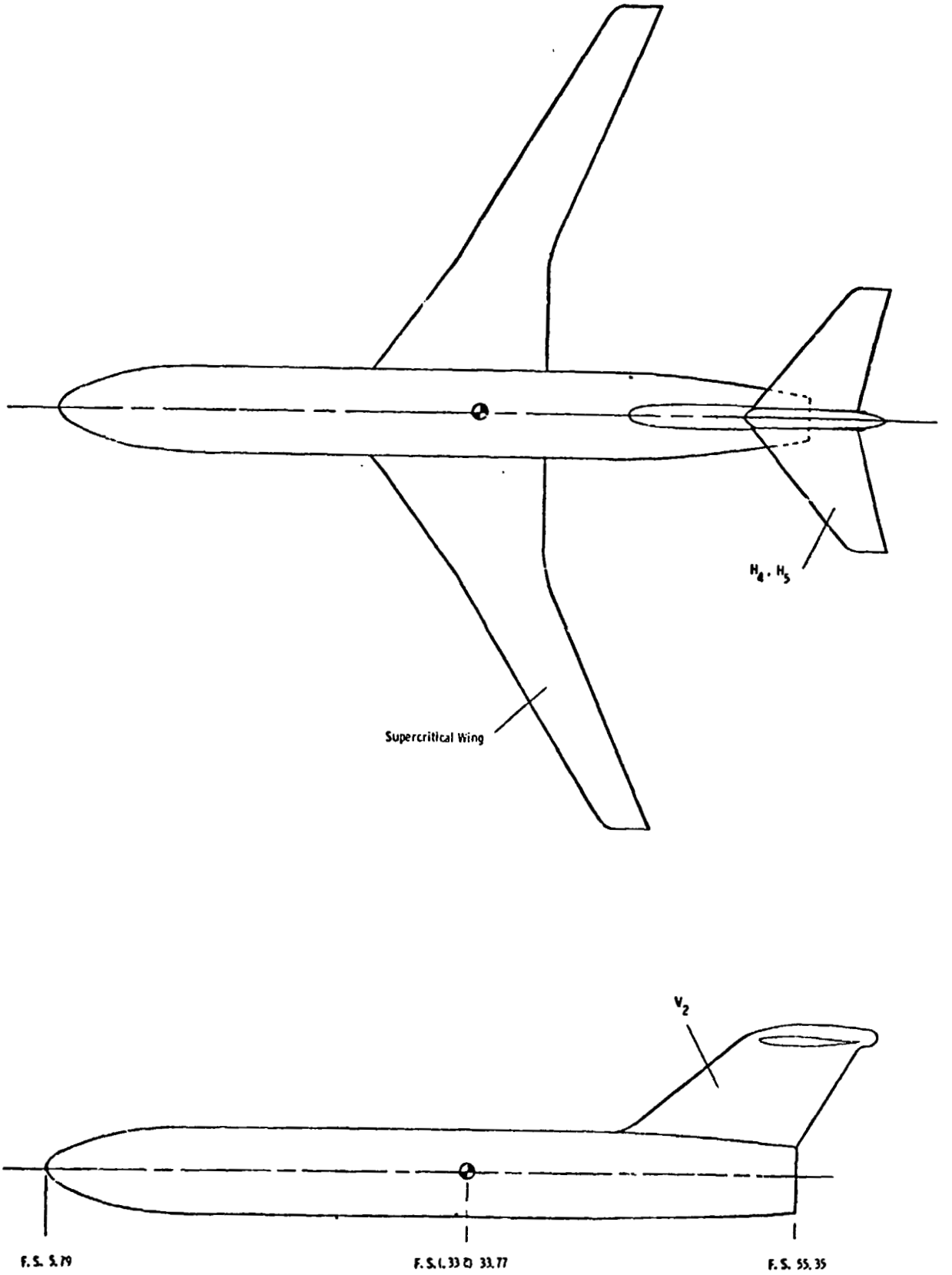

Figure 4. - Drawing of T-tail configurations.

Figure 5.- Photograph of typical low-tail configuration.

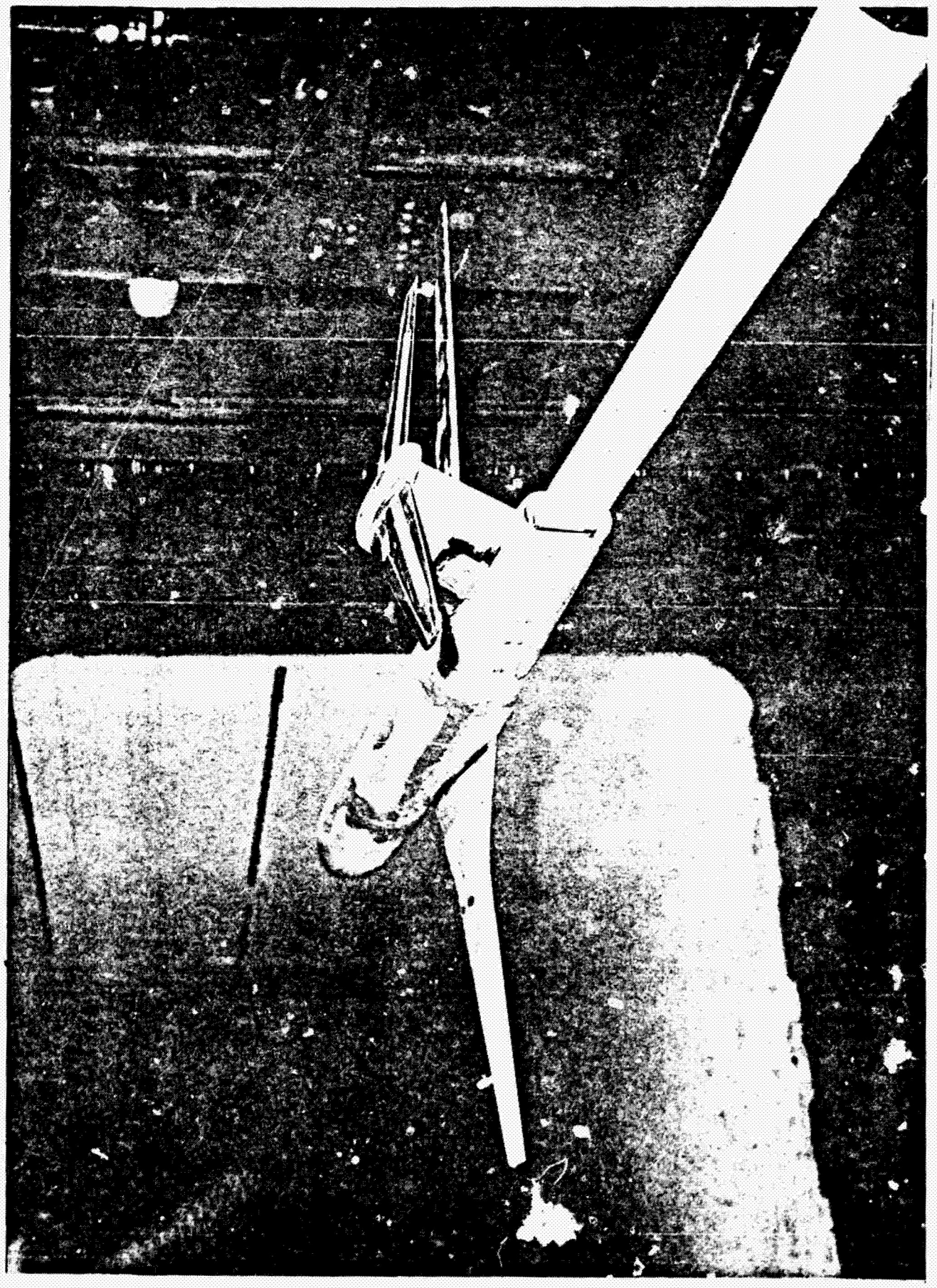

Figure 6.- Photograph of typical T-tail configuration.

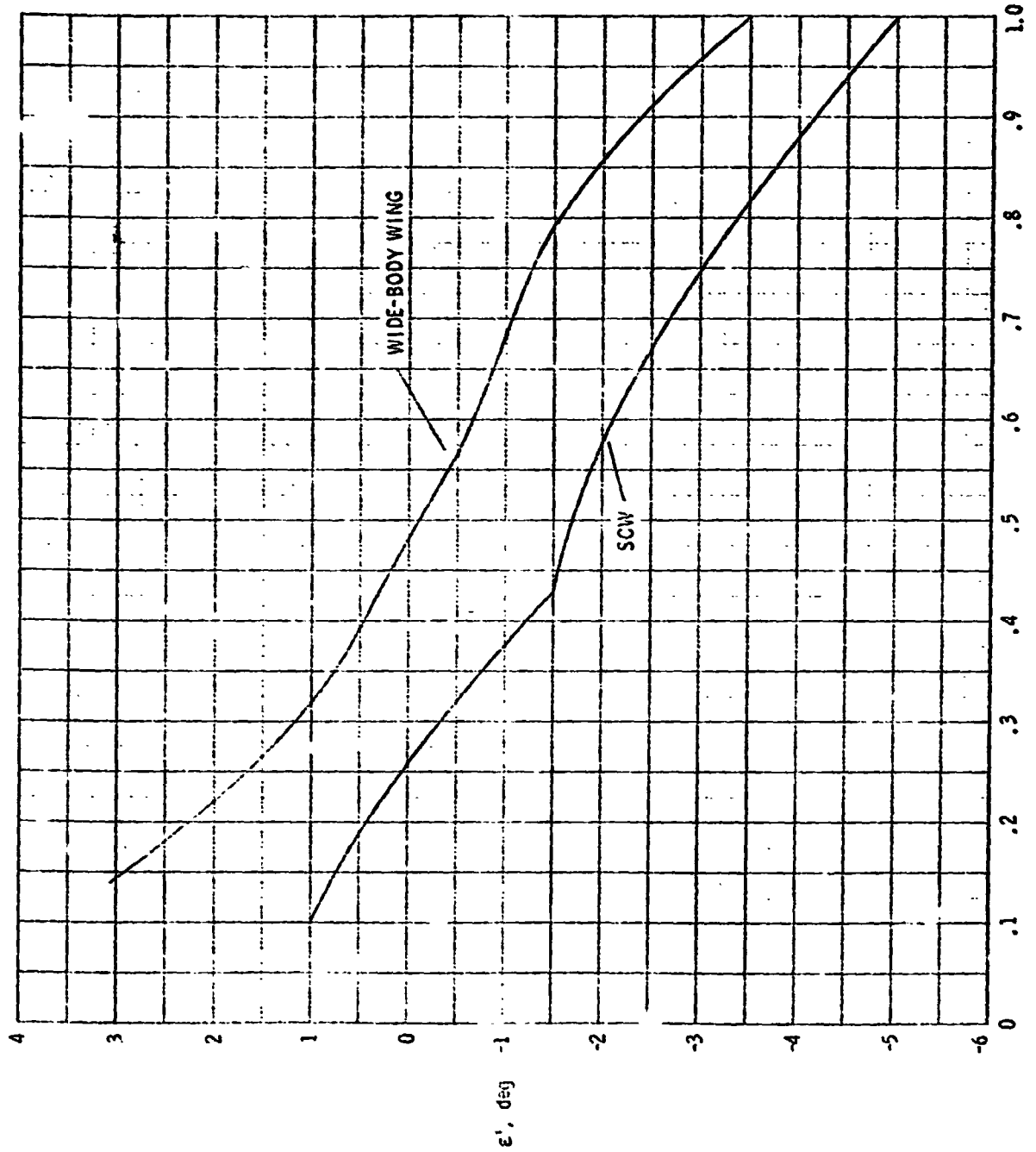

Figure 7.- Twist distribution for both wings.

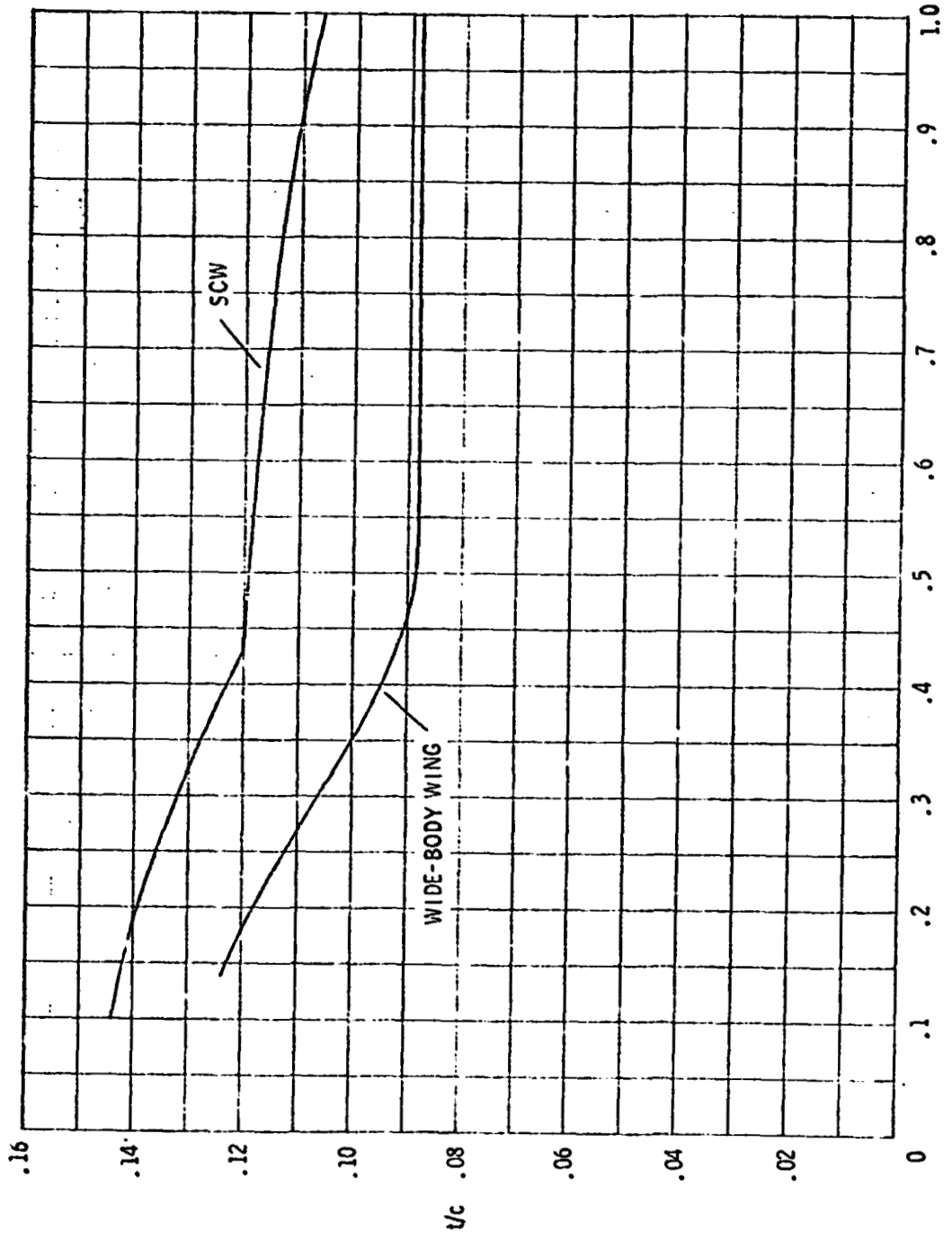

Figure 8.- Thickness distribution for both wings.

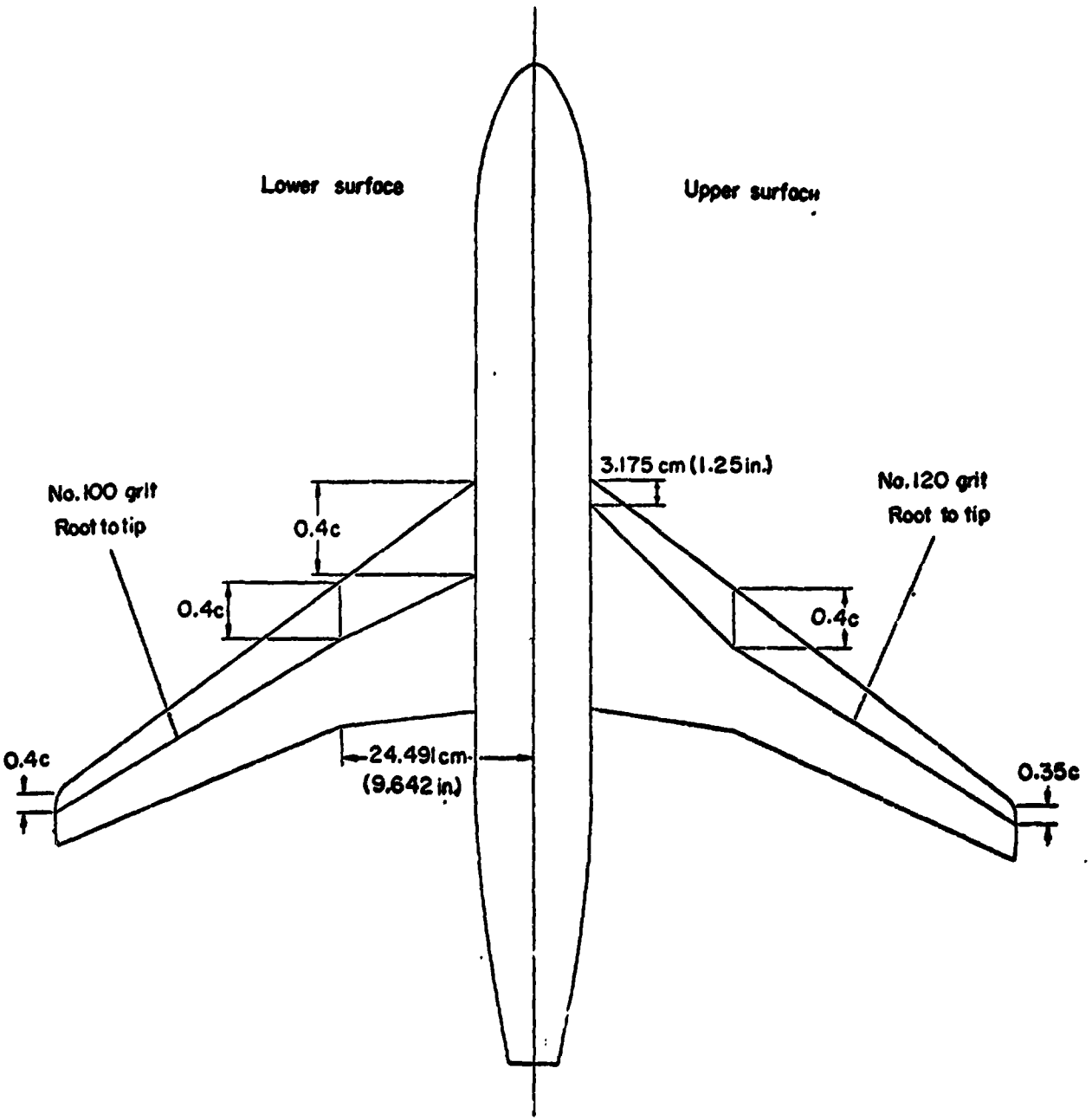

Figure 9.- Boundary-layer transition strip patterns for the wide-body wing.

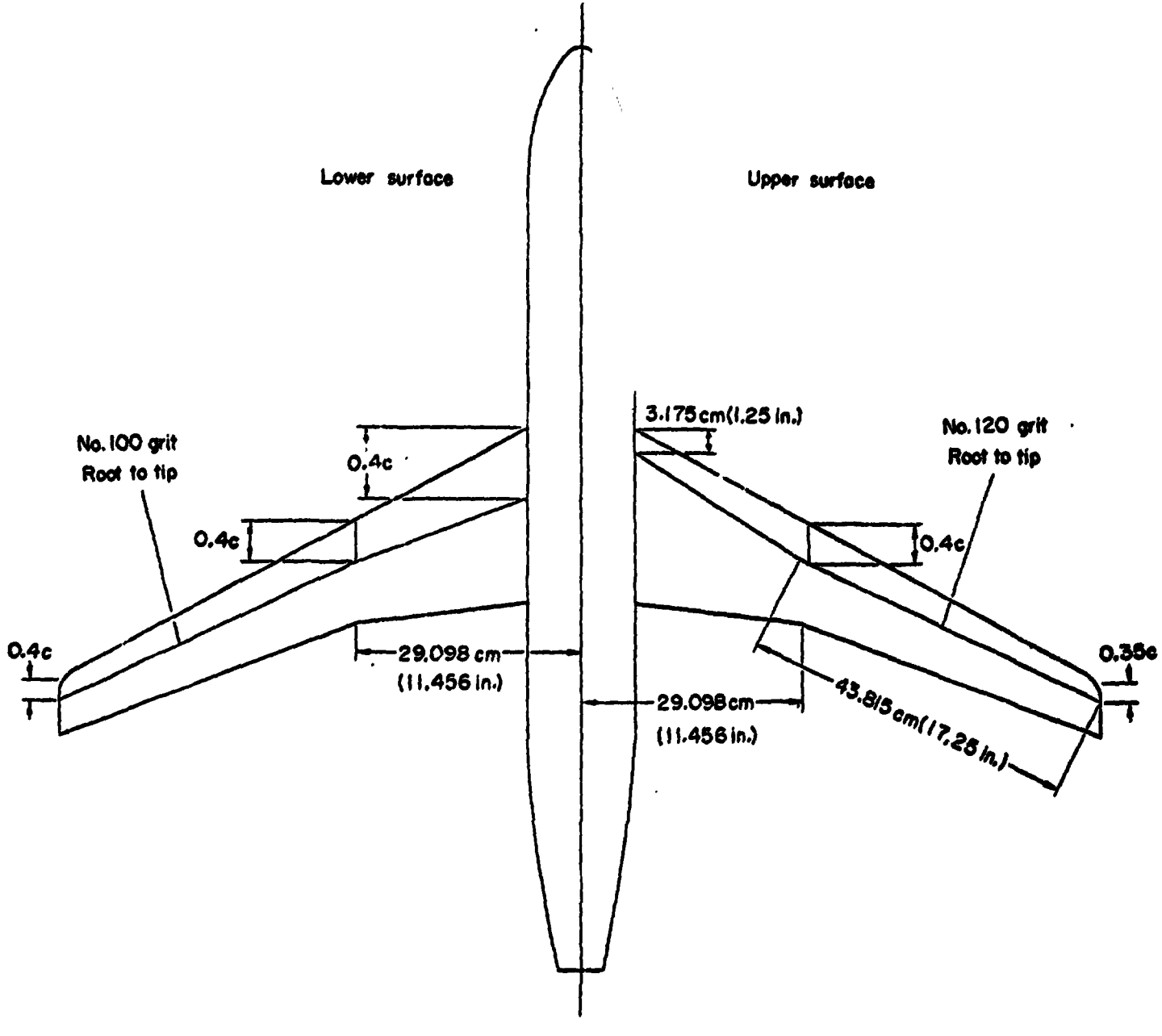

Figure 10.- Boundary-layer transition strip patterns for the supercritical wing

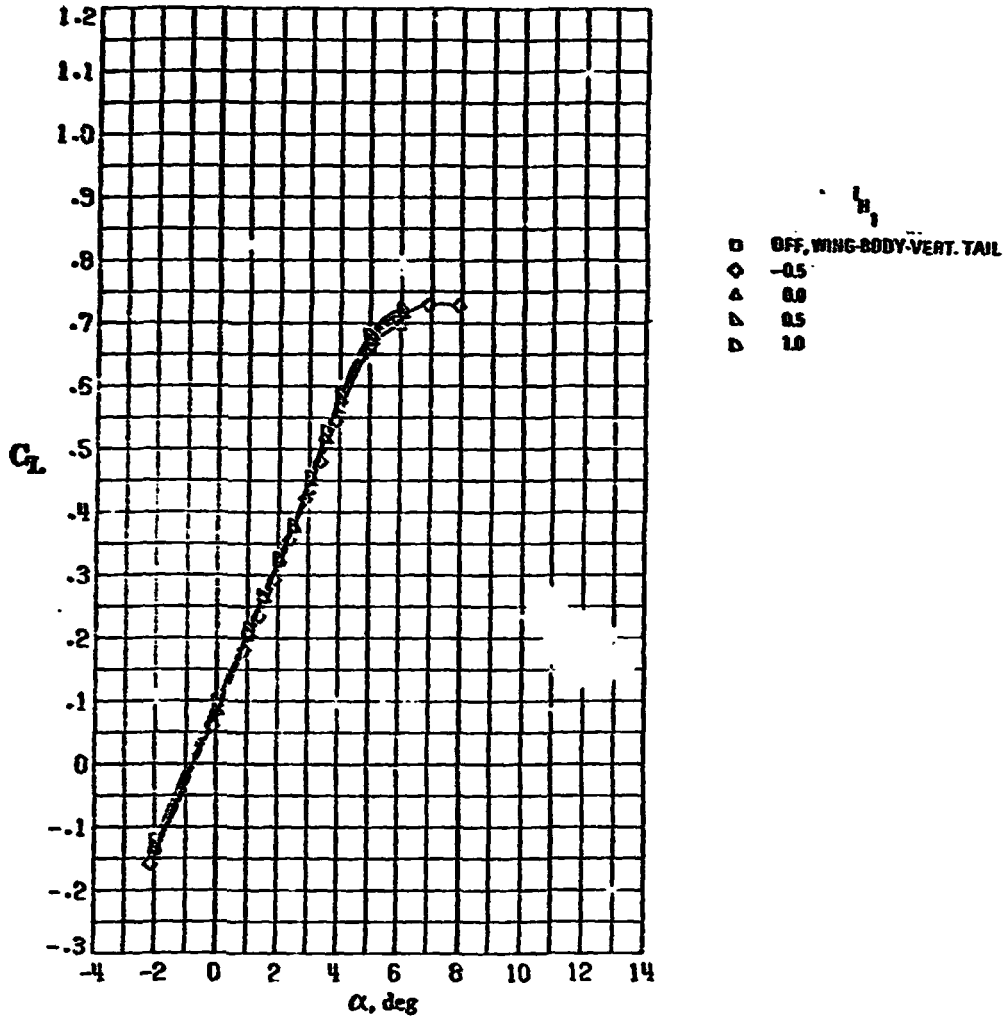

(a) H_1

Figure 11.- Variation of lift coefficient with angle of attack for wide-body wing configurations (M_∞=0.82).

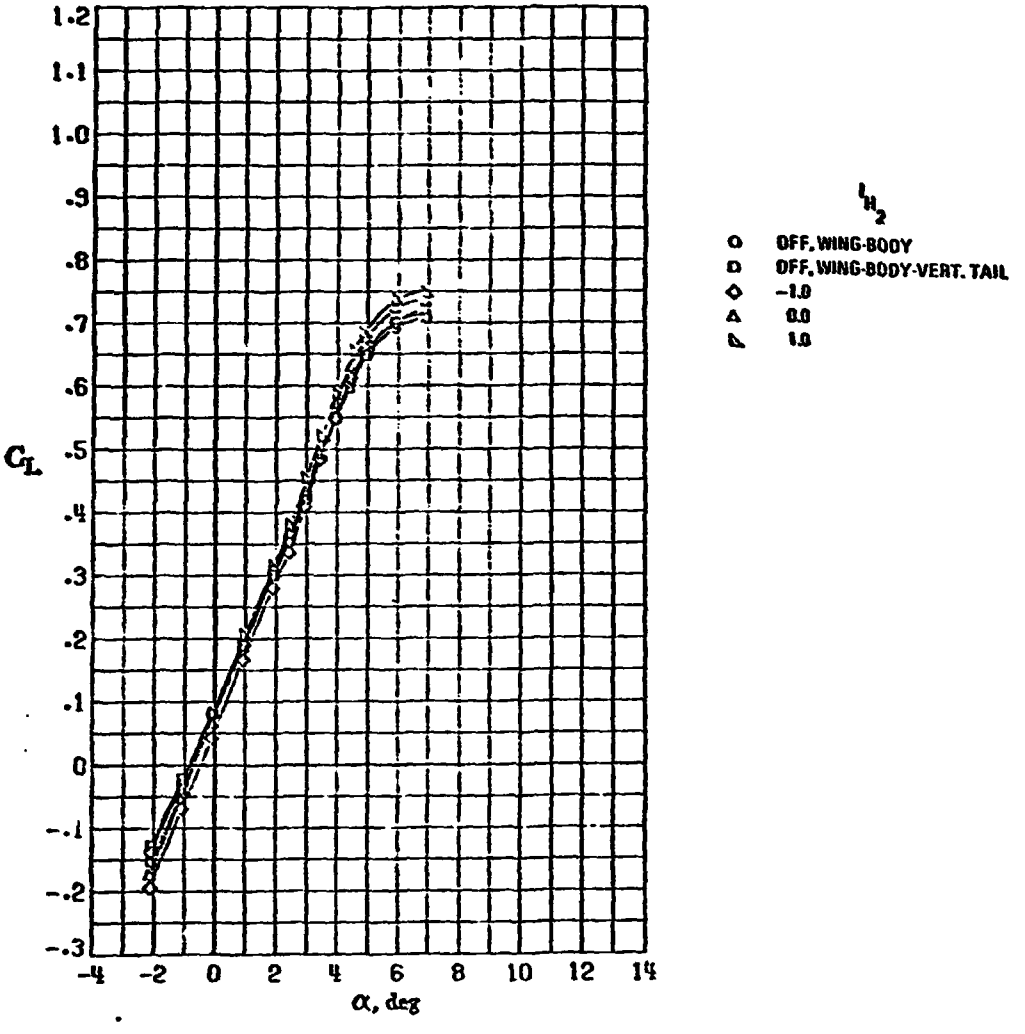

(b) H_2

Figure 11.-Continued.

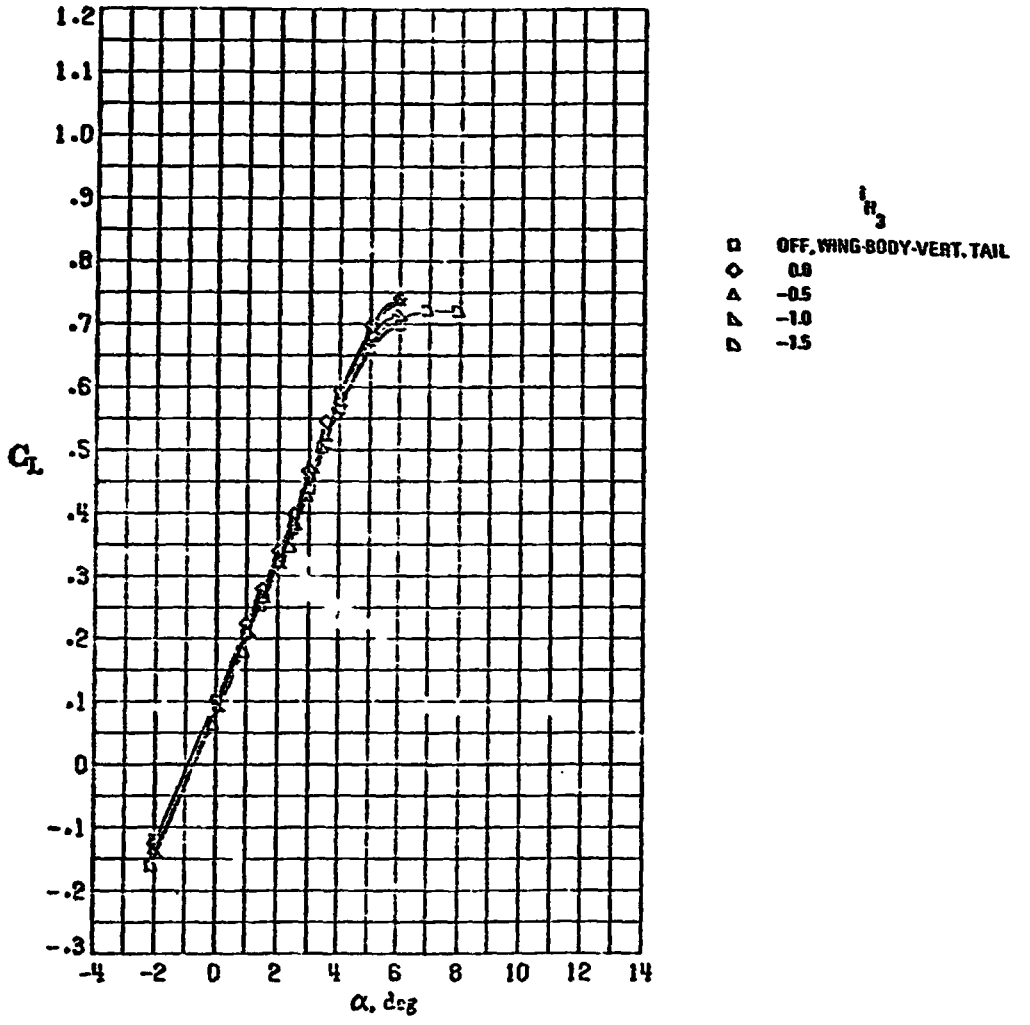

(c) H_3

Figure 11.- Continued.

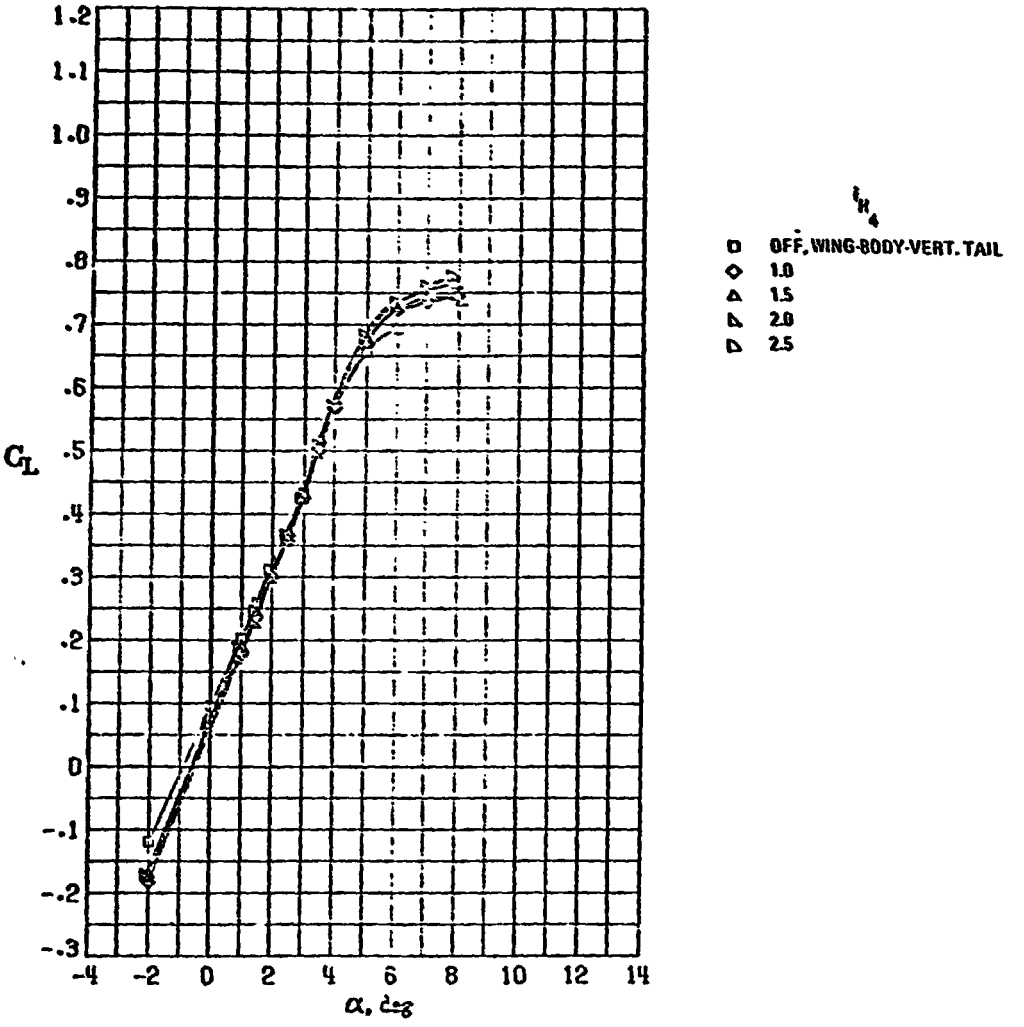

(d) H_4

Figure 11. -Continued.

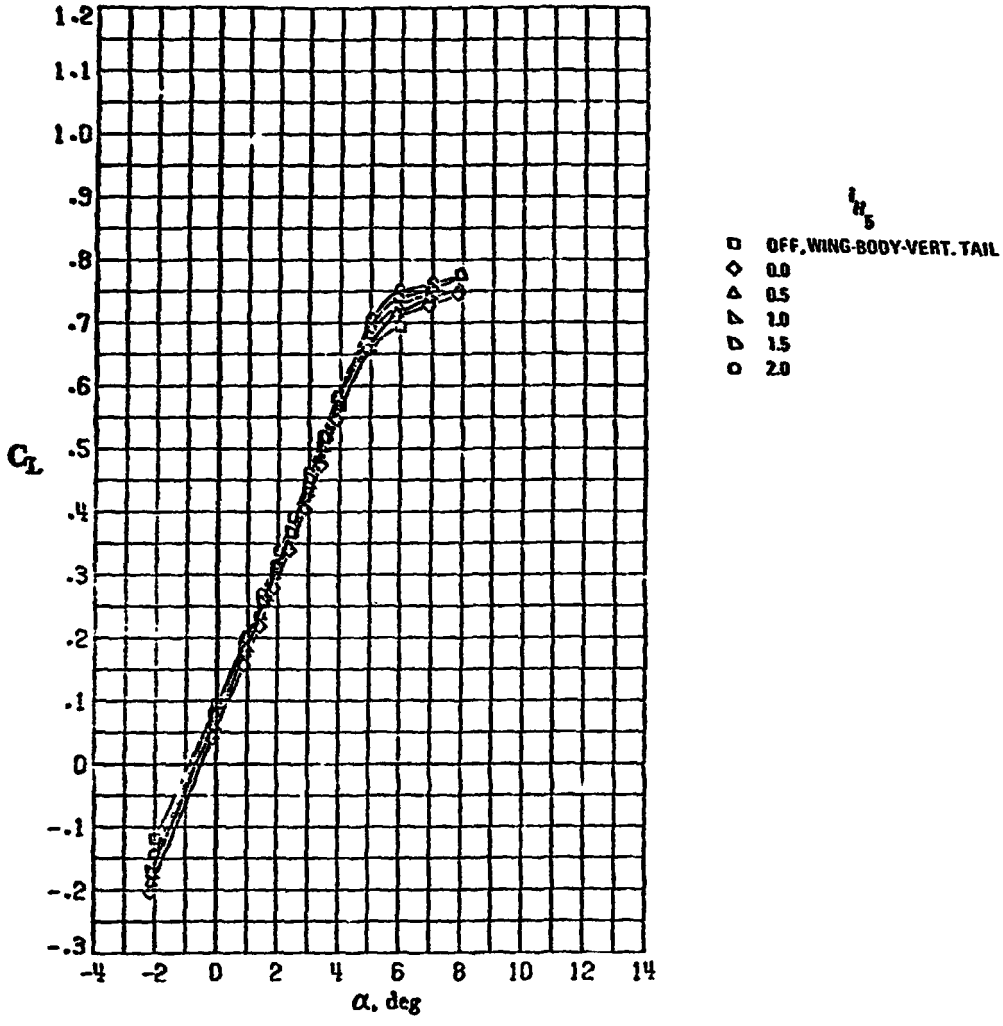

(e) H_5

Figure 11.- Concluded.

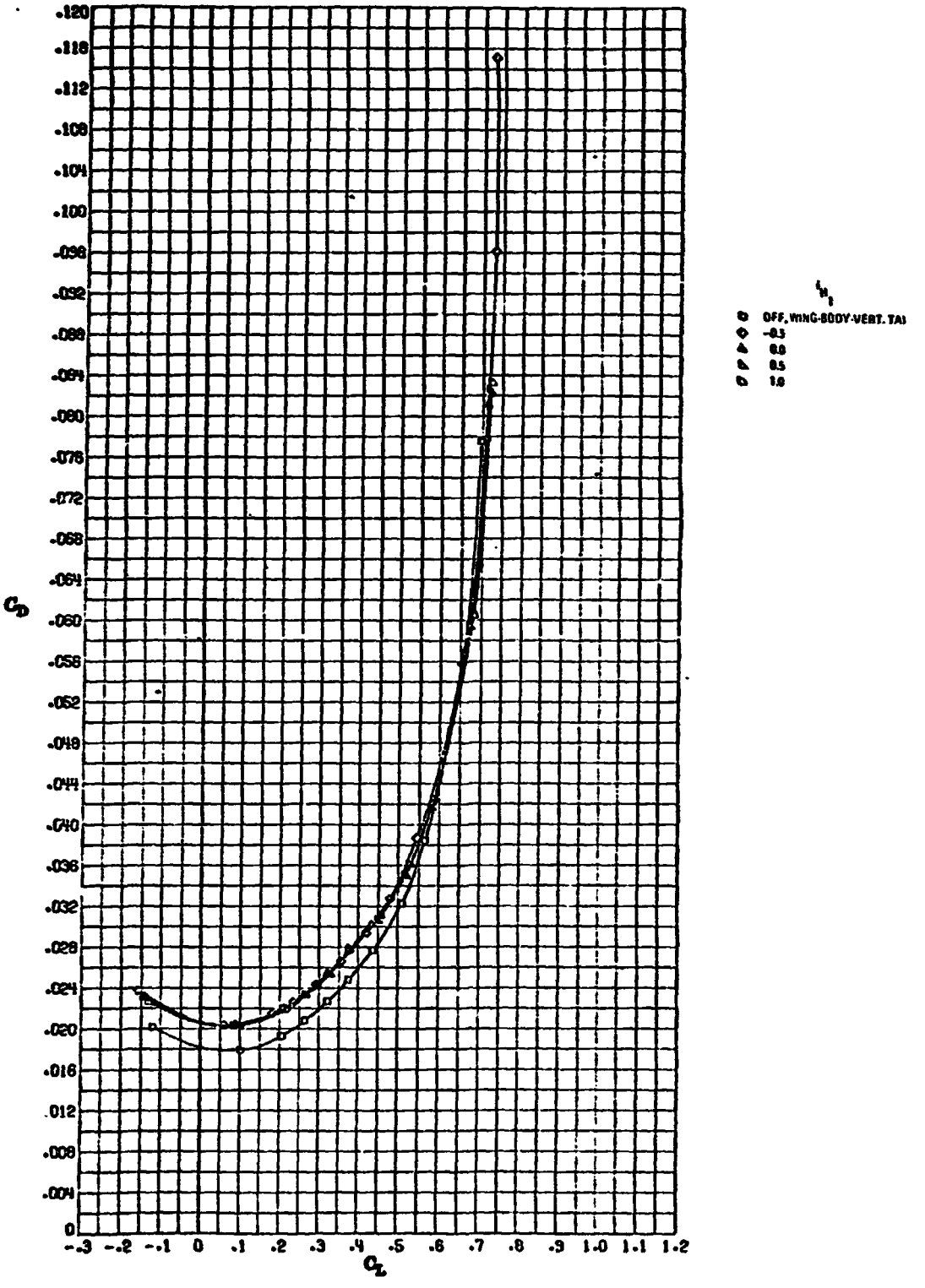

(a) H_1

Figure 12.- Variation of drag coefficient with lift coefficient for wide-body wing configurations (M_∞=0.82).

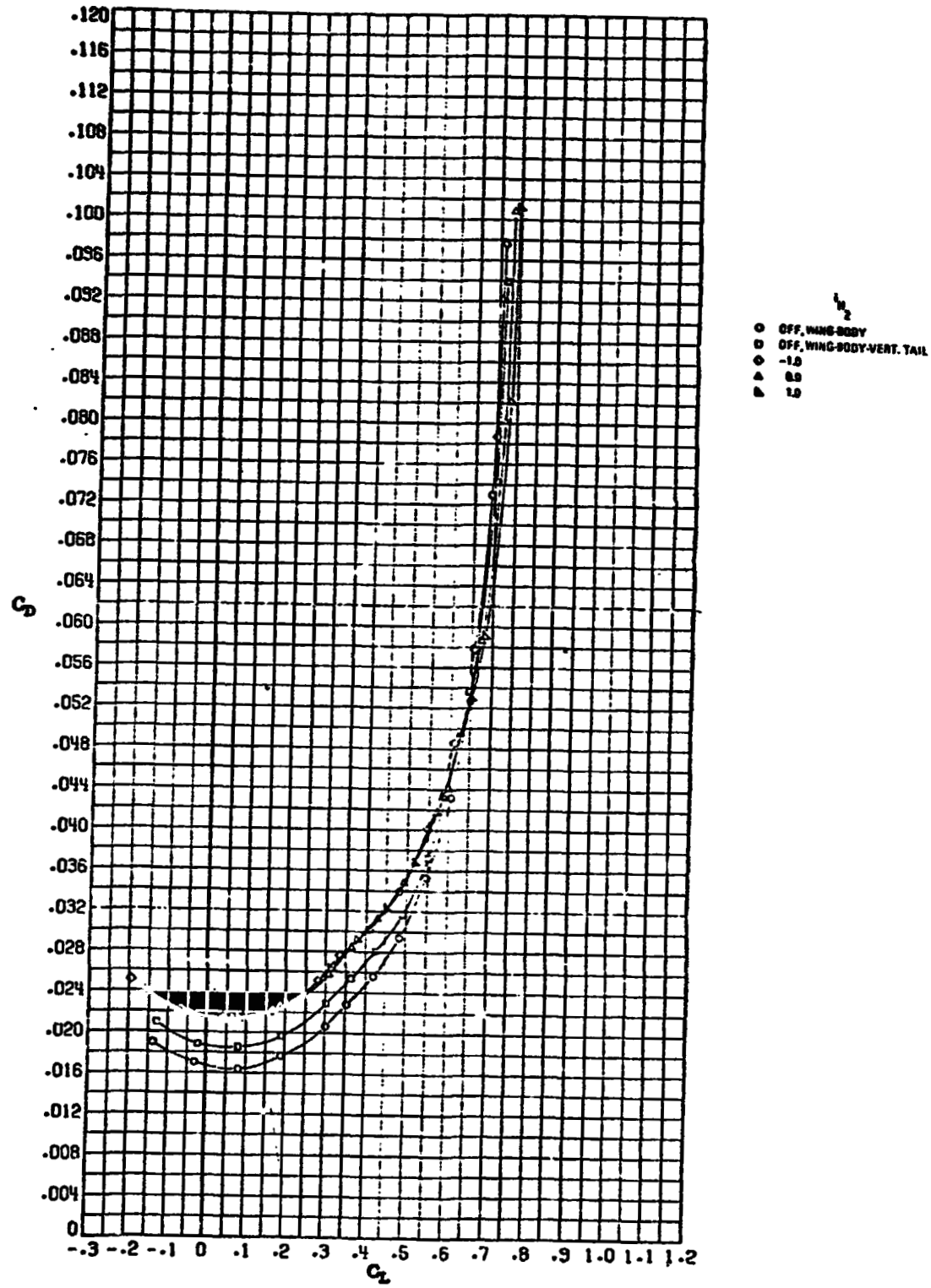

(b) H_2

Figure 12. - Continued.

ORIGINAL PAGE IS
OF POOR QUALITY

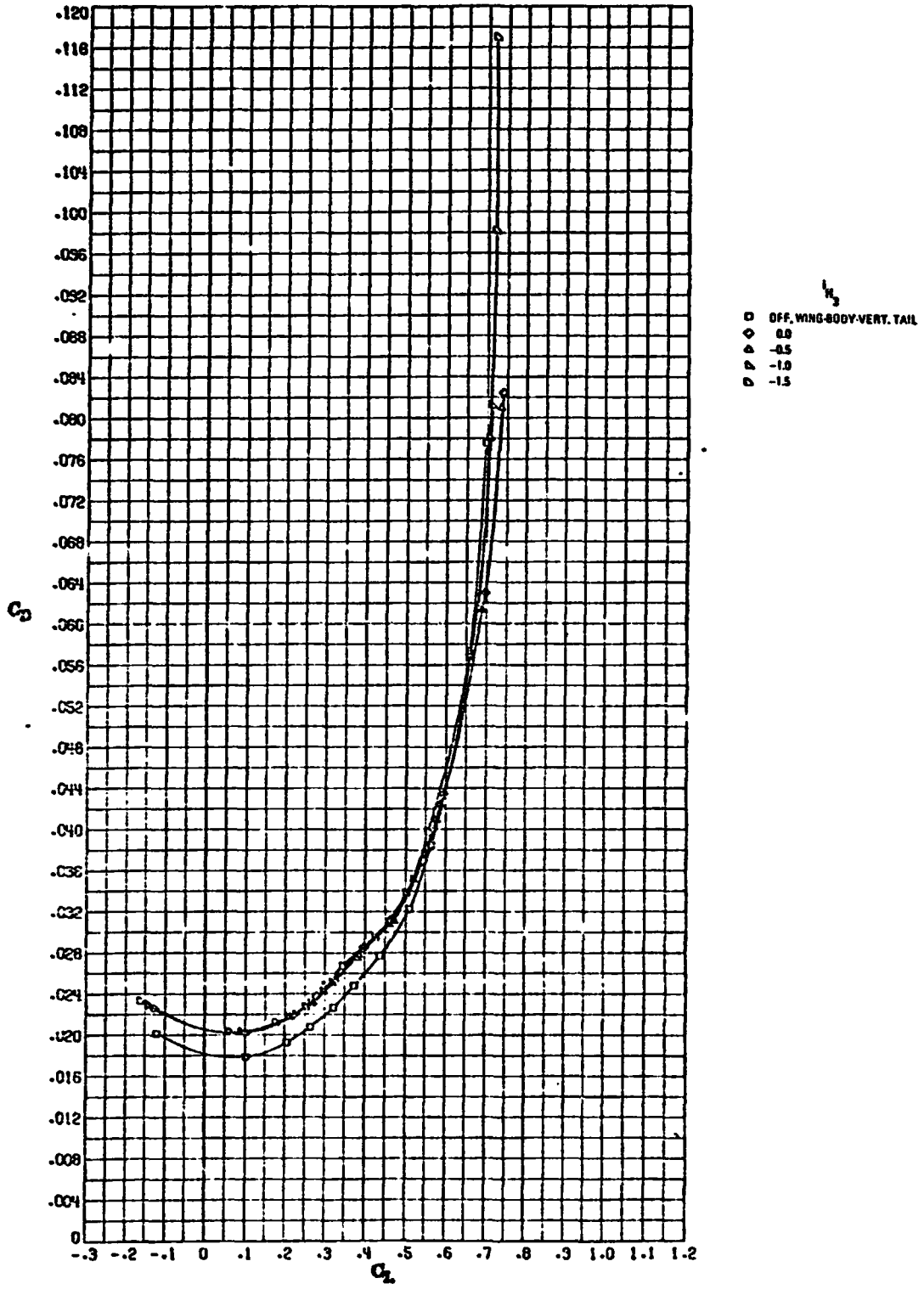

(c) H_3

Figure 12. - Continued.

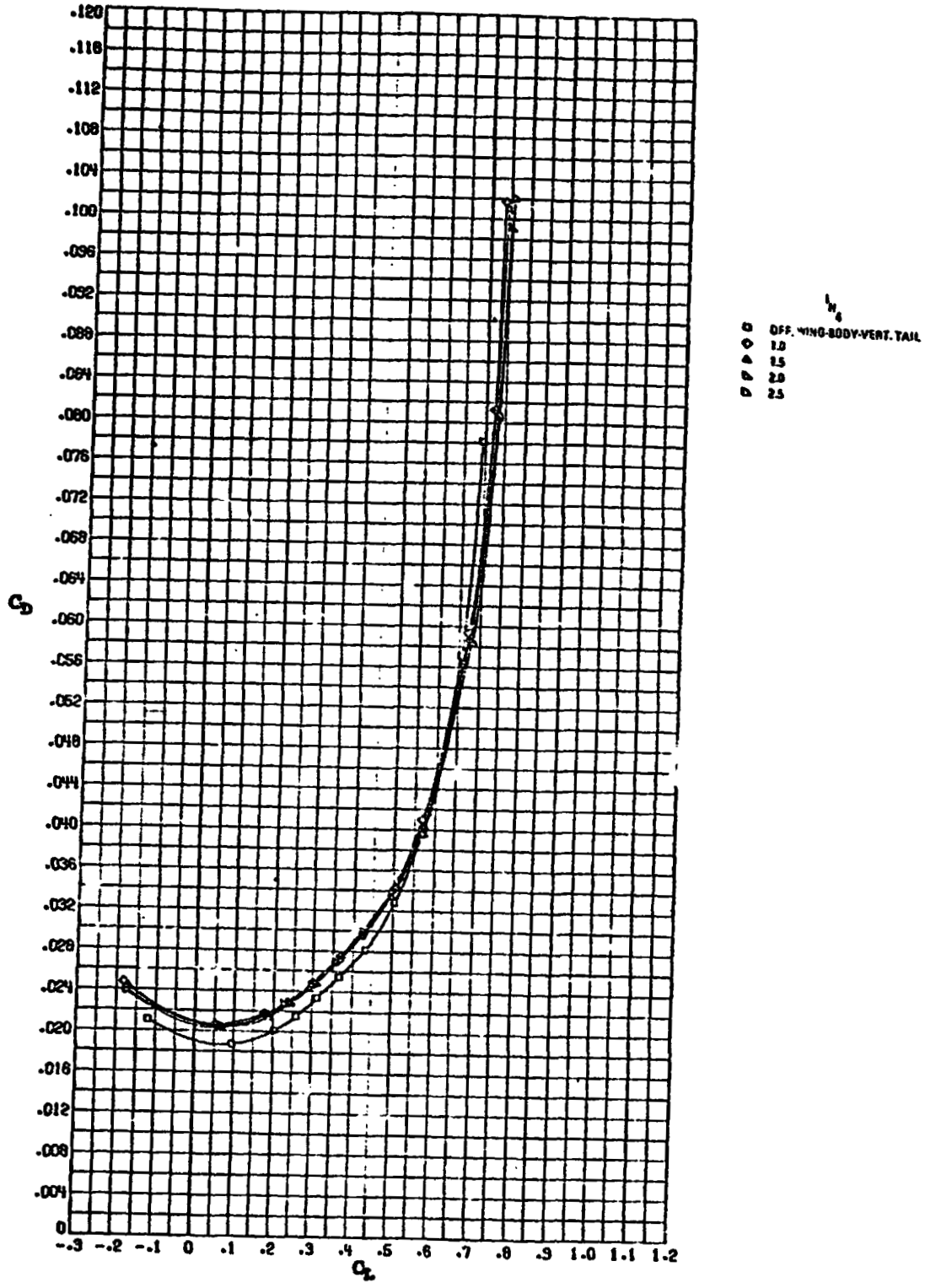

(d) H_4

Figure 12. - Continued.

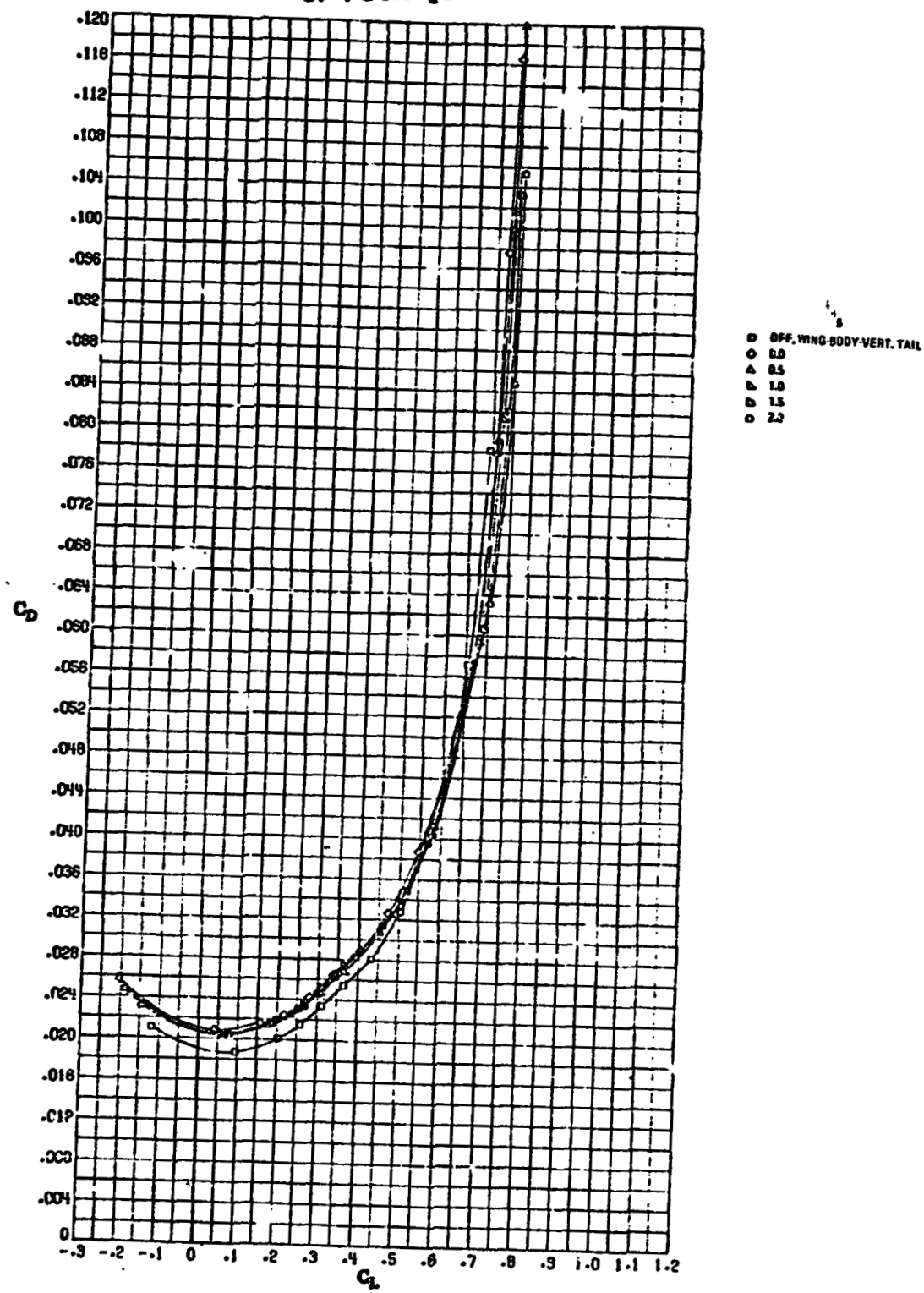

(e) H_5

Figure 12. - Concluded.

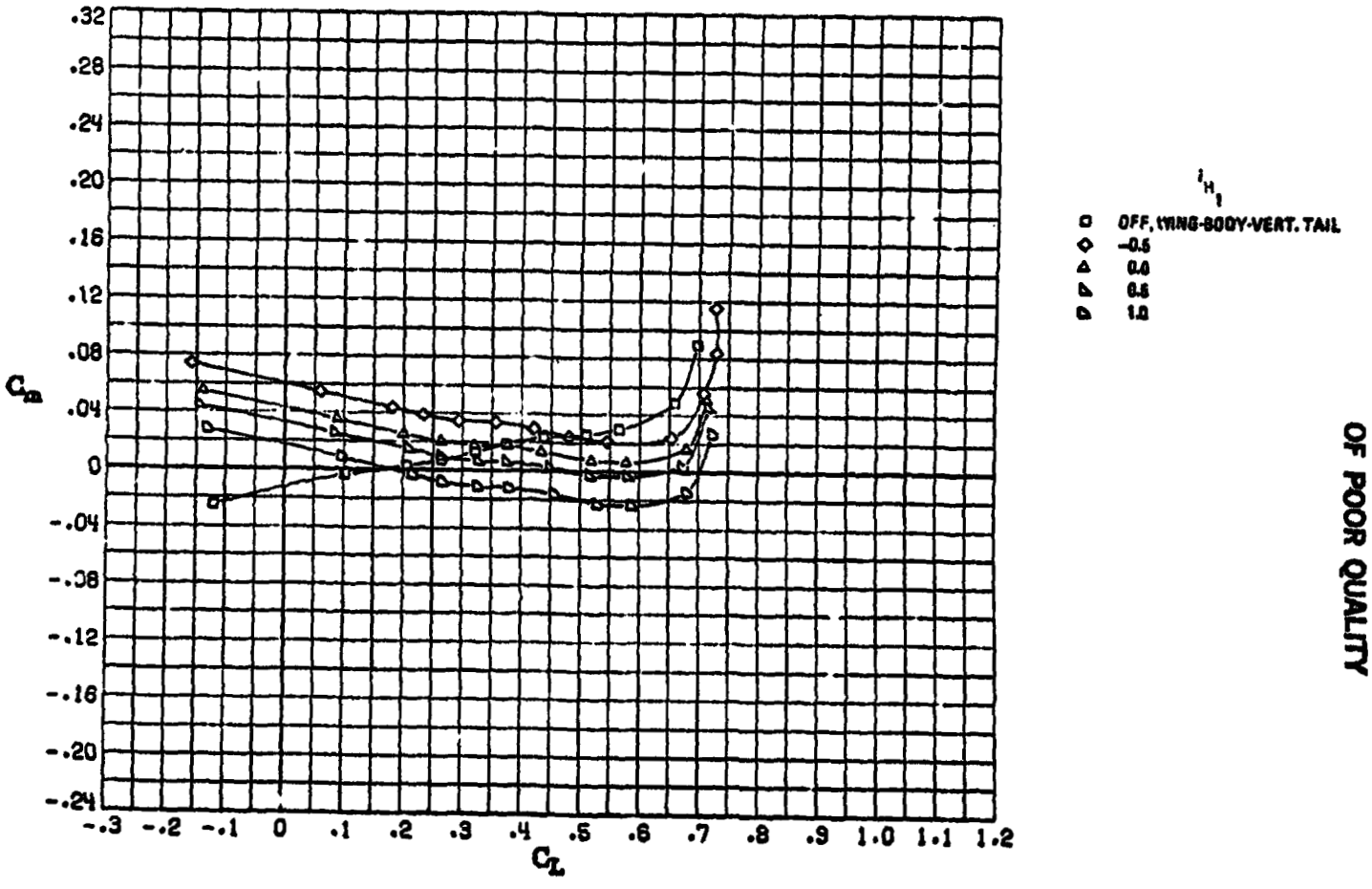

(a) H_1

Figure 13.- Variation of pitching-moment coefficient with lift coefficient for wide-body wing configurations (M = 0.82, c.g. = 0.35 $\bar{c}$).

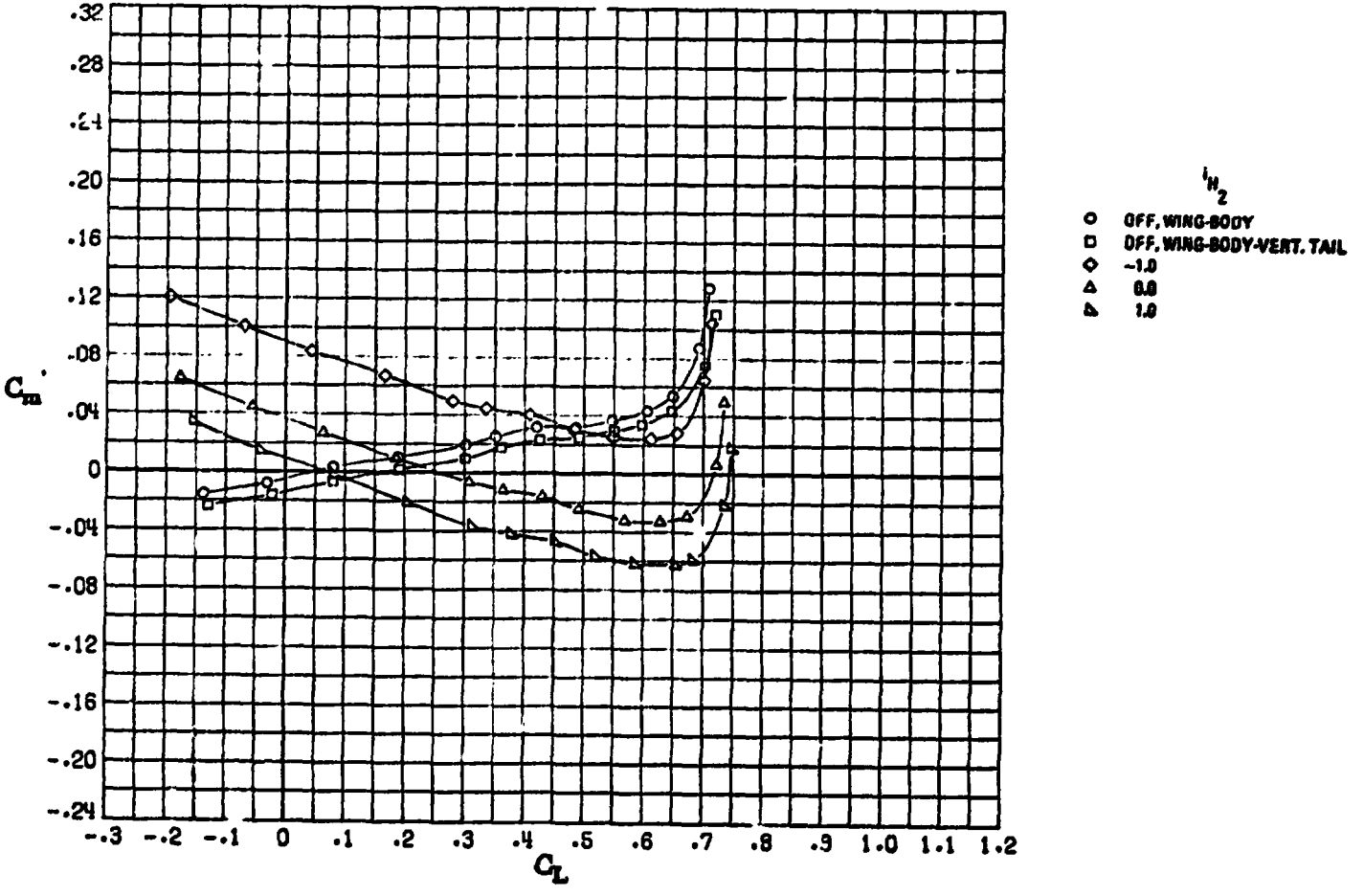

(b) H_2

Figure 13.- Continued.

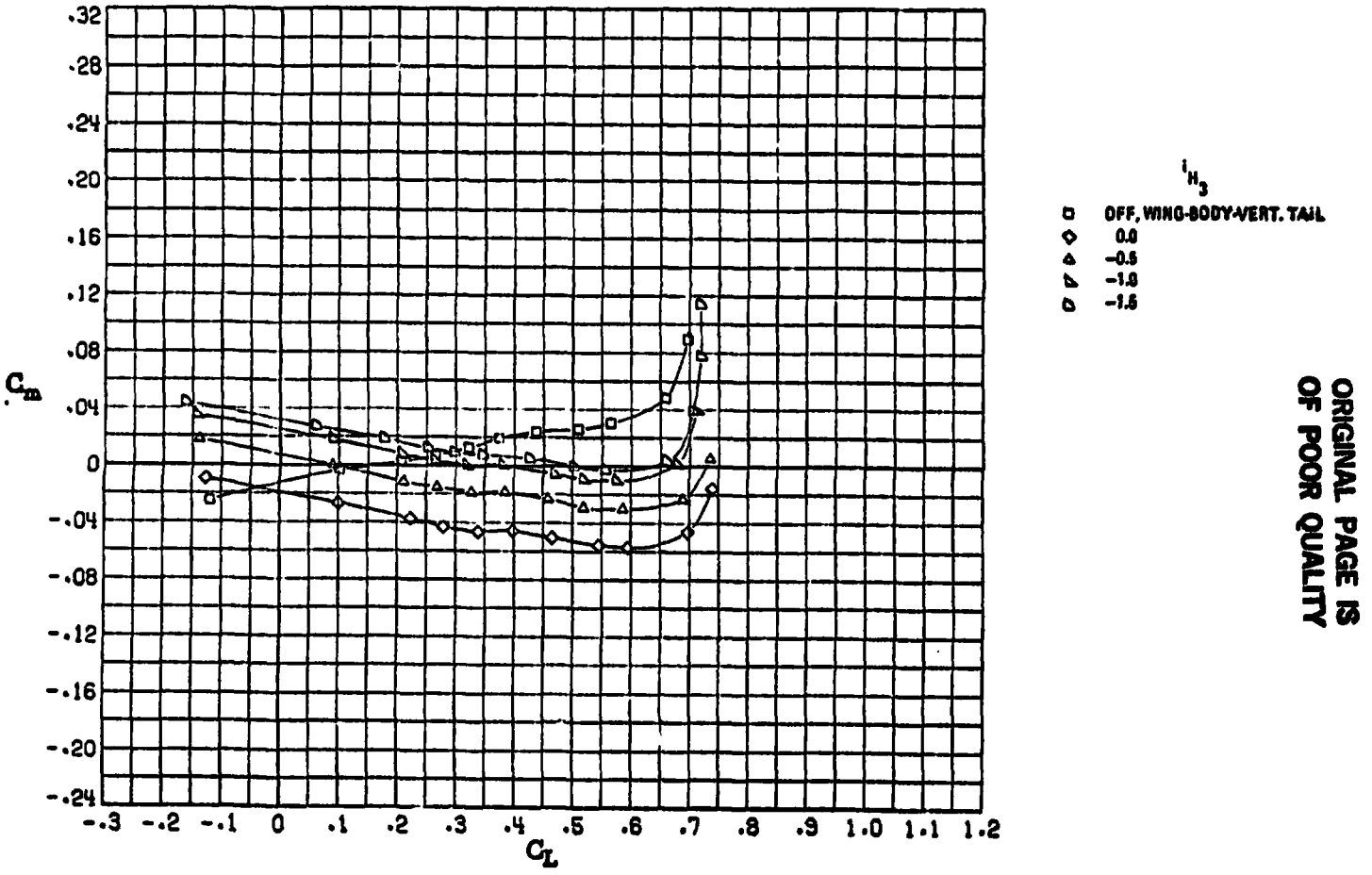

(c) H_3

Figure 13.- Continued.

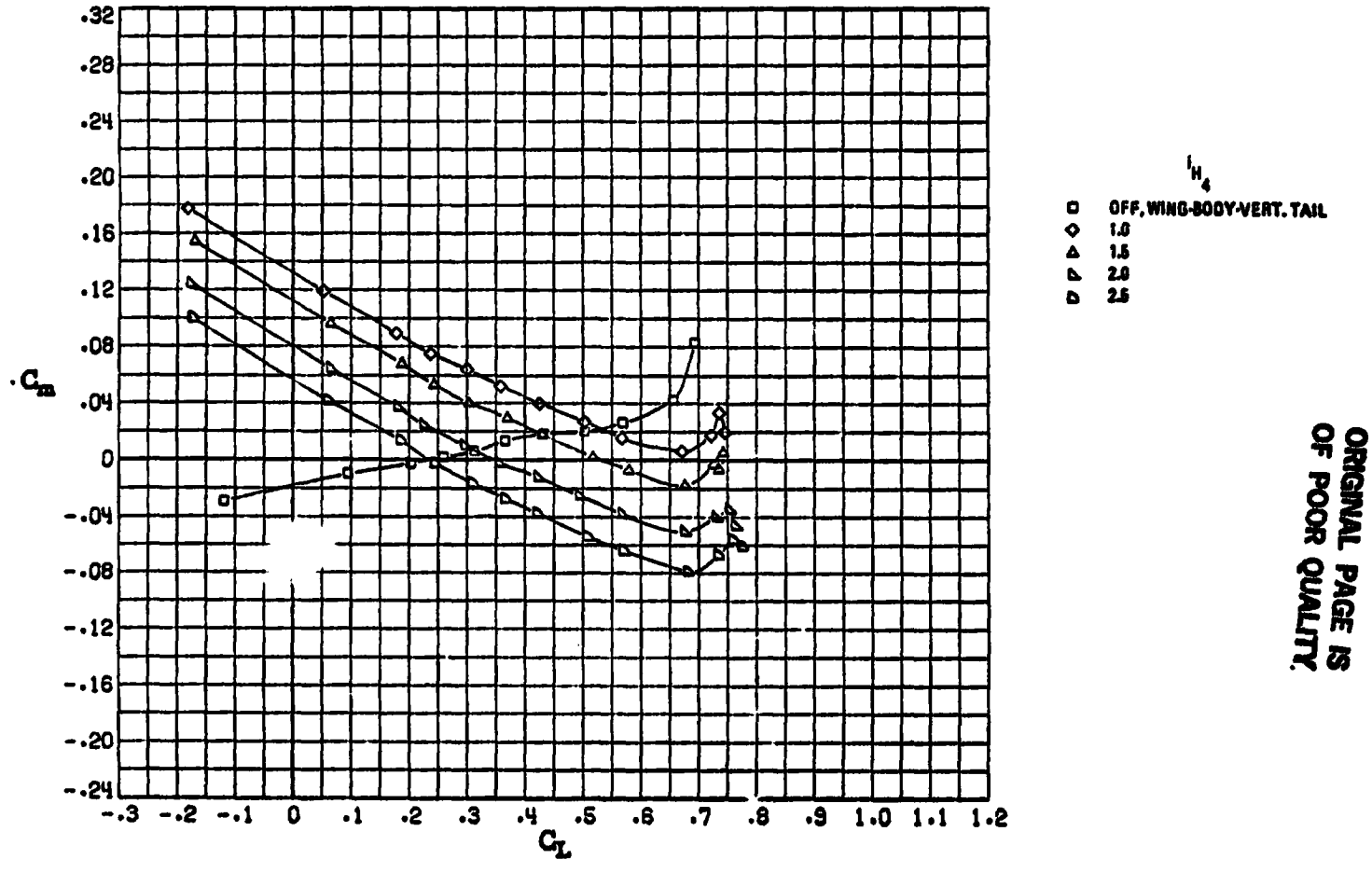

(d) H_4

Figure 13.- Continued.

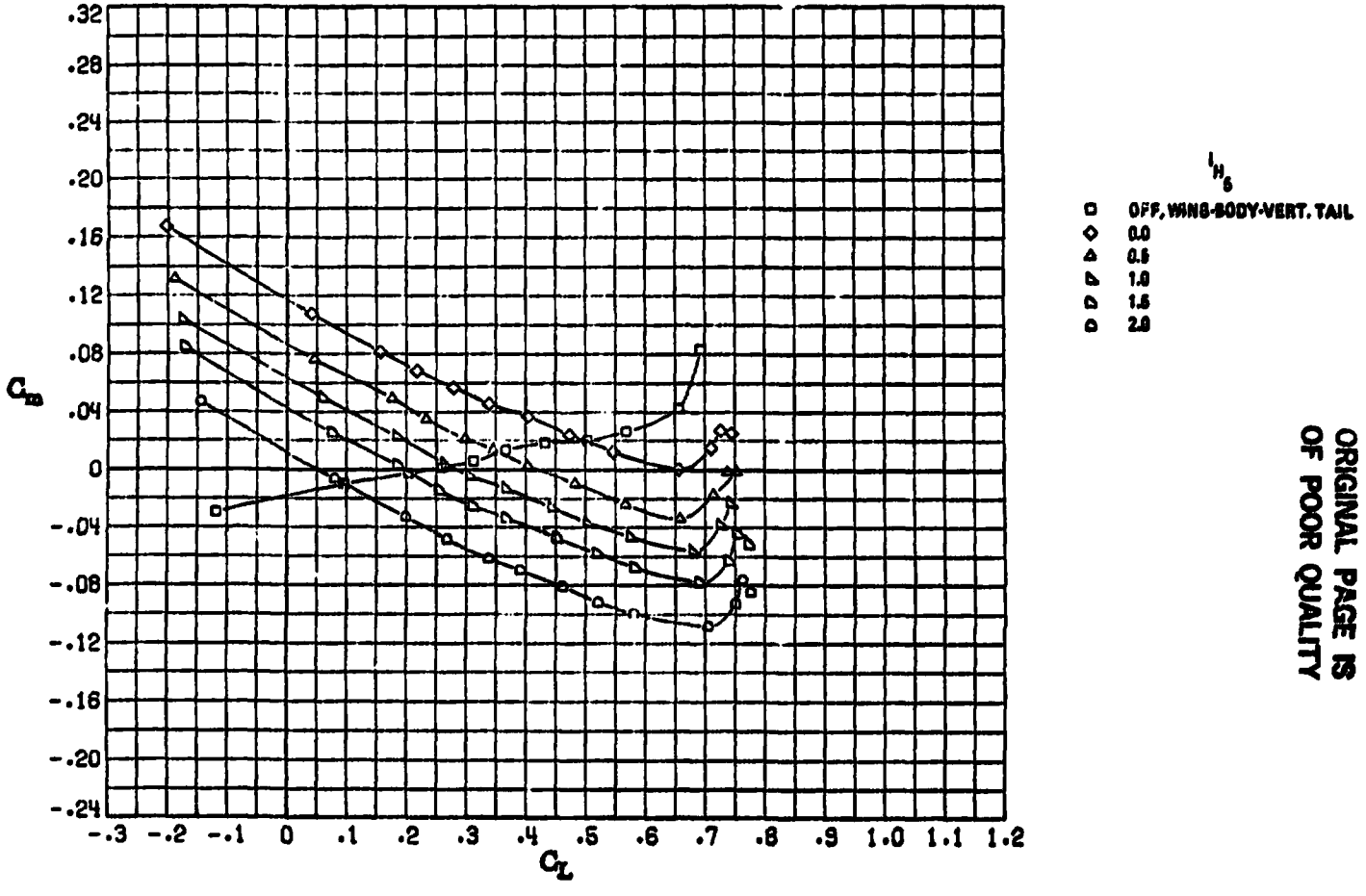

(e) H_5

Figure 13.- Concluded.

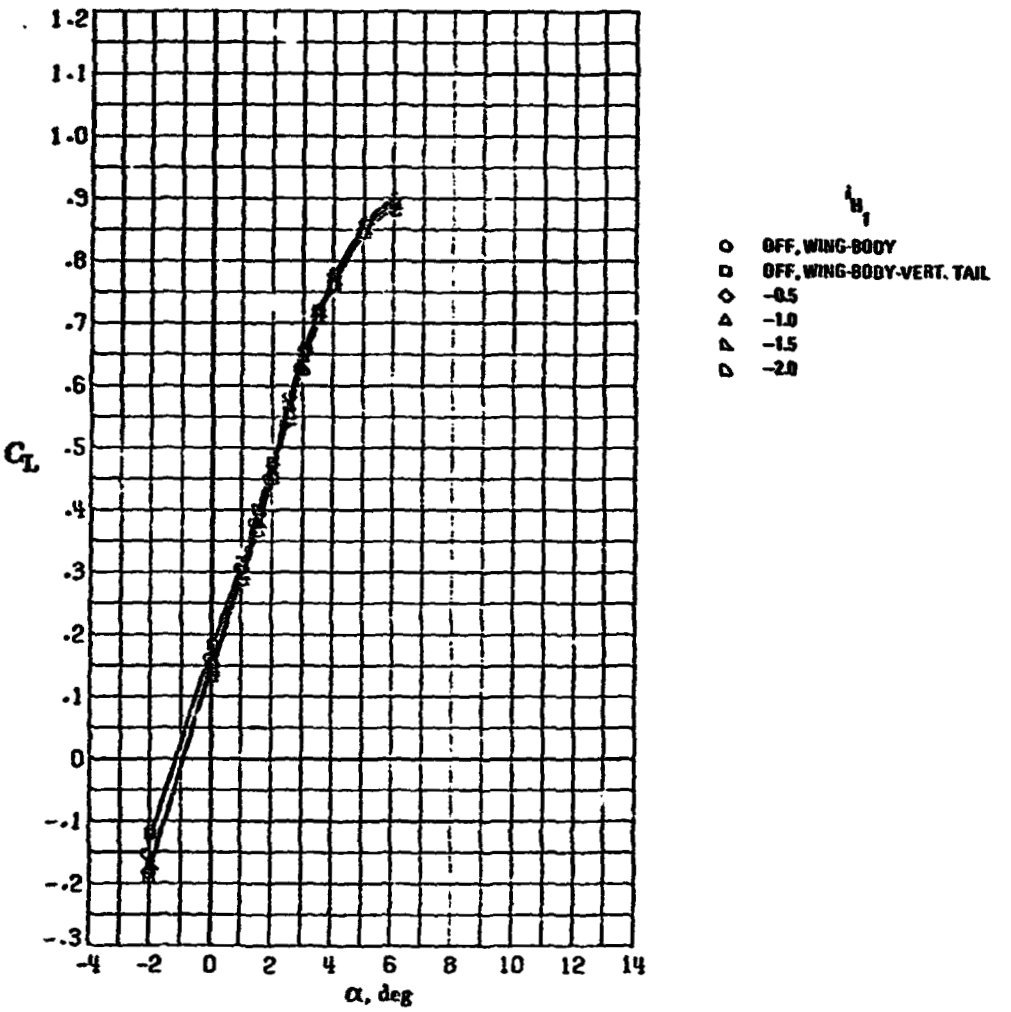

(a) H_1

Figure 14. - Variation of lift coefficient with angle of attack for supercritical wing configurations (M_∞ = 0.82).

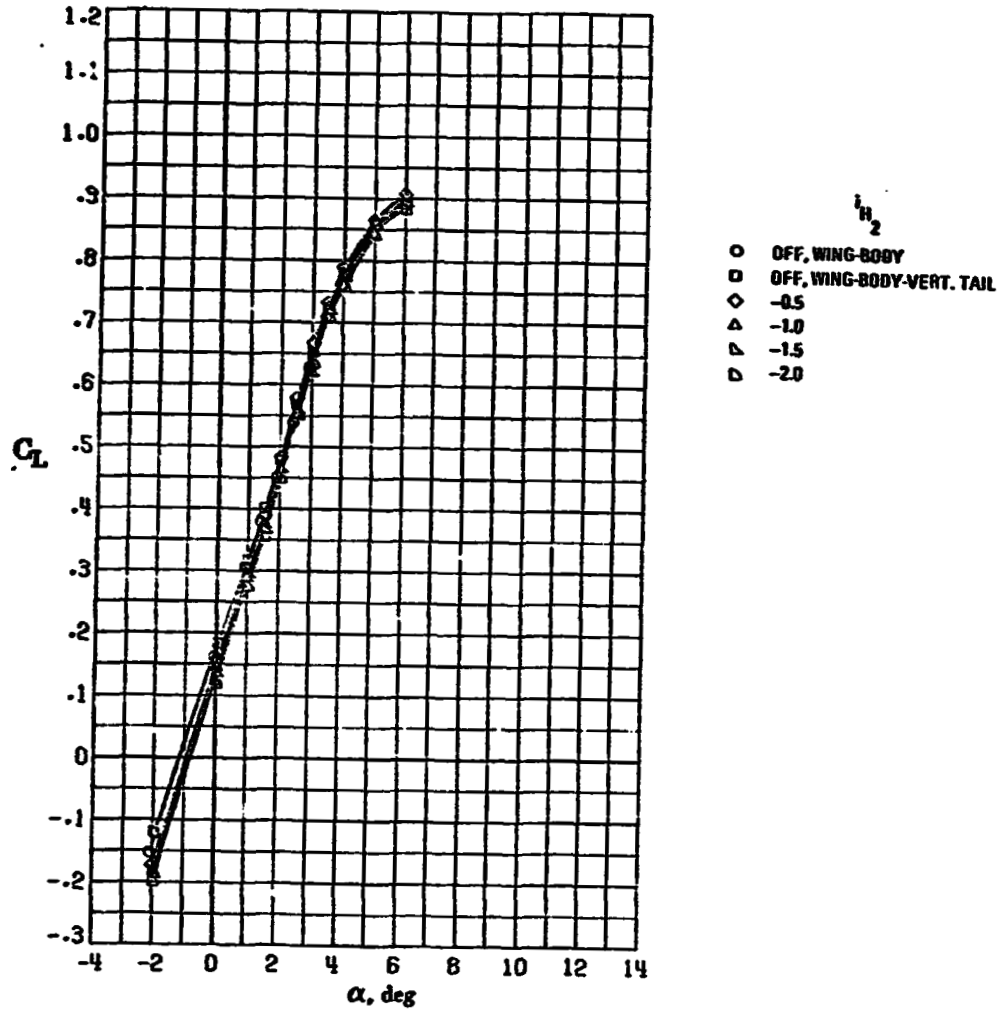

(b) H_2

Figure 14.- Continued.

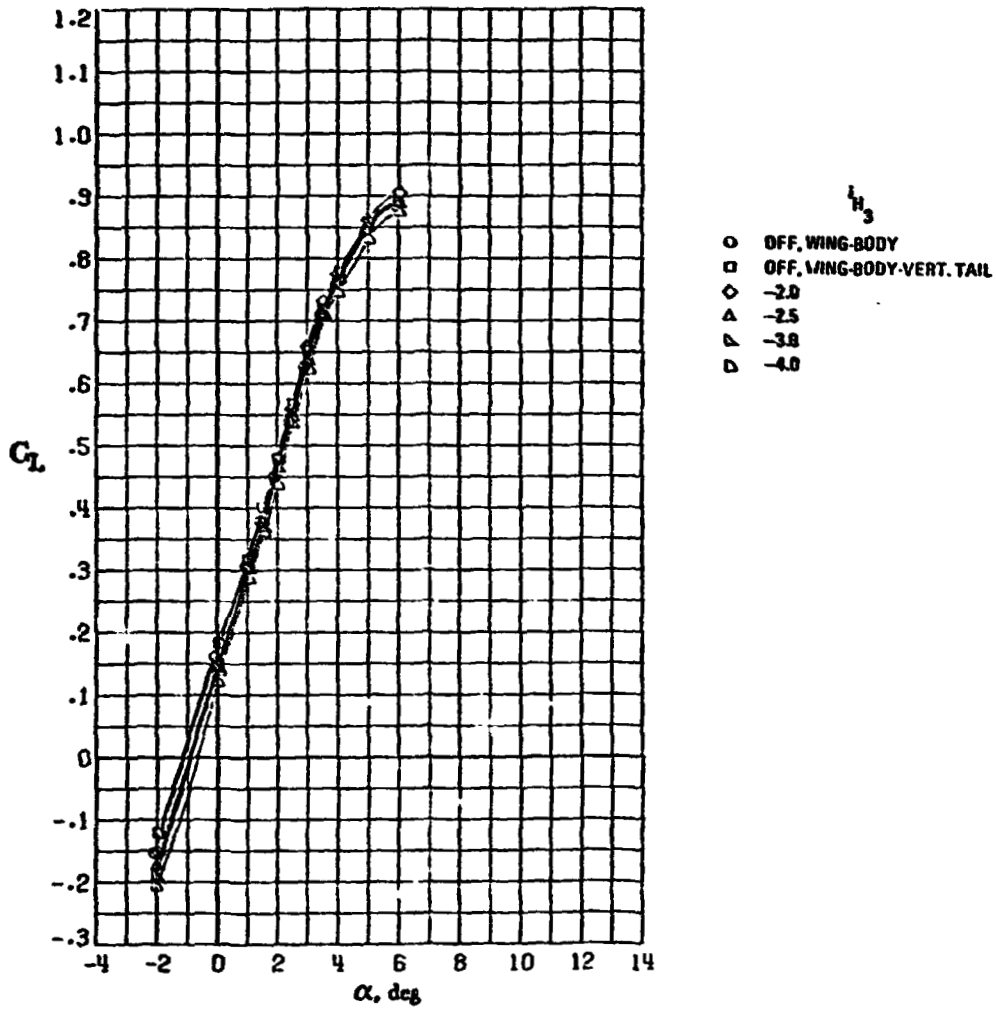

(c) H_3

Figure 14.- Continued.

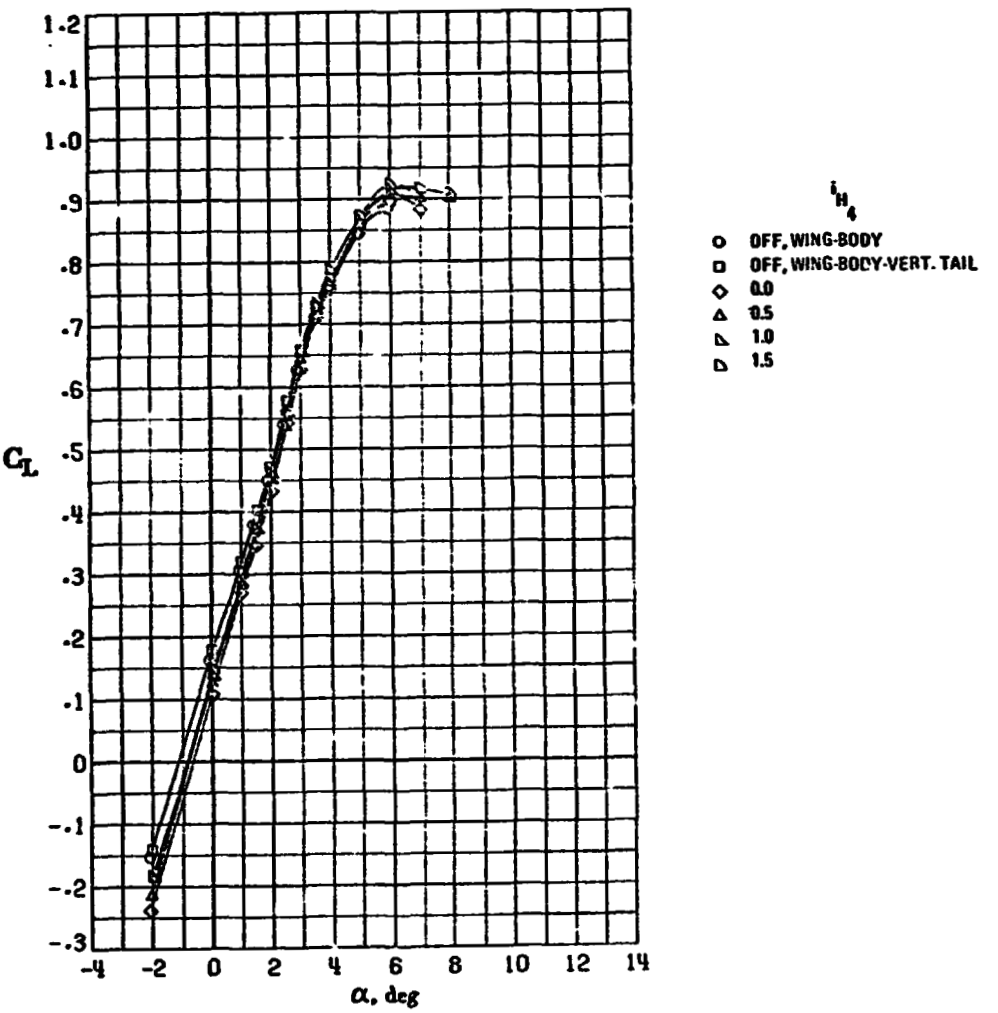

(d) H_4

Figure 14. - Continued.

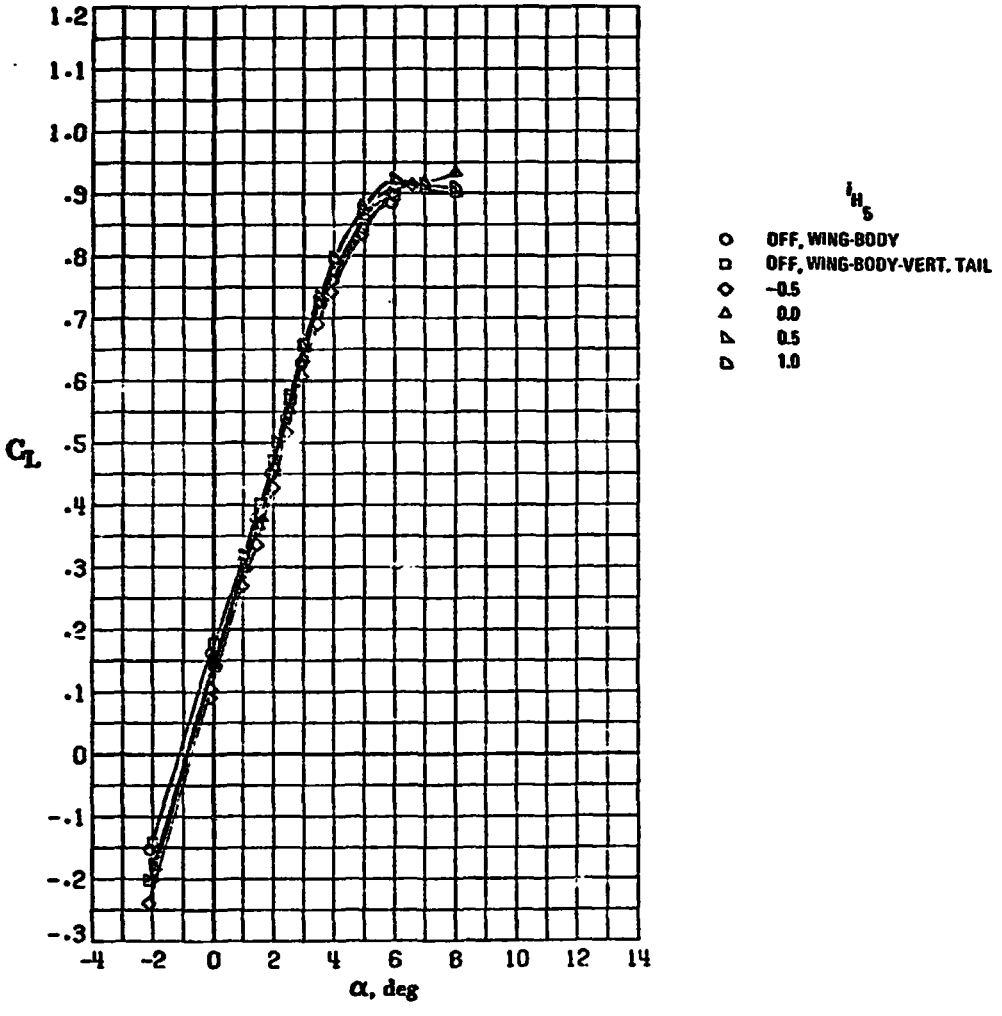

(e) H_5

Figure 14.- Concluded.

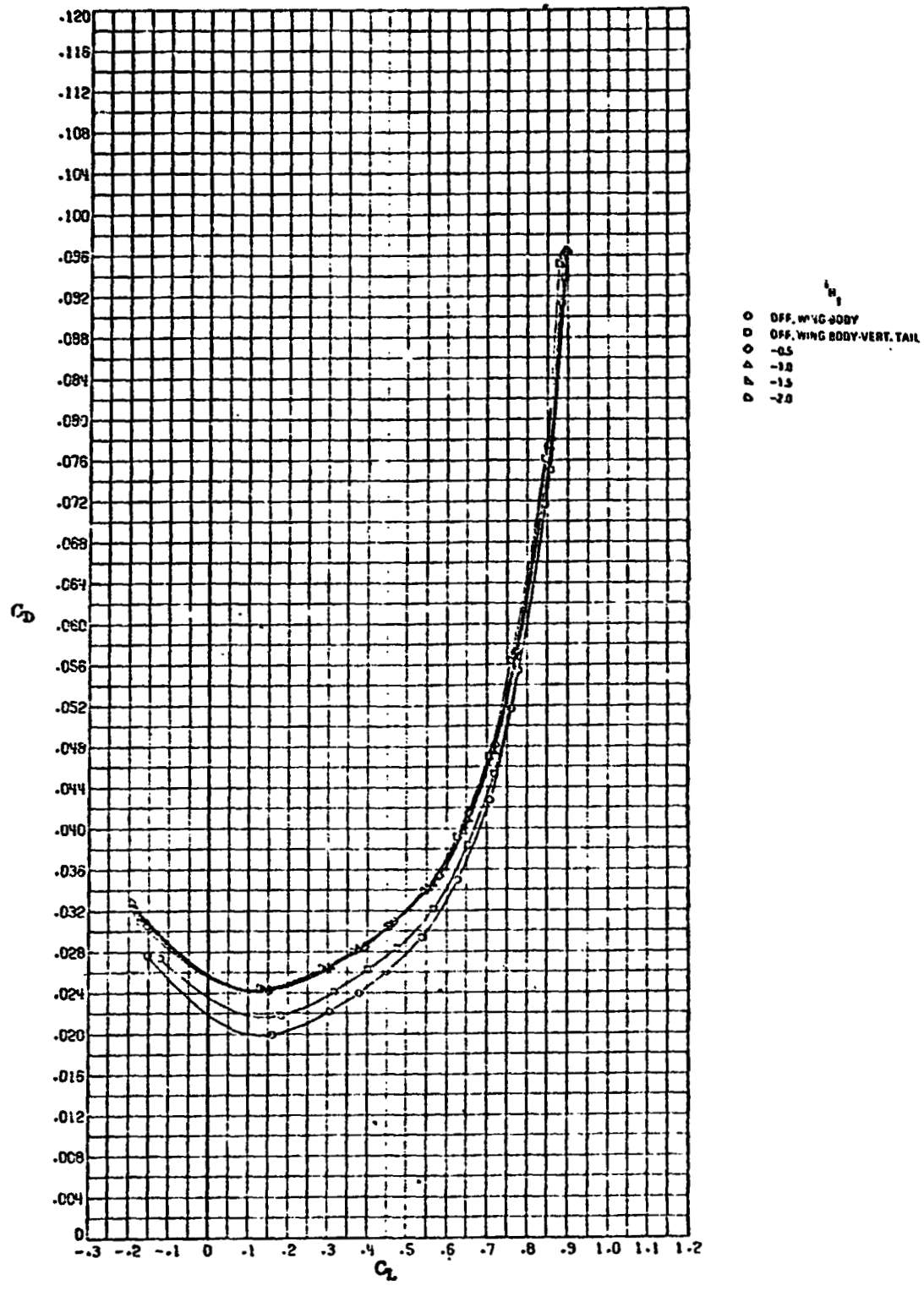

(a) H_1

Figure 15.- Variation of drag coefficient with lift coefficient for supercritical wing configurations ($M_\infty = 0.82$).

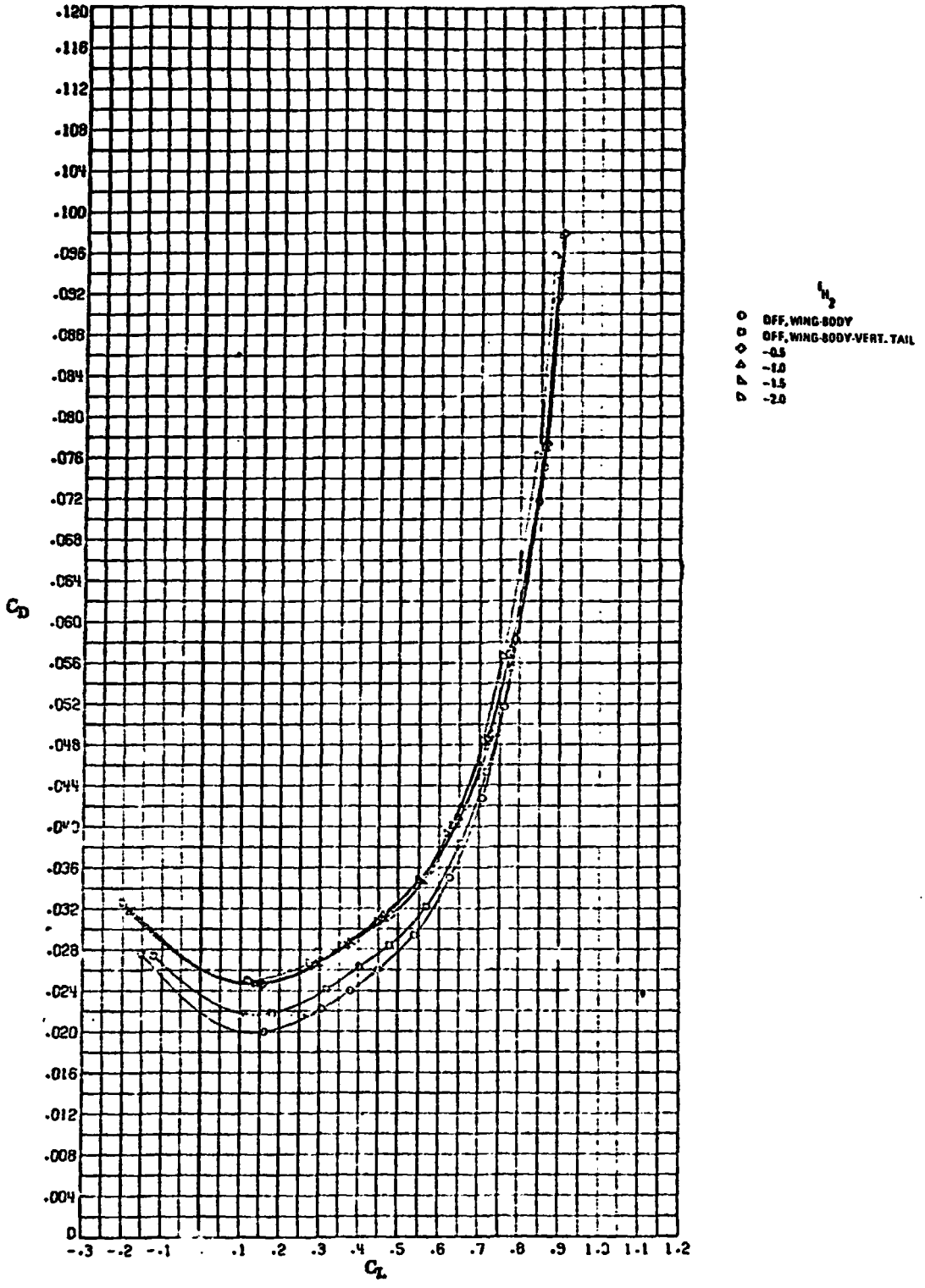

(b) H_2

ORIGINAL PAGE IS
OF POOR QUALITY

Figure 15. - Continued.

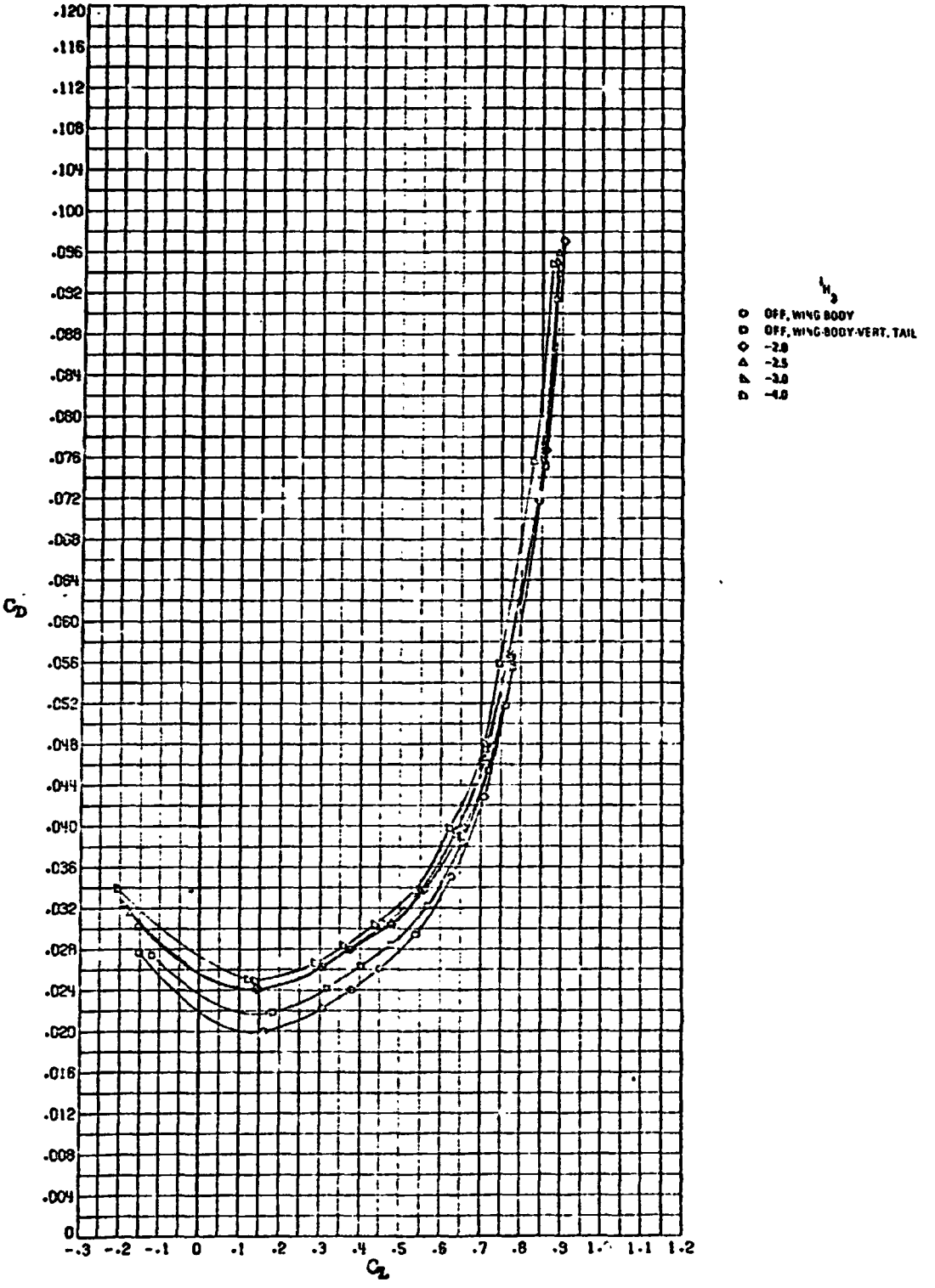

(c) H_3

Figure 15. - Continued.

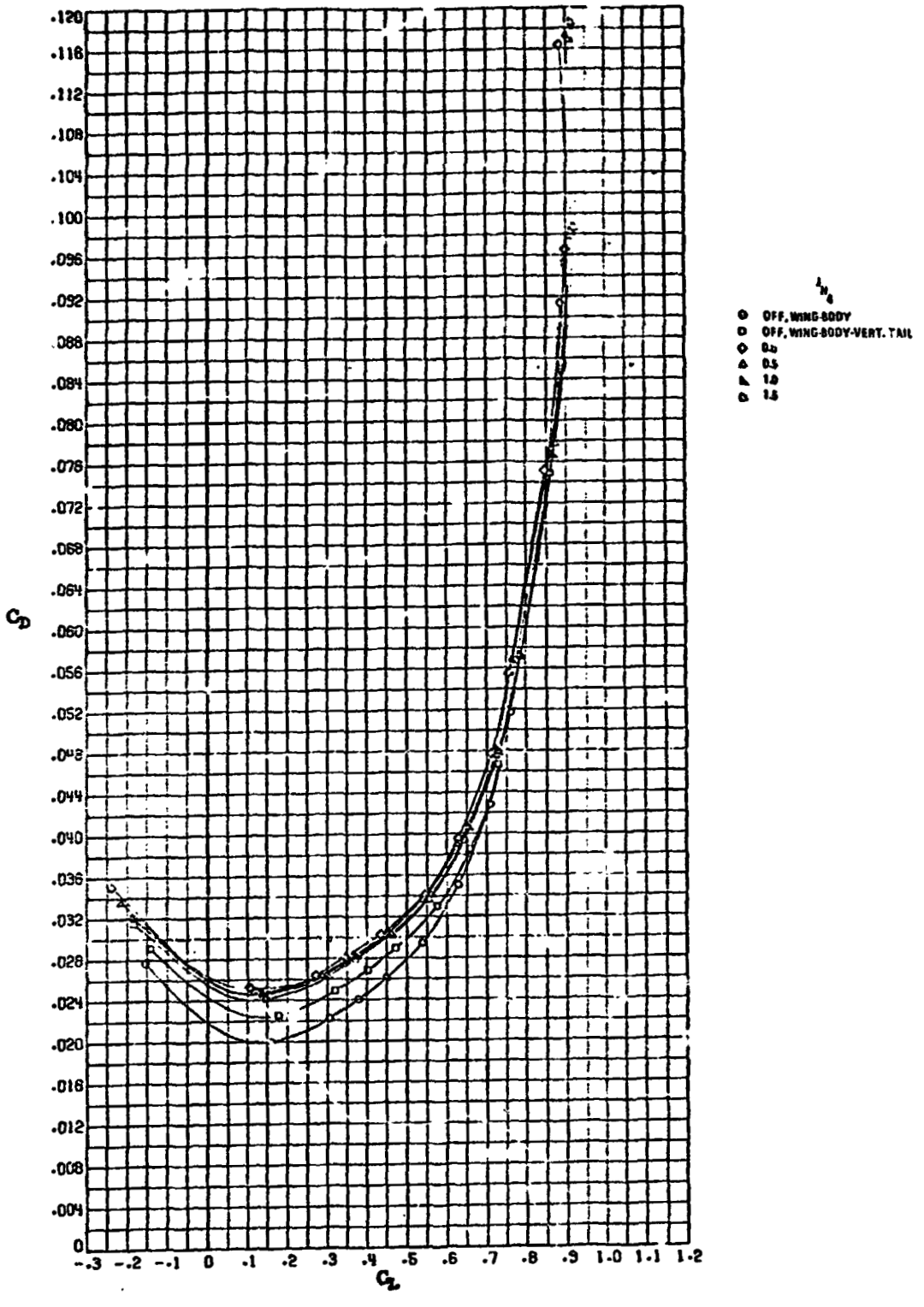

(d) H_4

Figure 15.- Continued.

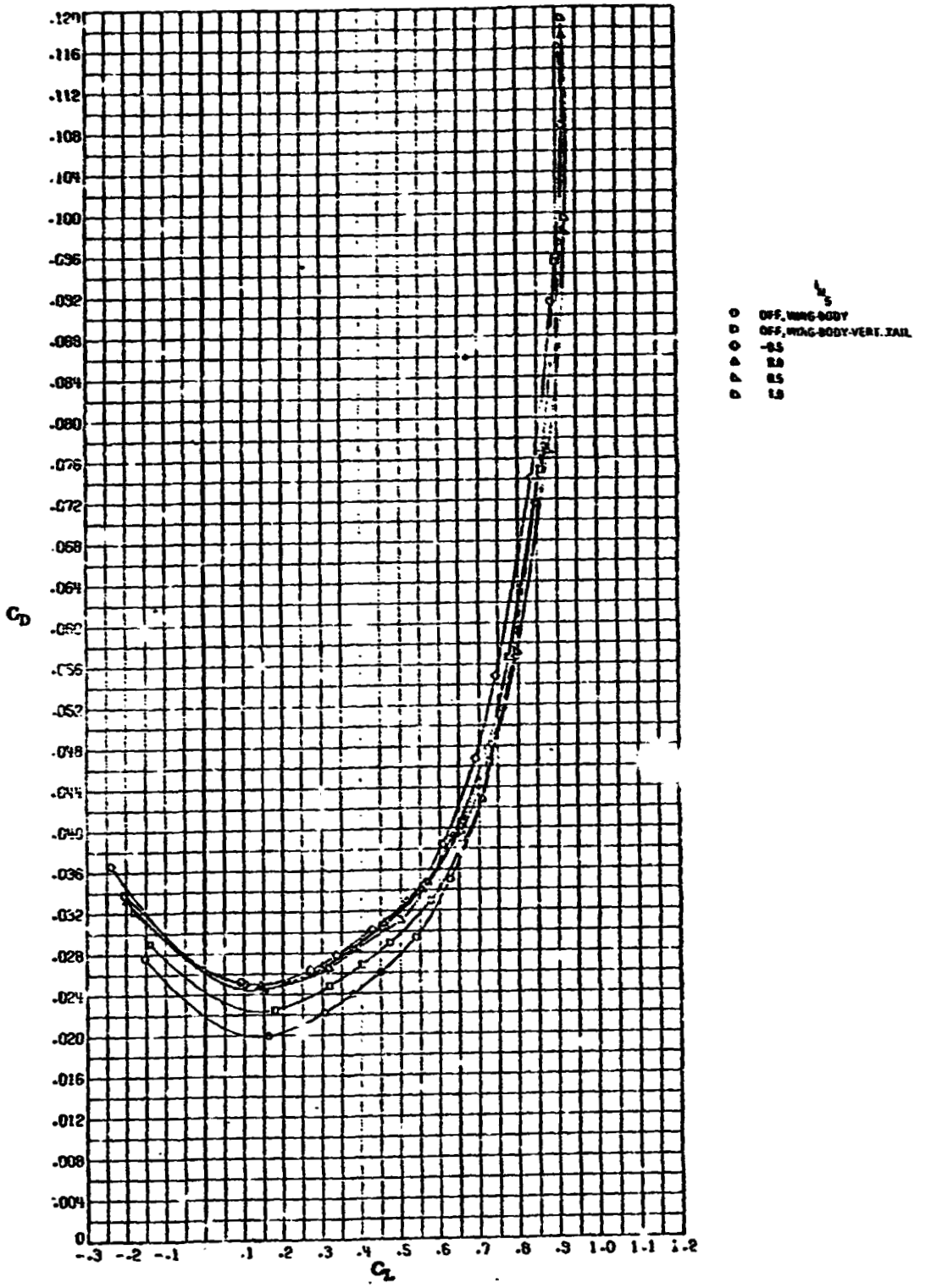

(e) H_5

Figure 15.- Concluded.

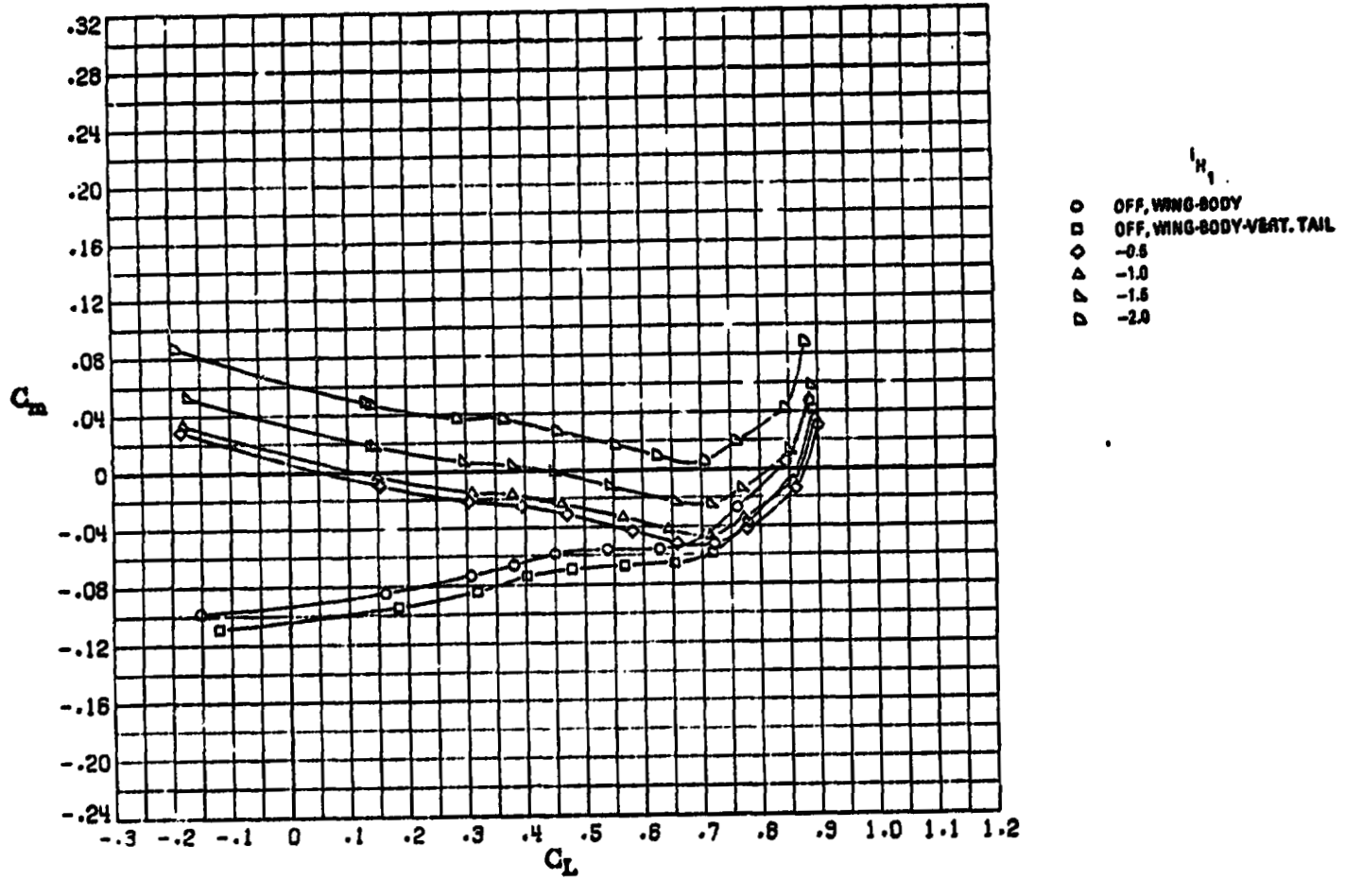

(a) H_1

Figure 16.- Variation of pitching - moment coefficient with lift coefficient for supercritical wing configurations ($M_\infty = 0.82$, c.g. $= 0.33\ \bar{c}$).

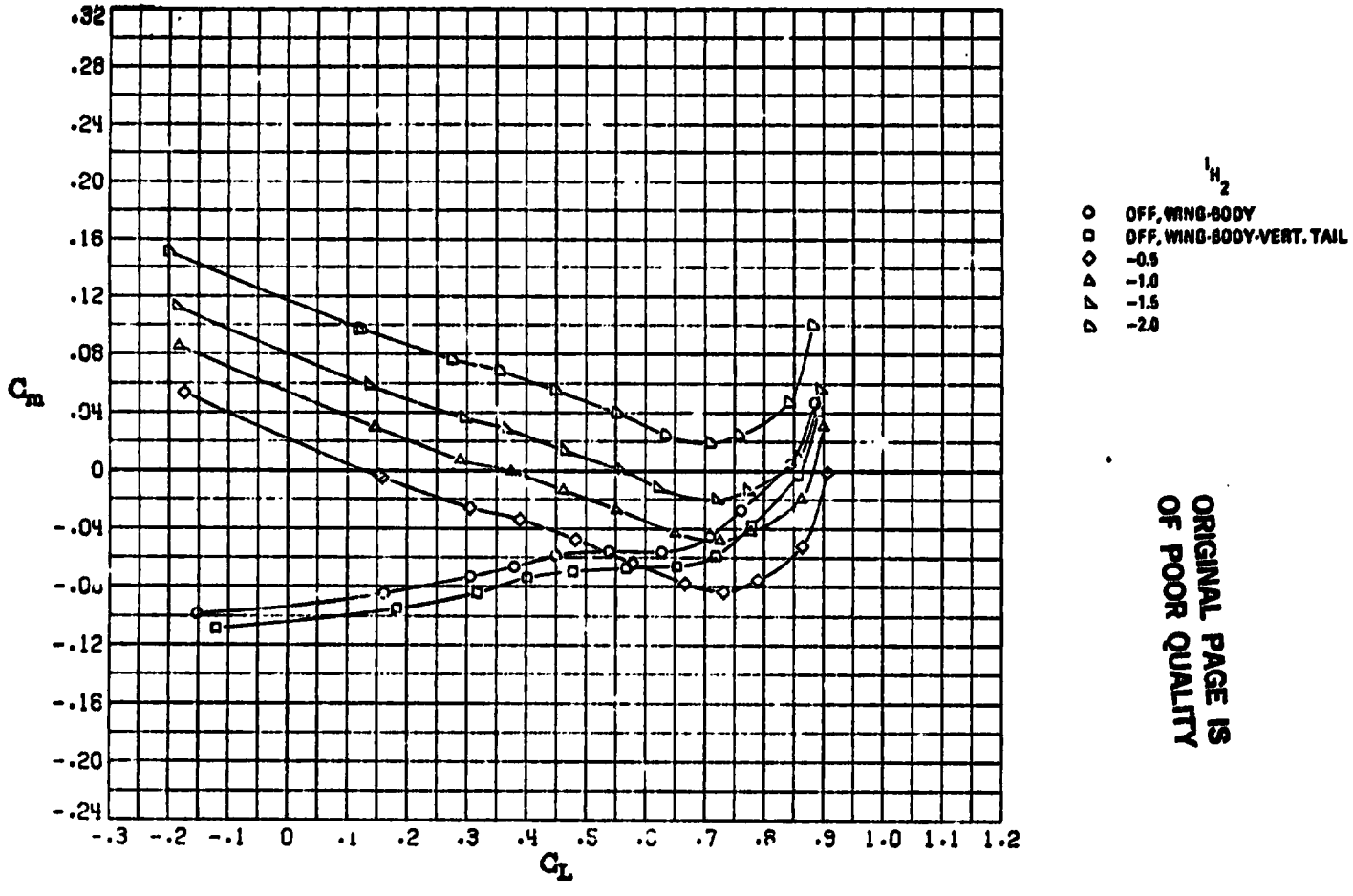

(b) H_2

Figure 16. - Continued.

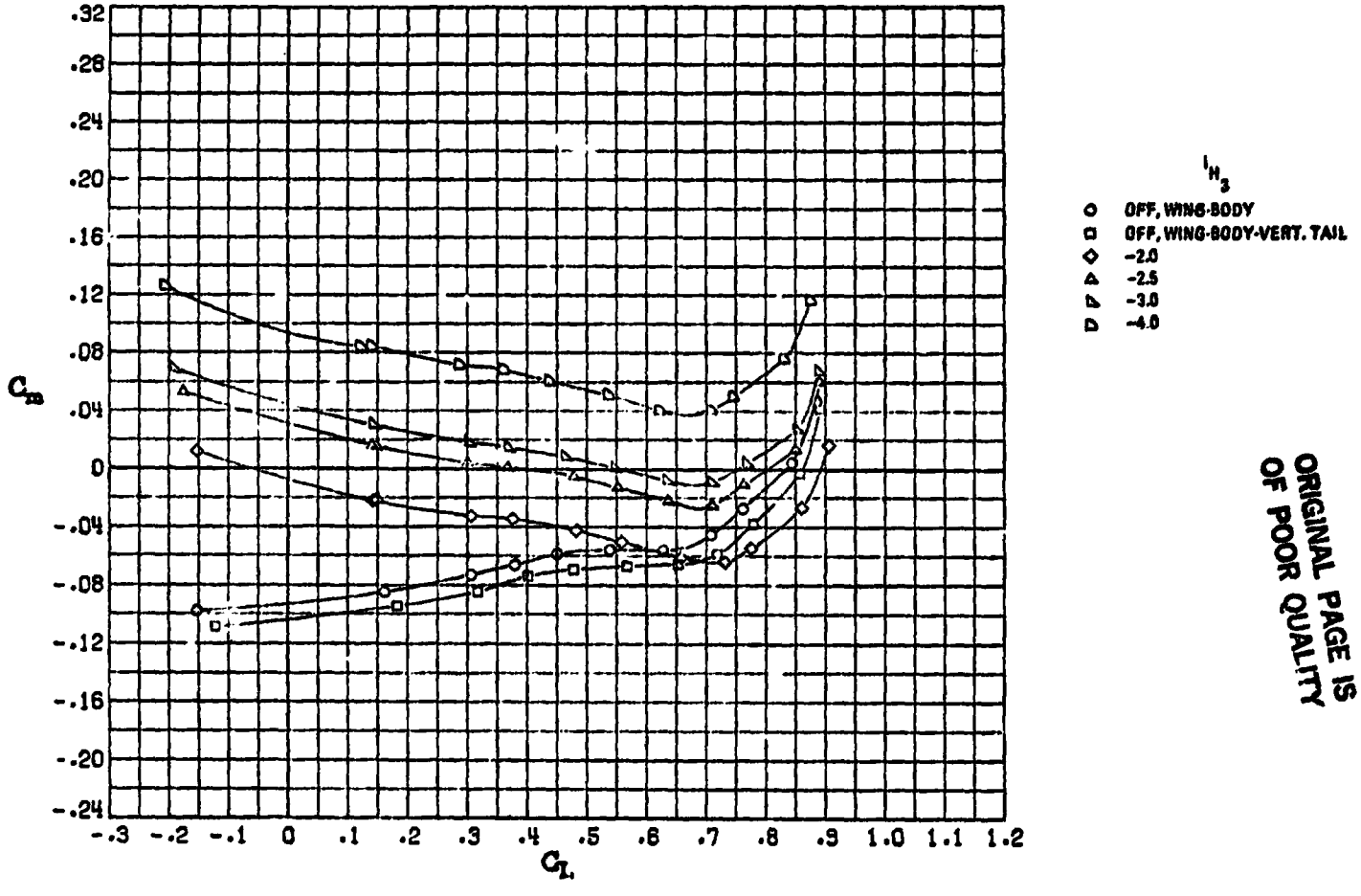

(c) H_3

Figure 16.- Continued.

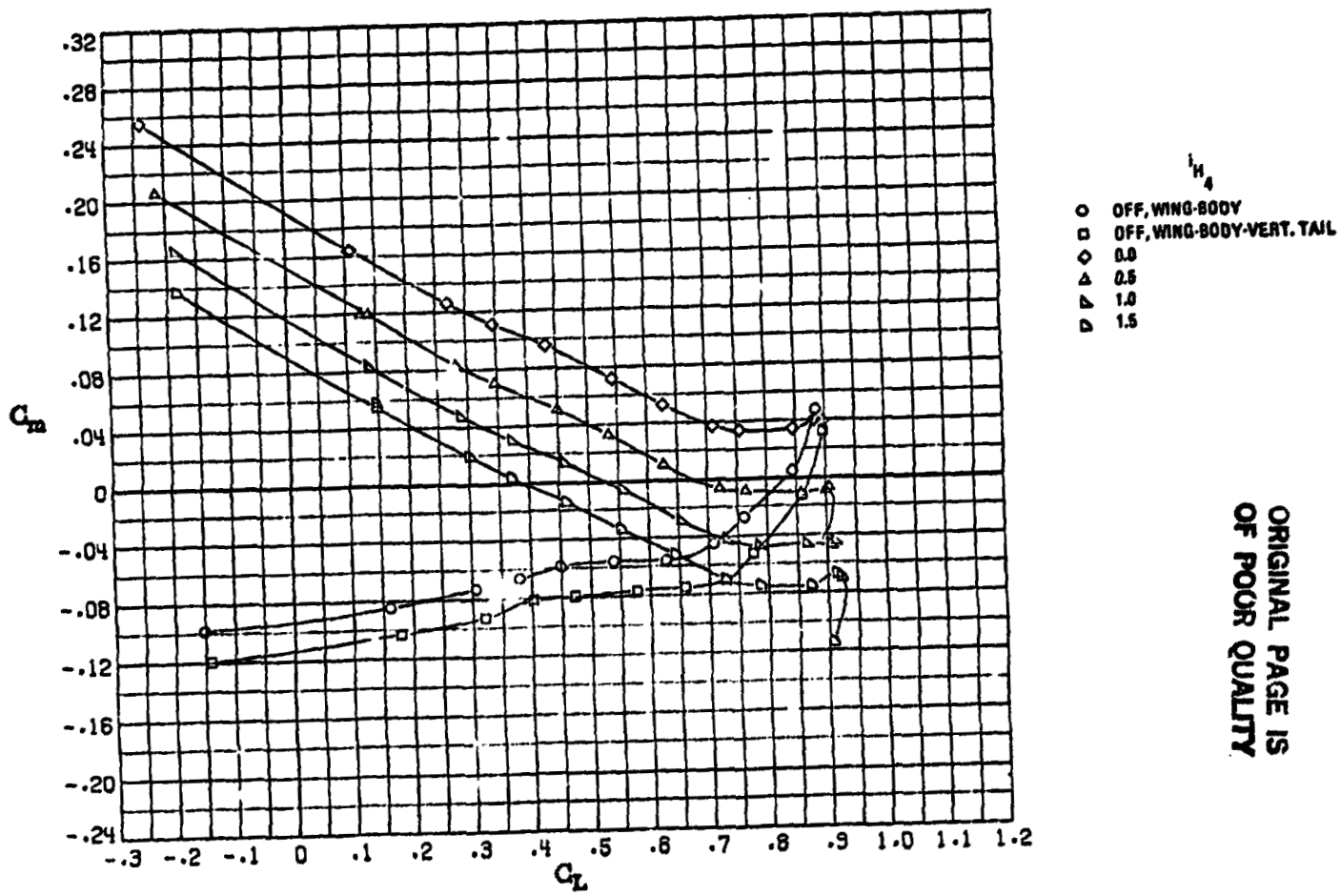

(d) H_4

Figure 16. - Continued.

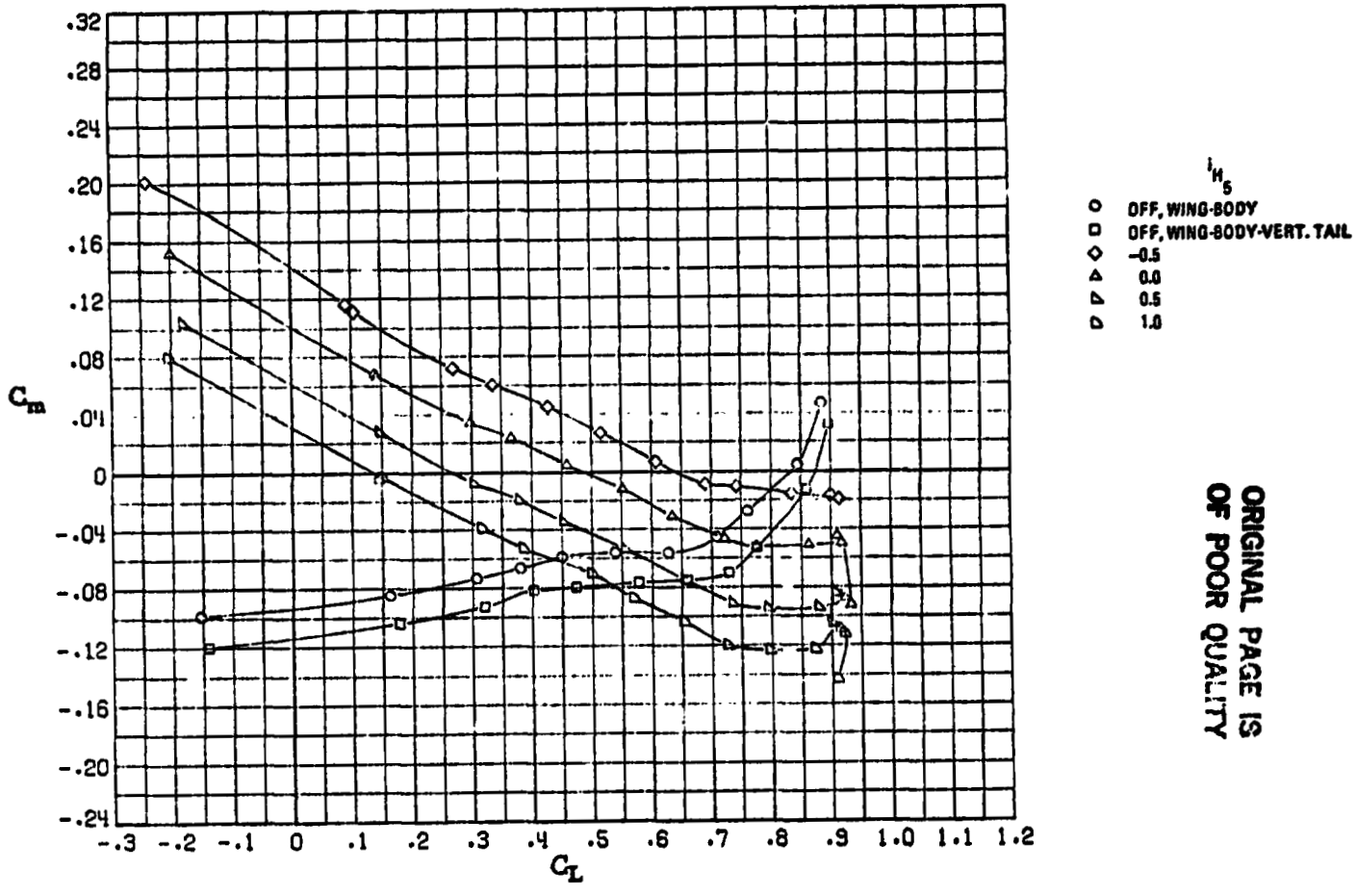

(e) H_5

Figure 16. - Concluded.

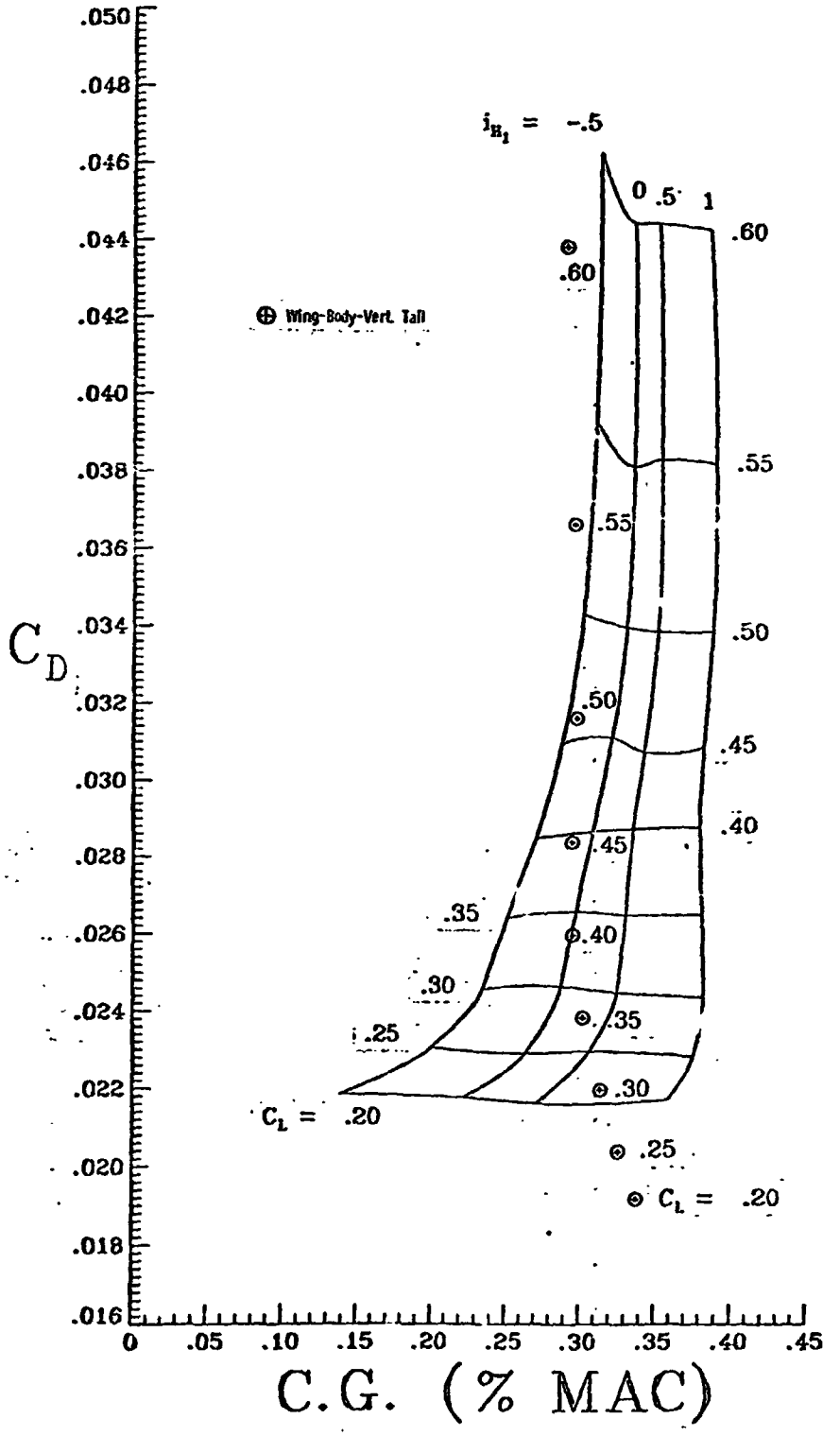

(a) H_1

17.- Variation of trimmed drag coefficient with c.g. position for wide-body wing configurations (M_∞ = 0.82).

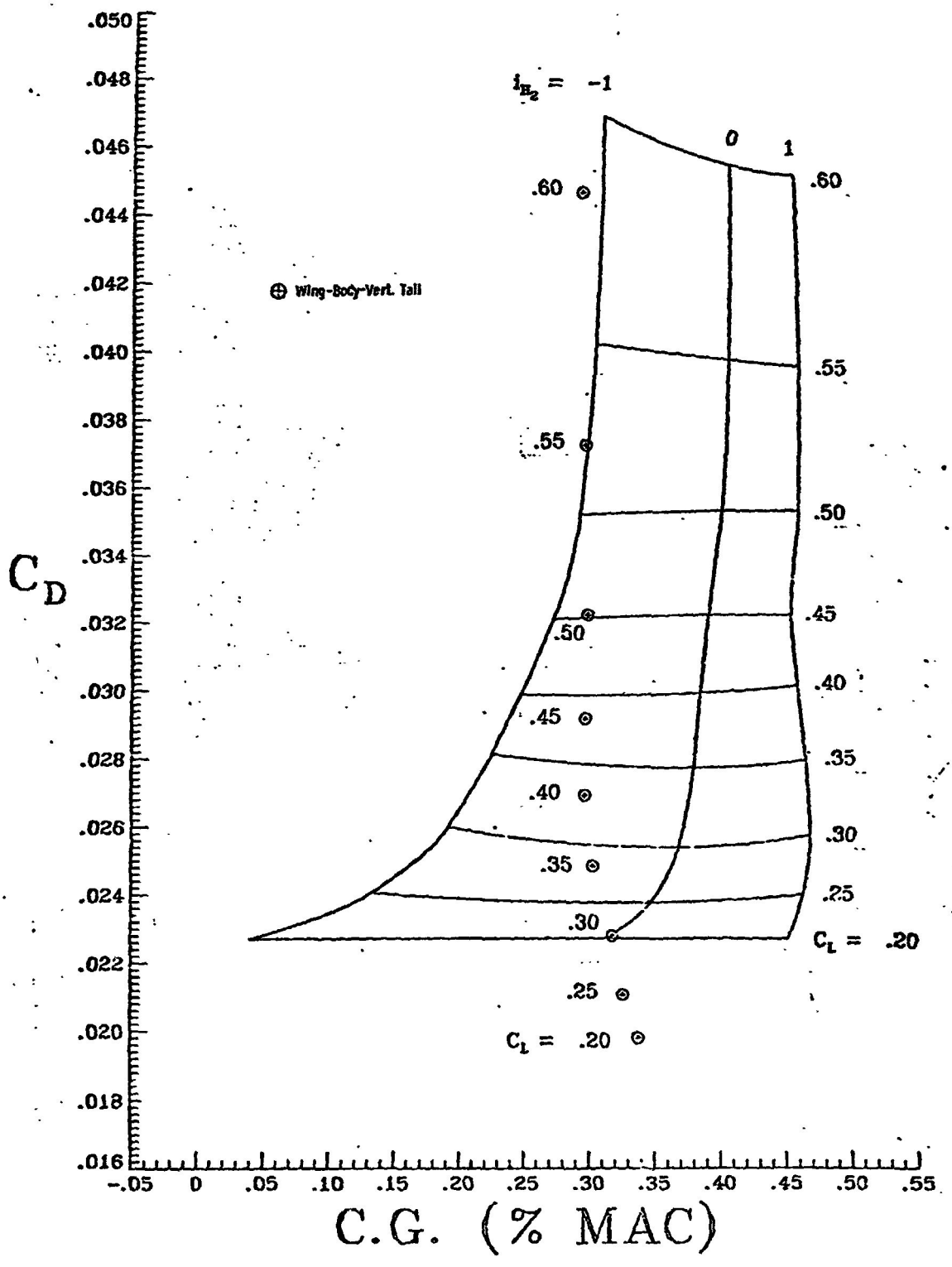

(b) H_2

Figure 17.- Continued.

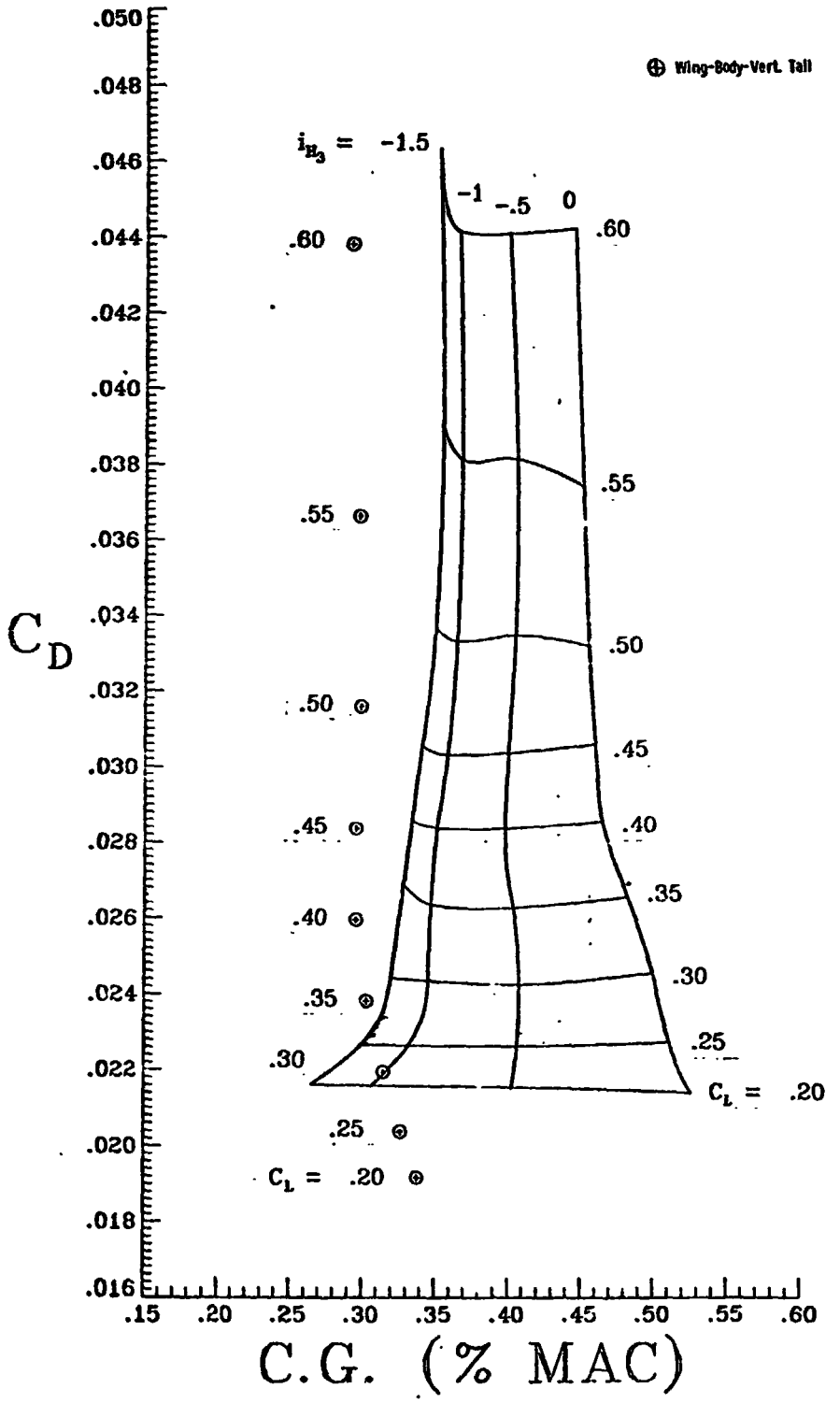

(c) H_3

Figure 17.- Continued.

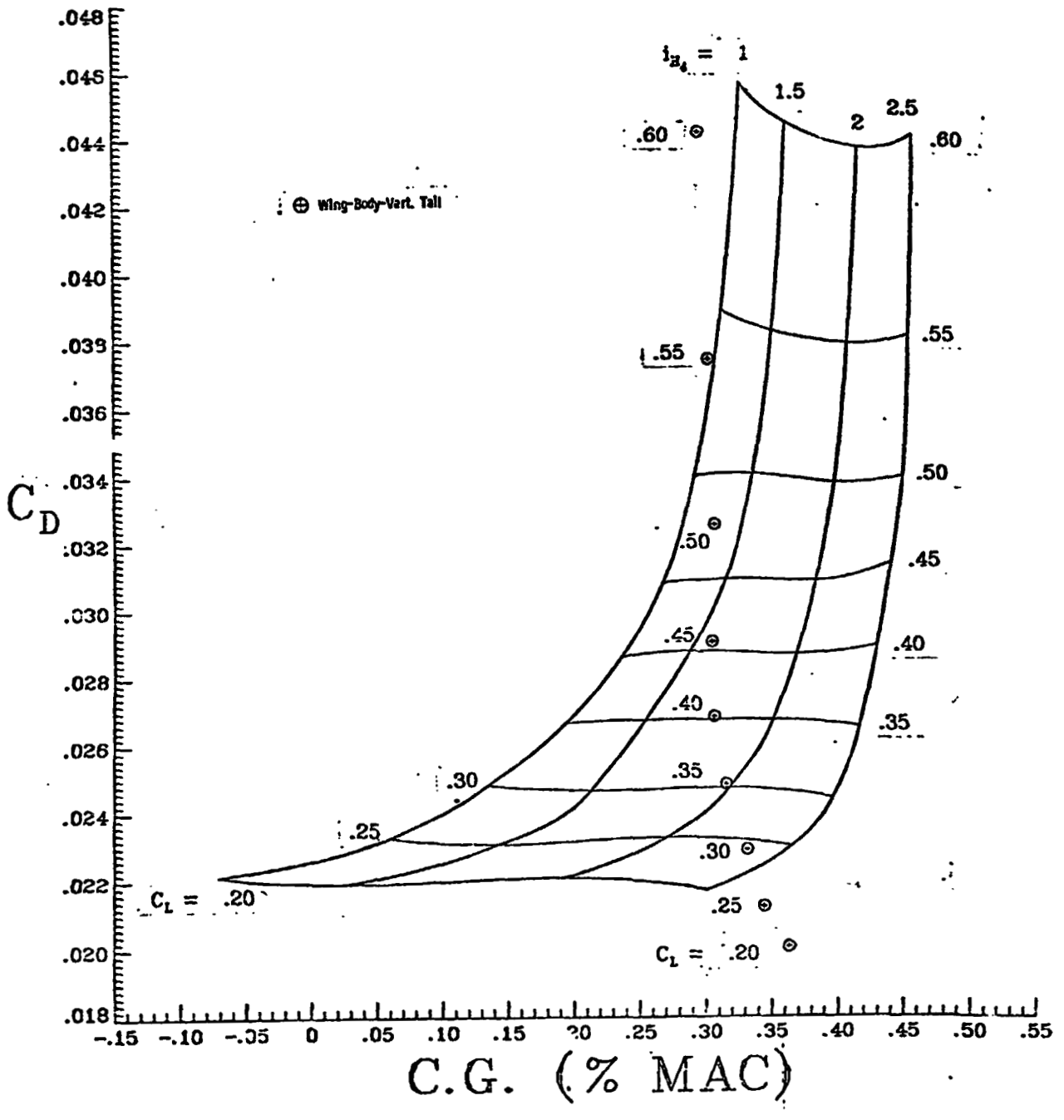

(d) H_4

Figure 17. - Continued.

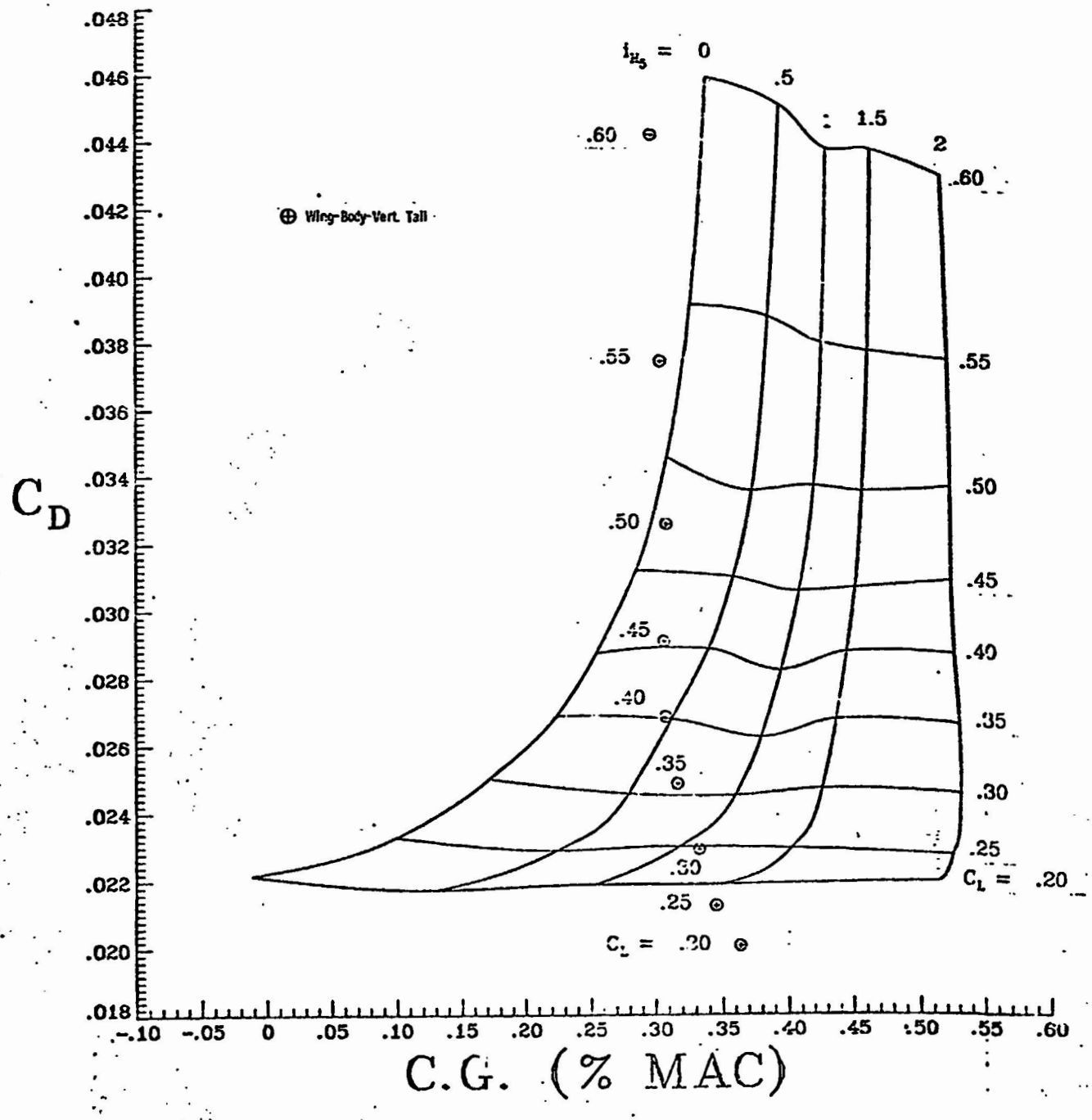

(e) H_5

Figure 17.- Concluded.

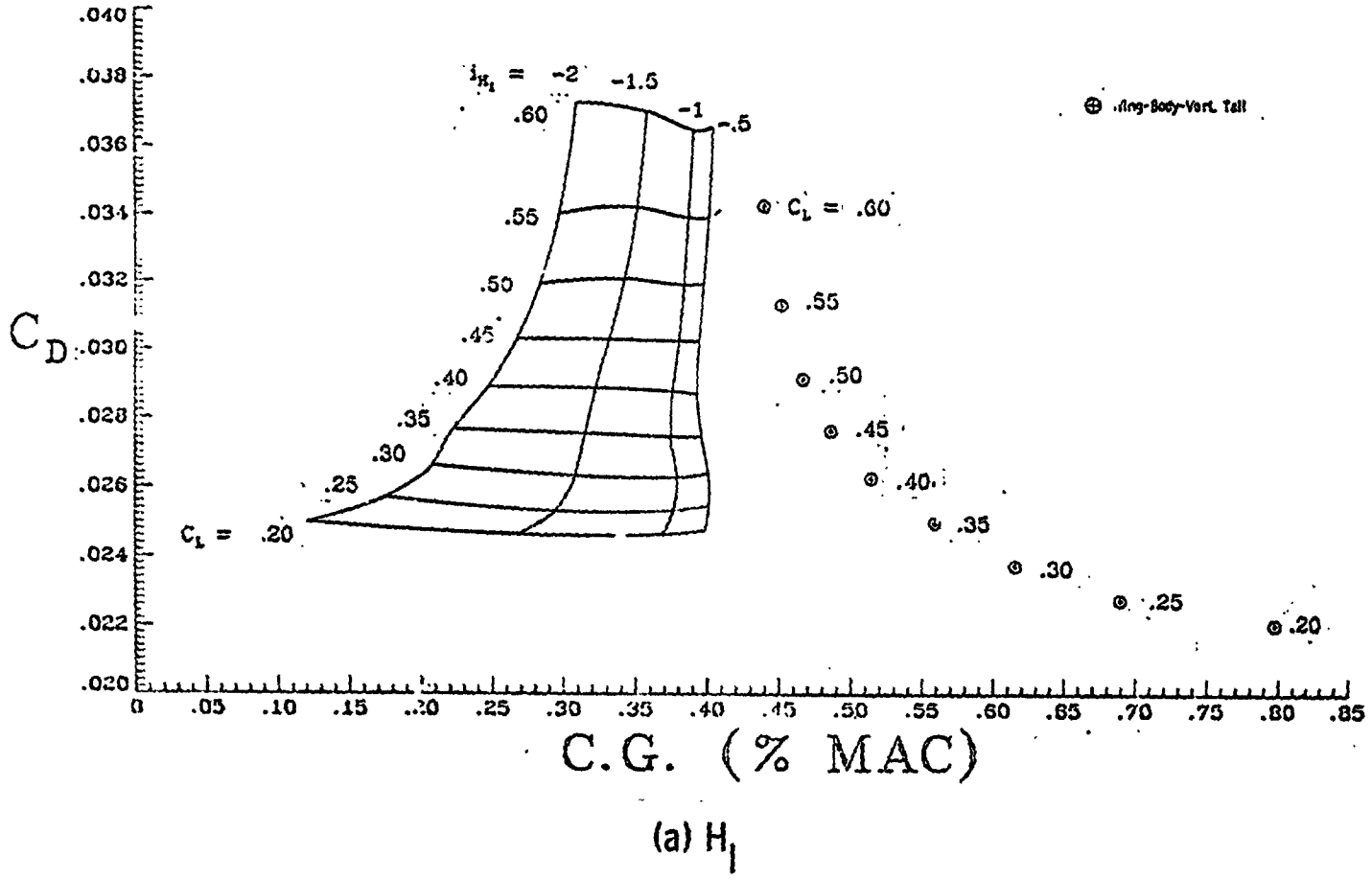

(a) H_1

Figure 18. - Variation of trimmed drag coefficient with c.g. position

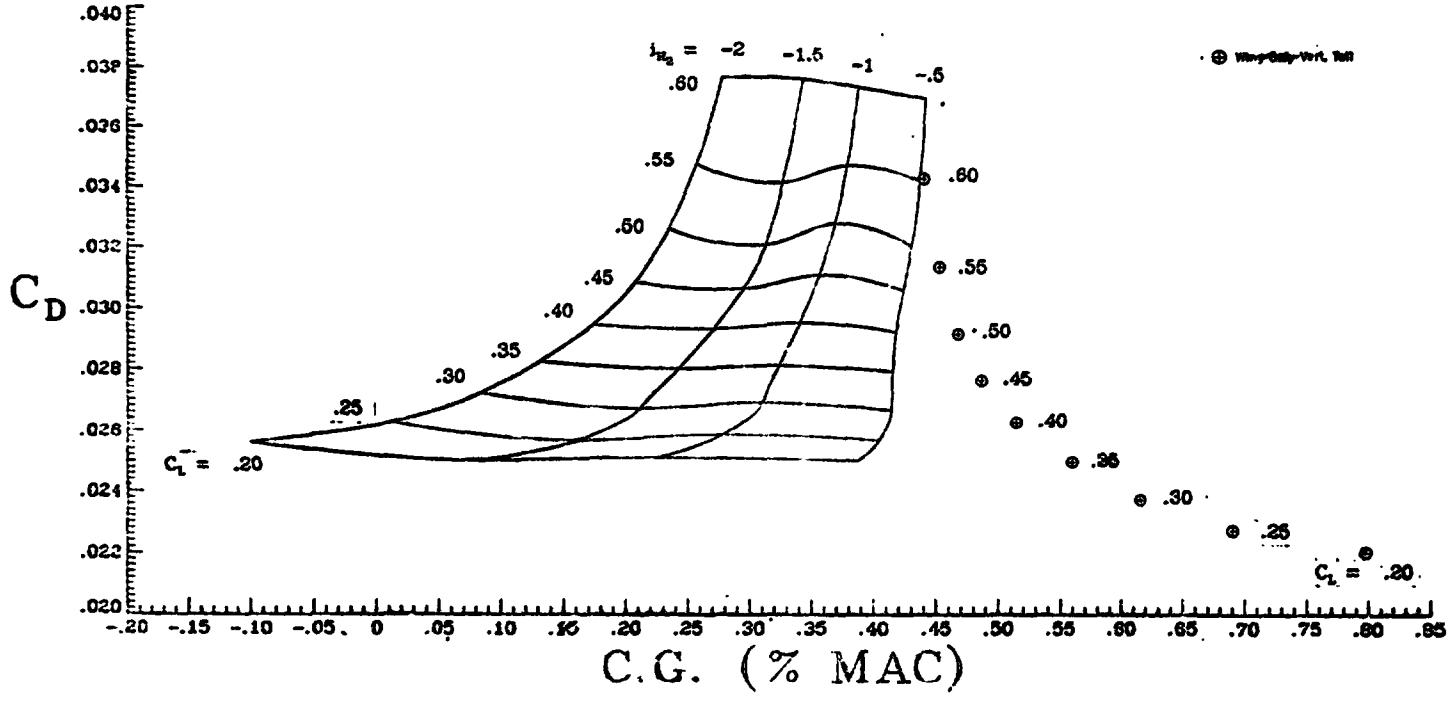

(b) H_2

Figure 18. - Continued.

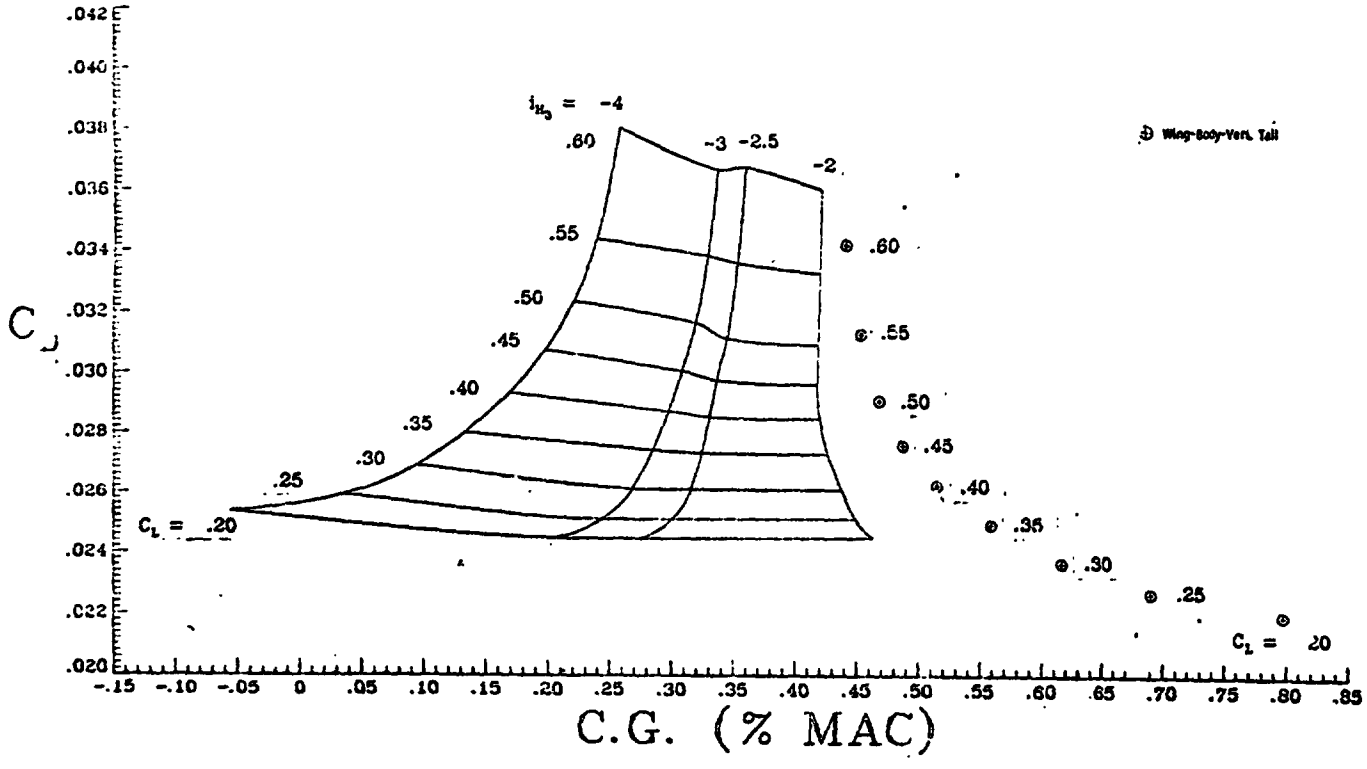

(c) H_3

Figure 18.- Continued.

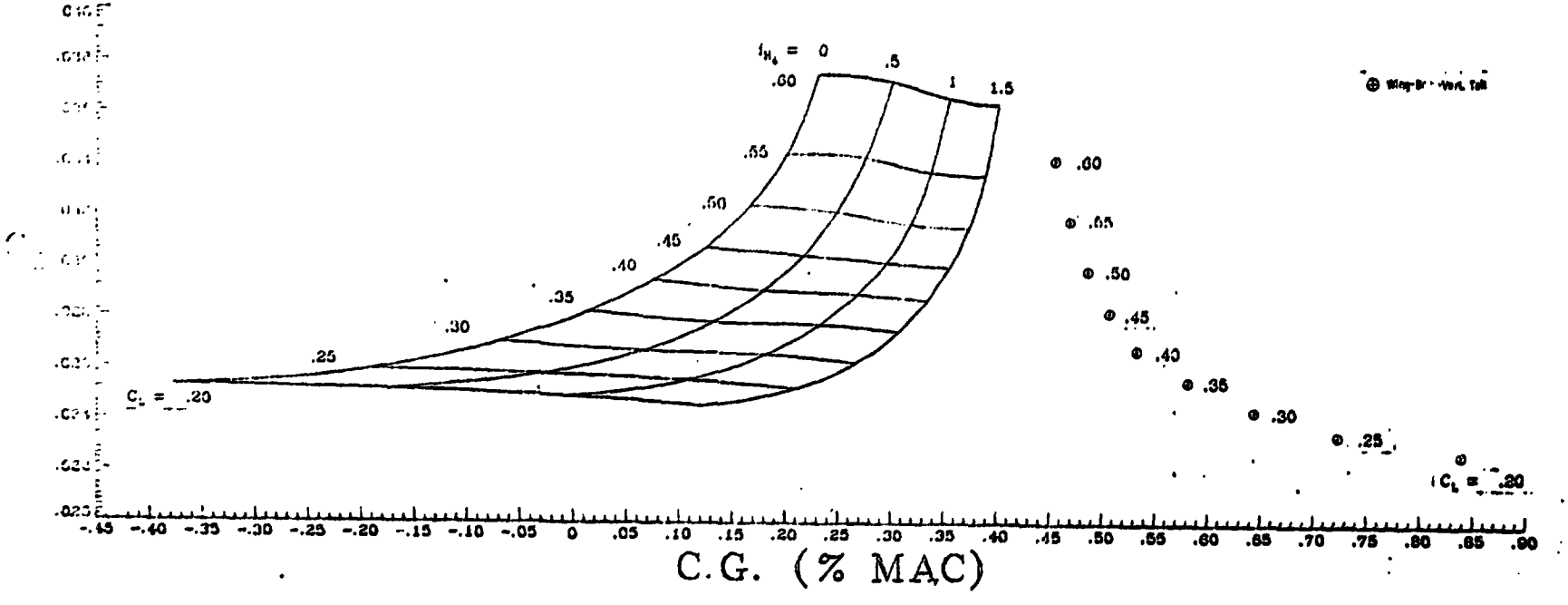

(d) H_4

Figure 18.- Continued.

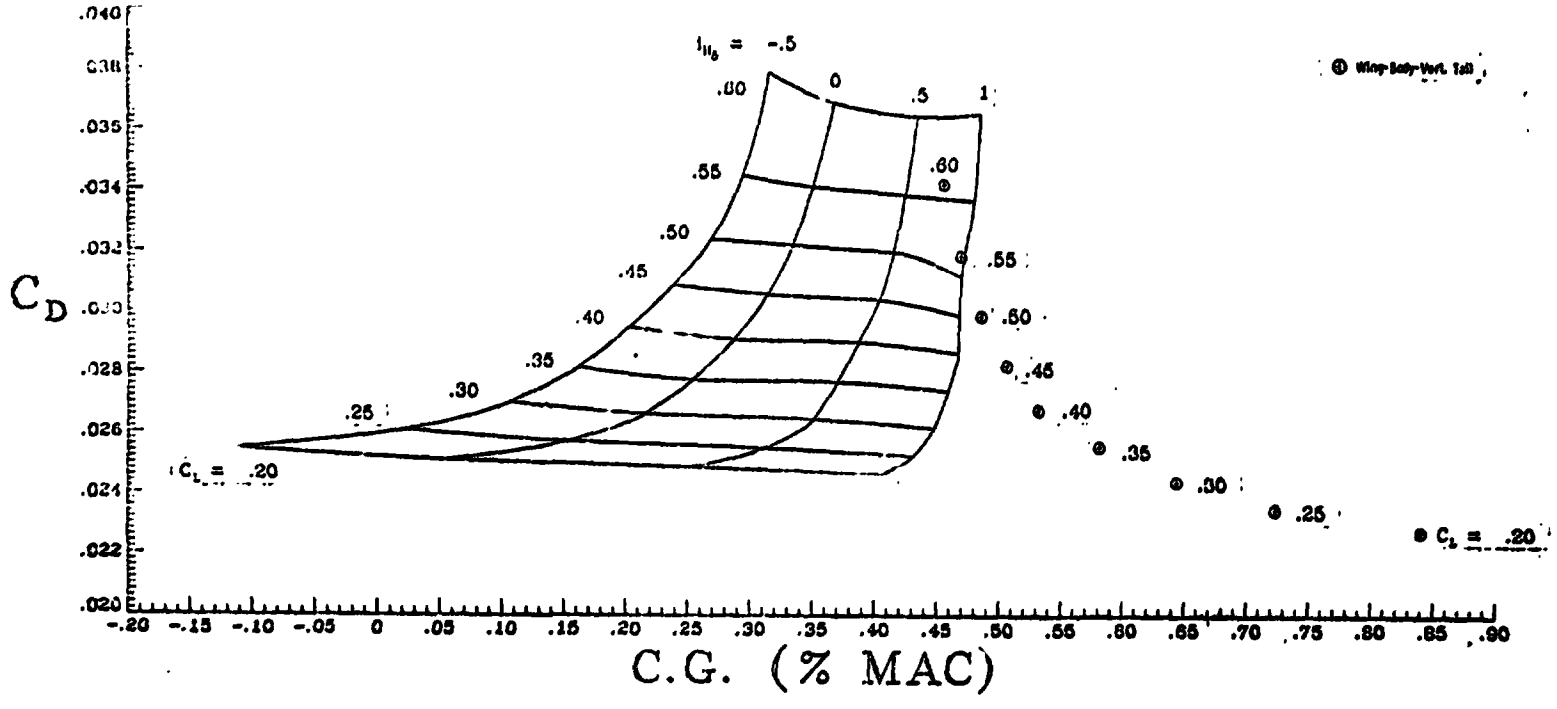

(e) H_5

Figure 18. - Concluded.

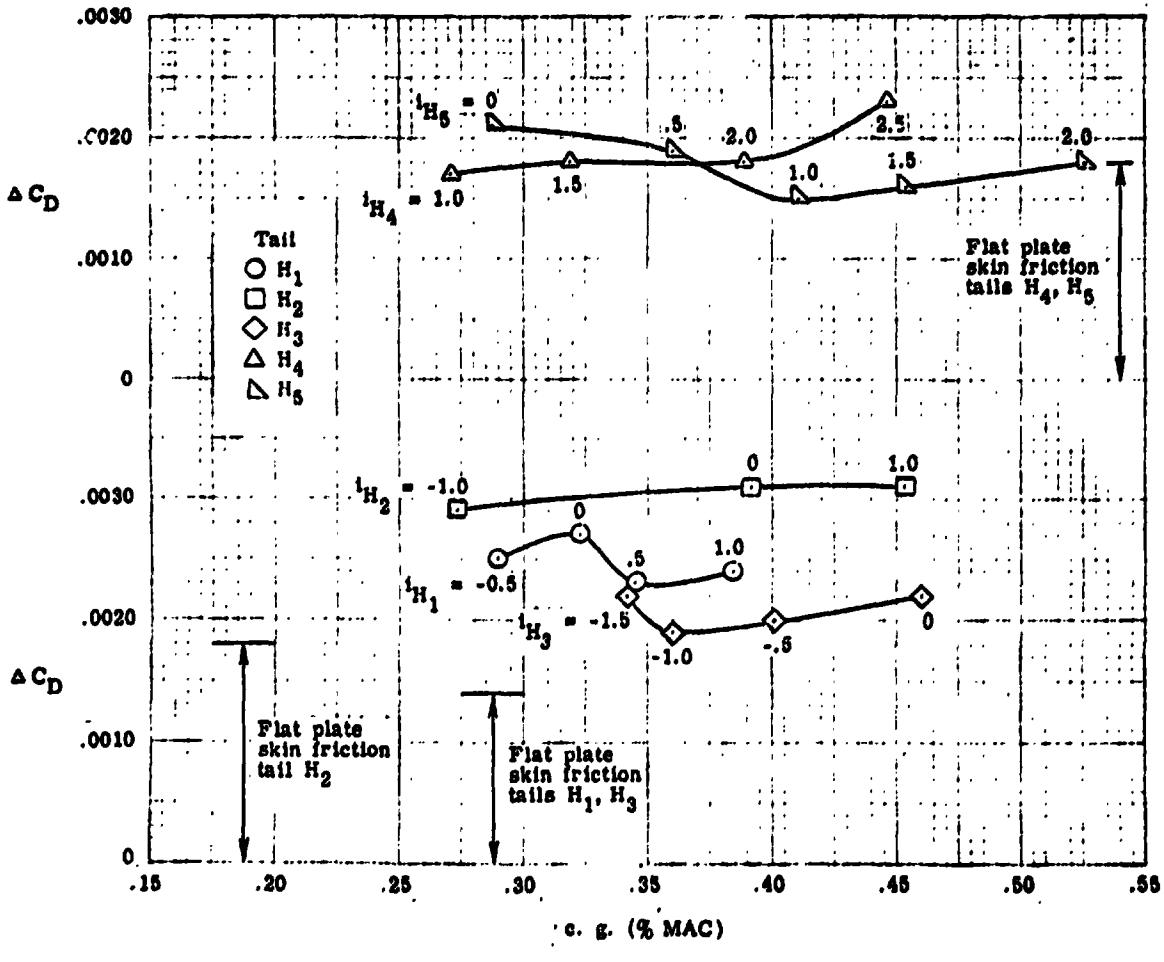

Figure 19.- Variation of trim drag increment with c.g. position for wide-body wing configurations ($M_\infty = 0.82$, $C_L = 0.45$).

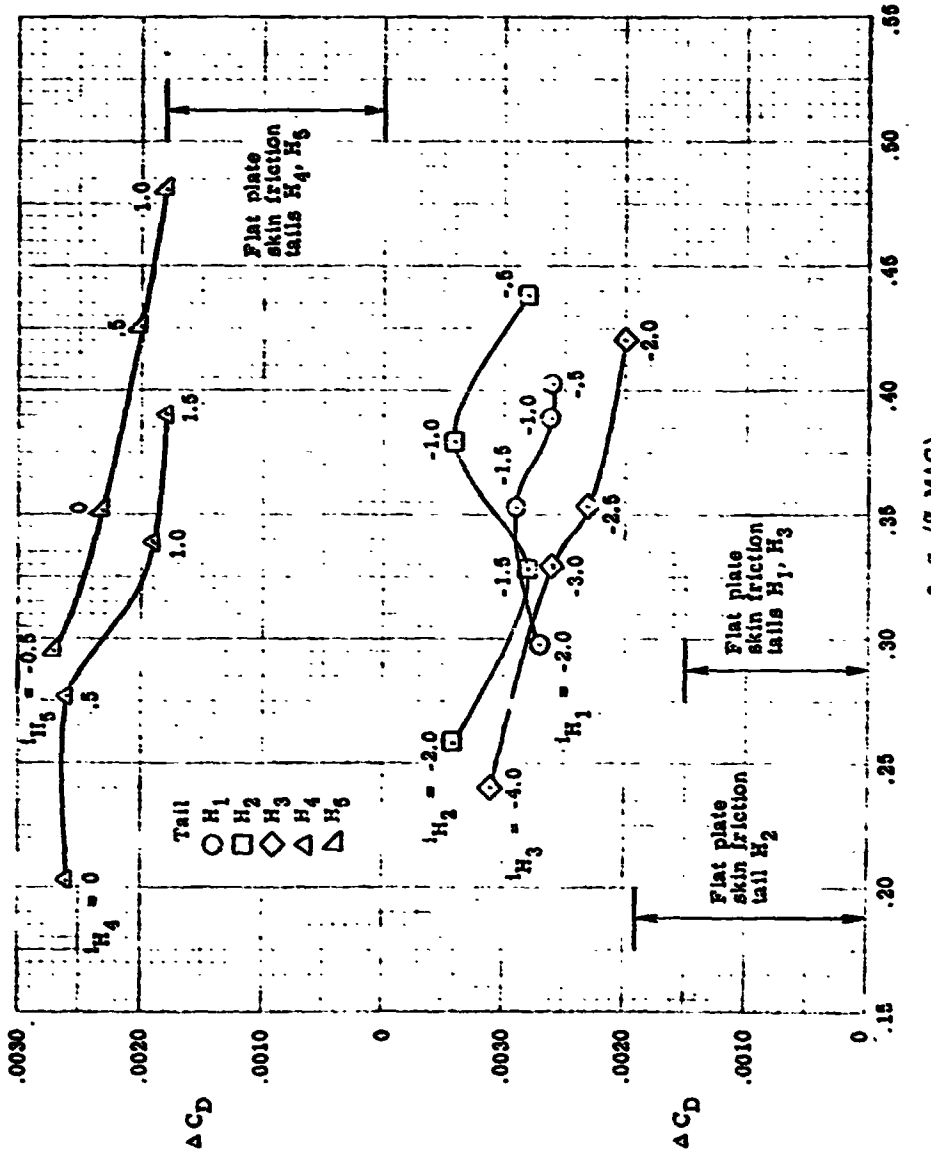

Figure 20.- Variation of trim drag increment with c.g. position for supercritical wing configurations (M_∞ = 0.82, C_L = 0.55).

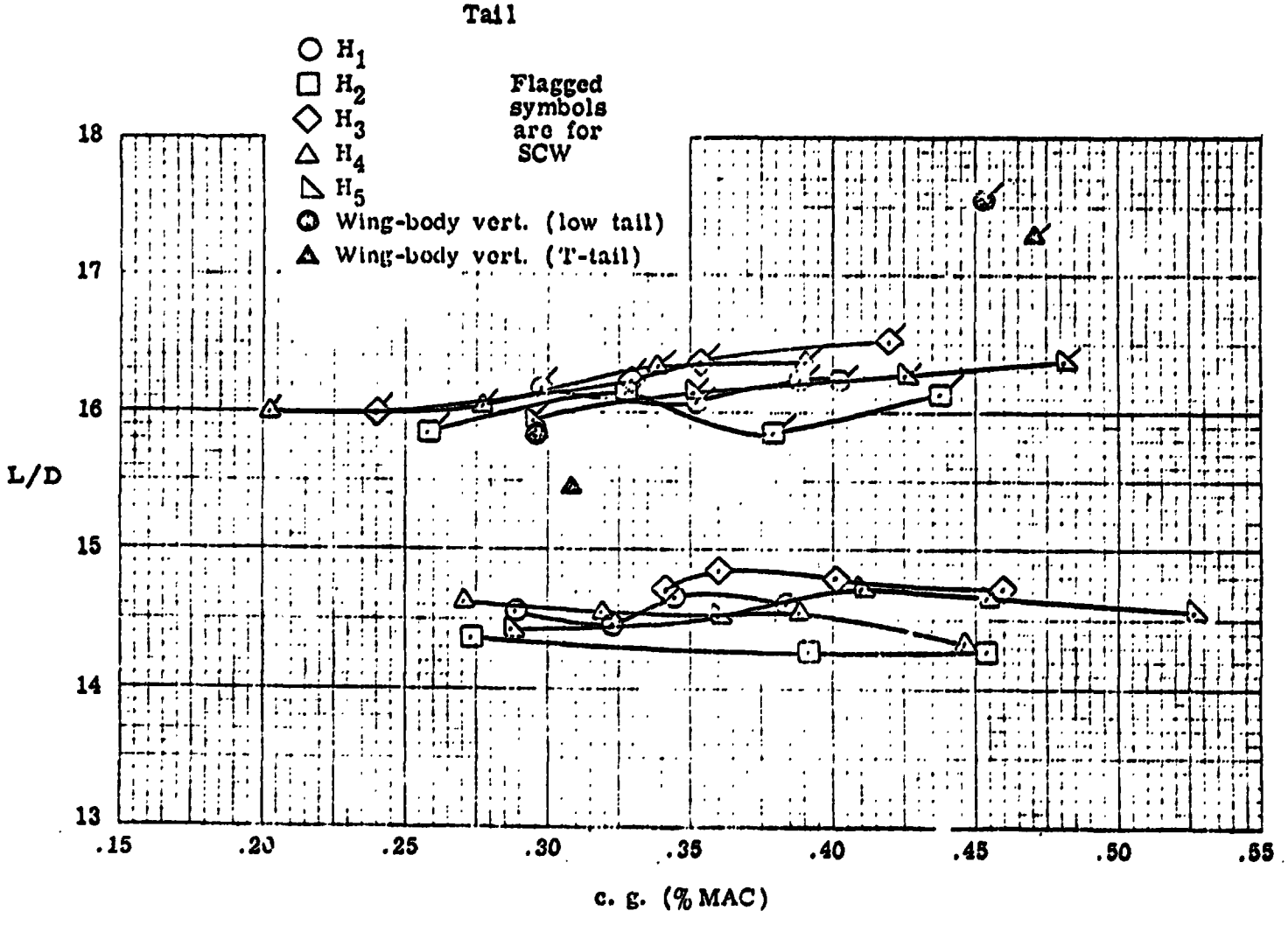

Figure 21. - Variation of lift-to-drag ratio with c.g. position for both wings at their cruise lift coefficients ($M_\infty = 0.82$).

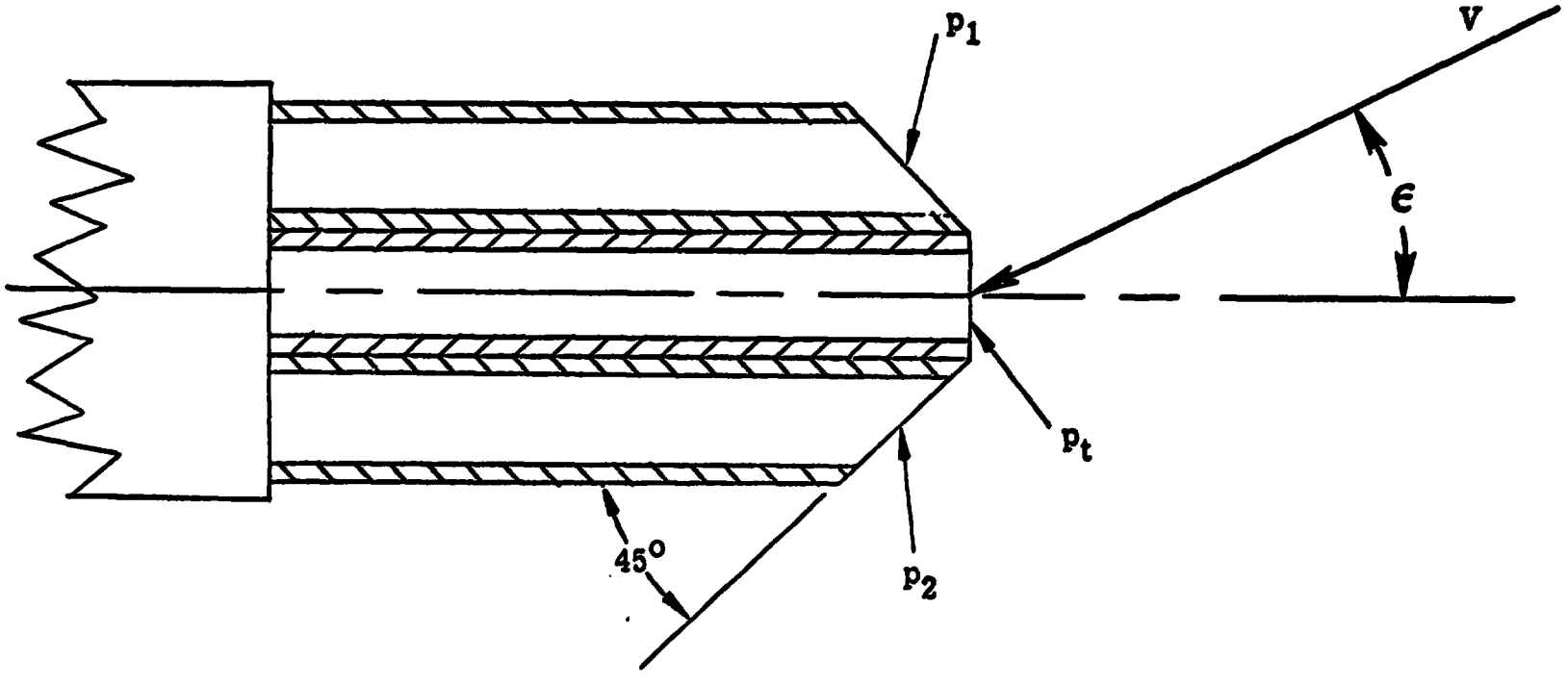

Figure 22. - Schematic drawing of a yaw head.

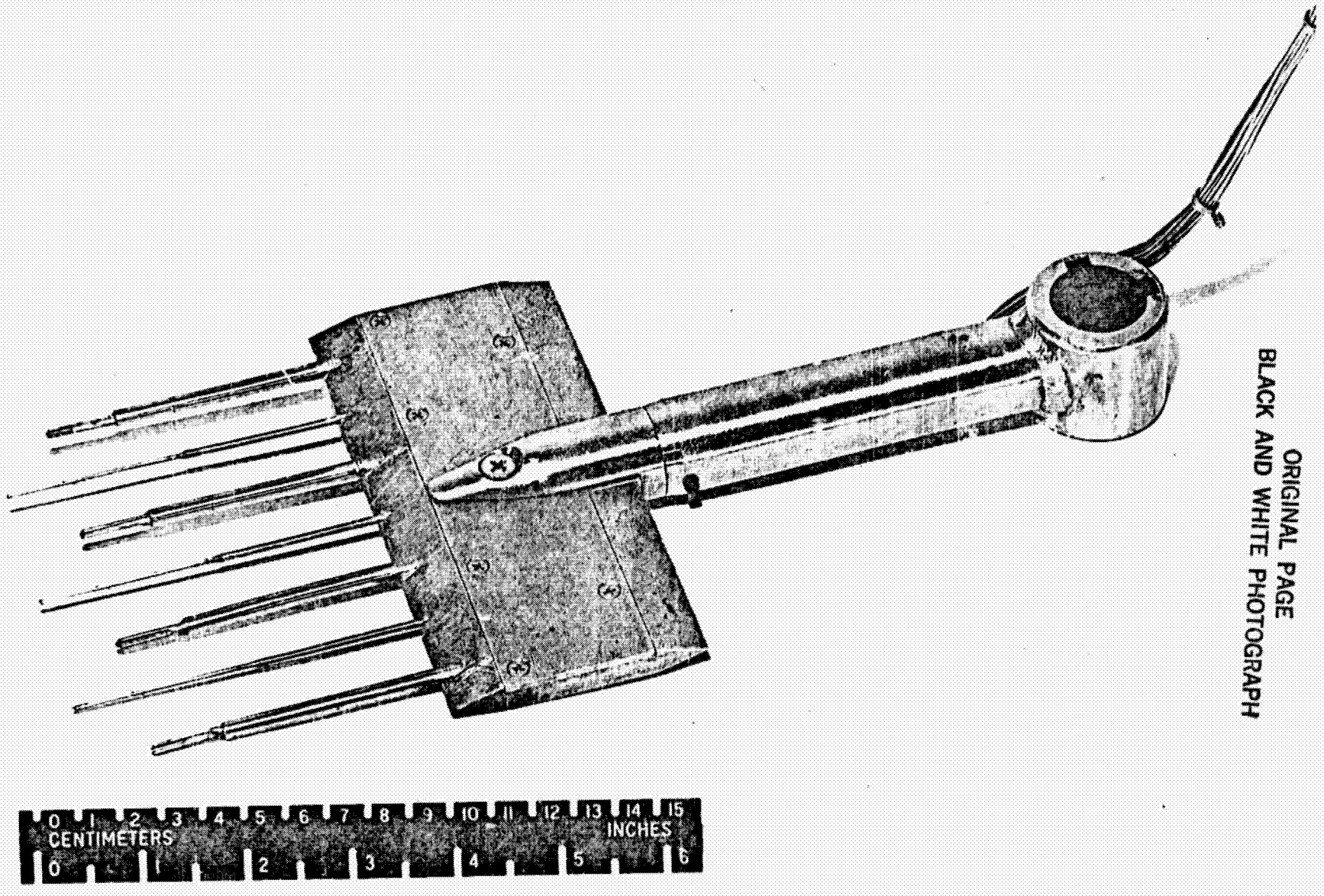

ORIGINAL PAGE
BLACK AND WHITE PHOTOGRAPH

Figure 23.- Photograph of yaw head rake for low-tail configurations.

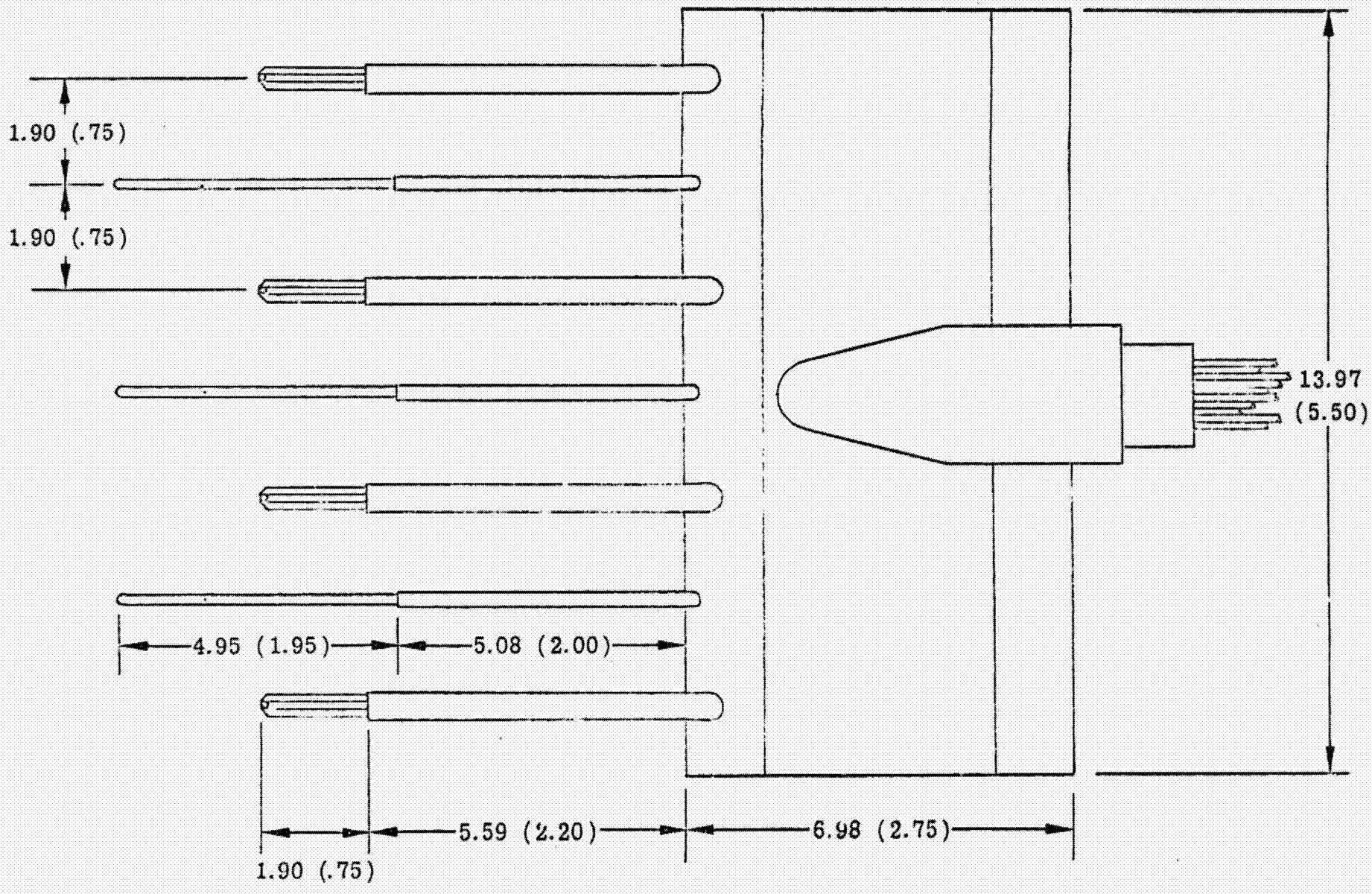

Figure 24.- Drawing of a yaw head rake.

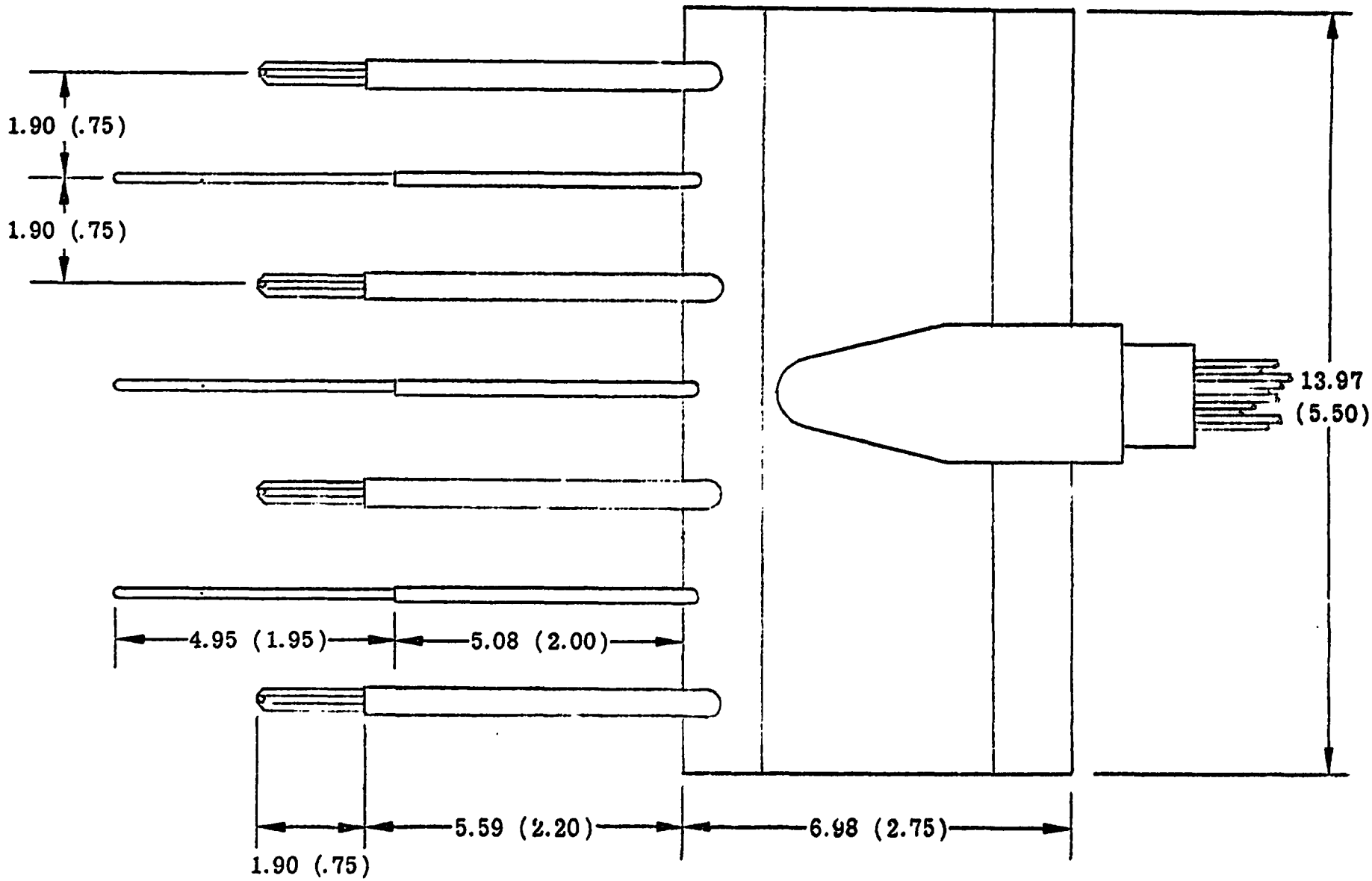

Figure 24.- Drawing of a yaw head rake.

Figure 25. - Photograph of typical yaw head rake installation for low-tail configurations.

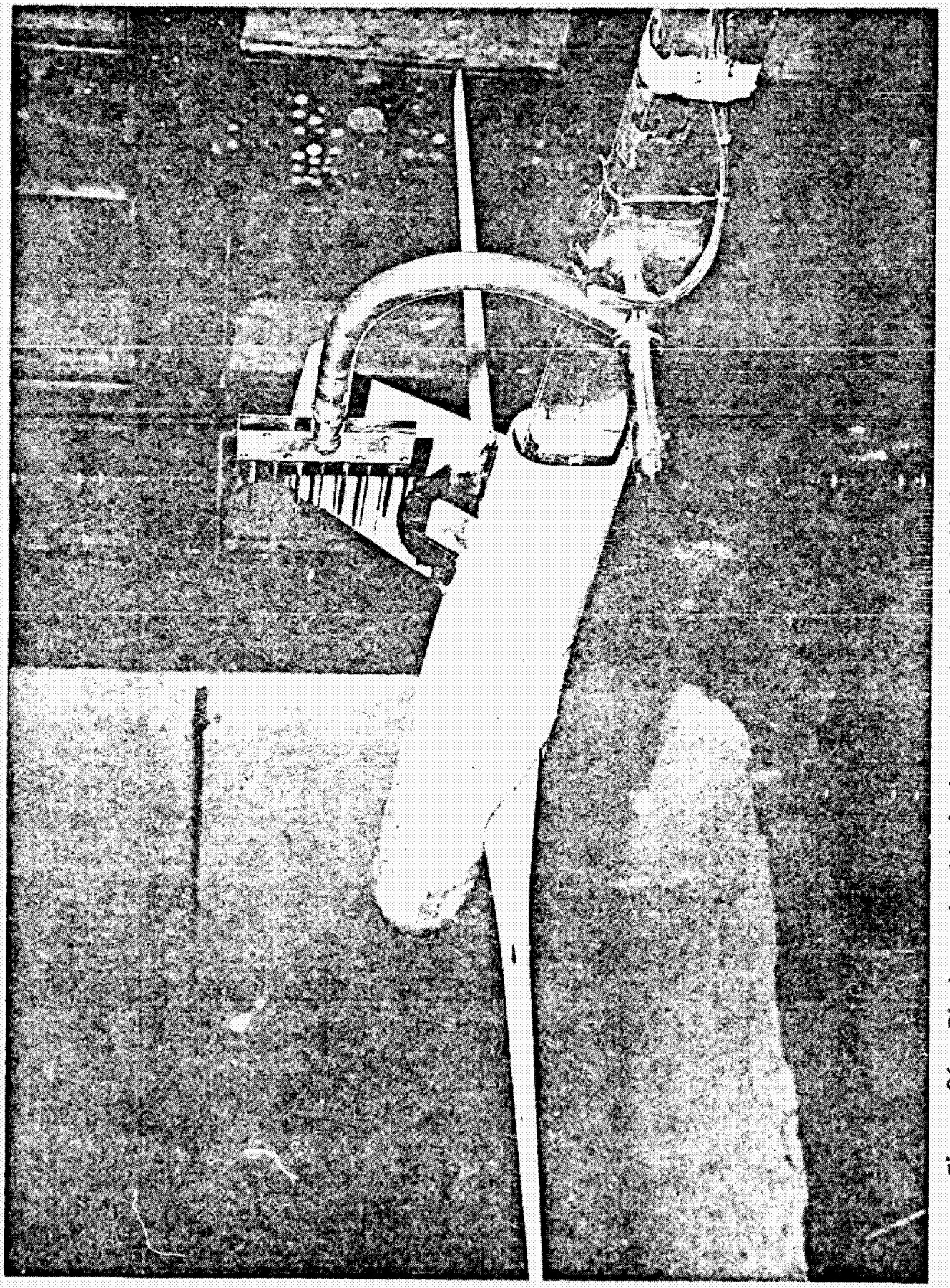

Figure 26. - Photograph of typical yaw head rake installation for T-tail configurations.

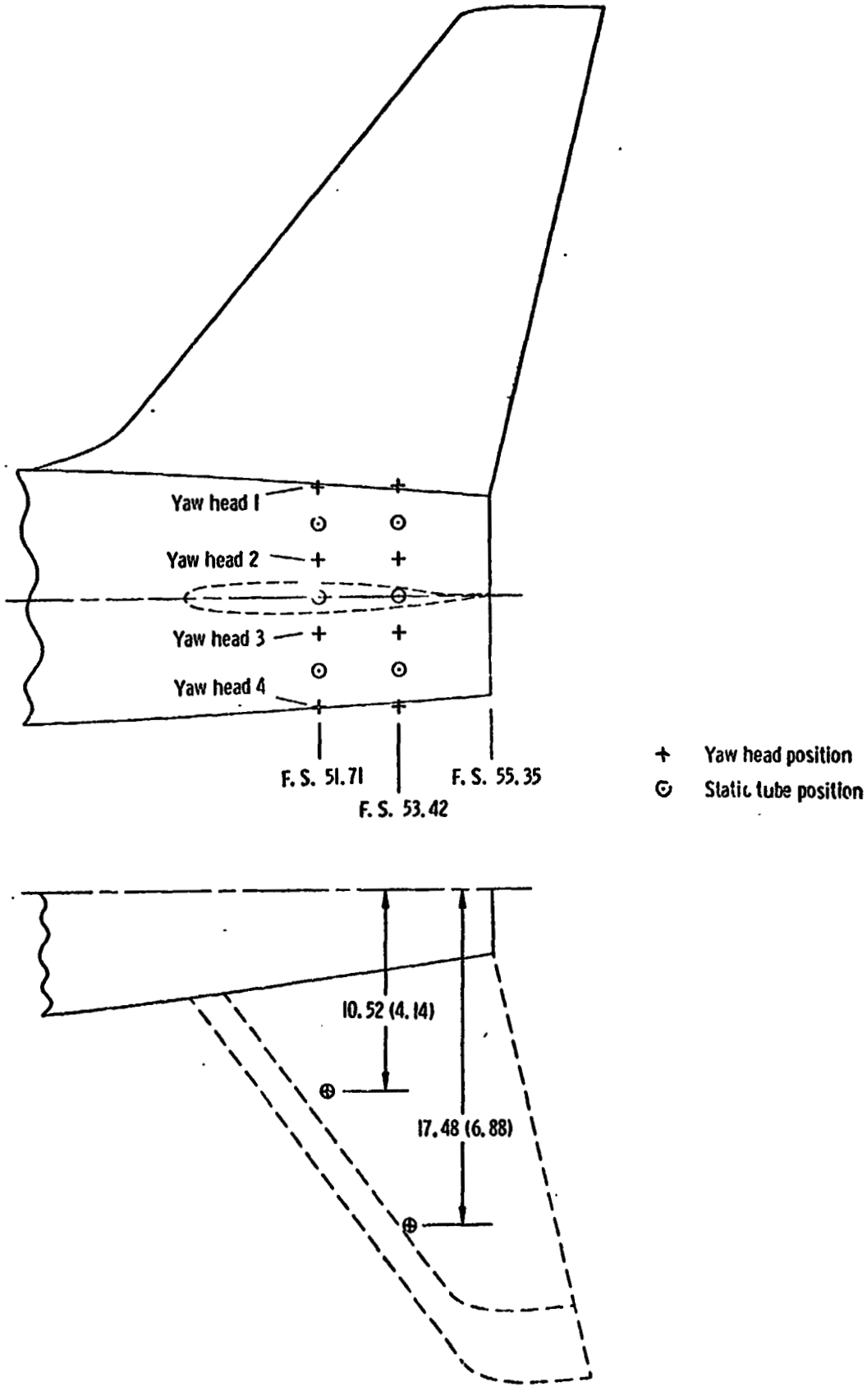

Figure 27.- Drawing of yaw head rake data positions for low-tail configurations.

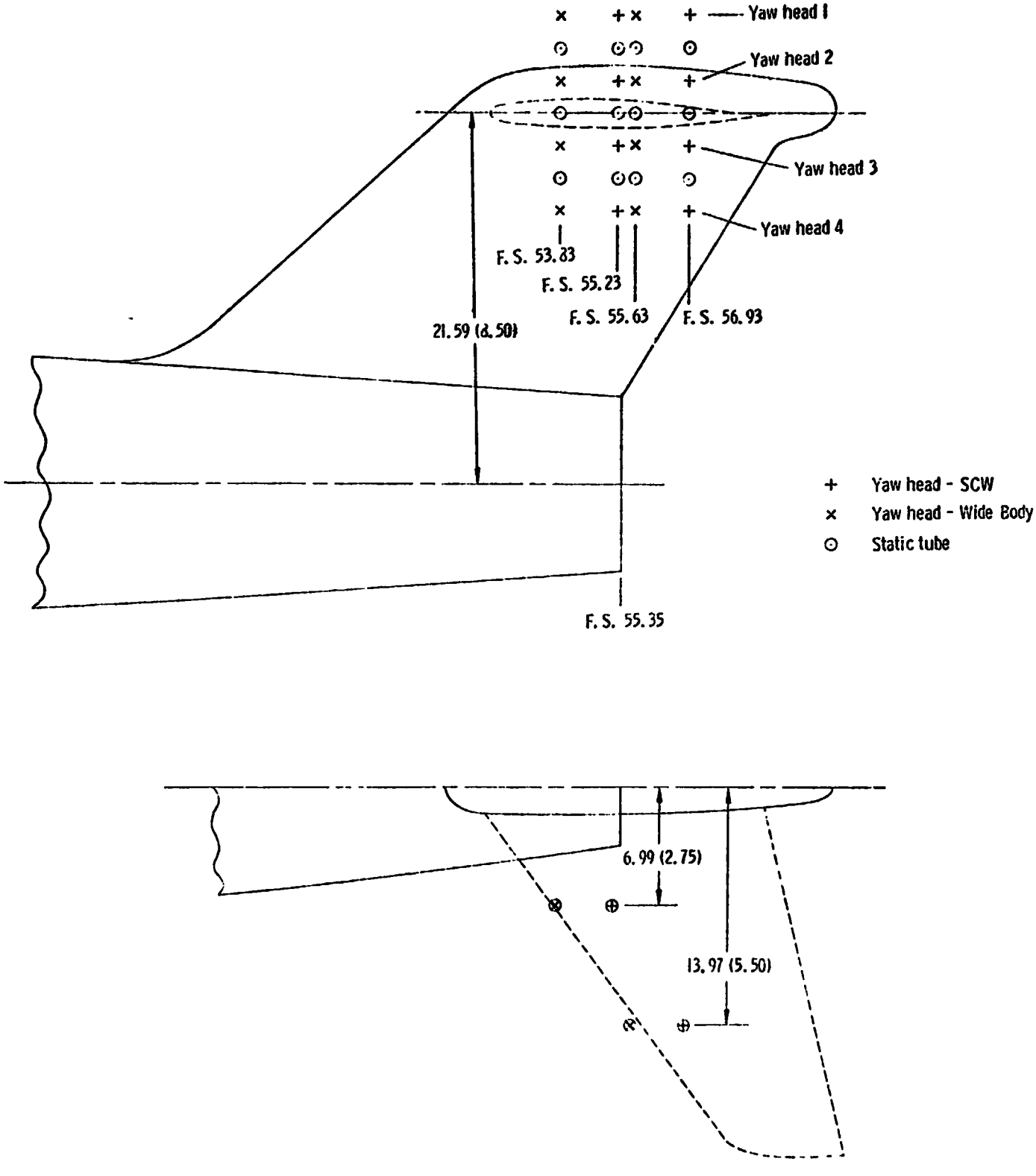

Figure 28.- Drawing of yaw head rake data positions for T-tail configurations.

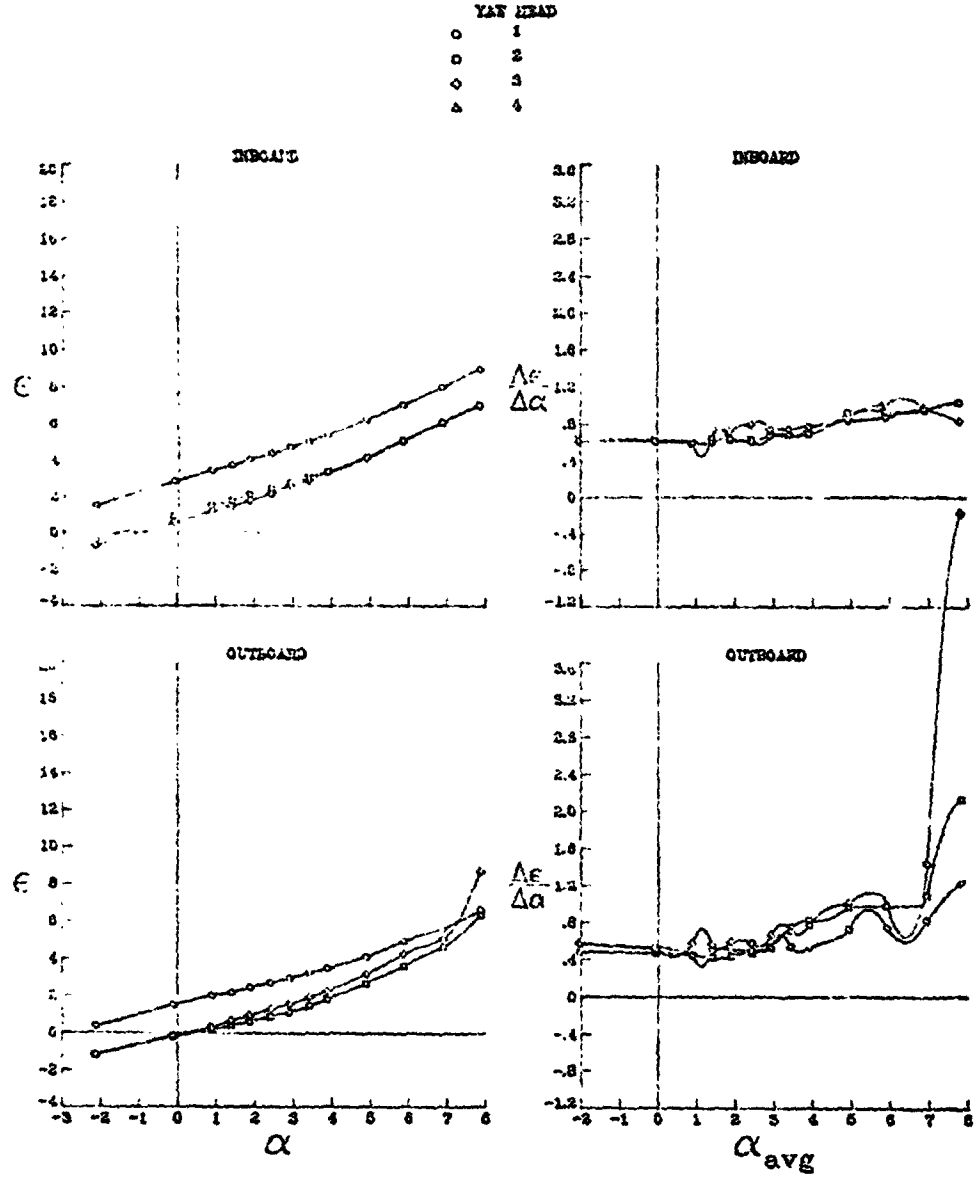

(a) Low-tail configurations

Figure 29. - Variation of downwash angle, and rate of change of downwash angle with angle of attack, [illegible] wide-body wing configurations (M = 0.22;

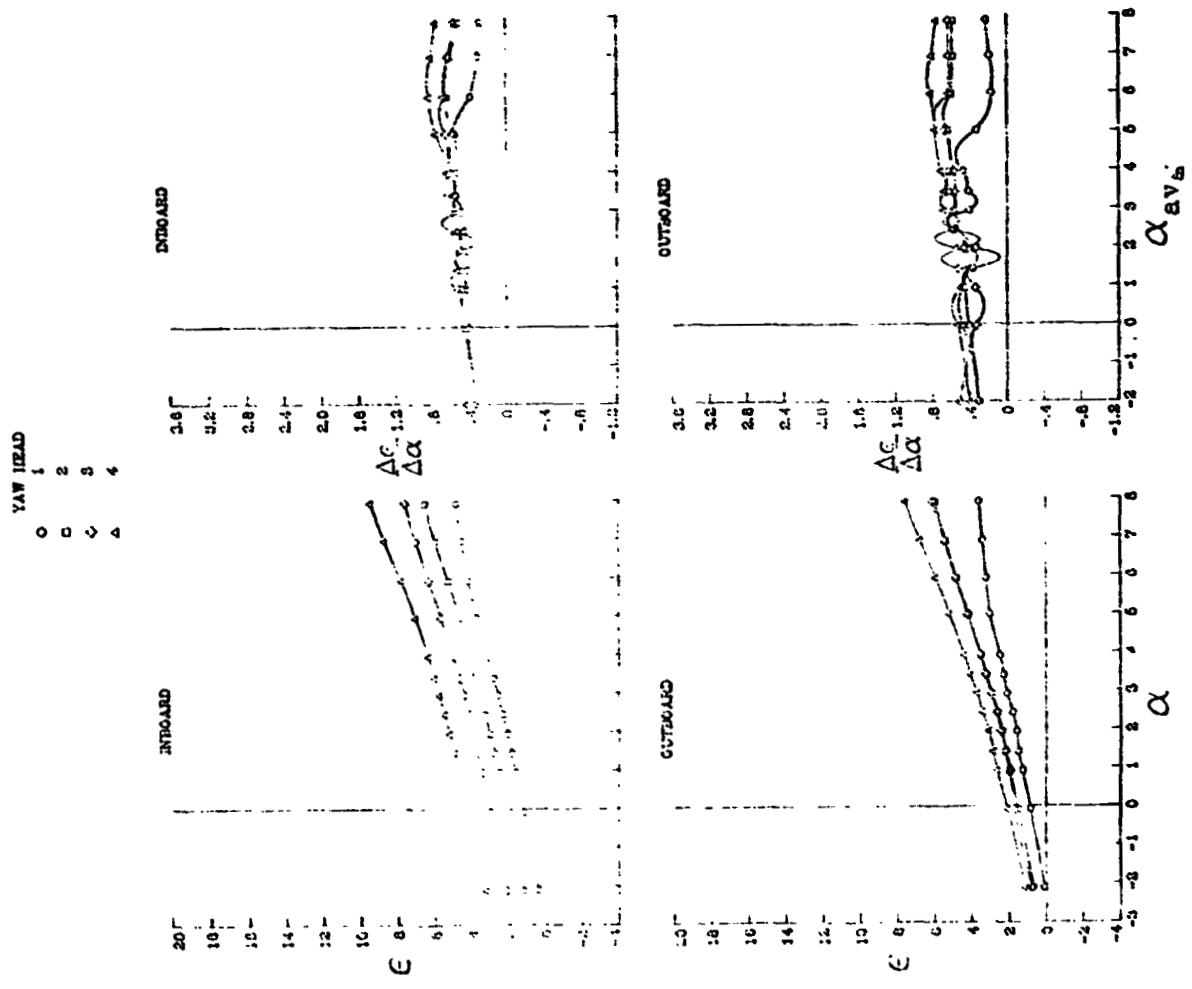

(b) T-tail configurations

Figure 29. - Concluded.

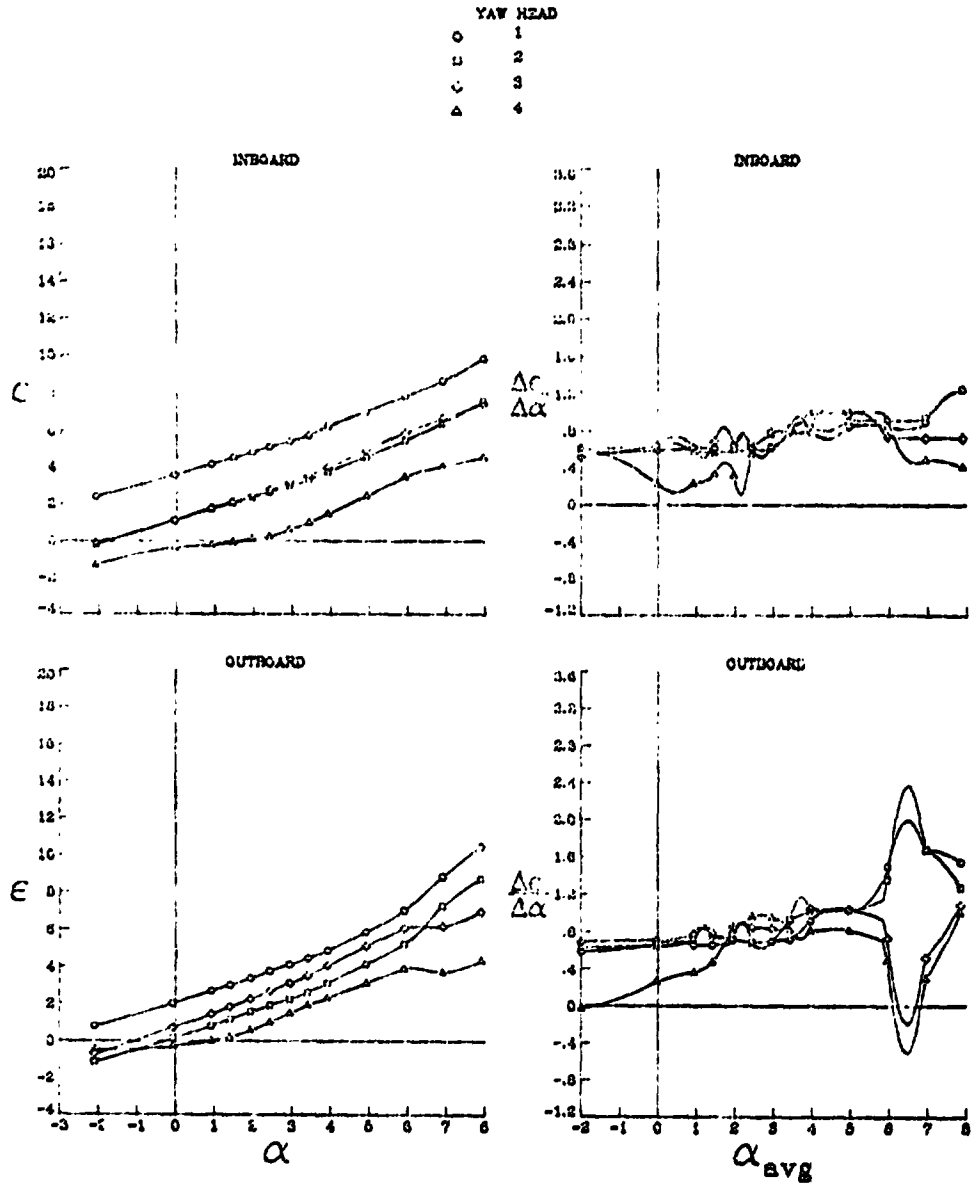

(a) Low-tail configurations

Figure 30. - Variation of downwash angle, and rate of change of downwash angle with angle of attack, with angle of attack for supercritical wing configurations (M = 0.82).

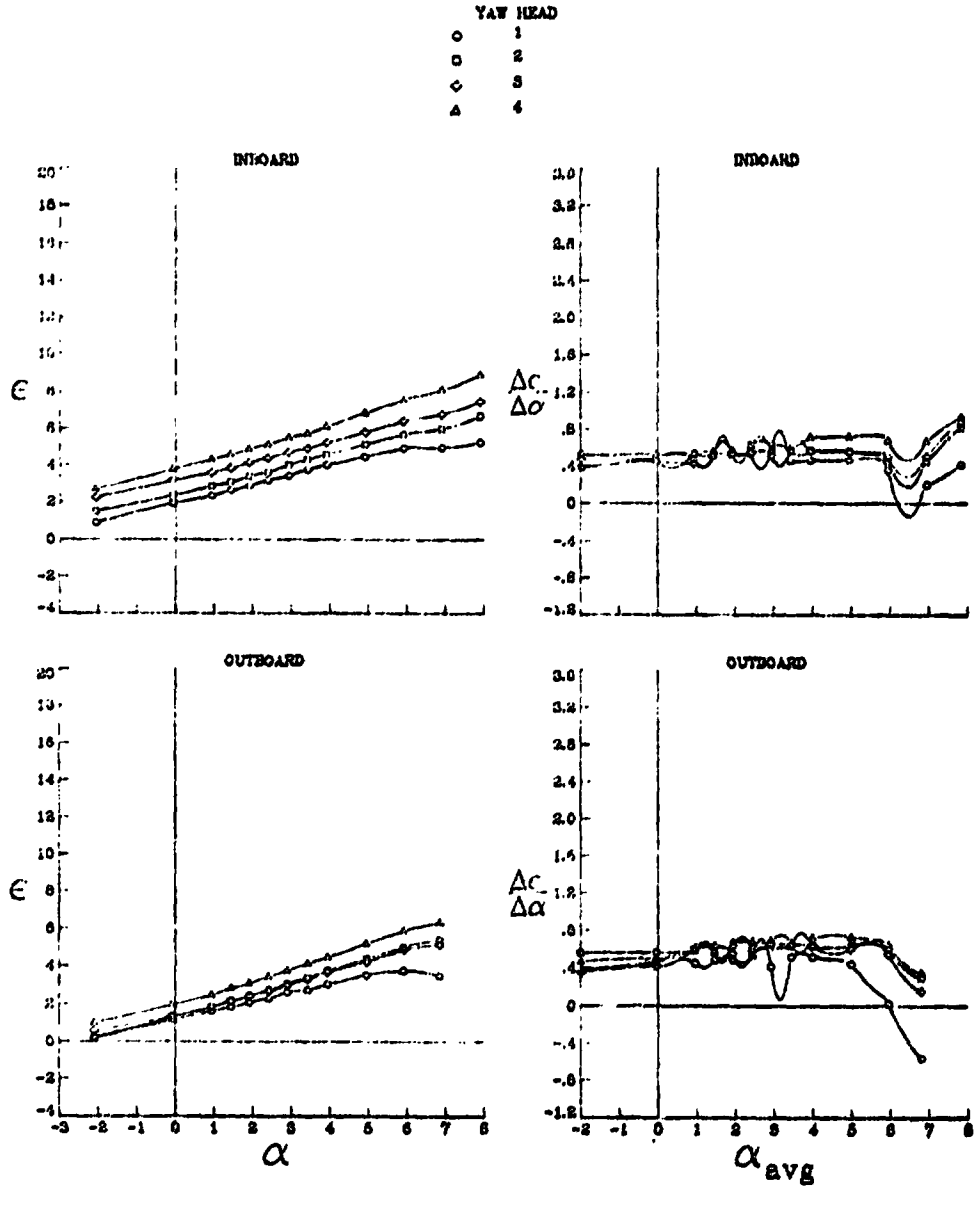

(b) T-tail configurations

Figure 30. - Concluded.

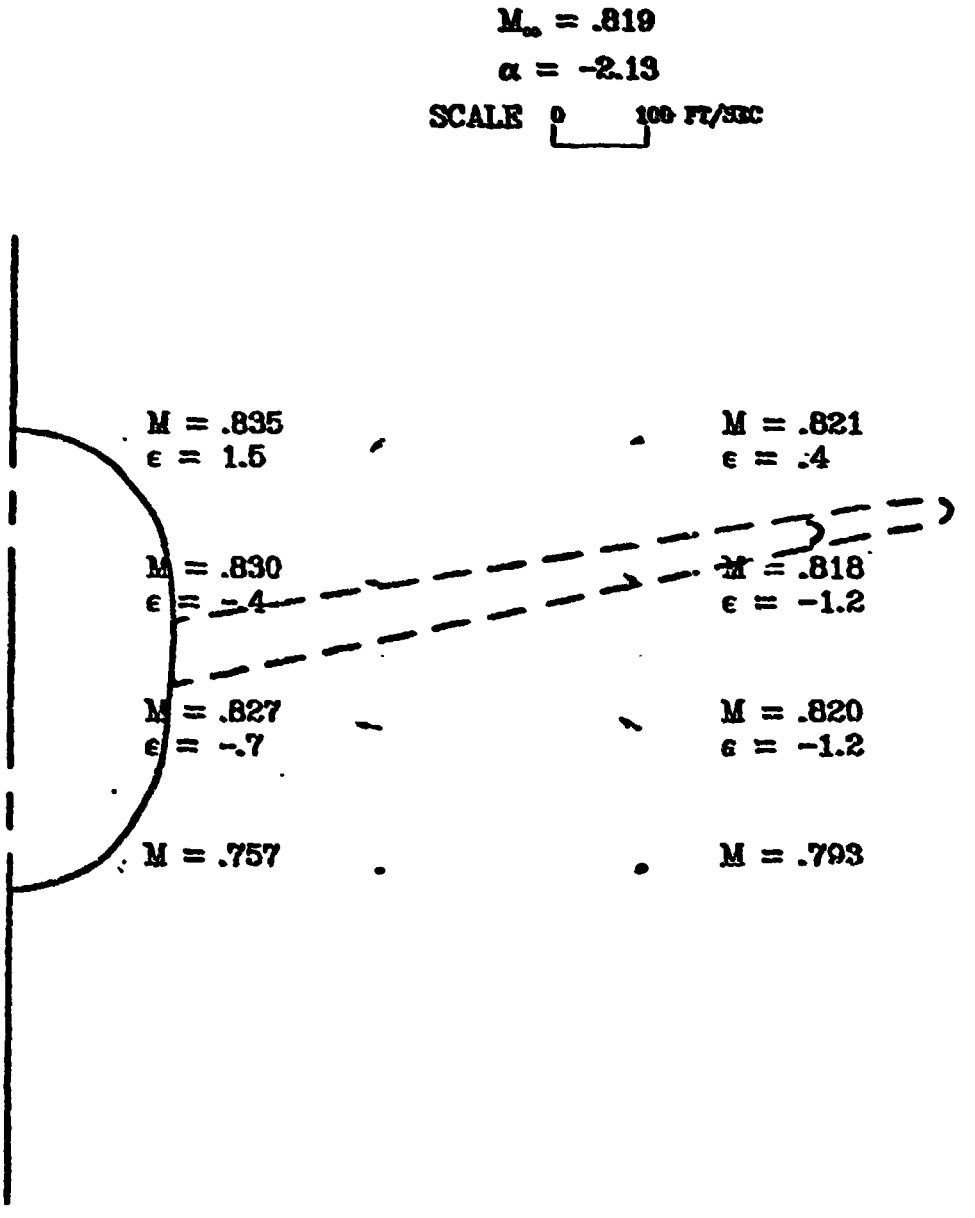

Figure 31.- Local Mach numbers and flow field velocity vectors behind the wide-body wing (low-tail configuration).

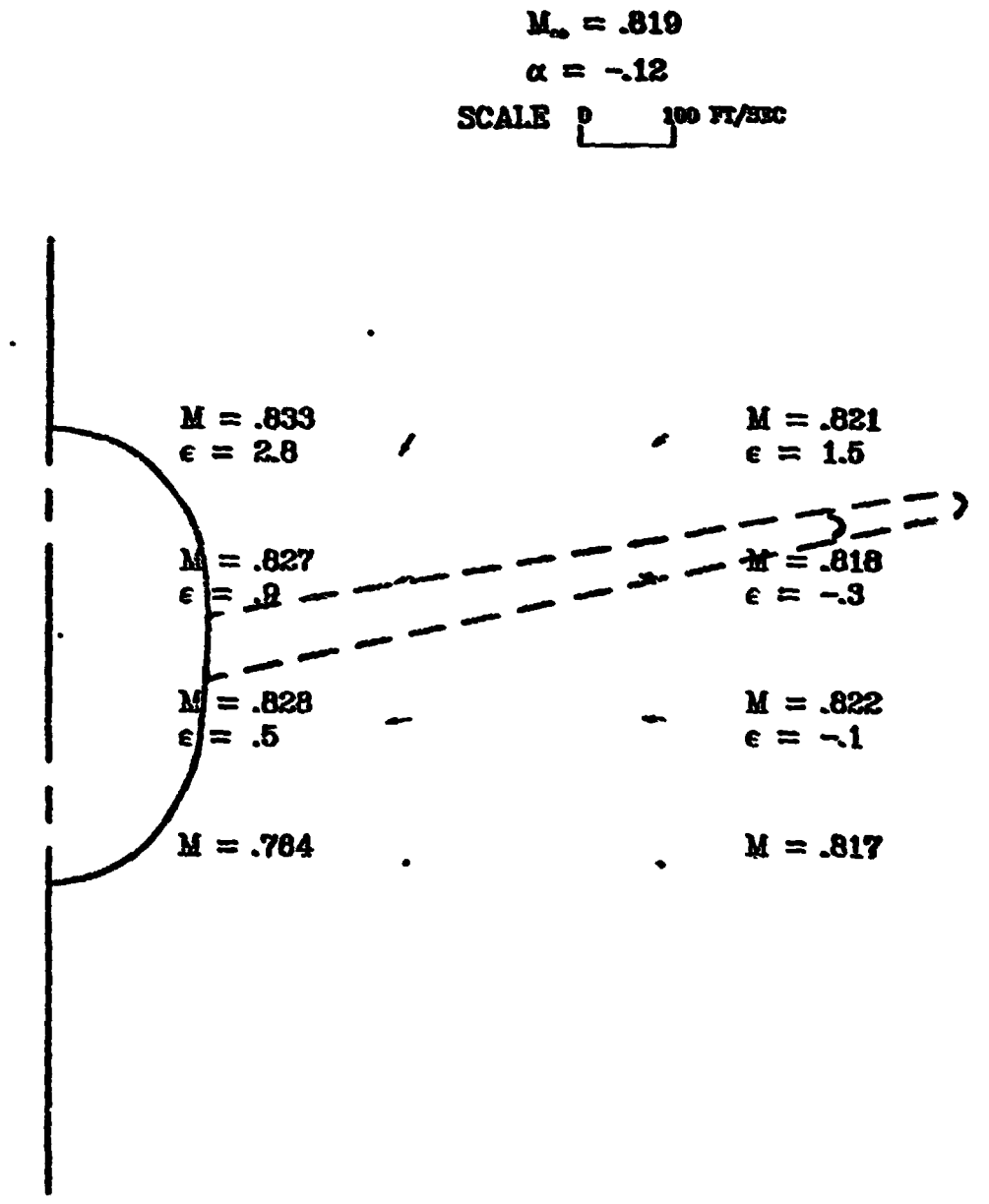

Figure 31.- Continued.

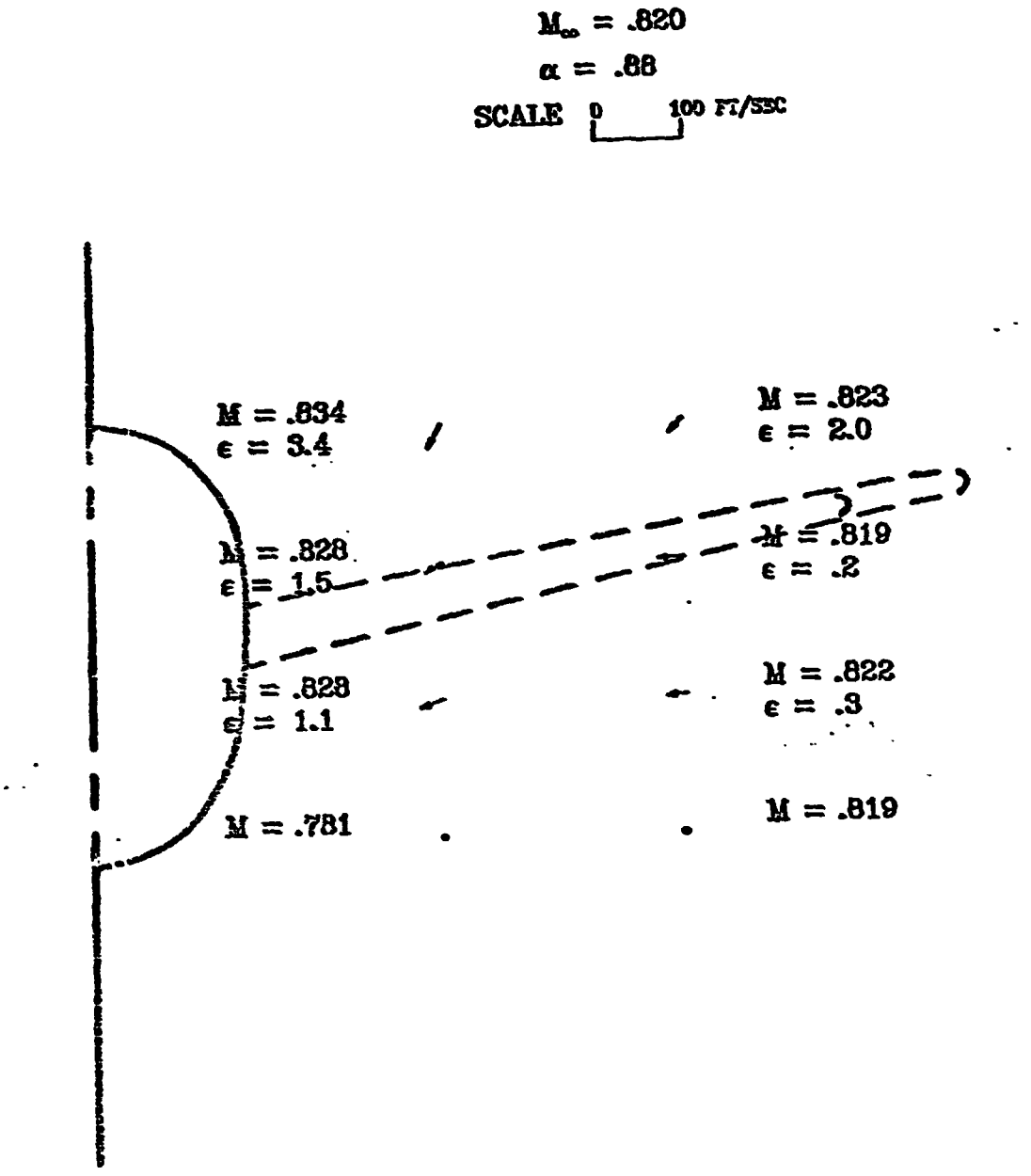

Figure 31. - Continued.

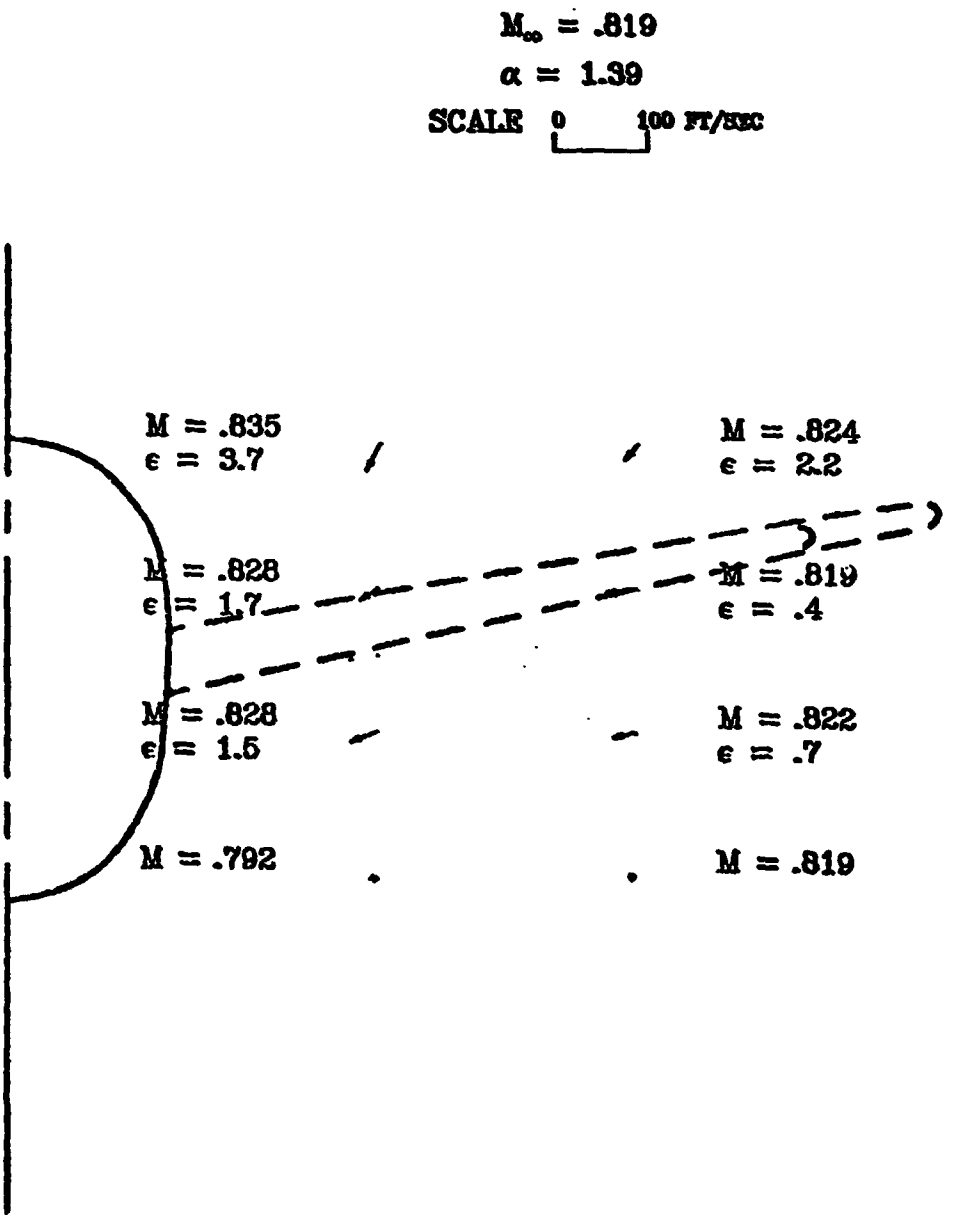

Figure 31. - Continued.

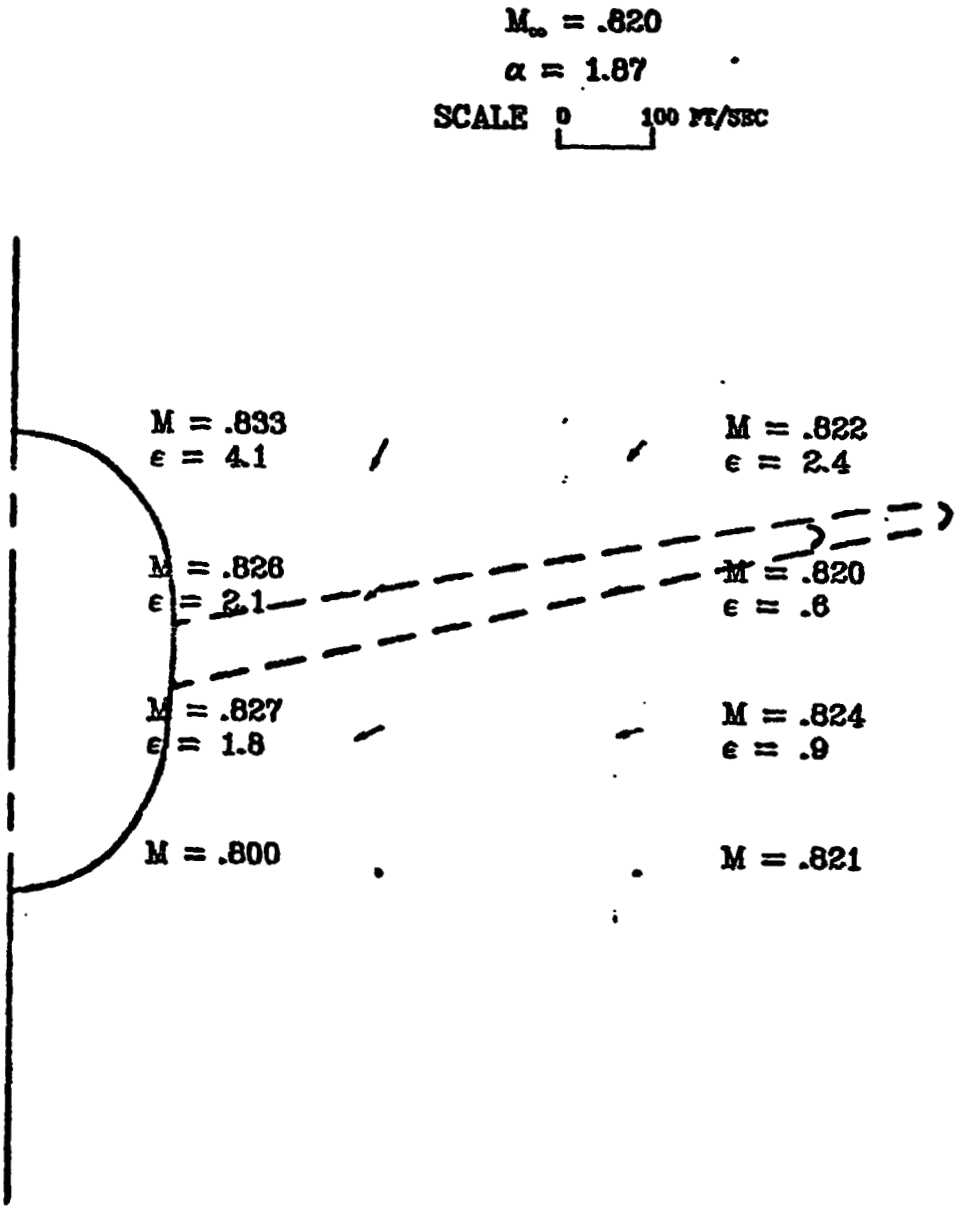

Figure 31.- Continued.

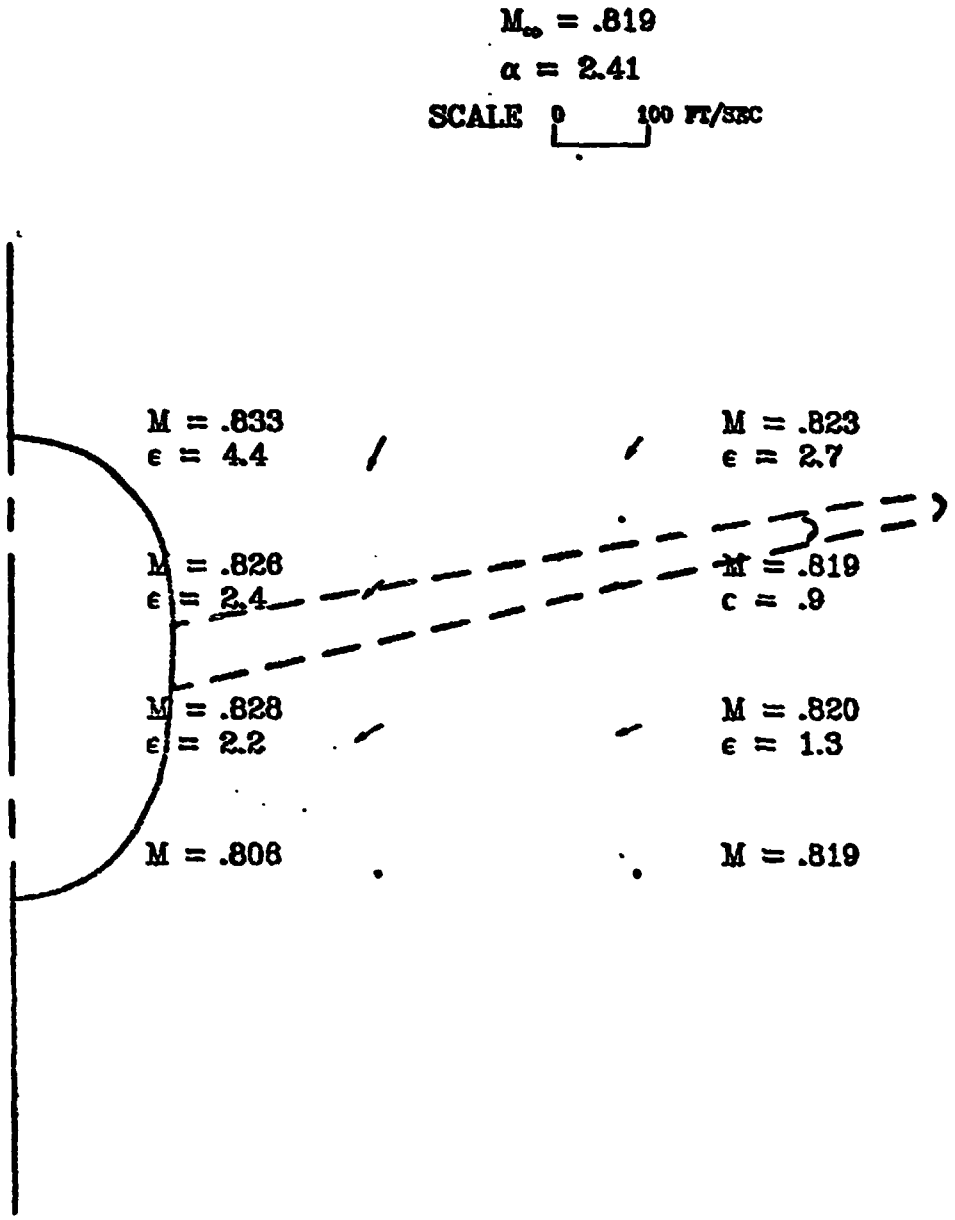

Figure 31.- Continued.

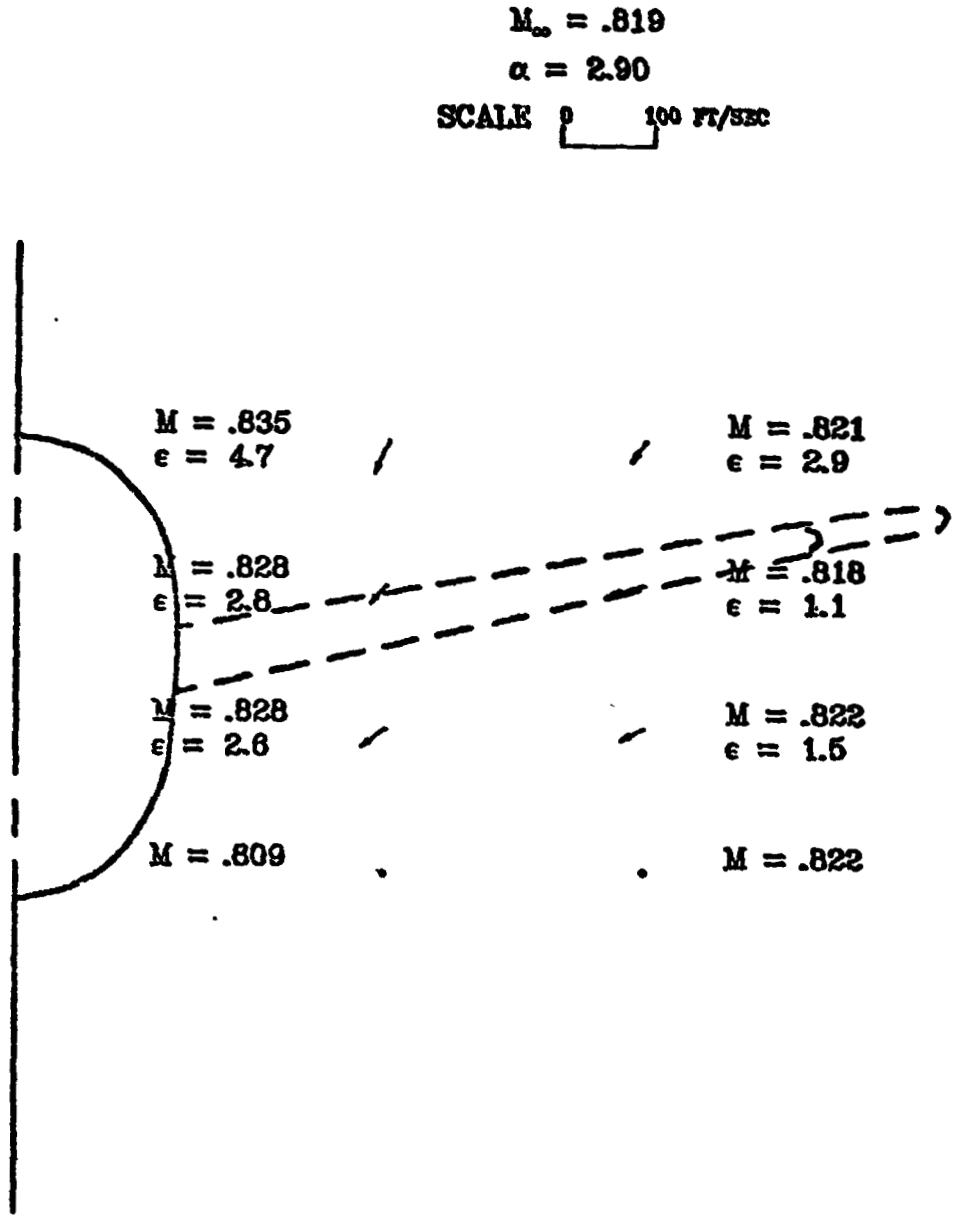

Figure 31. - Continued.

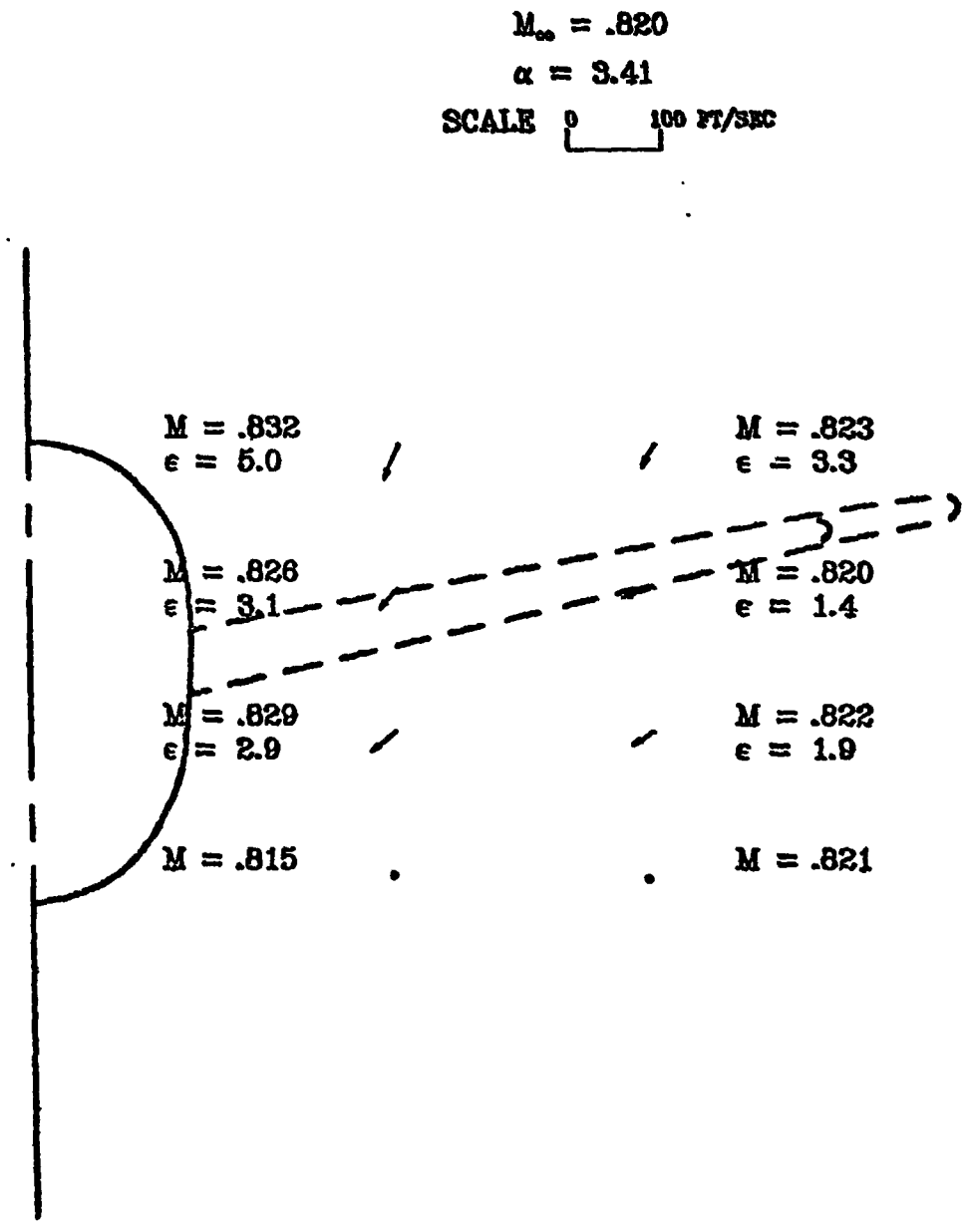

Figure 31.- Continued.

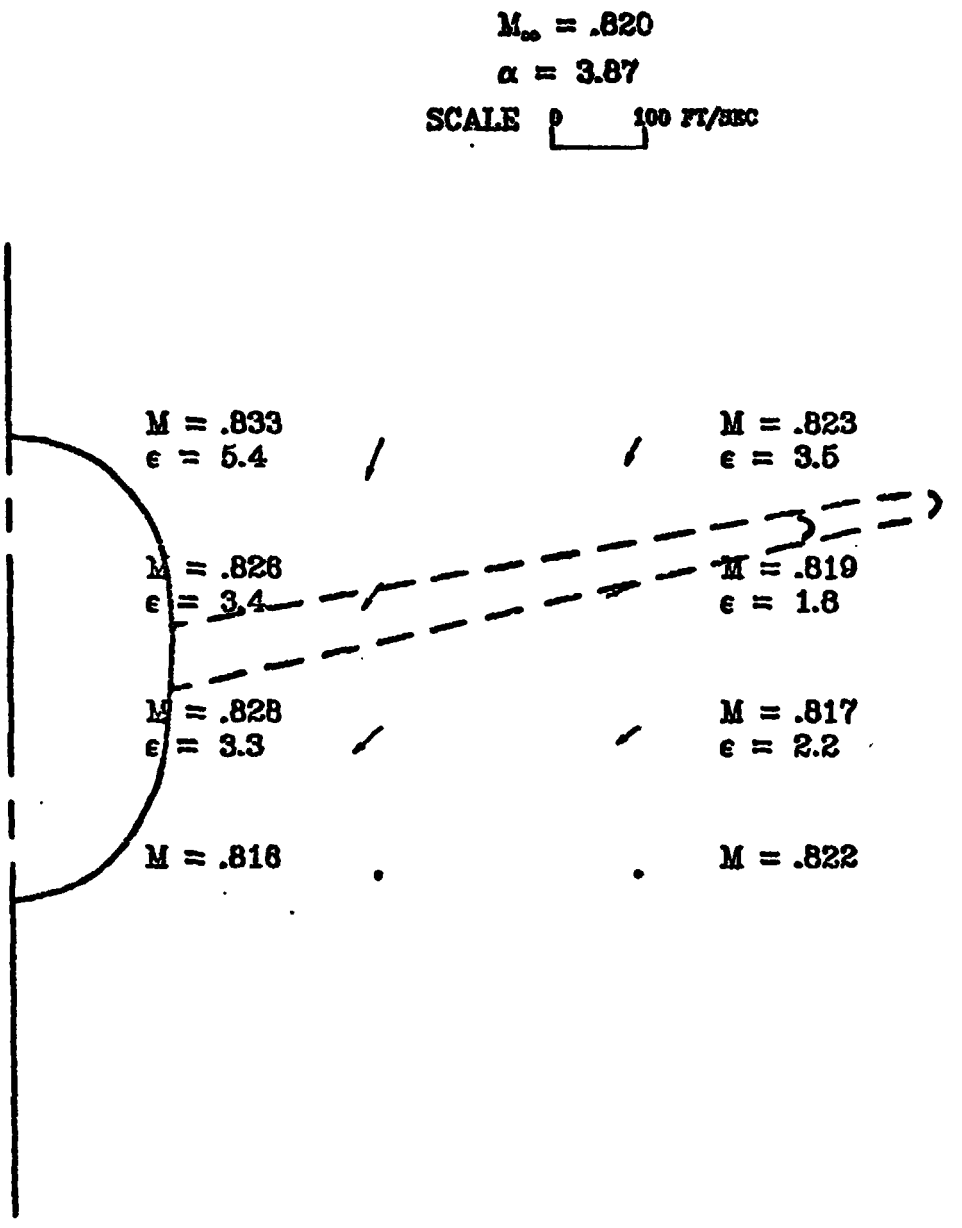

Figure 31.- Continued.

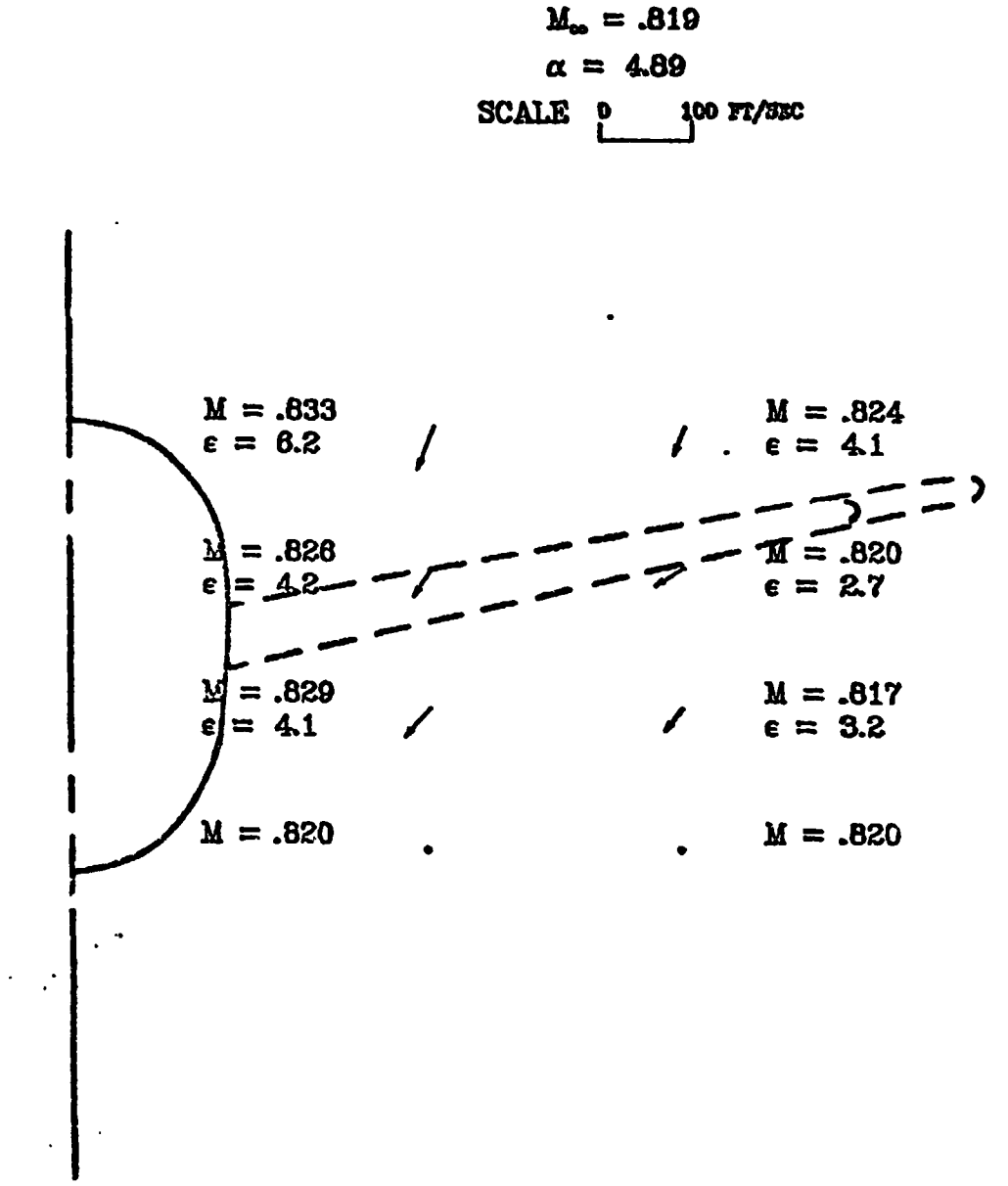

Figure 31. - Continued.

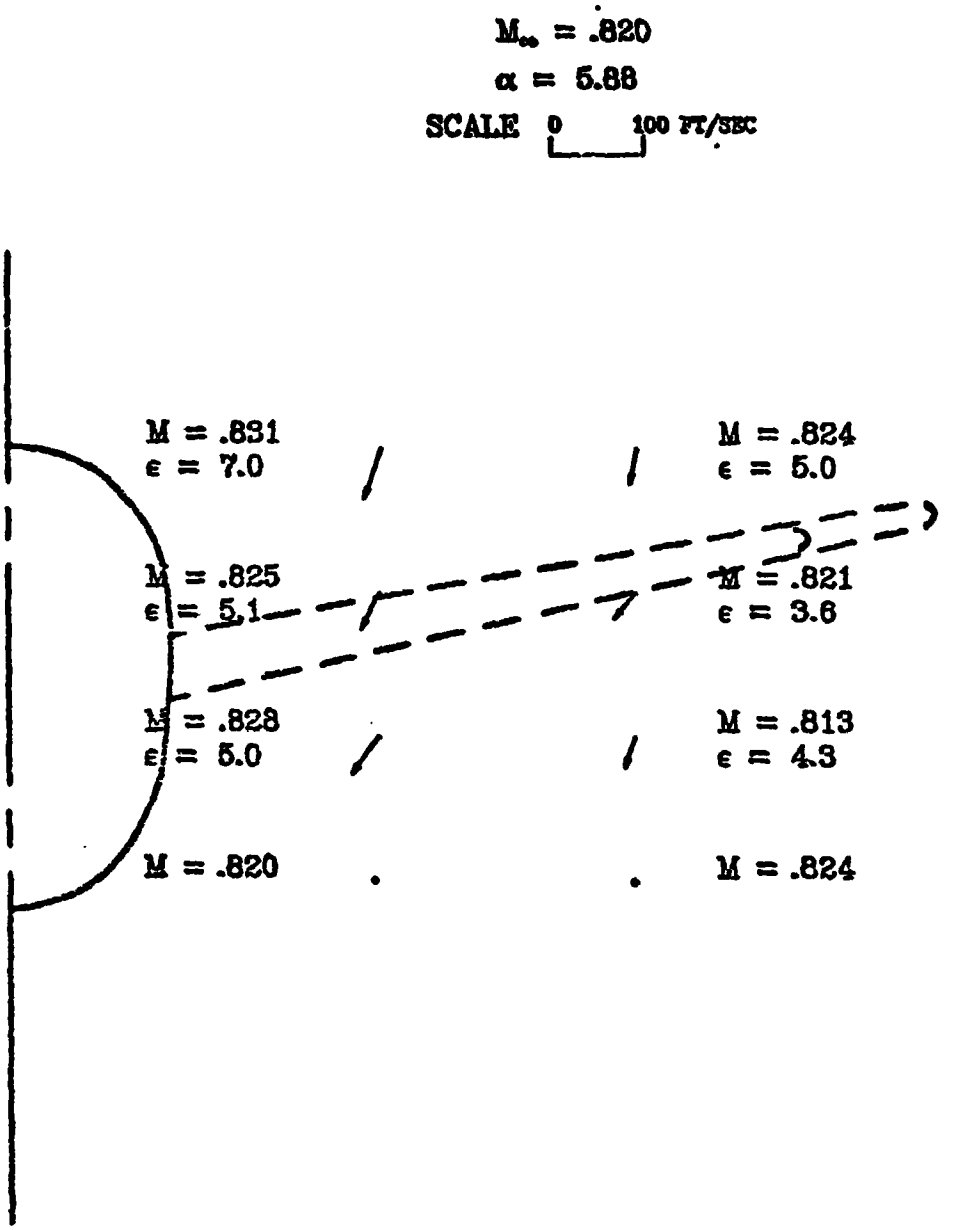

Figure 31. - Continued.

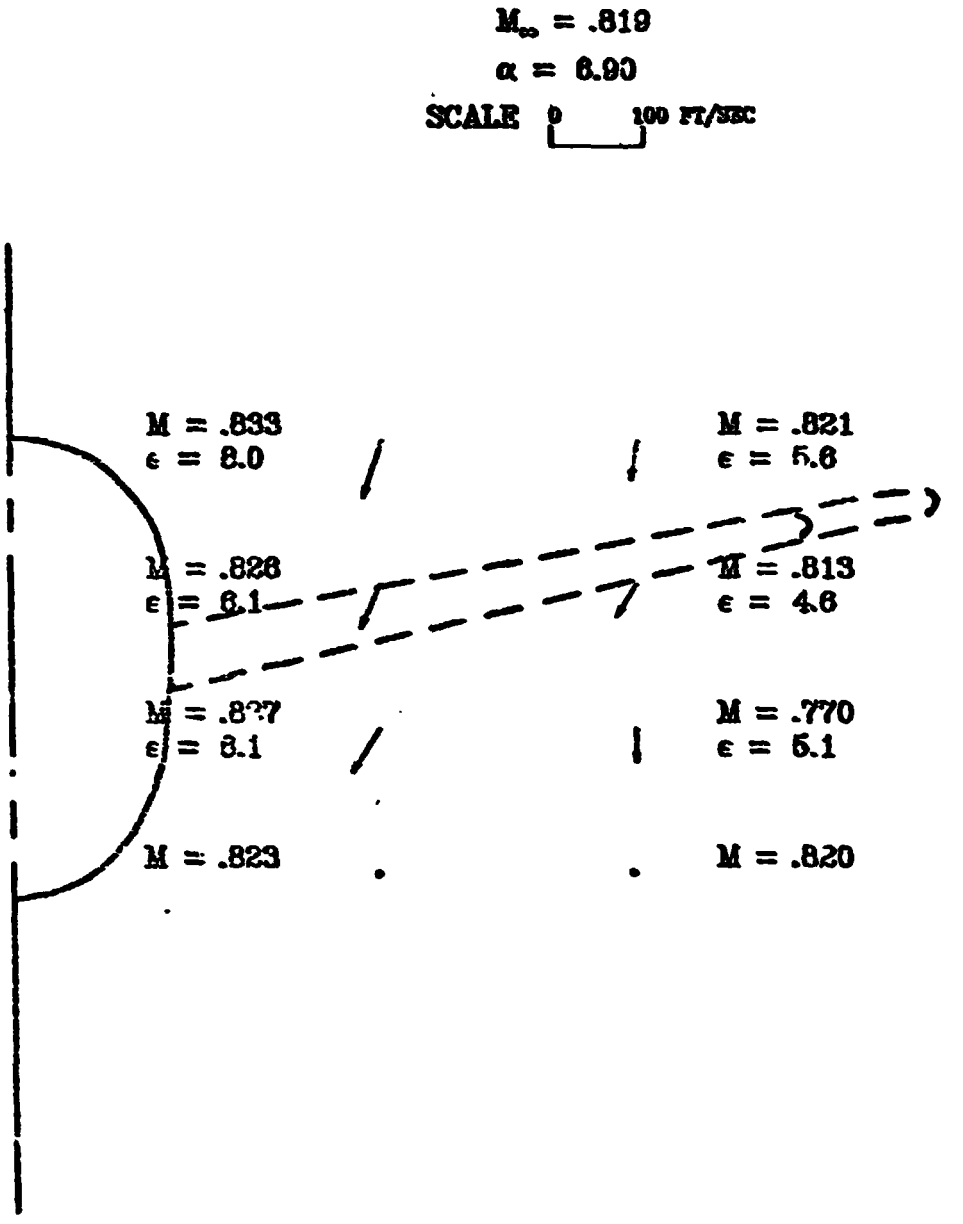

Figure 31. Continued.

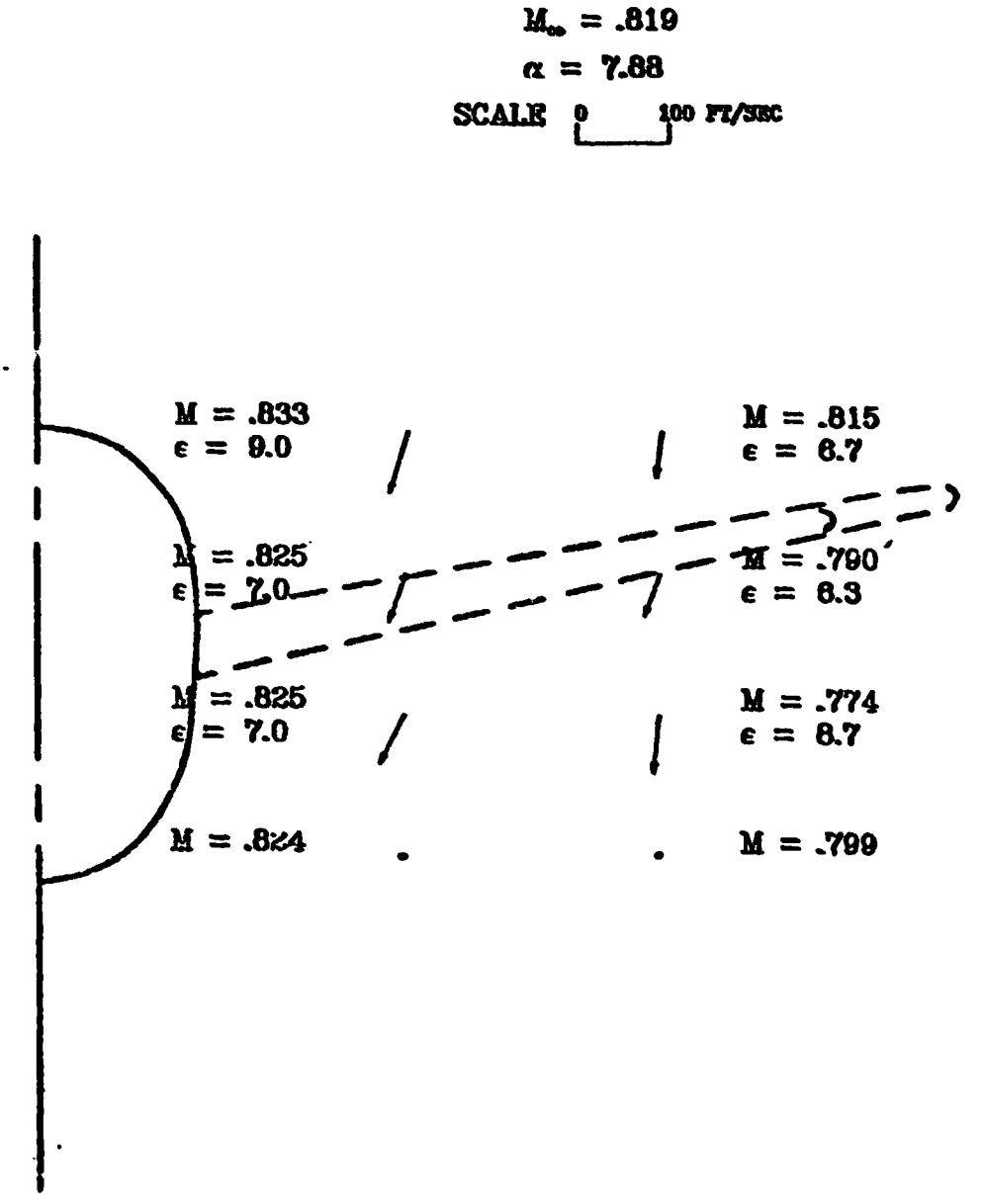

Figure 31. - Concluded.

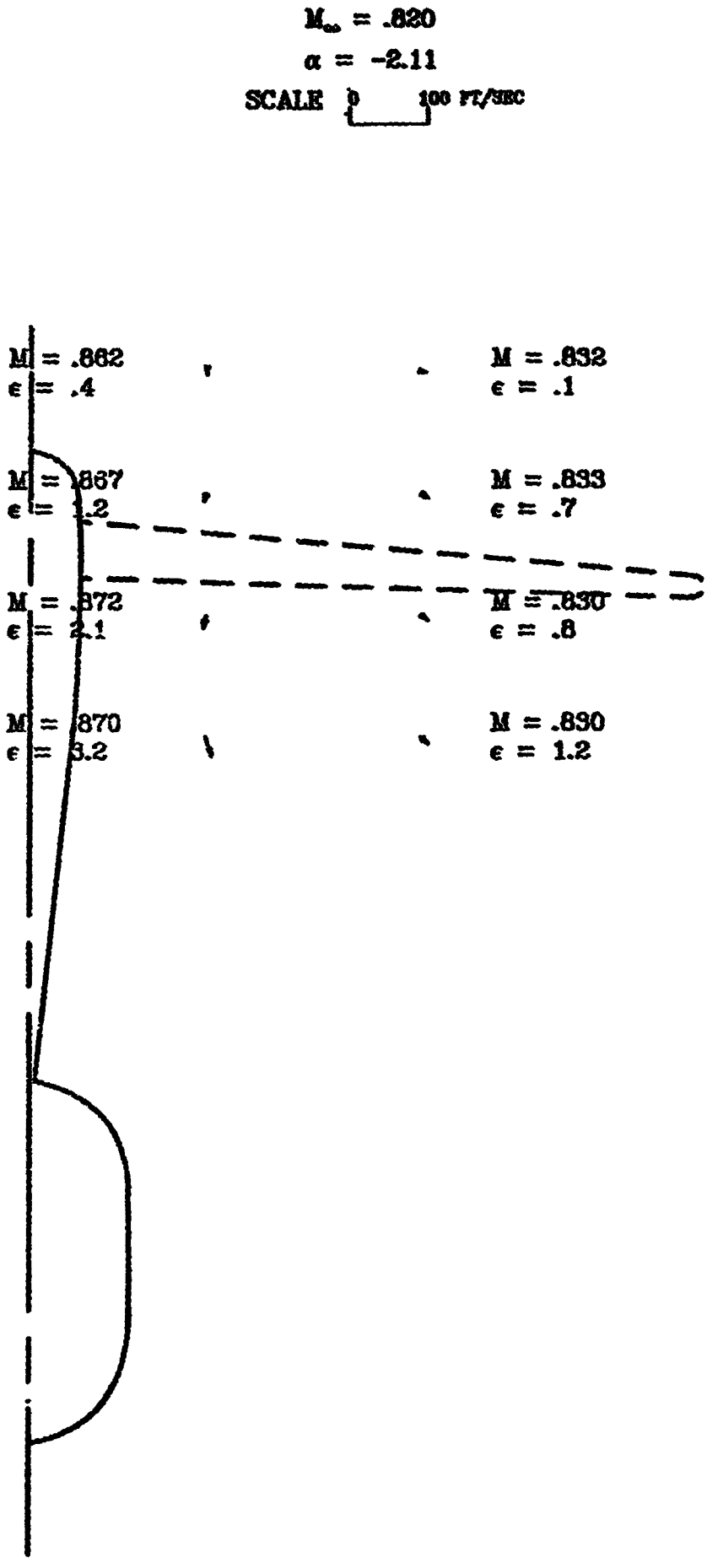

Figure 32.- Local Mach numbers and flow field velocity vectors behind the wide-body wing (T-tail configuration).

$M_\infty = .820$

$\alpha = -.09$

SCALE 0 100 FT/SEC

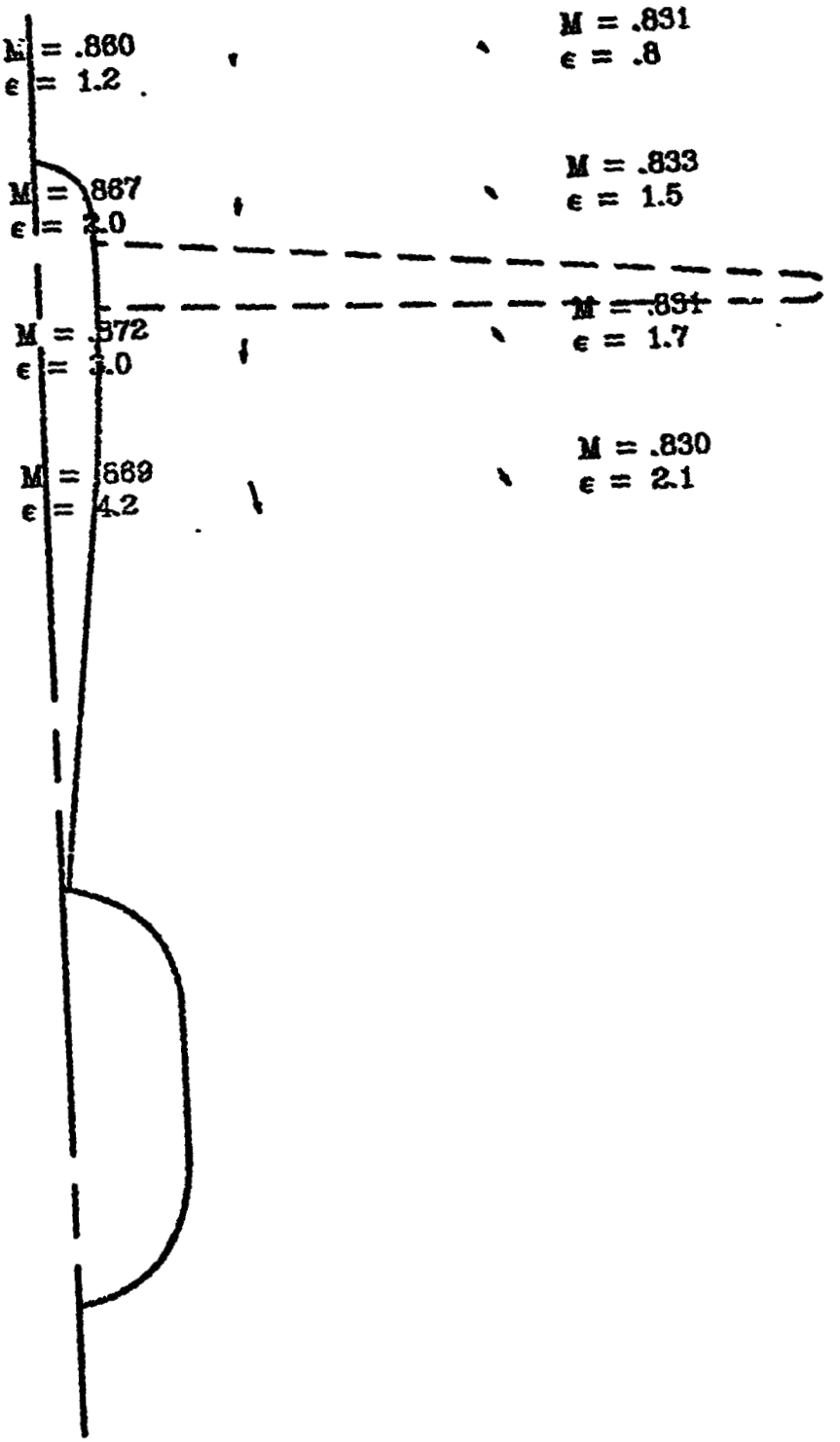

Figure 32.- Continued.

$M_\infty = .820$

$\alpha = .91$

SCALE 0 100 FT/SEC

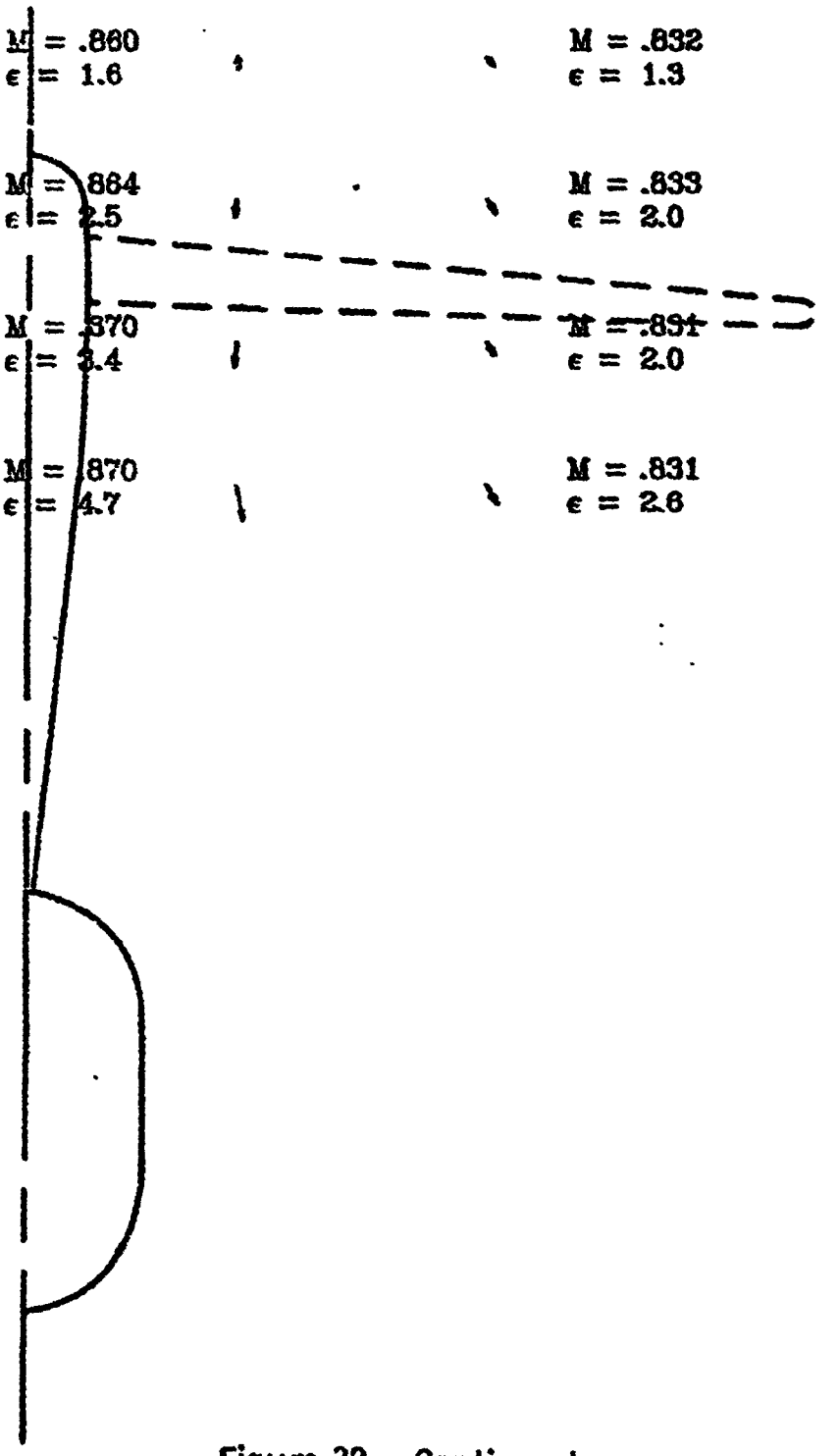

Figure 32. - Continued.

$M_\infty = .820$

$\alpha = 1.40$

SCALE 0 100 FT/SEC

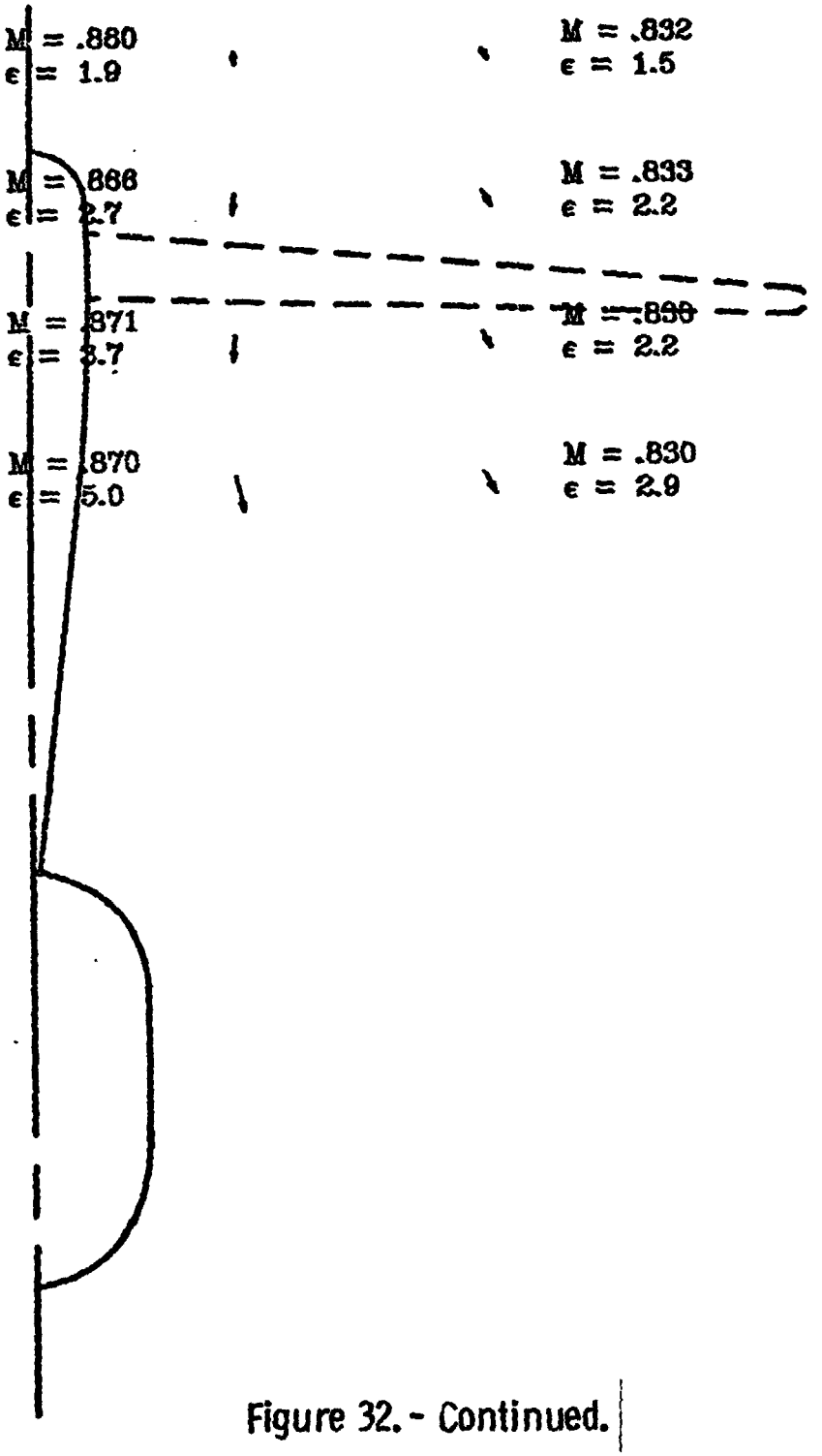

Figure 32. - Continued.

$M_\infty = .820$

$\alpha = 1.94$

SCALE 0 100 FT/SEC

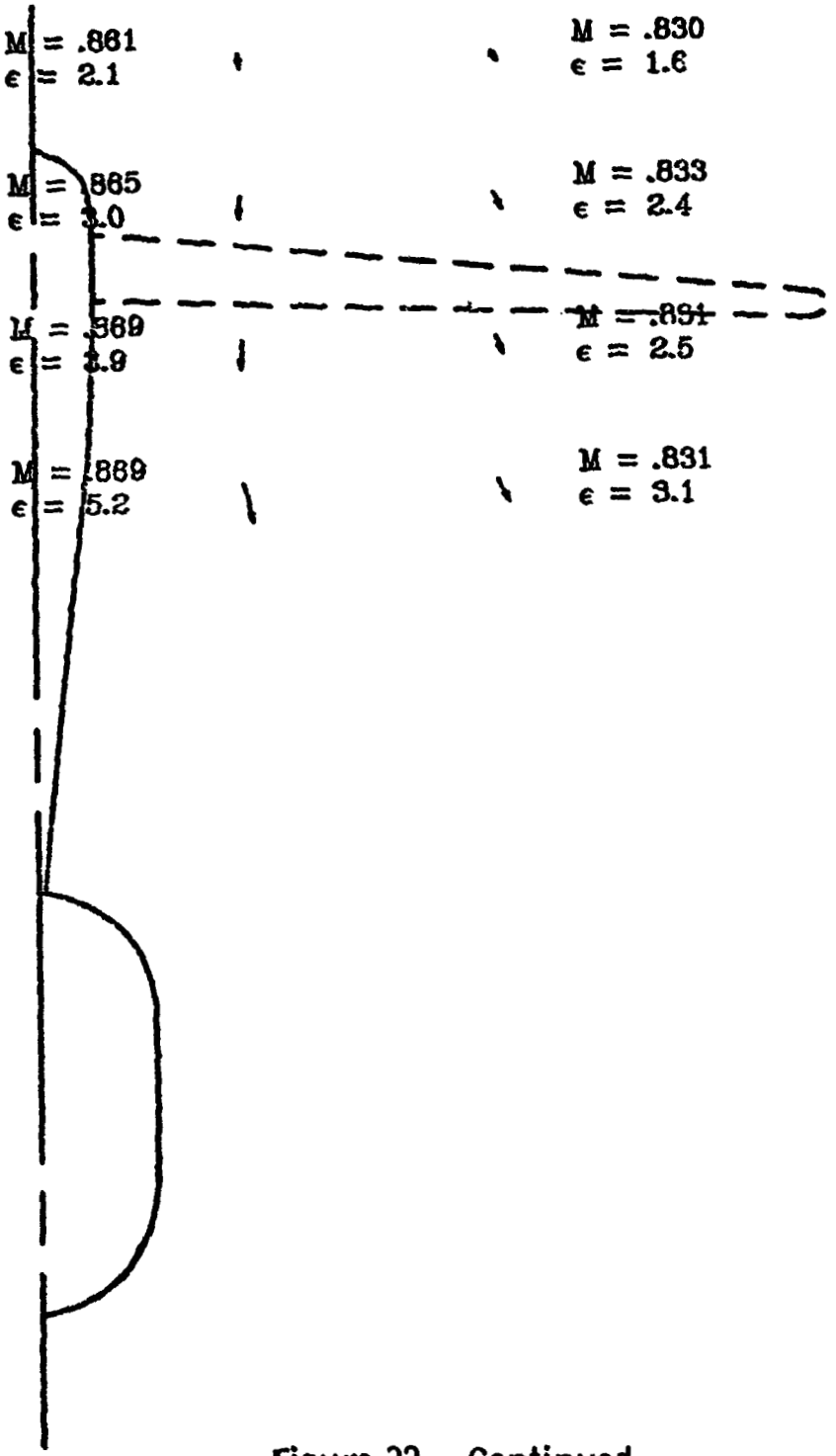

Figure 32. - Continued.

$M_\infty = .820$

$\alpha = 2.43$

SCALE 0 100 FT/SEC

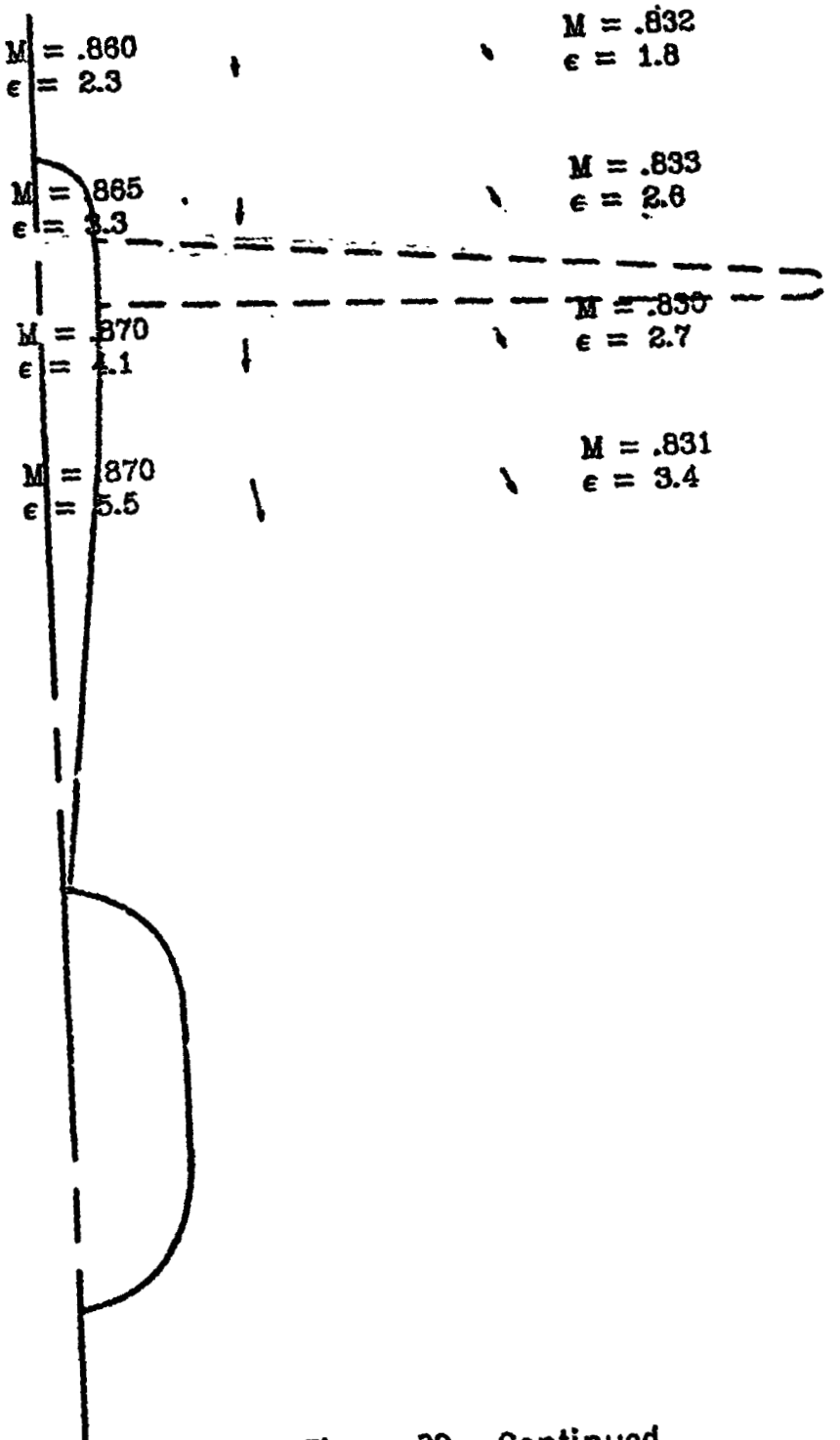

Figure 32.- Continued.

$M_\infty = .821$

$\alpha = 2.92$

SCALE 0 100 FT/SEC

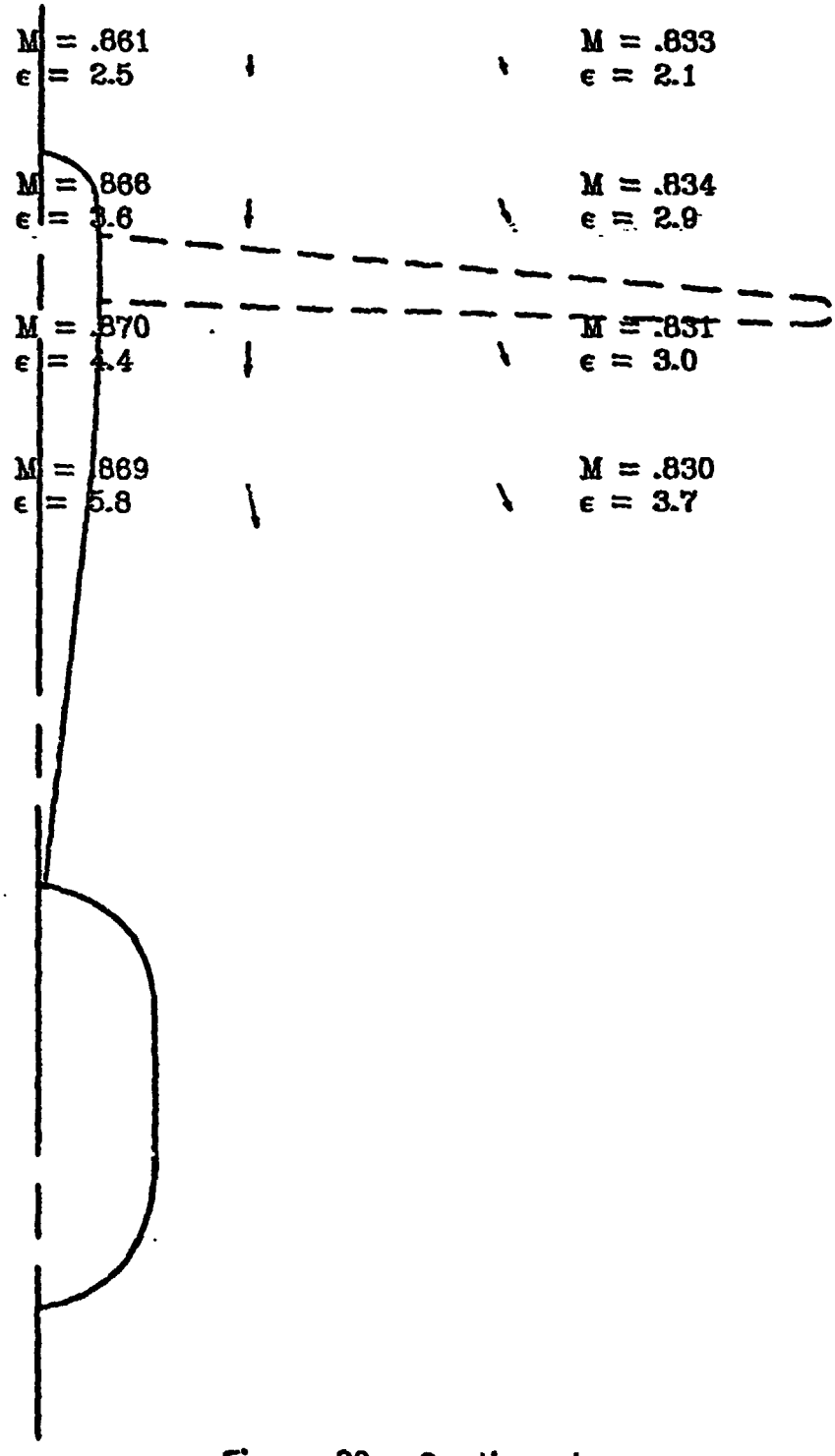

Figure 32.- Continued.

$M_\infty = .820$

$\alpha = 3.41$

SCALE 0 100 FT/SEC

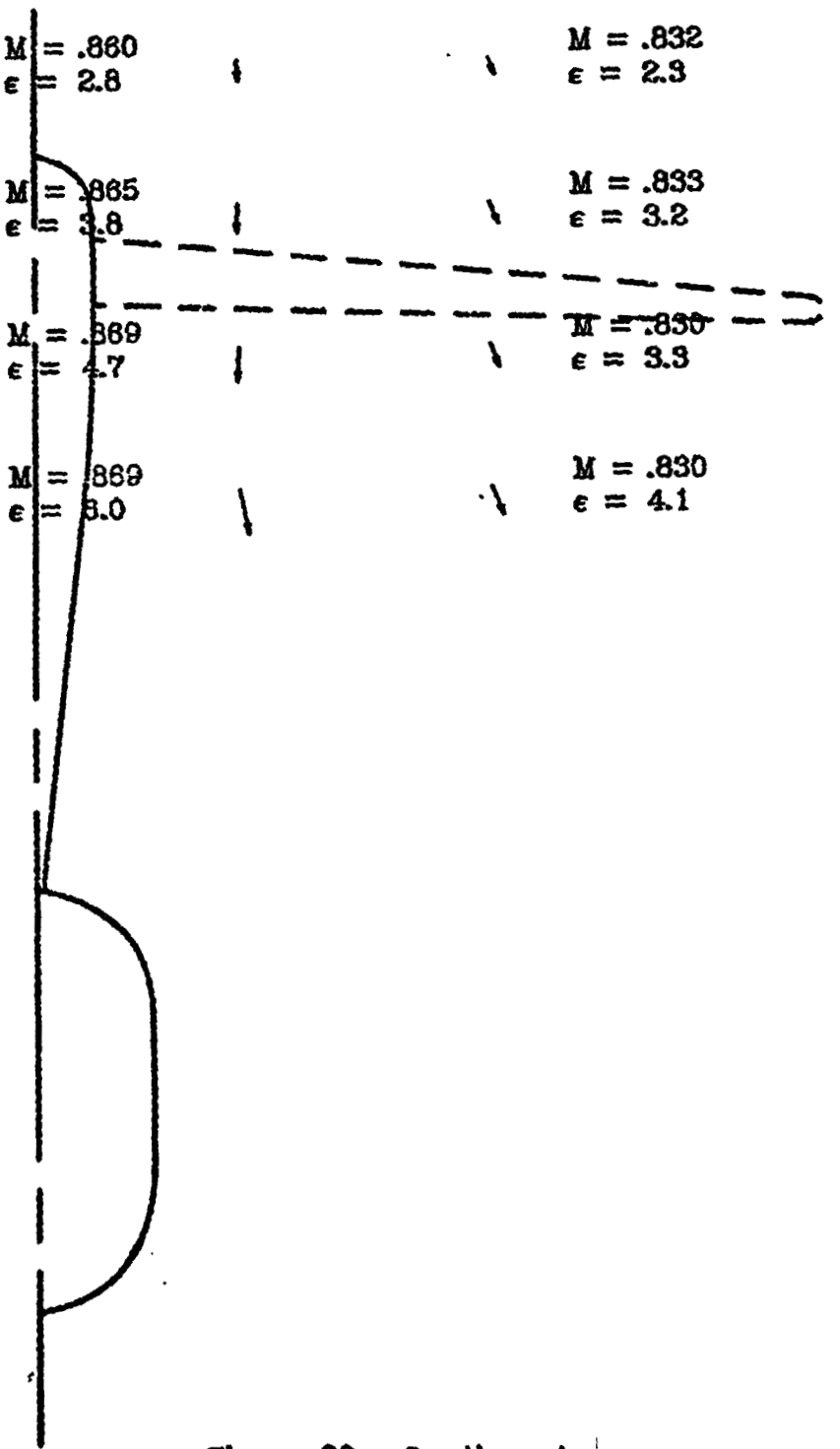

Figure 32.- Continued.

$M_\infty = .820$

$\alpha = 3.91$

SCALE 0 100 FT/SEC

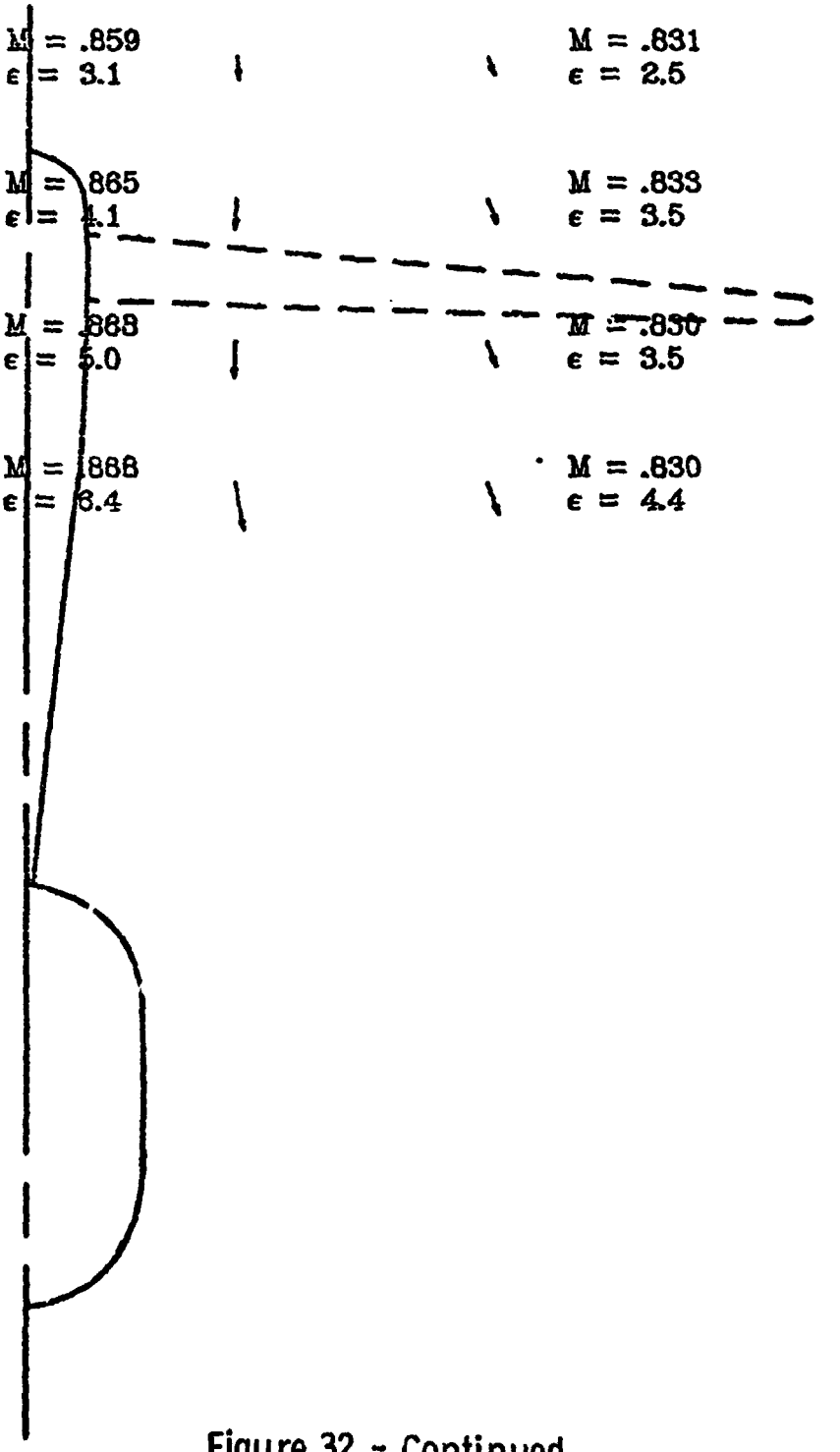

Figure 32.- Continued.

$M_\infty = .820$

$\alpha = 4.98$

SCALE 0 100 FT/SEC

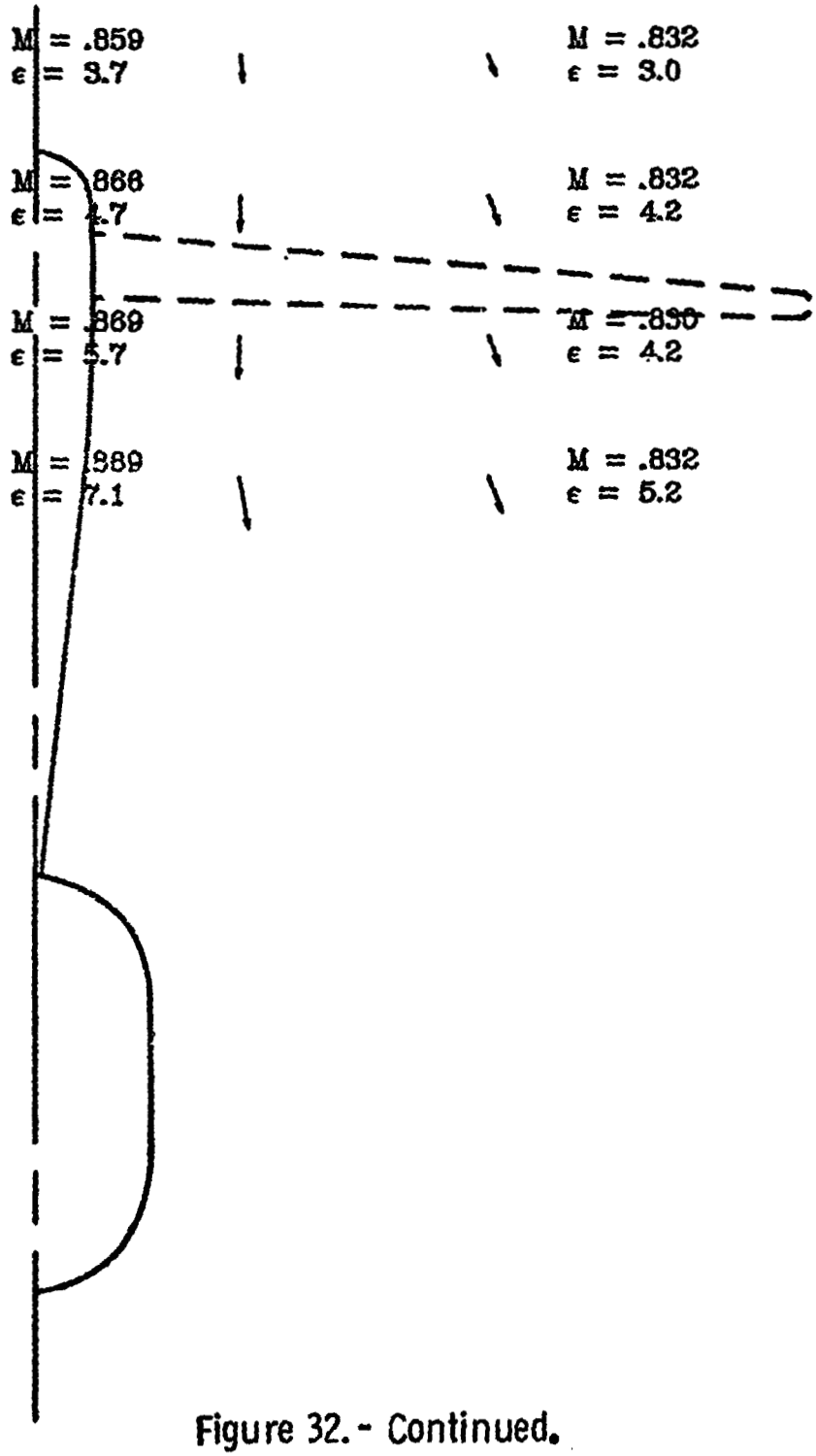

Figure 32. - Continued.

$M_\infty = .820$

$\alpha = 5.92$

SCALE 0 100 FT/SEC

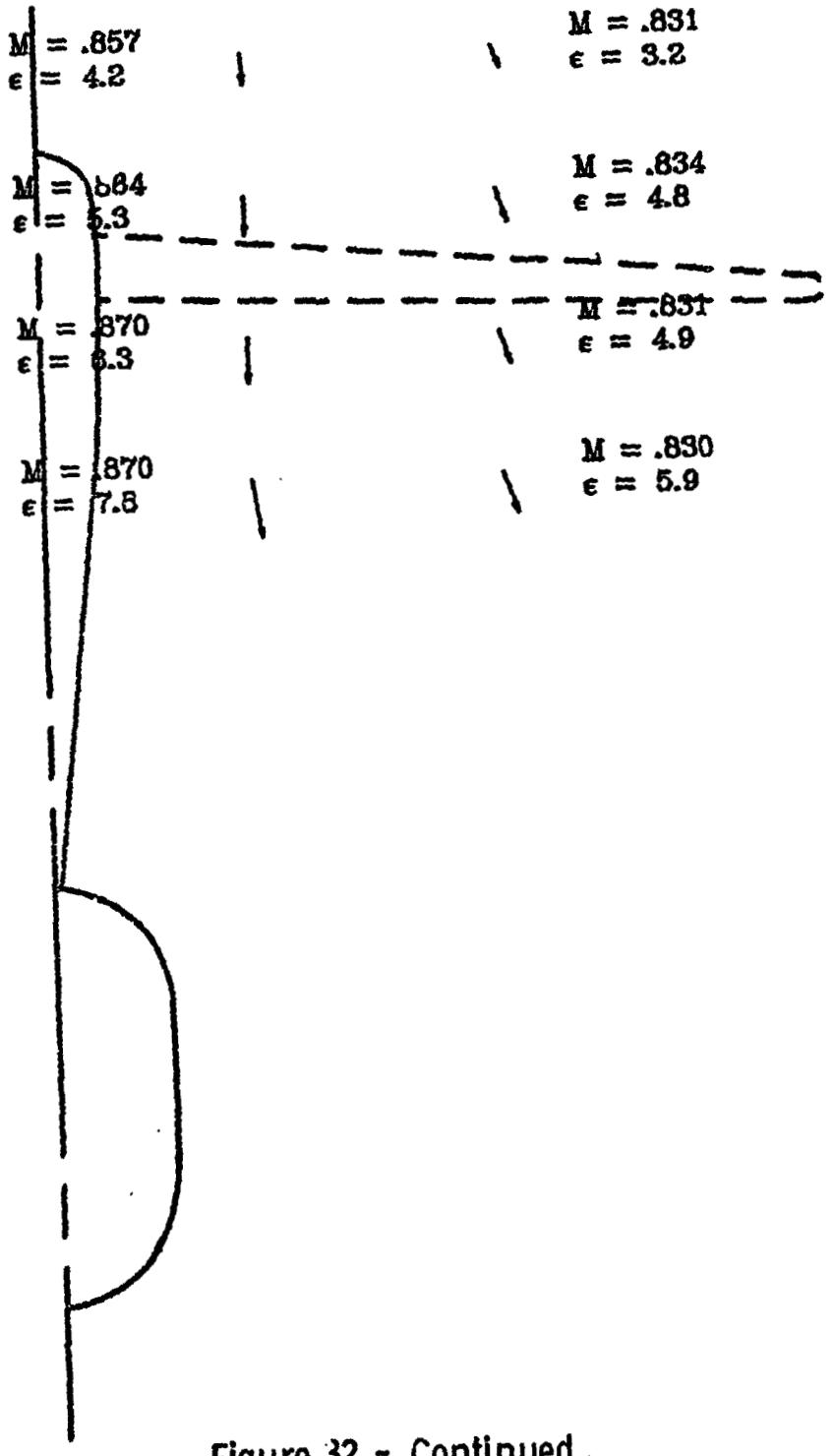

Figure 32.- Continued.

$M_\infty = .819$

$\alpha = 3.89$

SCALE 0 100 FT/SEC

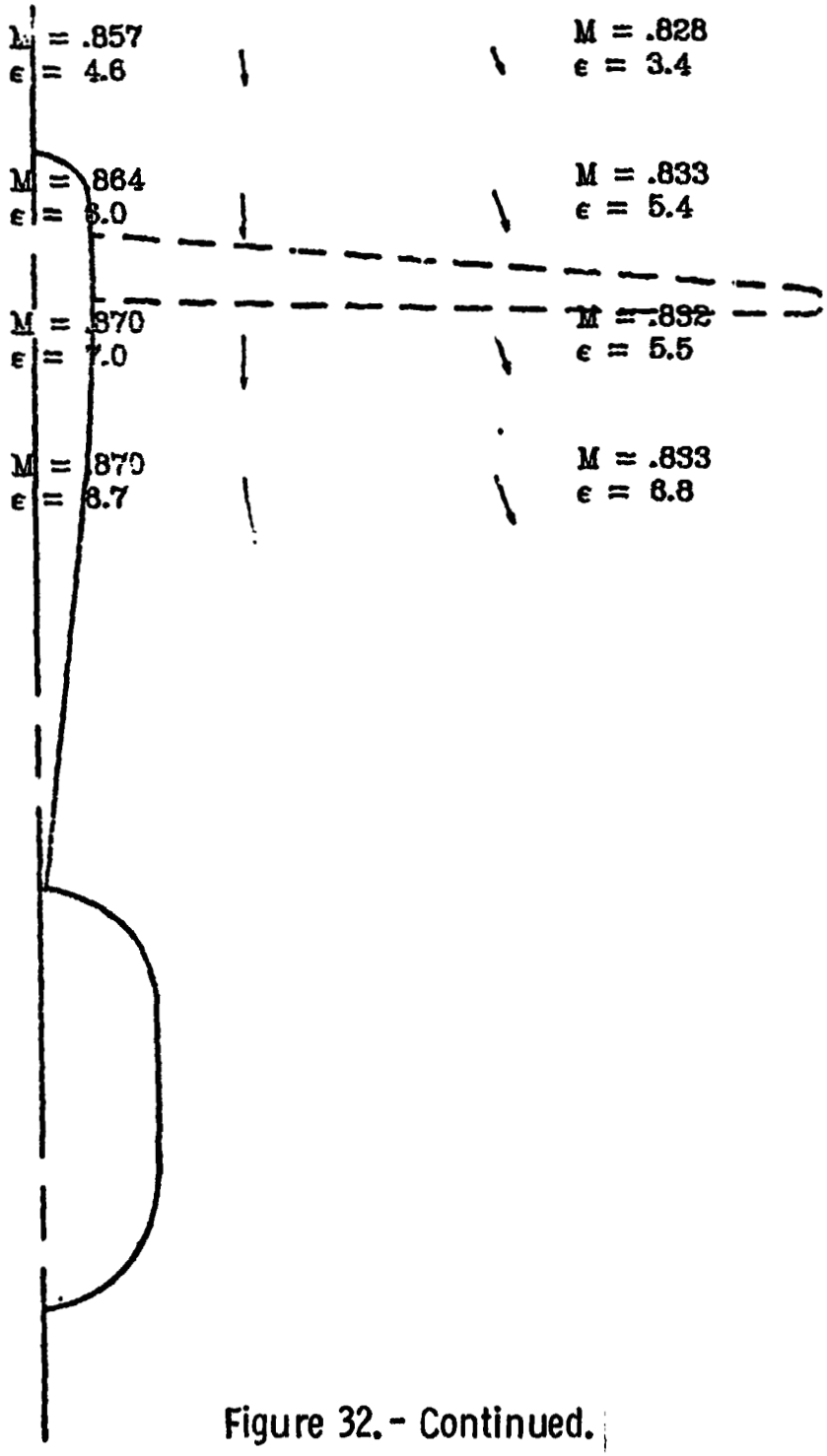

Figure 32.- Continued.

$M_\infty = .820$

$\alpha = 7.90$

SCALE 0 100 FT/SEC

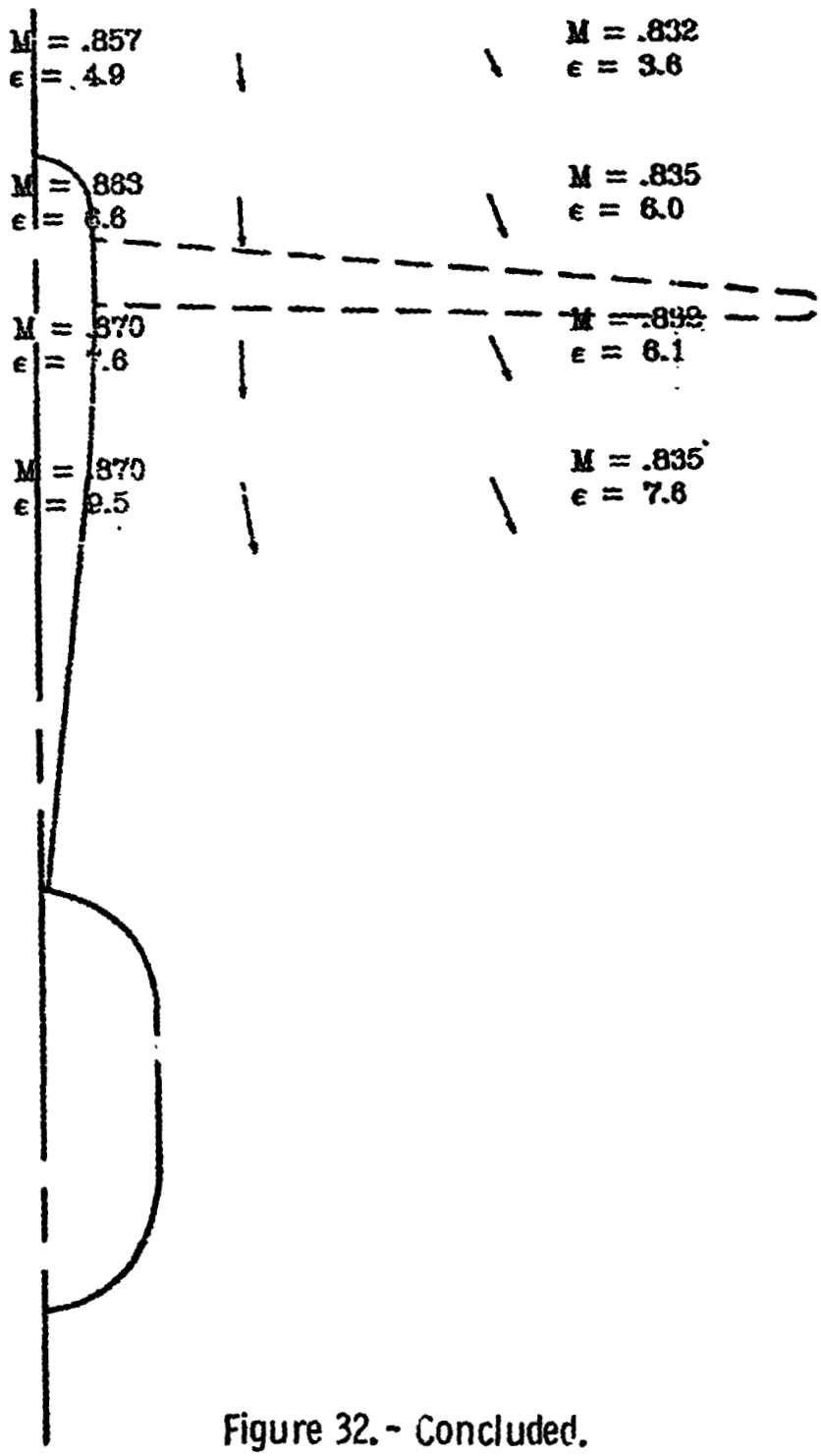

Figure 32.- Concluded.

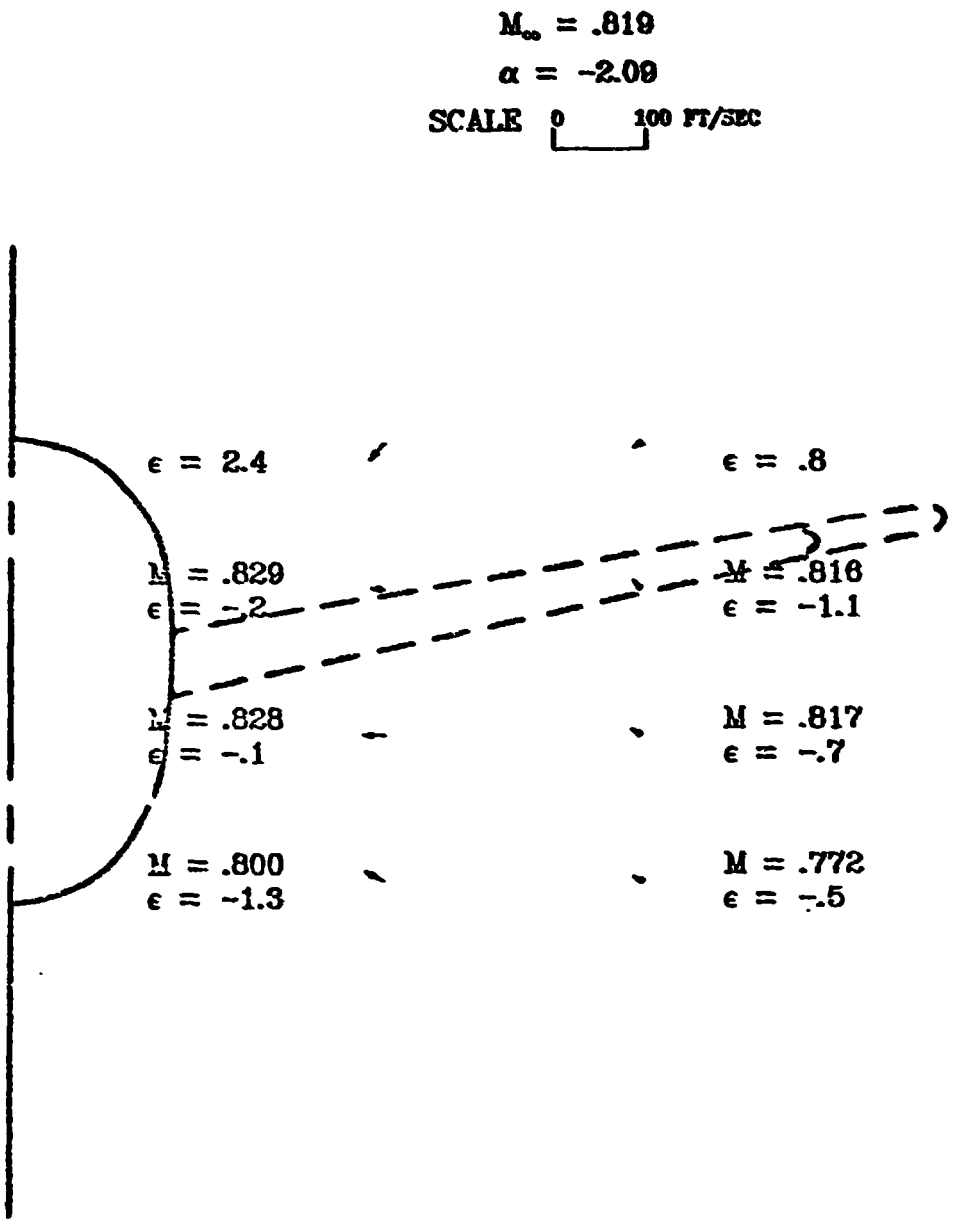

Figure 33.- Local Mach numbers and flow field velocity vectors behind the supercritical wing (low-tail configuration).

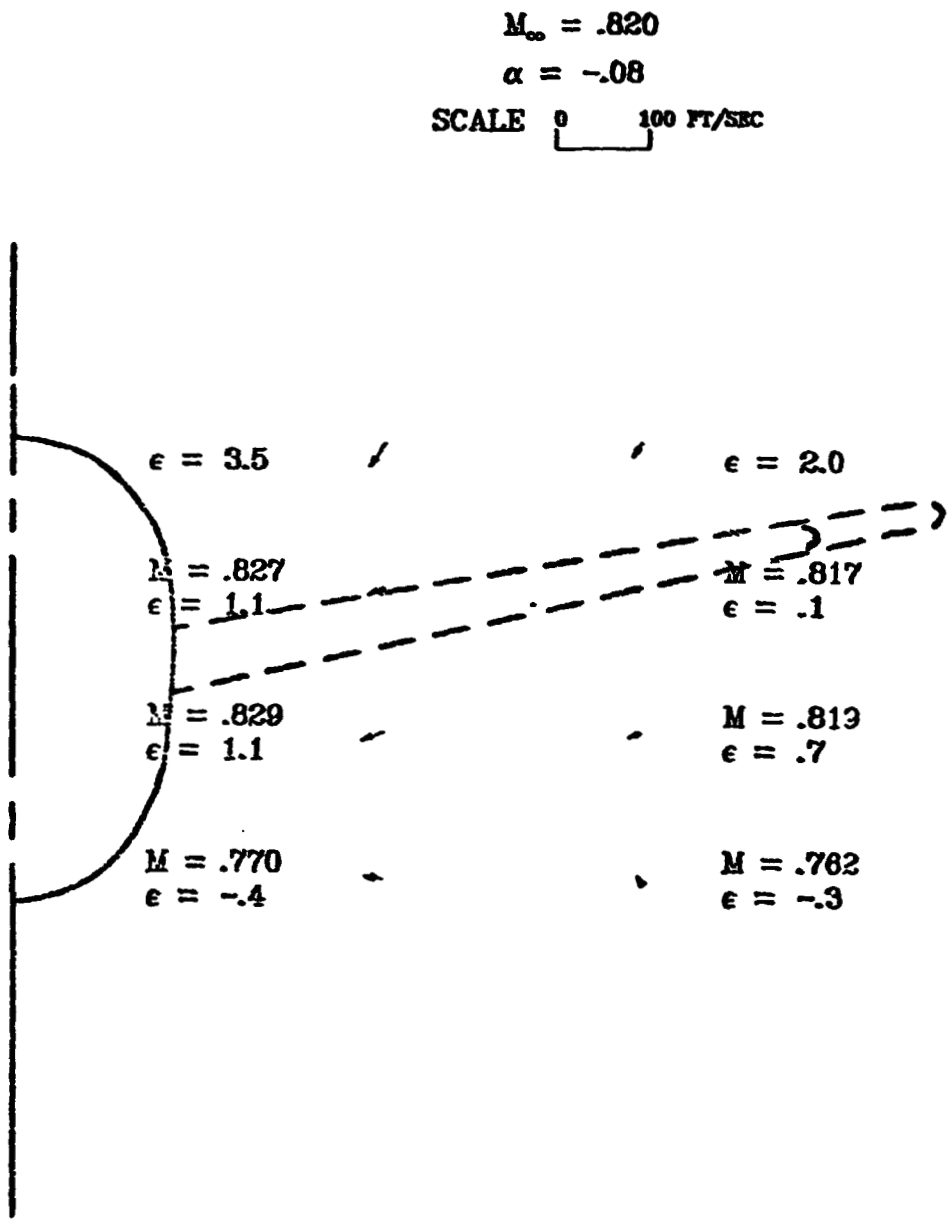

Figure 33. - Continued.

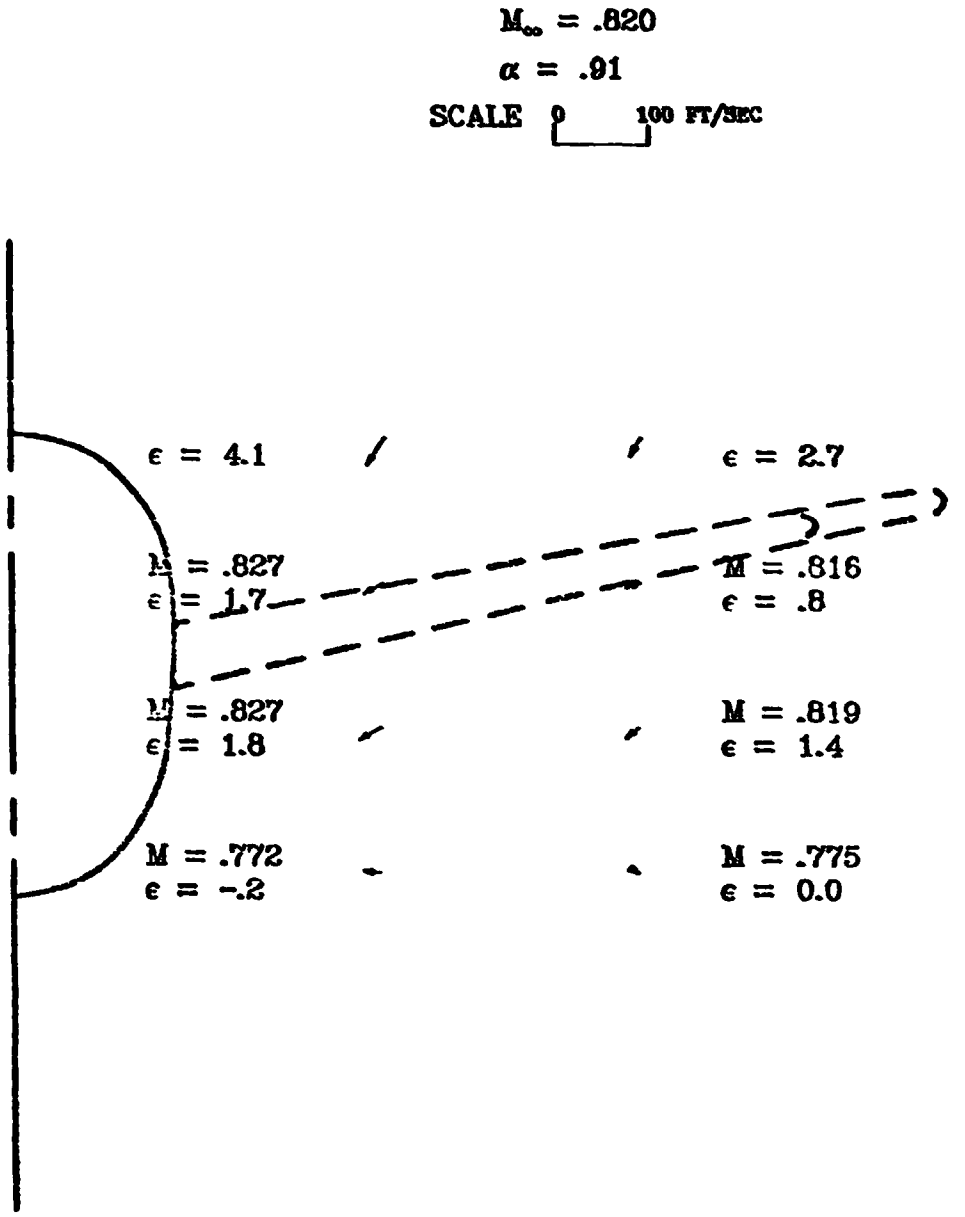

Figure 33. - Continued.

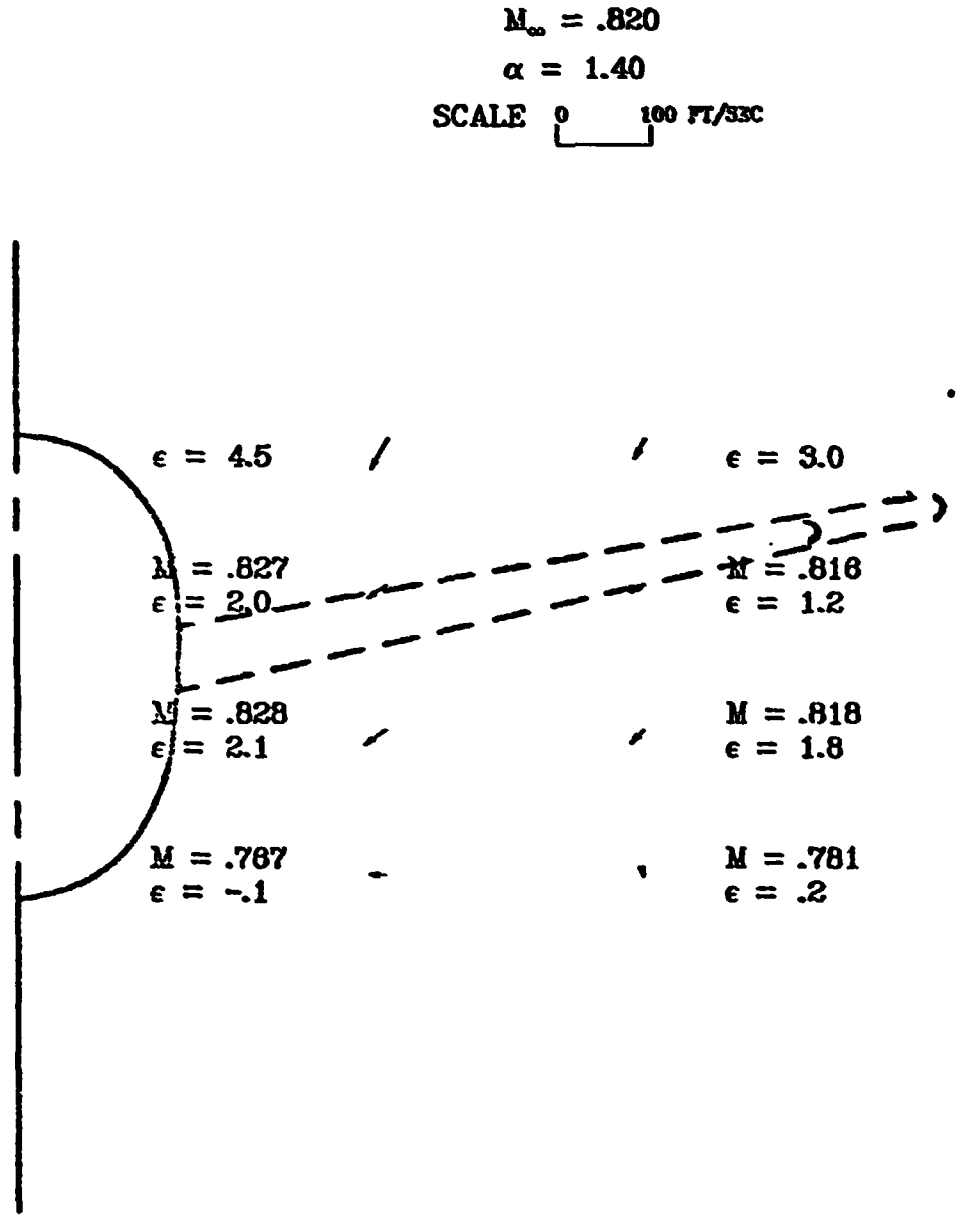

Figure 33. - Continued.

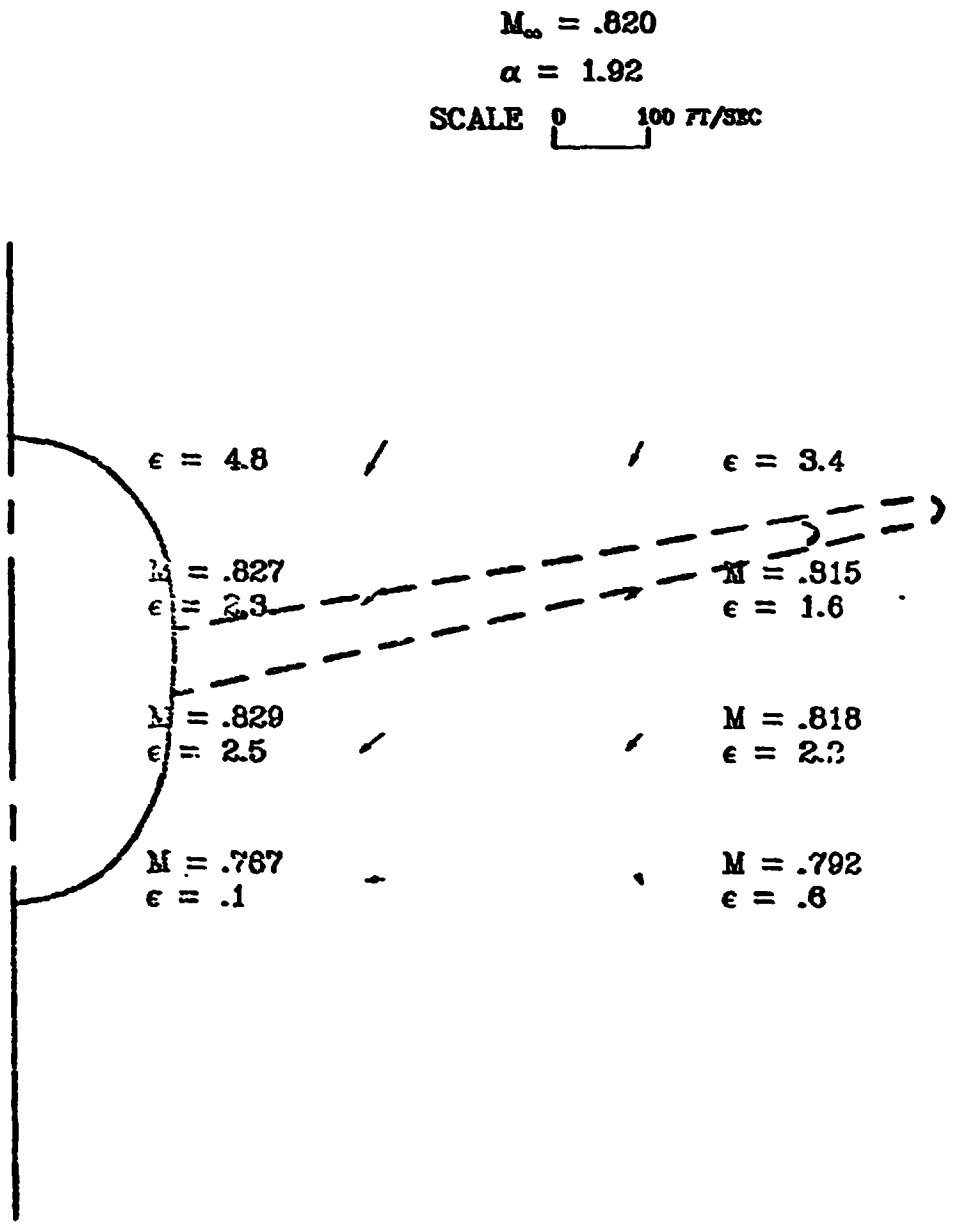

Figure 33. - Continued.

$M_\infty = .820$

$\alpha = 2.43$

SCALE 0 100 FT/SEC

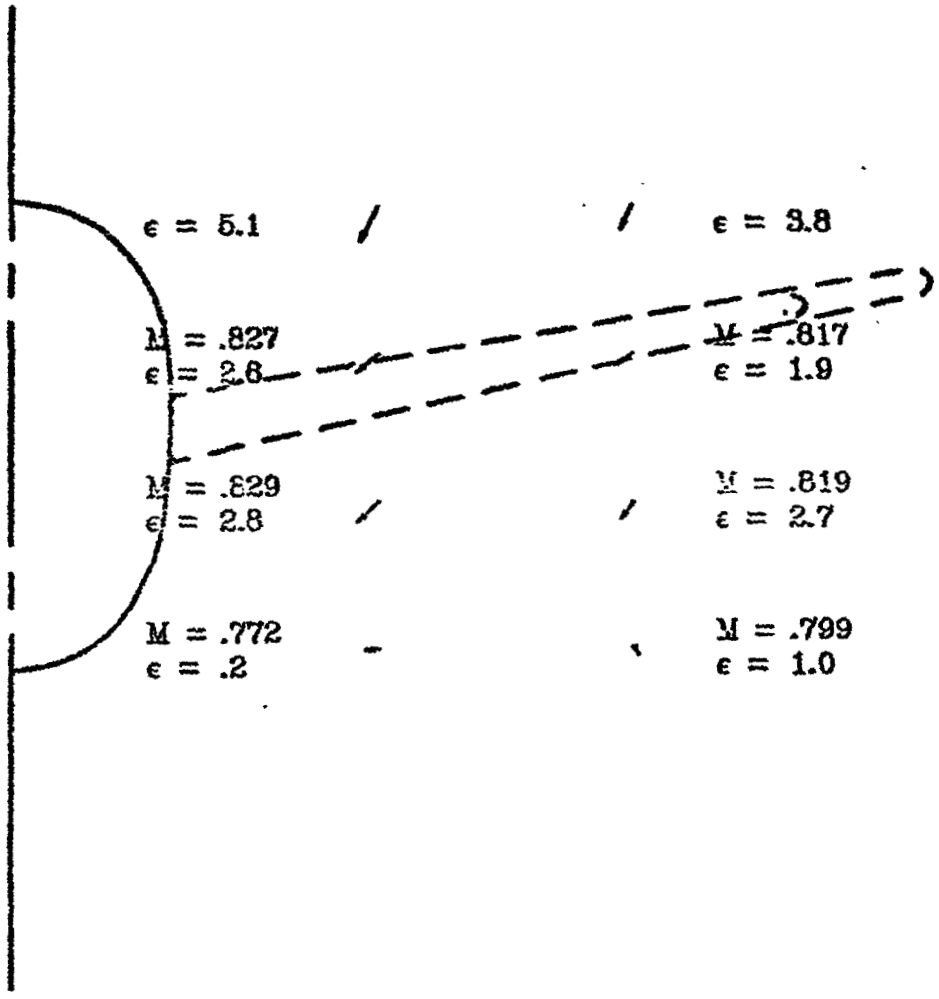

Figure 33. - Continued.

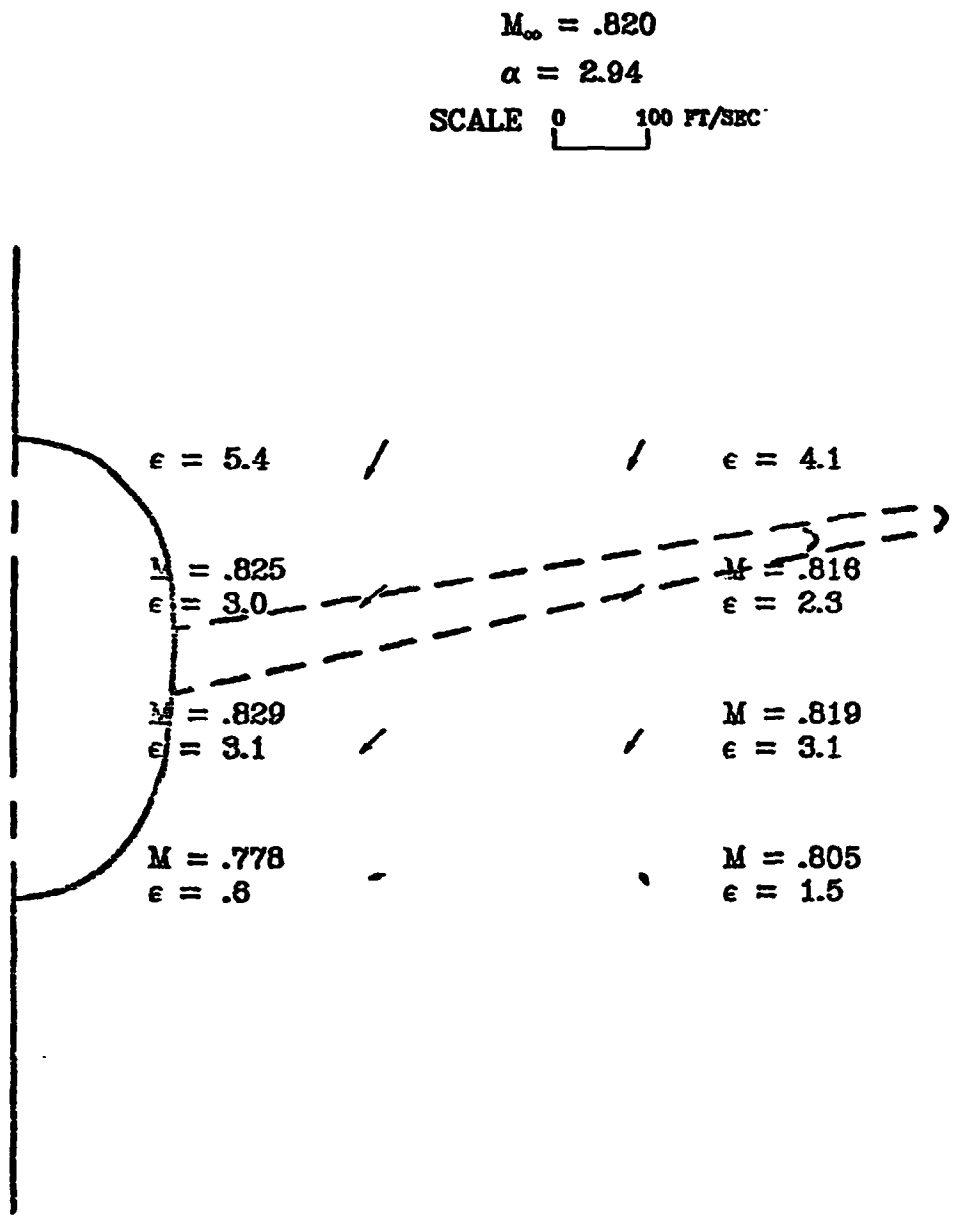

Figure 33. - Continued.

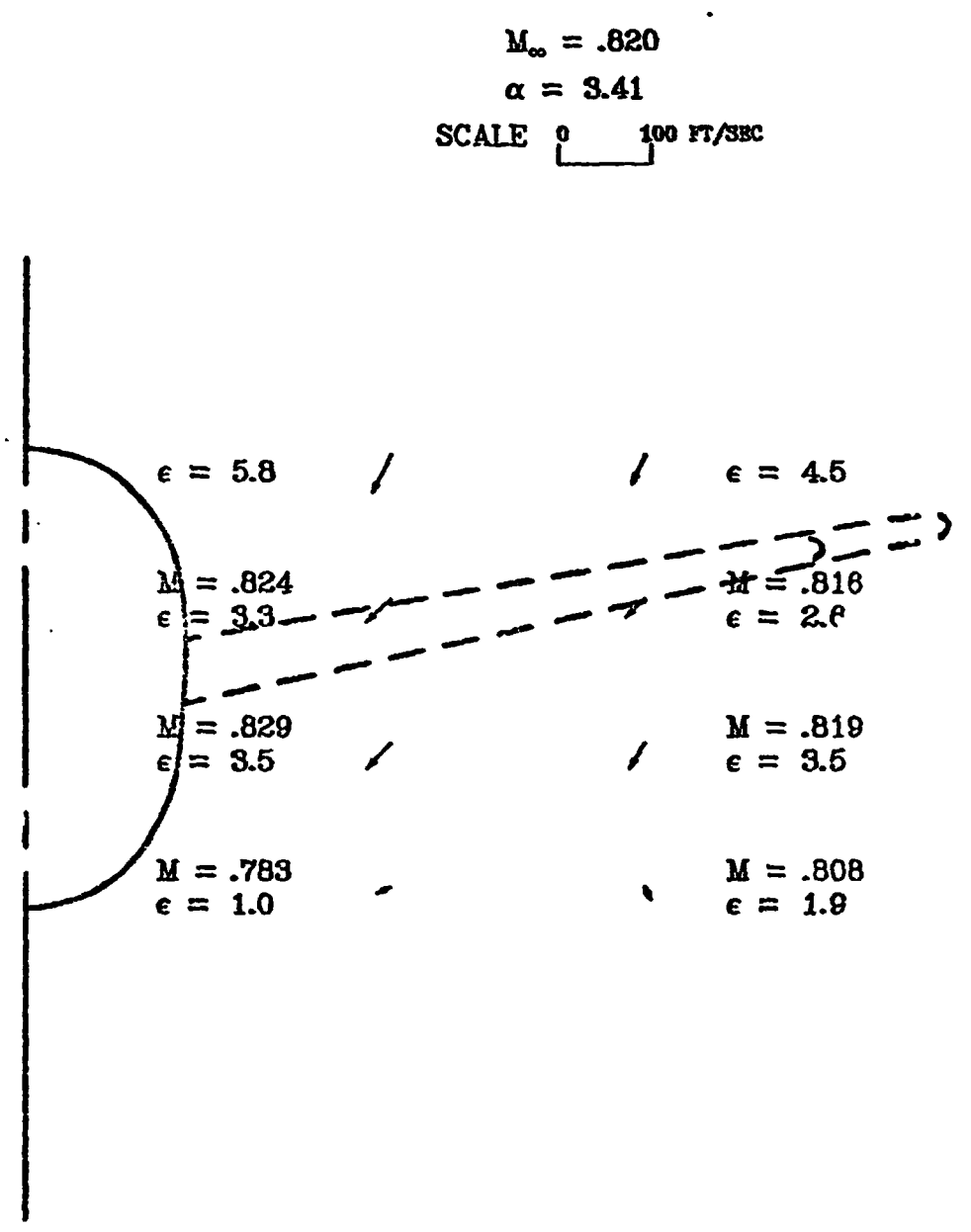

Figure 33.- Continued.

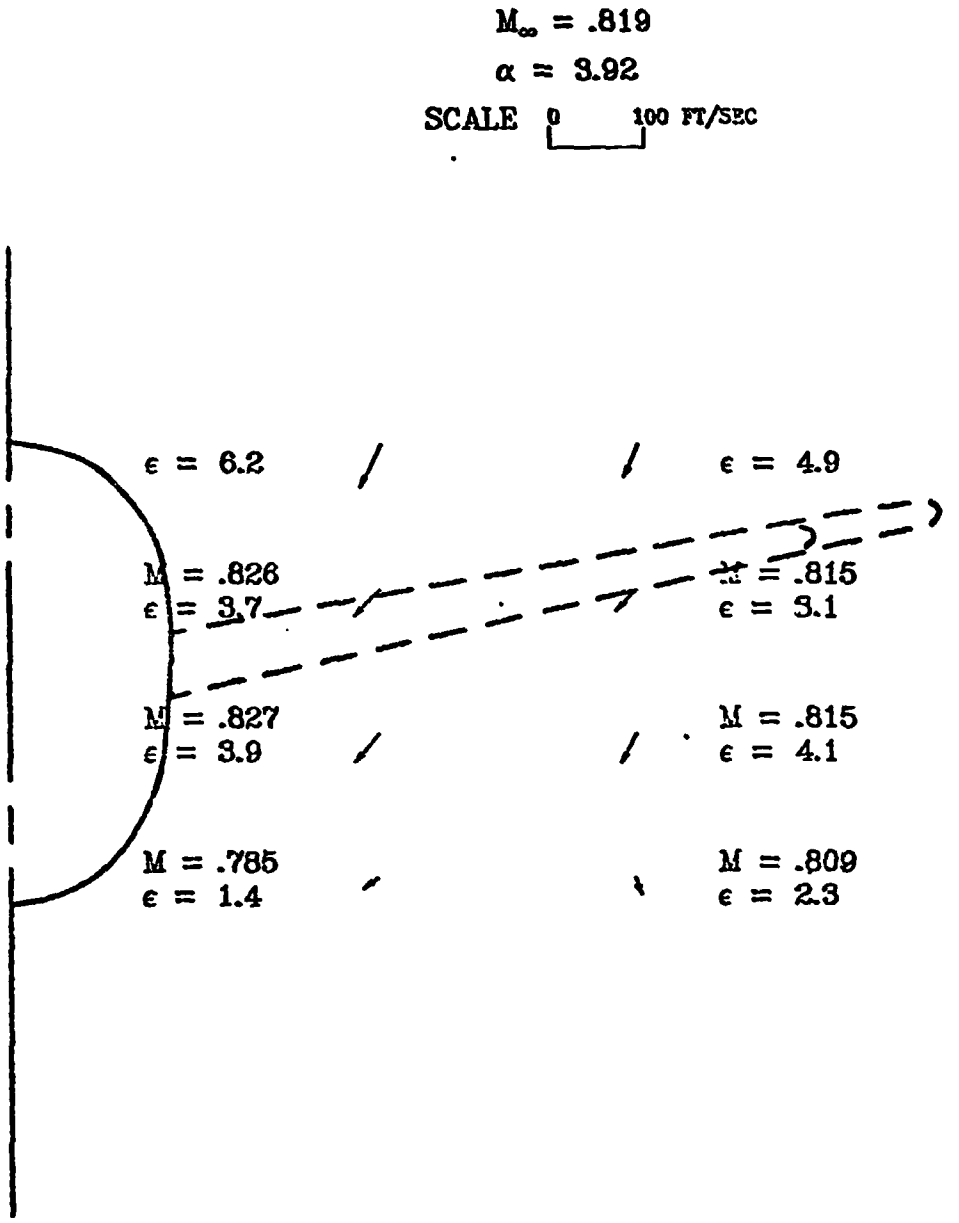

Figure 33.- Continued.

$M_\infty = .820$

$\alpha = 4.92$

SCALE 0 100 FT/SEC

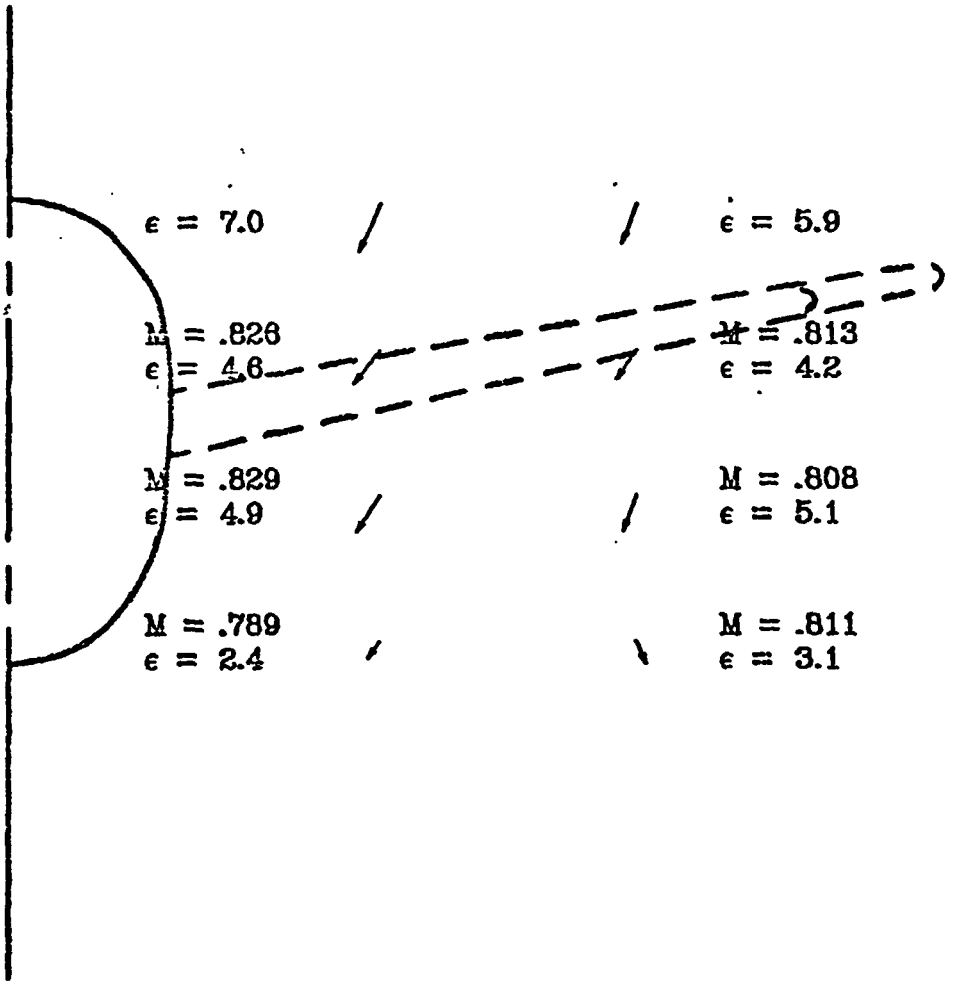

Figure 33. - Continued.

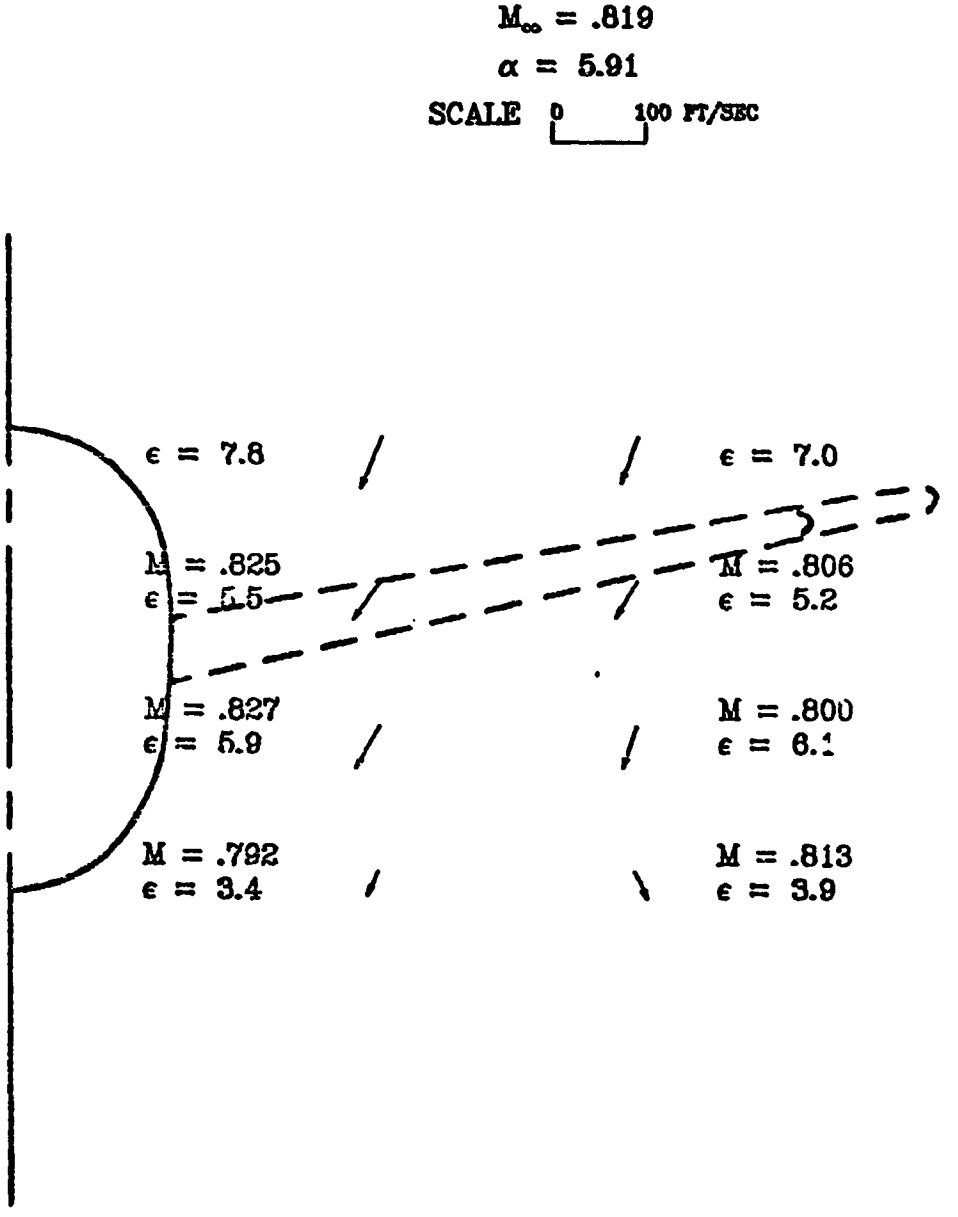

Figure 33. - Continued.

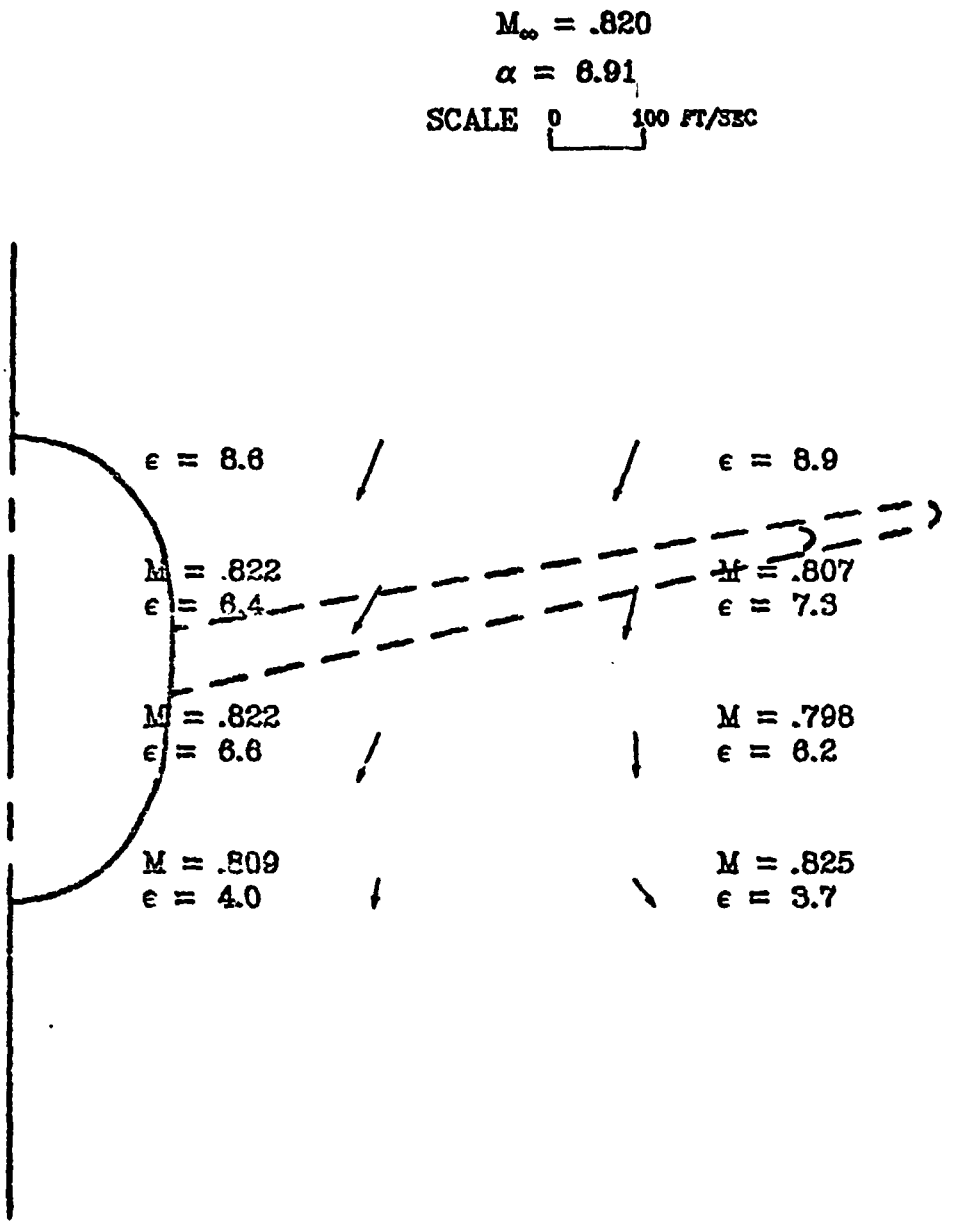

Figure 33. - Continued.

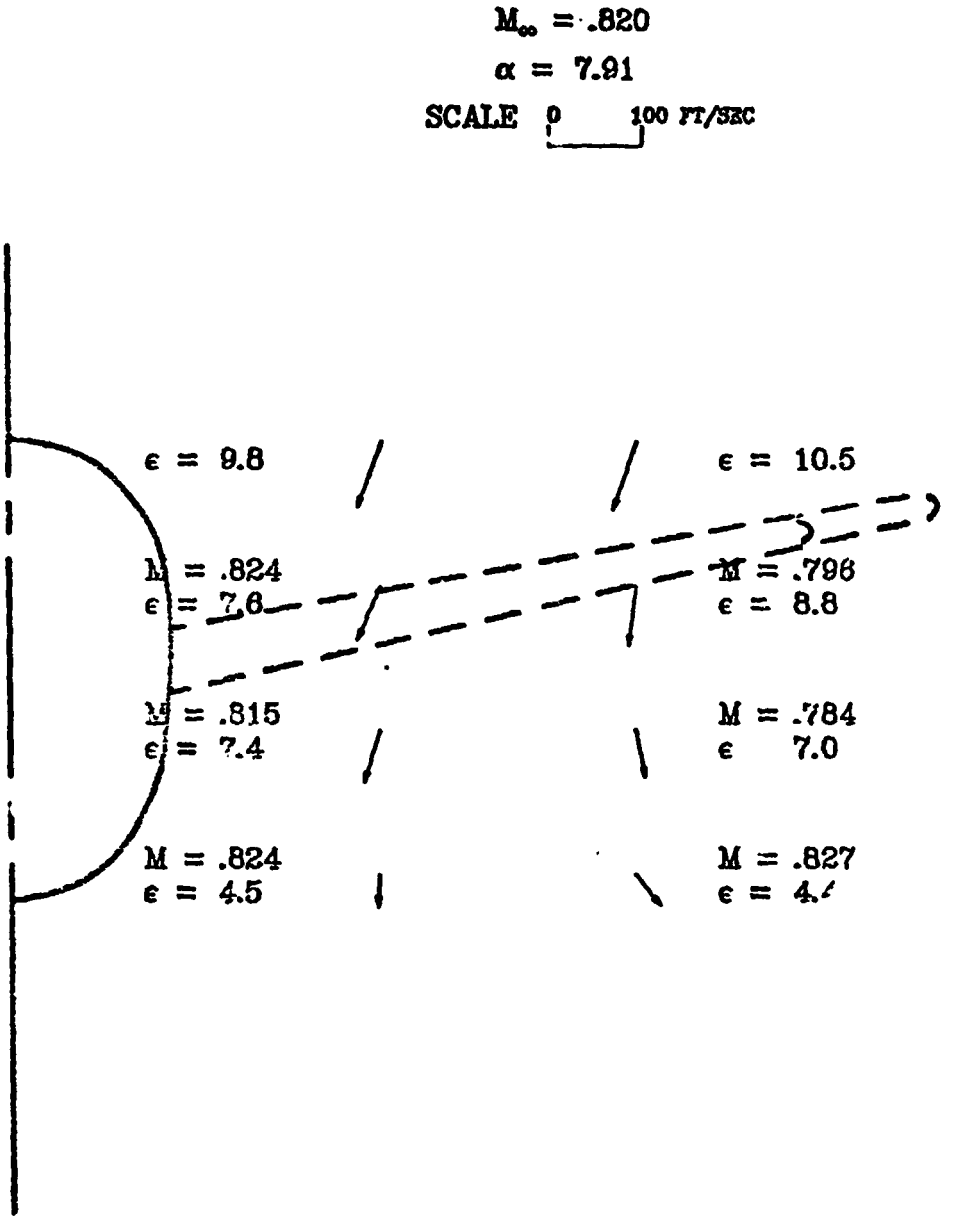

Figure 33. - Concluded.

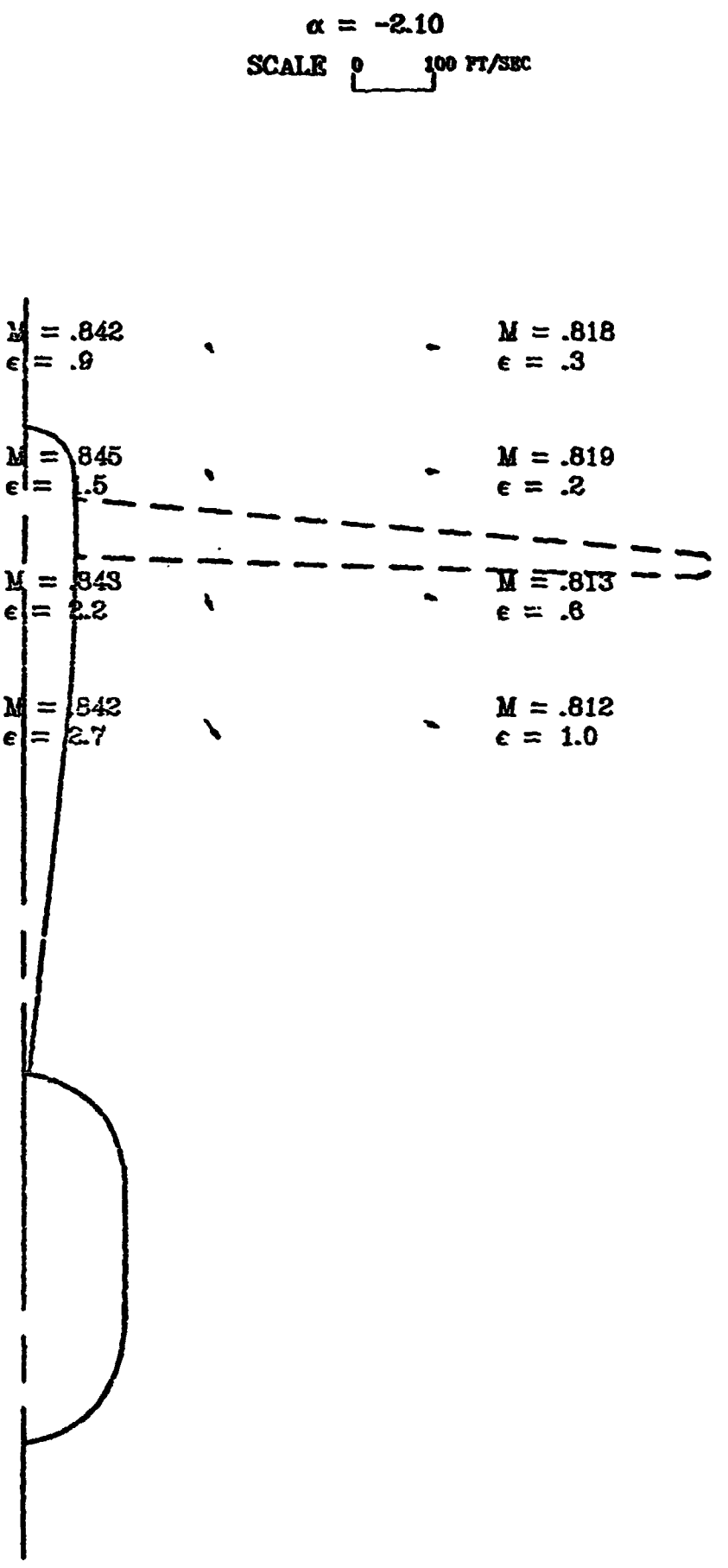

Figure 34.- Local Mach numbers and flow field velocity vectors behind the supercritical wing (T-tail configuration).

$M_\infty = .819$

$\alpha = -.09$

SCALE 0 100 FT/SEC

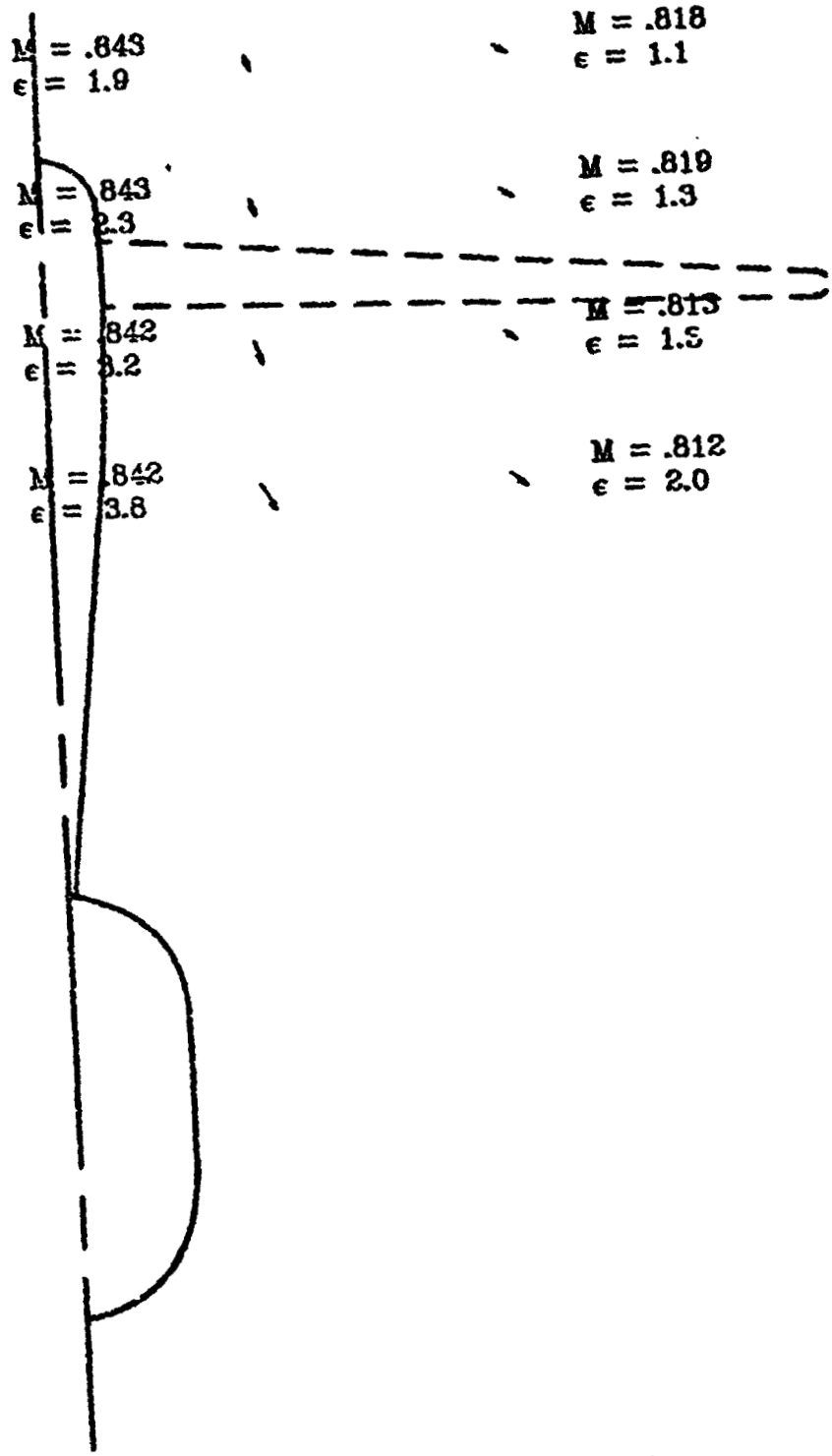

Figure 34.- Continued.

$M_\infty = .819$

$\alpha = .93$

SCALE 0 100 FT/SEC

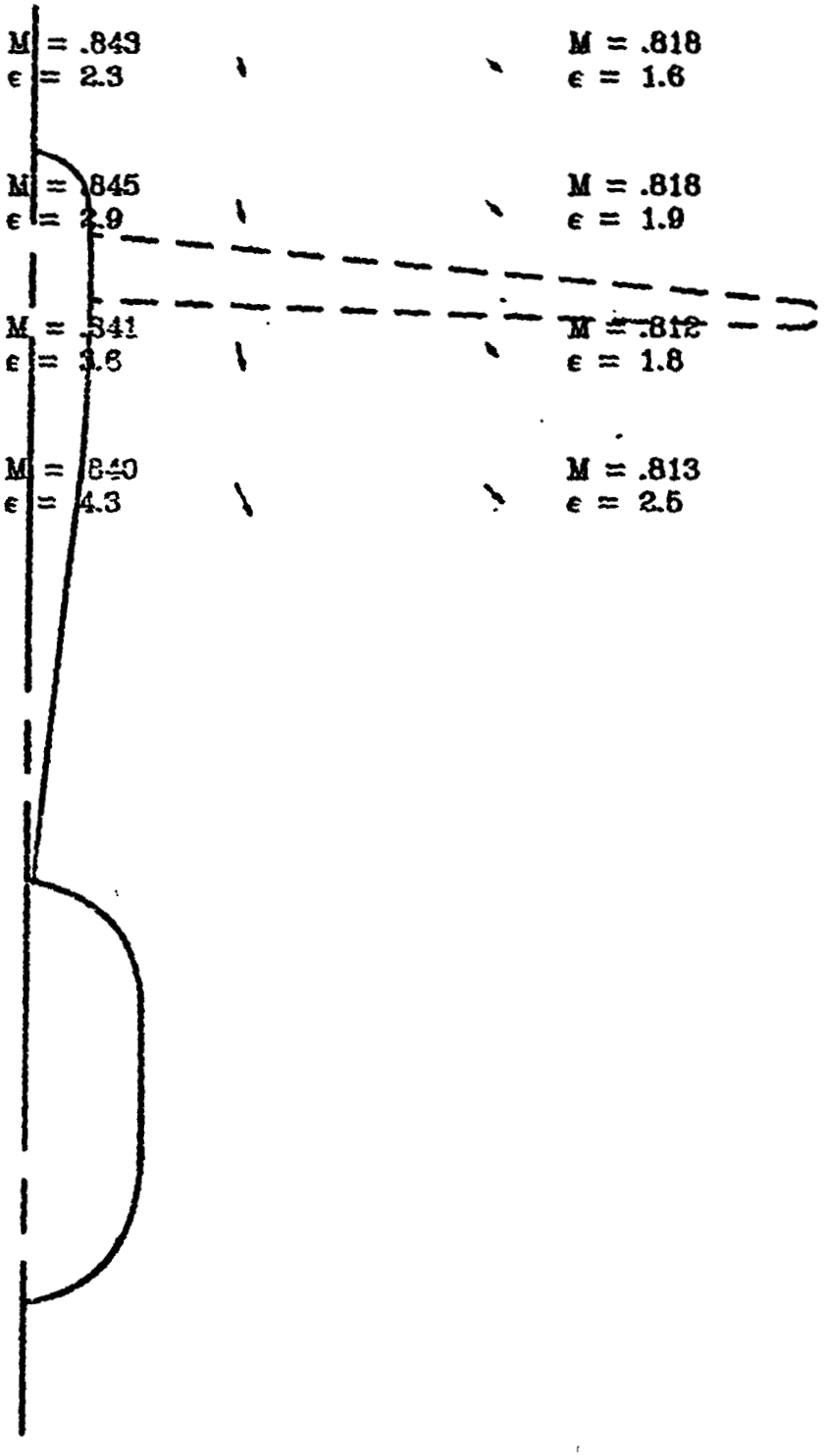

Figure 34. - Continued.

$M_\infty = .819$

$\alpha = 1.44$

SCALE 0 100 FT/SEC

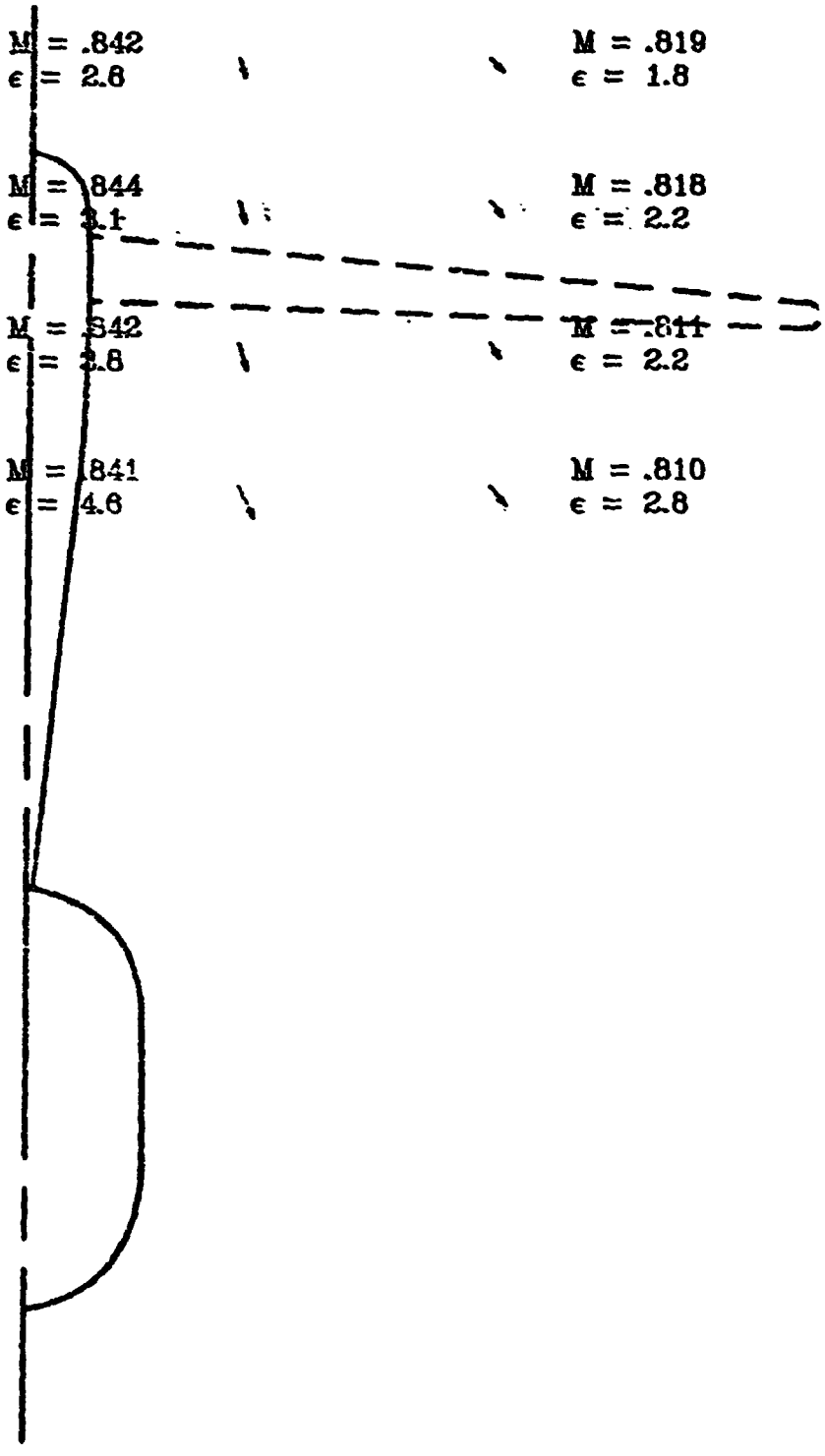

Figure 34. - Continued.

M_∞ = .818

α = 1.92

SCALE 0 100 FT/SEC

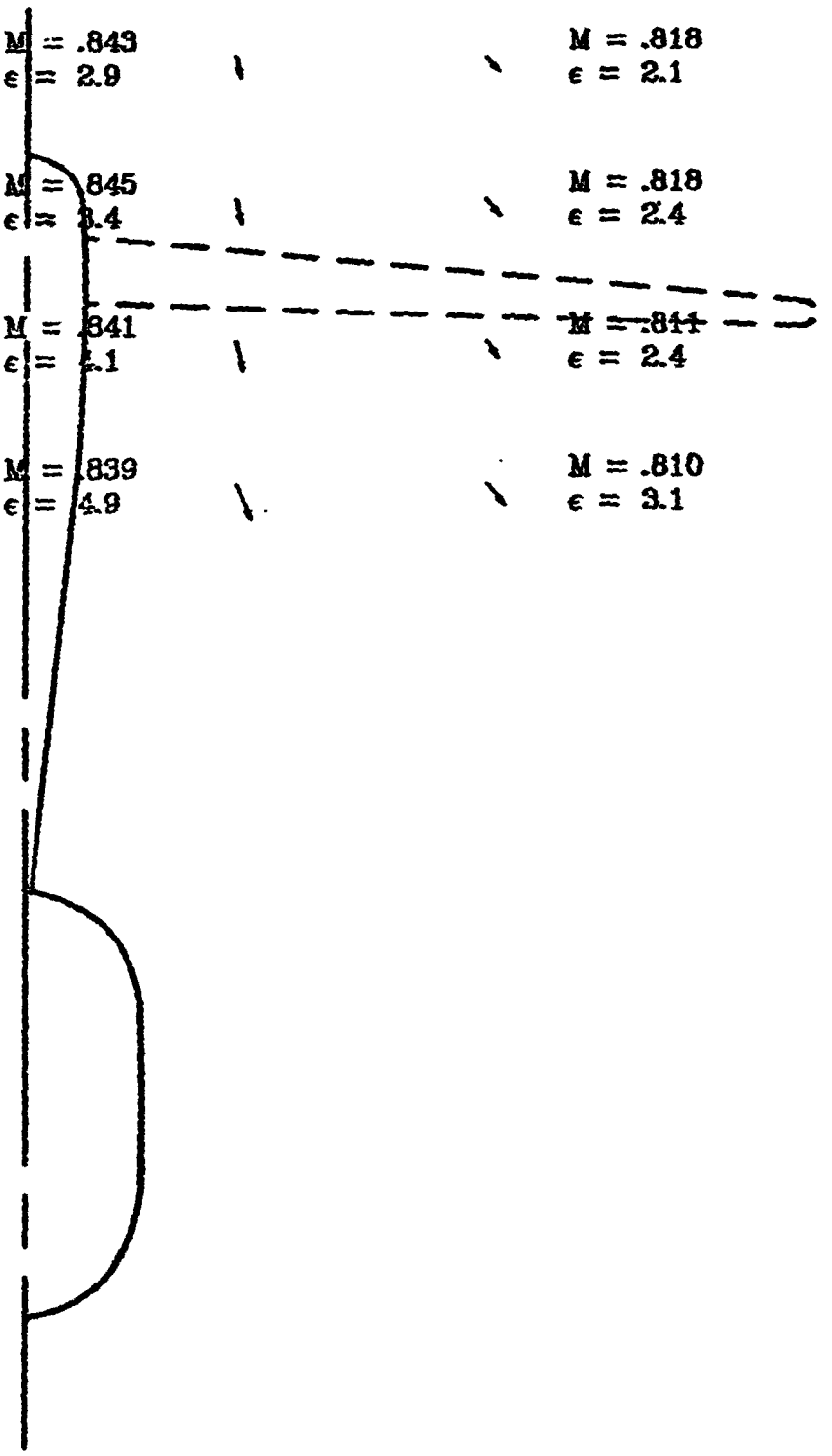

Figure 34. - Continued.

$M_\infty = .819$

$\alpha = 2.42$

SCALE 0 100 FT/SEC

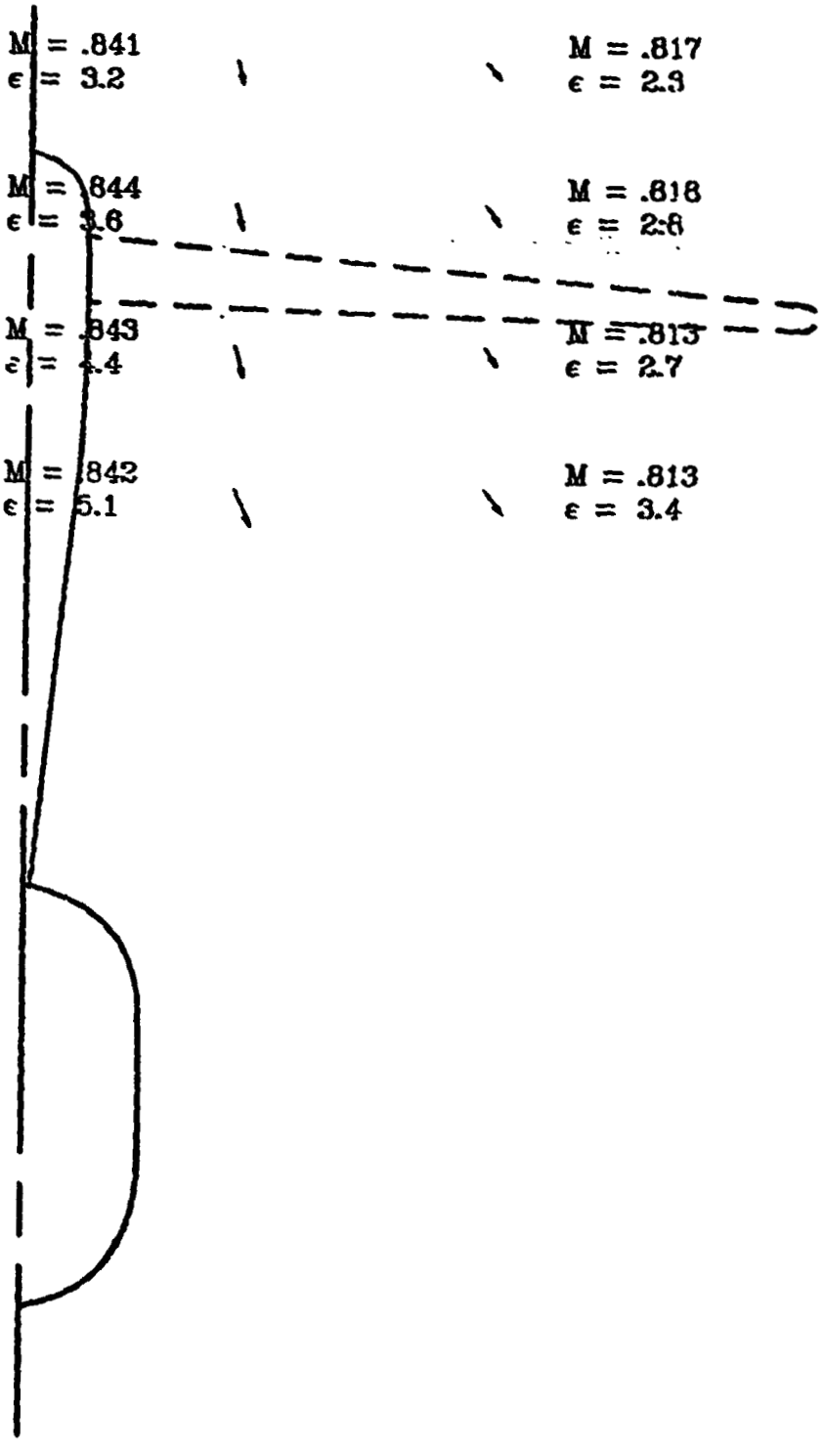

Figure 34. - Continued.

$M_\infty = .820$

$\alpha = 2.90$

SCALE 0 100 FT/SEC

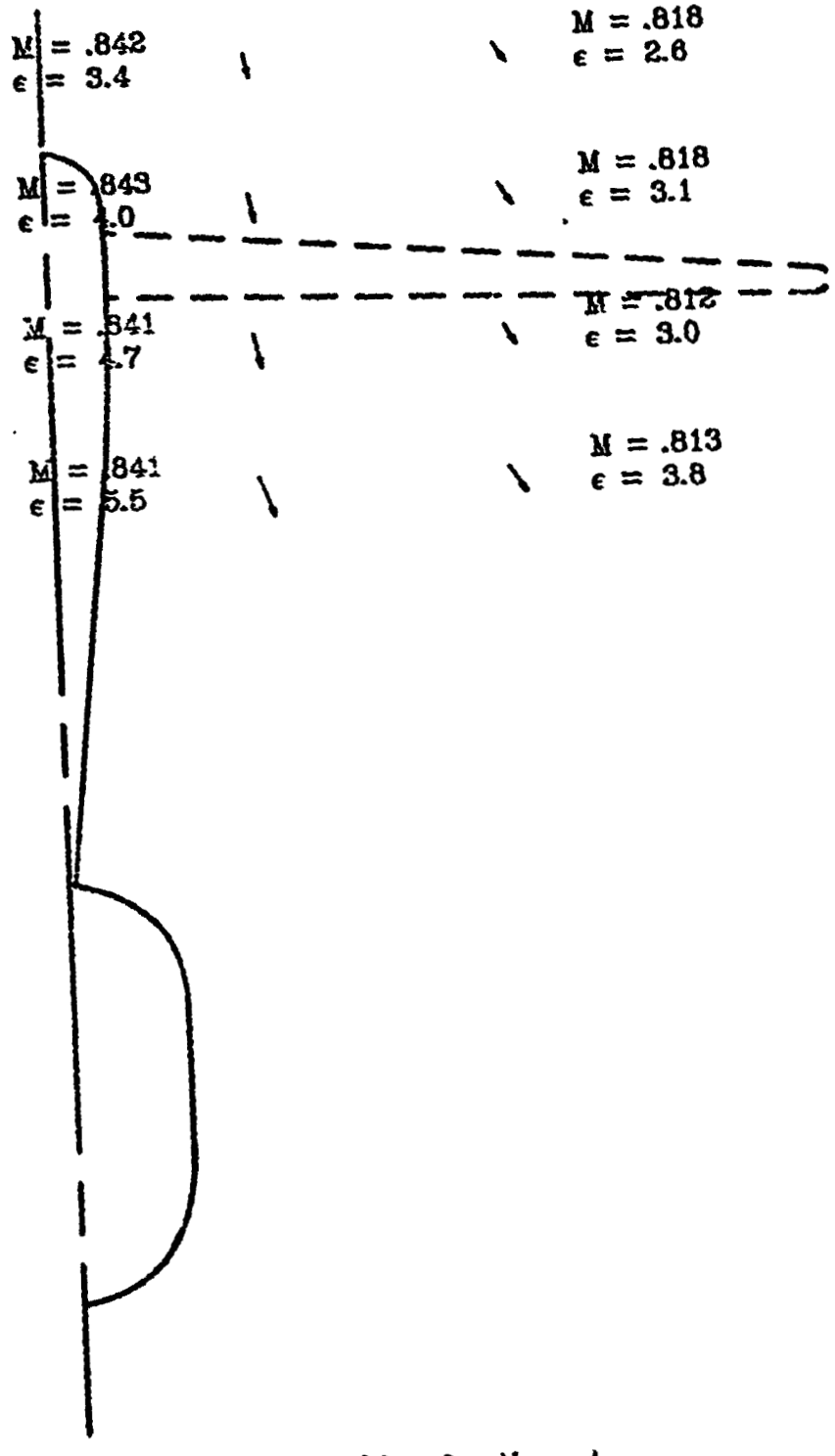

Figure 34. - Continued.

$M_\infty = .818$

$\alpha = 3.43$

SCALE 100 FT/SEC

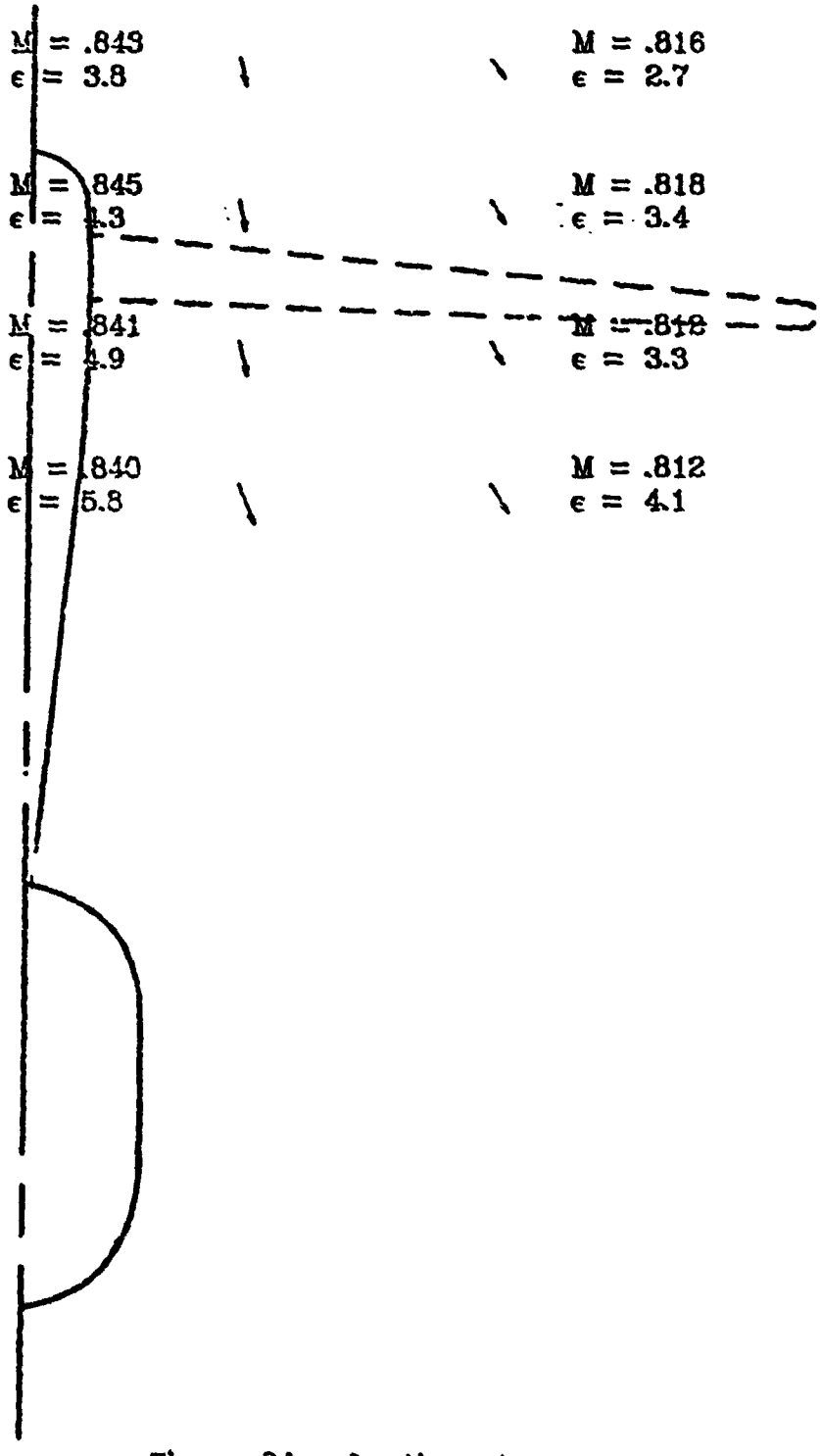

Figure 34.- Continued.

$M_\infty = .820$

$\alpha = 3.95$

SCALE 0 100 FT/SEC

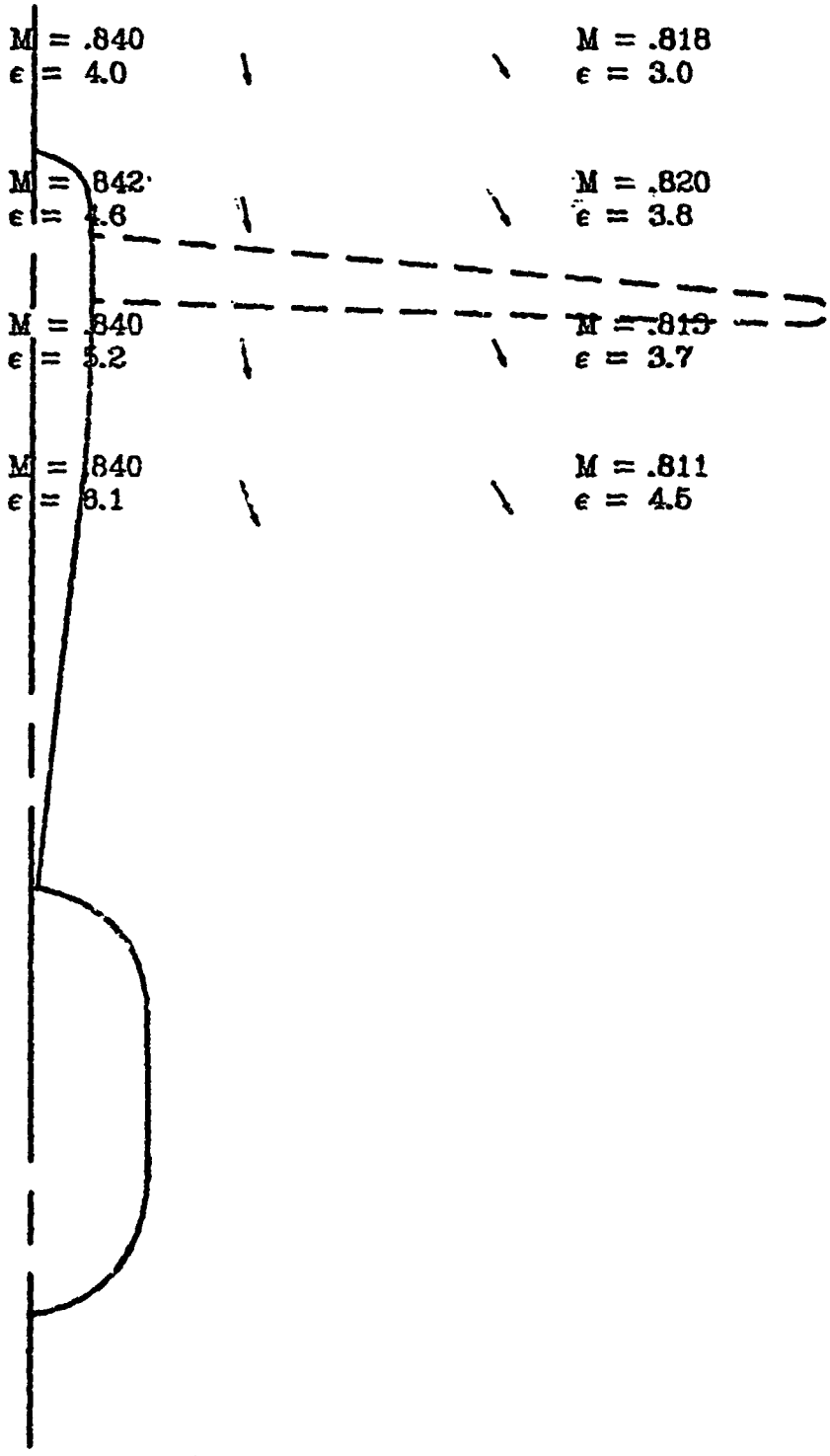

Figure 34. - Continued.

$M_\infty = .820$

$\alpha = 4.96$

SCALE 0 100 FT/SEC

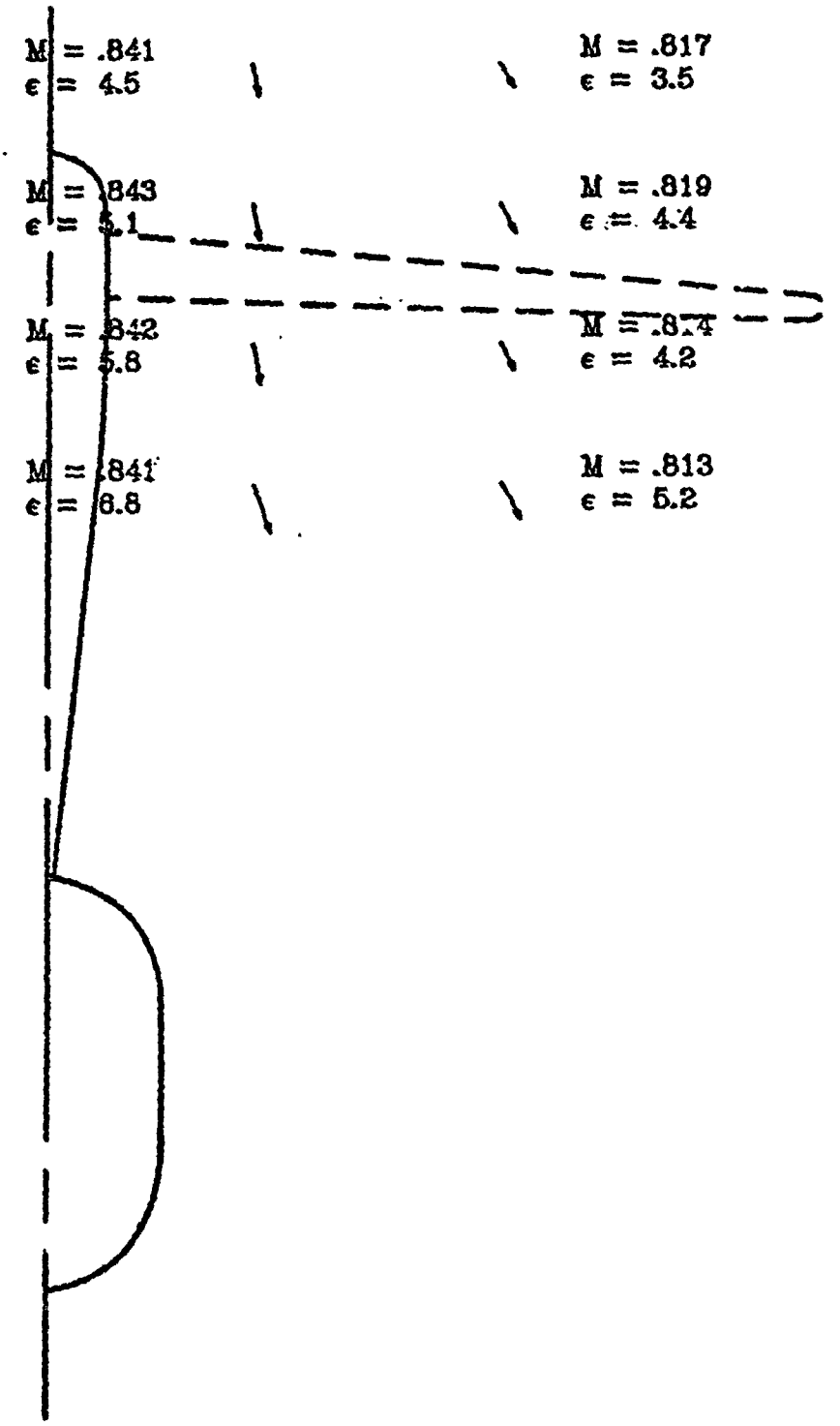

Figure 34. - Continued.

$M_\infty = .819$

$\alpha = 5.91$

SCALE 0 100 FT/SEC

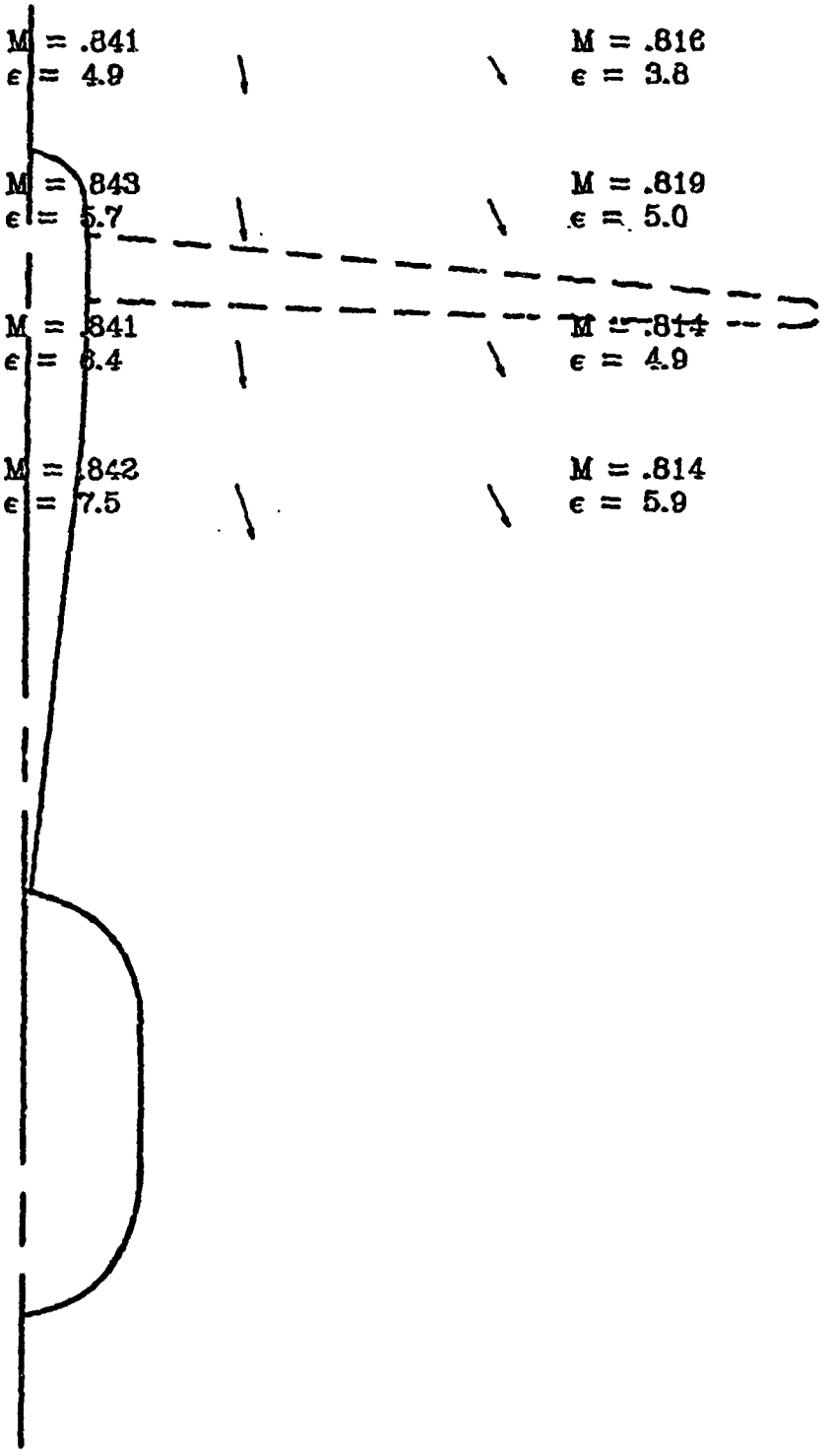

Figure 34. - Continued.

$M_\infty = .819$

$\alpha = 6.85$

SCALE 0 100 FT/SEC

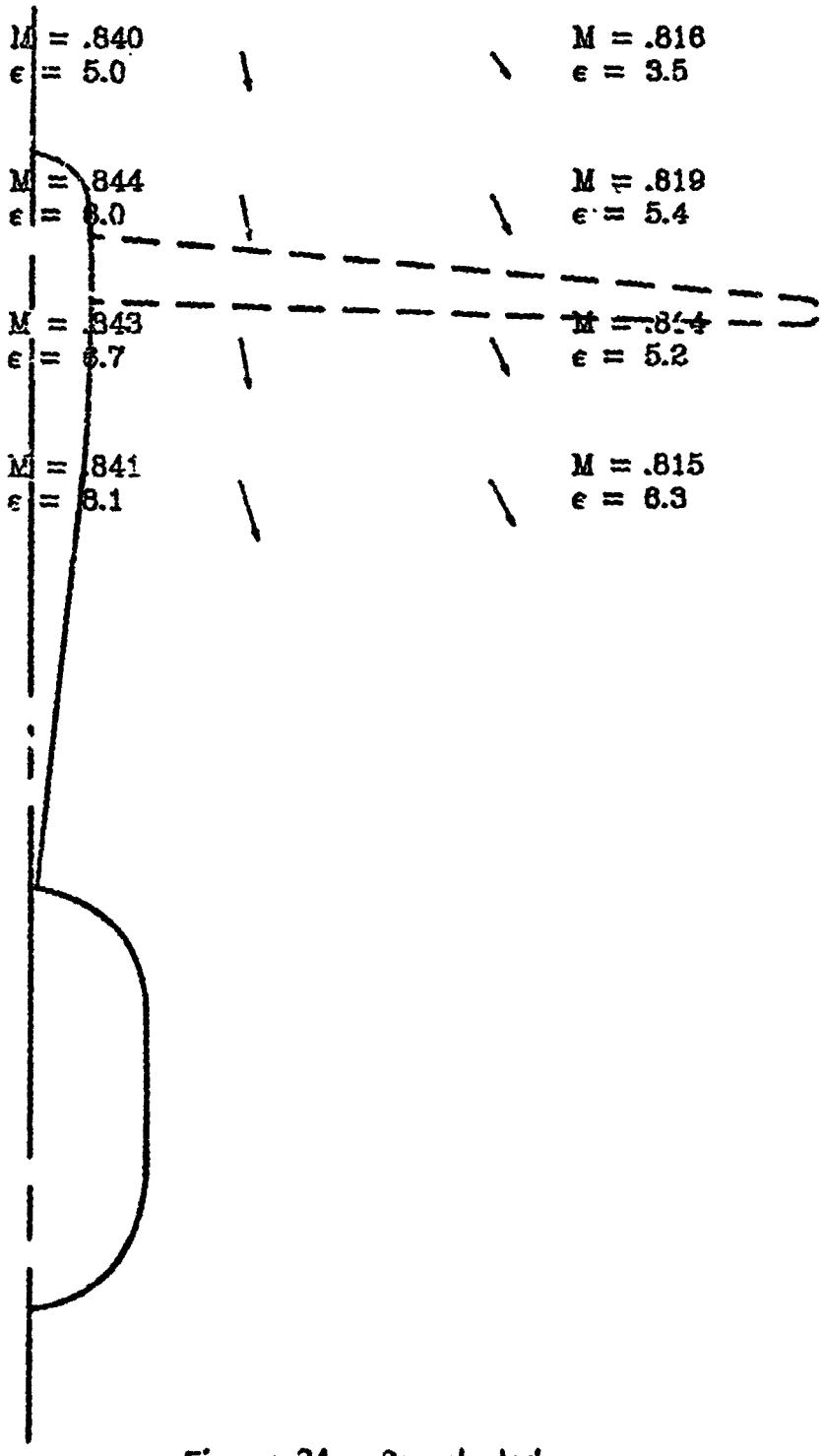

Figure 34. - Concluded.

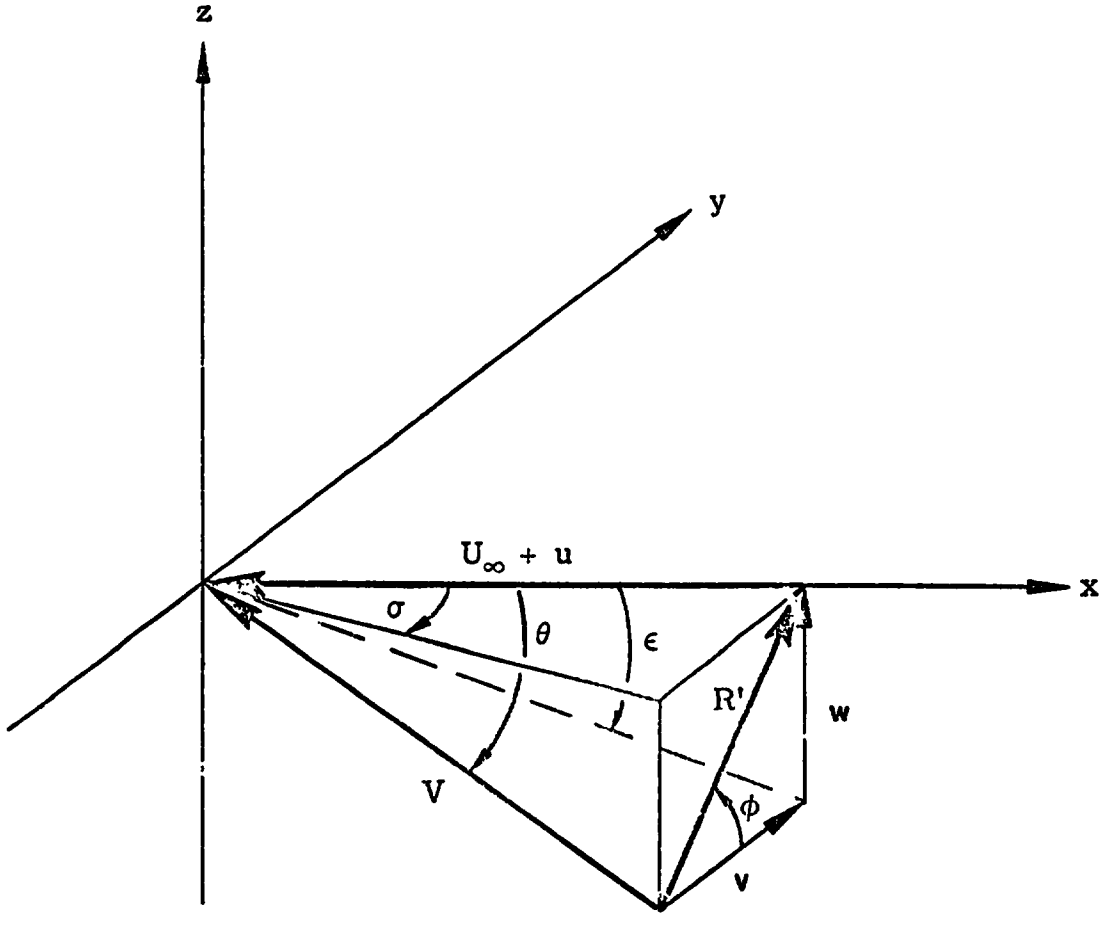

Figure 35.- Schematic drawing of flow field velocity vectors.

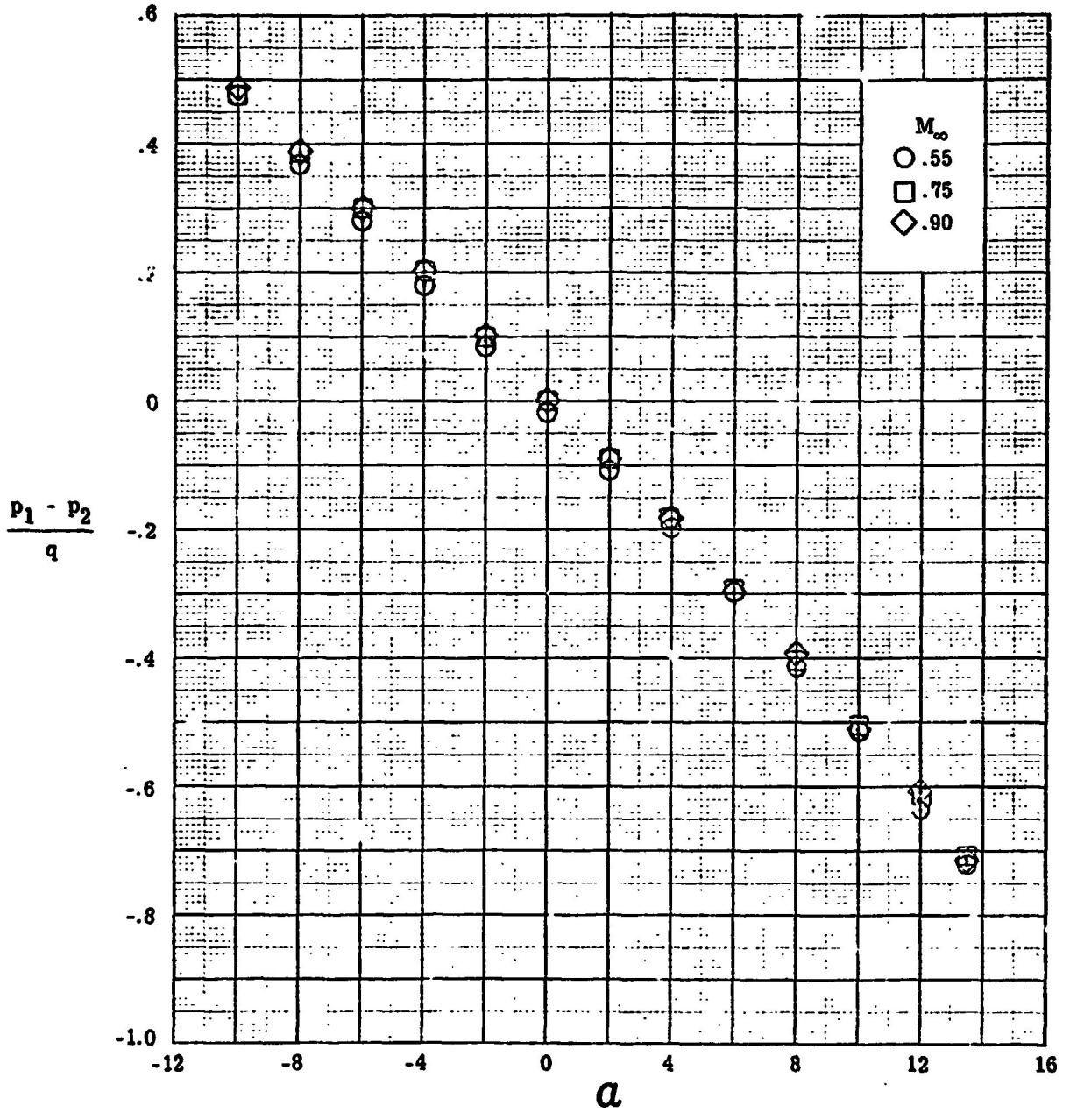

Figure 36.- Variation of nondimensionalized pressure difference with angle of attack for typical yaw head.

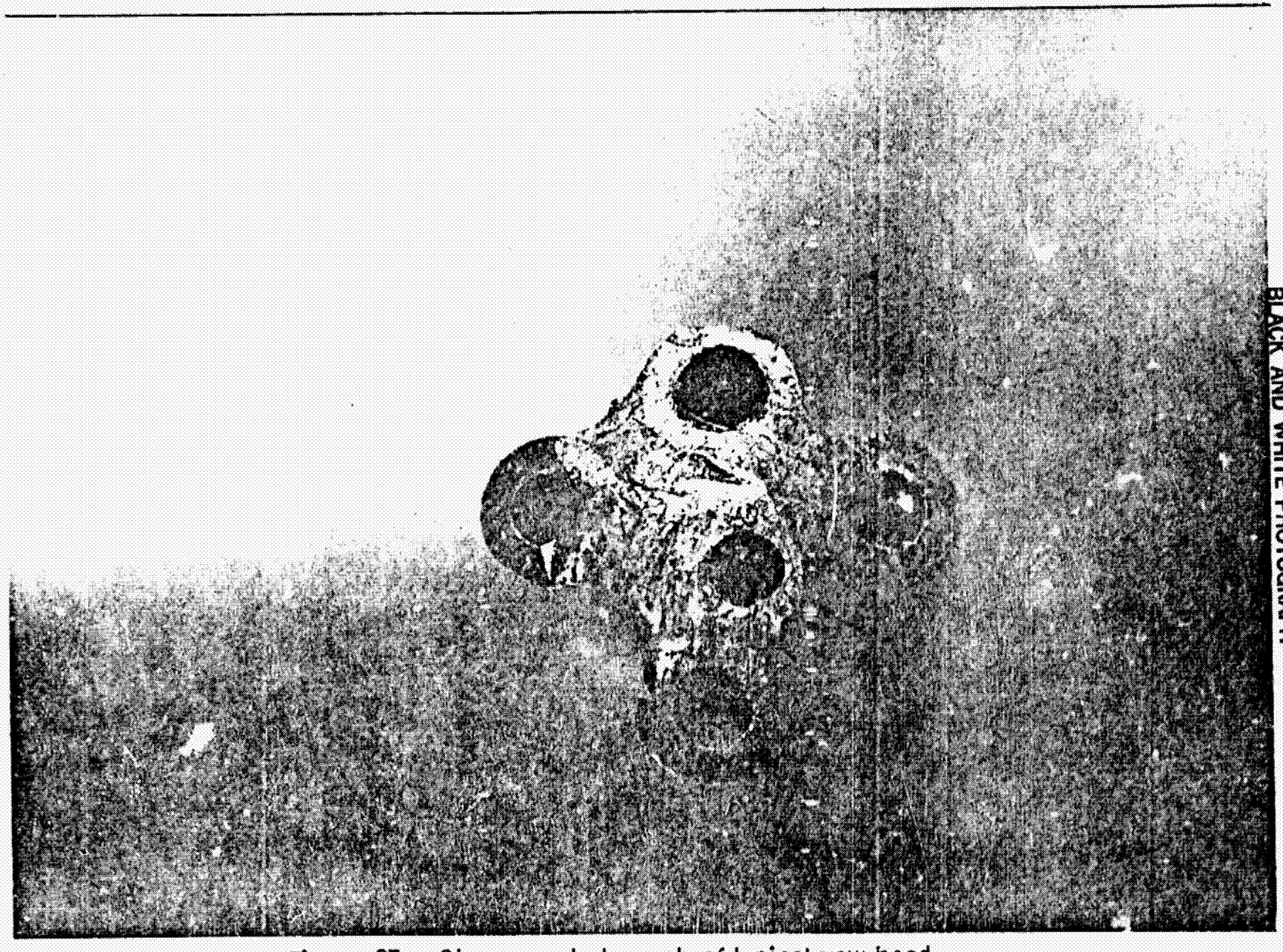

ORIGINAL PAGE
BLACK AND WHITE PHOTOGRAPH

Figure 37.- Close-up photograph of typical yaw head.